Structure and reactivity of nanoparticles

CO dissociation on Ruthenium, CO induced surface reconstruction of Platinum, Platinum and Platinum-Yttrium alloys for electrochemical Oxygen Reduction Reaction

Strebel, Christian Ejersbo

Publication date:
2012

Document Version
Publisher's PDF, also known as Version of record

Center for Individual Nanoparticle Functionality

Technical University of Denmark

STRUCTURE AND REACTIVITY OF NANOPARTICLES

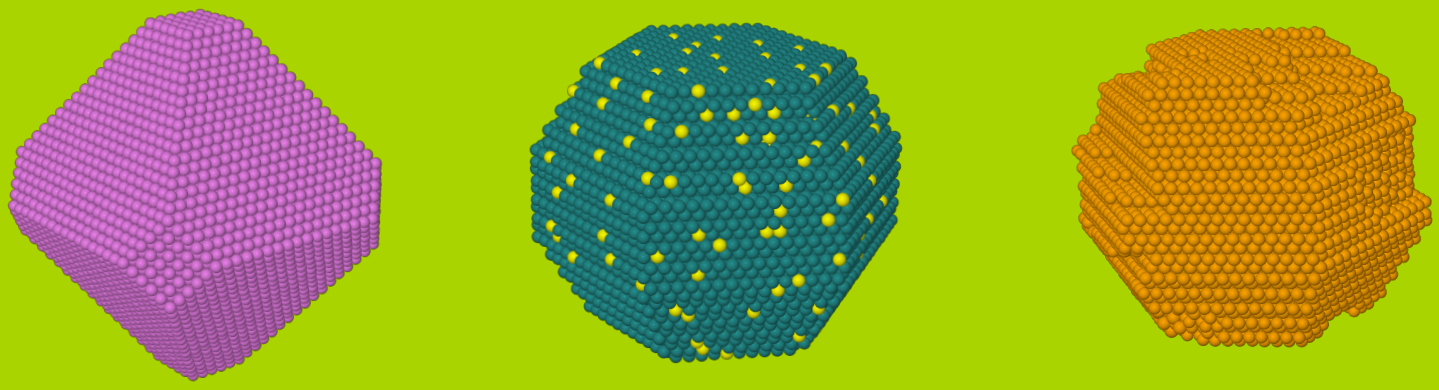

CO dissociation on Ruthenium
CO induced surface reconstruction of Platinum
Platinum and Platinum-Yttrium alloys for Oxygen Reduction Reaction

CENTER FOR INDIVIDUAL NANOPARTICLE FUNCTIONALITY
DEPARTMENT OF PHYSICS
TECHNICAL UNIVERSITY OF DENMARK
CHRISTIAN STREBEL
OCTOBER 2012

PhD thesis
Department of Physics
Center For Individual Nanoparticle Functionality (CINF)
The Technical University of Denmark (DTU)

Structure and reactivity of nanoparticles

CO dissociation on Ruthenium.

CO induced surface reconstruction of Platinum.

Platinum and Platinum-Yttrium alloys for electrochemical Oxygen Reduction Reaction.

Christian Strebel
October 2012

Preface

The work presented in this thesis was carried out at the center for individual nanoparticle functionality (CINF) funded by the Danish National Research Foundation placed at the Technical University of Denmark, Department of Physics. The research has been carried out from september 2009 to october 2012 with Professor Ib Chorkendorff as main supervisor and Professor Jane Hvolbæk Nielsen as co-supervisor. CINF is funded by the Danish National Research Foundation which is greatly acknowledged for its support to this project.

My work on this project has been performed on an ultra high vacuum (UHV) chamber utilizing surface science techniques, but a large part of the results has been achieved through a fruitful collaboration with the electro chemistry lab at CINF. Such collaborations are, in my mind, highly productive and by combining the skills from each field we were able to gain a broad understanding and a high level of detailed information on the systems examined.

I have had a great time as a PhD student at CINF, and I feel privileged for the opportunity to work with such elaborate experimental equipment and with such an inspiring group of people. The open and collaborative working atmosphere at CINF has truly been a pleasure to be a part of. I would like to thank my supervisor Ib Chorkendorff and co-supervisor Jane H. Nielsen for excellent supervision and giving me inspiration through our discussions. I would also like to thank Dr. Shane Murphy, Dr. David Norman McCarthy and Anders Nierhoff with whom I have worked closely on the experimental setup, and also Dr. Francisco J. Perez-Alonso, Dr. Patricia Hernandez-Fernandez and Dr. Ifan E. L. Stephens from the electro chemical lab for great collaboration and their work that contributes greatly to my thesis. Furthermore I would like to thank all my colleagues at CINF, and in particular, Thomas Andersen, Robert Jensen, Kenneth Nielsen, Christian Conradsen, Christian Holse, Tobias Johansson, Jan Kehres, Paolo Malacrida and Thomas Pedersen.

Most importantly, I would like to thank my wife Anna and my three fantastic girls Karen, Søs and Ebba for all their support and great spirit. I dedicate this thesis to you.

Lyngby, October 12th 2012

Christian Strebel

Abstract

The correlation between the structure and reactivity of mass-selected nanoparticles have been investigated by the surface science approach for two model systems: 1) The dissociation of CO on ruthenium and 2) platinum and platinum-yttrium alloy tested for the electrochemical Oxygen Reduction Reaction (ORR). Furthermore, surface reconstructions of platinum nanoparticles induced by CO have been studied for various particle sizes.

All the model catalysts consisted of mass-selected nanoparticles supported on planar oxide or carbon substrates. The nanoparticles were produced in a ultra high vacuum (UHV) setup by the magnetron sputter gas-aggregation technique and mass-selected before deposition onto the support. This approach provides well-defined model catalysts with mono-dispersed nanoparticles where the particle size and particle coverage can be varied independently, ideal for studying particle size effects. The model catalysts are furthermore compatible with UHV surface science techniques which enables detailed characterisation of the particle structure, elemental composition and reactivity.

In the study of CO dissociation on ruthenium, nanoparticles in the size range from 3 to 15 nm were deposited onto Highly Ordered Pyrolytic Graphite (HOPG) and the active sites for CO dissociation were probed by temperature programmed desorption spectroscopy using isotopically labelled CO. Combined with transmission electron microscopy we gain insight on how the size and morphology of the nanoparticles affect the CO dissociation activity. Surprisingly, it was found that larger particles exposed a higher fraction of active sites. It is suggested that this is due to larger particles exposing a more rough surface, that contain a high fraction of under-coordinated sites, than the smaller particles. The variation in surface roughness with particle size is a proposed to be a consequence of the growth processes in the gas-aggregation chamber. Furthermore, we provided a link in the CO desorption behaviour from Ru single crystal model catalysts to nanoparticulate model catalyst, in order to narrow the materials gap.

The activity of platinum and platinum-yttrium nanoparticles supported on glassy

carbon for the electrochemical ORR was studied in the size range from 2 to 11 nm, and a size dependence for both pure platinum and platinum-yttrium nanoparticles was established. For pure platinum, the specific activity was found to increase with increasing particle size, and the specific activity correlates to the fraction of terrace sites. It was therefore concluded that the active sites for ORR on platinum are located on the terraces, in good agreement with earlier theoretical predictions. A maximum in the mass activity was found for ∼3 nm diameter particles. For the Pt_xY nanoparticles, a clear enhancement of the ORR activity compared to pure platinum nanoparticles was observed, and to the best of our knowledge, the 9 nm Pt_5Y nanoparticles display the highest ORR activity ever measured on supported nanoparticles. The origin of the enhanced activity is speculated to be caused by a compressed platinum overlayer covering a Pt_xY alloy core.

The topic of adsorbate induced surface reconstructions was elucidated for a model catalyst of platinum nanoparticles on SiO_2 support and a Pt(111) single crystal, which was exposed to an elevated pressure of CO. Exposing the roughened Pt(111) crystal to mbar range pressures of CO at elevated temperatures gave rise to a promotion of the annealing process whereas the same treatment of the 3 nm and 6 nm platinum particles induced an apparent surface roughening. The 11 nm particles showed only a minor increase in surface roughening. We hypothesize that the differences in CO induced surface reconstruction with particle size is related to the facets size and the distribution of surface atoms with low coordination number.

The results highlight the structure sensitivity of catalytic reactions and the influence of adsorbates and gaseous environment on the structure of nanoparticles. The results furthermore demonstrated the use of temperature programmed desorption experiments as a sensitive probe of the configuration of surface sites and the ability to distinguish between low index facets and under-coordinated atoms on both single crystal and nanoparticle model catalysts.

Dansk Resumé

Sammenhængen mellem struktur og reaktivitet af masse-selekterede nanopartikler er blevet undersøgt gennem en "surface science" tilgang til to modelsystemer: 1) dissociation af CO på ruthenium og 2) platin og platin-yttrium legering testet for den elektrokemiske Oxygen ReduktionsReaktion (ORR). Desuden er overfladen rekonstruktioner af platin nanopartikler induceret af CO blevet undersøgt for forskellige partikelstørrelser.

Alle model-katalysatorer bestod af masse-udvalgte nanopartikler på plane oxid- eller kulsubstrater. Nanopartiklerne blev fremstillet i et ultra højt vakuum (UHV) kammer ved hjælp af magnetron sputter gas-aggregerings-teknikken og masse-selekteret, før deponering på substratet. Denne fremgangsmåde giver veldefinerede model katalysatorer med mono-dispergerede nanopartikler, hvor partikelstørrelse og partikel dækning kan varieres uafhængigt, ideel til undersøgelse partikelstørrelses effekter. Model-katalysatorerne er desuden kompatible med UHV "surface science" teknikker, som muliggør detaljeret karakterisering af partikelstrukturen, grundstofsammensætning og reaktivitet.

I undersøgelsen af CO dissociation på ruthenium, blev nanopartikler i størrelsesområdet 3 - 15 nm deponeret på yderst ordnet pyrolytisk grafit (HOPG) og de aktive sites for CO dissociation blev probet ved temperaturprogrammeret-desorptions-spektroskopi med isotop mærket CO. Kombineret med transmissionselektronmikroskopi opnår vi indsigt i, hvordan størrelse og morfologi af nanopartiklerne påvirker aktiviteten for CO dissociation. Overraskende blev det konstateret, at større partikler eksponerer en højere fraktion af aktive sites. Det foreslås, at dette skyldes at de store partikler eksponerer en mere ru overflade, der indeholder en høj fraktion af under-koordinerede sites, end de mindre partikler. Variationen i overfladeruhed med partikelstørrelse foreslåes at være en konsekvens af vækstprocesserne i gas-aggregerings-kammerret. Endvidere har vi tilvejebragt et link mellem CO desorption kendetegnene fra Ru enkeltkrystallinske model-katalysatorer til nanopartikulære model katalysator, for at mindske kløften mellem de to typer materialerne.

Aktiviteten af platin og platin-yttrium nanopartikler på glassy carbon for den

elektrokemiske ORR blev undersøgt i størrelsesområdet fra 2 til 11 nm, og en størrelsesafhængighed for både ren platin og platin-yttrium nanopartikler blev etableret. For ren platin, blev den specifikke aktivitet fundet til at stige med stigende partikelstørrelse, og den specifikke aktivitet korrelerer med fraktionen af terrasse sites. Det blev derfor konkluderet, at de aktive sites for ORR på platin er placeret på terrasserne, i god overensstemmelse med tidligere teoretiske forudsigelser. Et maksima i massen-aktivitet blev fundet for partikler med $\sim$3 nm i diameter. For Pt_xY nanopartikler blev der observeret en klar forbedring af ORR aktivitet i forhold til rene platin nanopartikler, og efter vores bedste overbevisning, udviste de 9 nm Pt_5Y nanopartikler den højeste ORR aktivitet nogensinde målt på nanopartikler. Det foreslås at oprindelsen af den forøgede aktivitet er forårsaget af et komprimeret platin overlag som dækker en kerne bestående af en Pt_xY legering.

Emnet for adsorbat inducerede overflade rekonstruktioner blev belyst med en model katalysator af platin nanopartikler på et SiO_2 substrat og en Pt(111) enkeltkrystal, som blev udsat for et forhøjet tryk af CO. Den ru Pt(111) krystal blev udsat for et mbar tryk af CO ved høje temperaturer hvilket gav anledning til en forfremmelse af udglatningsprocessen hvorimod samme behandling af 3 nm og 6 nm platin partikler tilsyneladende inducerede en overflade ruhed. 11 nm partiklerne viste kun en mindre stigning i overfladen ruhed. Hypotesen er at de observerede forskelle i CO induceret overflade rekonstruktion med partikelstørrelse er relateret til facet-størrelsen og fordelingen af overfladeatomer med lav koordinationstal.

Resultaterne fremhæver struktur-følsomheden af katalytiske reaktioner og påvirkning fra adsorbater og gas-atmosfæren på strukturen af nanopartikler. Resultaterne viser desuden, at brugen af temperatur-programmeret-desorptions-eksperimenter er en følsom metode til at probe konfigurationen af overflade sites og til at skelne mellem lav-indeks facetter og under-koordinerede atomer på både enkeltkrystal og nanopartikel model-katalysatorer.

List of included papers

Paper I:

A comparative STM study of Ru nanoparticles deposited on HOPG by mass-selected gas aggregation versus thermal evaporation

R.M. Nielsen, S. Murphy, **C. Strebel**, M. Johansson, J.H. Nielsen, I. Chorkendorff
Published in Surface Science **603** (2009), 3420-3430

Paper II:

The morphology of mass selected ruthenium nanoparticles from a magnetron-sputter gas-aggregation source

R. M. Nielsen, S. Murphy, **C. Strebel**, M. Johansson, I. Chorkendorff, J. H. Nielsen
Published in J Nanopart Res **12** (2010), 1249-1262

Paper III:

Catalytic oxidation of graphite by mass-selected ruthenium nanoparticles

S. Murphy, R.M. Nielsen, **C. Strebel**, M. Johansson, J.H. Nielsen
Published in Carbon **49** (2011), 376-385

Paper IV:

Probing the crossover in CO desorption from single crystal to nanoparticulate Ru model catalysts

S. Murphy, **C. Strebel**, S. B. Vendelbo, C. Conradsen, Y. Tison, K. Nielsen, L. Bech, R. M. Nielsen, M. Johansson, I. Chorkendorff and J. H. Nielsen
Published in Phys. Chem. Chem. Phys. **13** (2011), 10333-10341

Paper V:

Probing the active sites for CO dissociation on ruthenium nanoparticles

Christian Strebel, Shane Murphy, Rasmus M. Nielsen, Jane H. Nielsen and Ib Chorkendoff
Published in Phys. Chem. Chem. Phys. **14** (2012), 8005-8012

Paper VI:

The Effect of Size on the Oxygen Electroreduction Activity of Mass-Selected Platinum Nanoparticles

Dr. Francisco J. Perez-Alonso, Dr. David N. McCarthy, Anders Nierhoff, Dr. Patricia Hernandez-Fernandez, **Christian Strebel**, Dr. Ifan E. L. Stephens, Prof. Jane H. Nielsen, Prof. Ib Chorkendorff
Published in Angew. Chem. Int. Ed. **51** (2012), 4641-4643

Paper VII:

Structural modification of Pt model systems under high pressure CO annealing

D.N. McCarthy, **C.E. Strebel**, T.P. Johansson, A. den Dunnen, A. Nierhoff, J.H. Nielsen, and Ib Chorkendorff
Published in The Journal of Physical Chemistry **116** (2012), 15353-15360

Contents

Chapter 1

Introduction

The work presented in this thesis involves fundamental research in the area of heterogeneous catalysis, limited to solid model catalysts interacting with gas phase molecules. The work has been focussed around how the reactivity of supported nanoparticles correlate to the particle morphology. This subject has been studied experimentally by fabricating model catalysts consisting of mass selected nanoparticles deposited onto planar supports. The model catalysts have primarily been investigated by surface science techniques using an ultra high vacuum setup, with the exception of one model system that was tested in an electrochemical cell by collaboration with the electrochemical lab at CINF. In general, it has been a collaborative project involving several other PhD students and post-docs at other ultra high vacuum setups and at an electrochemical cell setup, very much in line with the scientific philosophy at CINF.

In this chapter the research topic will be motivated and key concepts within heterogeneous catalysis and the reactivity of supported nanoparticles will be introduced and serve as the basis for understanding the origin of the catalytic properties of a catalyst and how it is possible to tailor the properties of a catalyst.

1.1 Heterogeneous Catalysis

A chemical reaction between molecules involve a transformation by bond breaking and bond making. Thermodynamics determine the possible extent of this transformation, i.e. the equilibrium constants. A catalyst is defined as a compound that accelerates the reaction (influences the kinetics) by providing an alternative reaction pathway, as illustrated in Figure 1.1, without being consumed in the process. The catalyst works by interacting with the reactant molecules (forming chemical bonds

with them) leading to lower activation barriers and, hence, a higher rate of reaction.

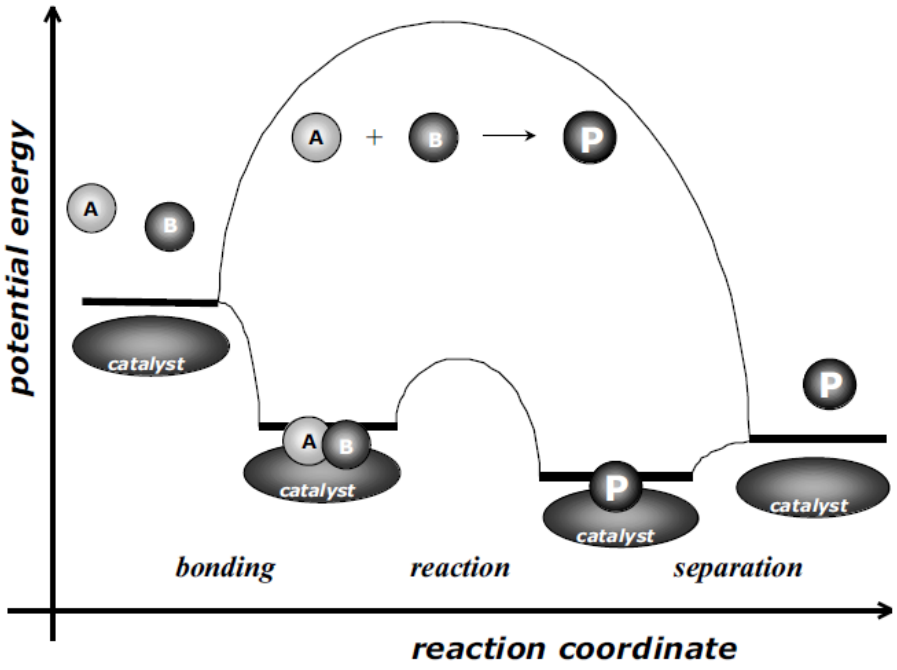

Figure 1.1: Potential energy diagram of a catalysed and non-catalysed reaction. It illustrates the role of the catalyst, providing an alternative reaction pathway. Note that the alternative reaction pathway facilitated by the catalyst has a much lower energy barrier than the non-catalysed pathway. Adapted from [1].

Catalysis is, and has historically been, very important in the development of modern society. Catalysis is involved in nearly 90% of all chemical processes in the production of important products such as fuels, plastics, pharmaceuticals and ammonia (nitrate fertilizer)[1]. As an example, the ammonia production world-wide consumes ∼1 % of the total human related energy consumption, despite the use of catalysts and considerable improvements in the energy effectiveness of the process. Ammonia is primarily used to produce the agricultural fertilizer which is indispensable in the food production for the worlds growing population. The production of chemicals through catalytic processes can in many cases be utilized to avoid the use of toxic and hazardous reagents and solvents and to minimize the production of undesirable bi-products. The development of better catalysts is therefore essential for making the chemical industry more environmental friendly by minimizing the energy consumption and the production unwanted side products. Another great challenge lies within ensuring the future energy supply from sustainable energy sources such as wind, hydro and solar energy. The electric power production from these sources has a variable and intermittent output. In this regard, the conversion and storage

of renewable energy is essential. One approach is to convert electrical energy into chemical energy and in this conversion catalysis is a key component. The conversion of energy is unavoidably associated with an energy loss and the efficiency is primarily determined by the performance of the catalyst in use. Research in catalysis, leading to the development of better and economically viable catalysts is therefore essential if a larger part of the future energy production is to come from renewable energy sources.

Catalytic reactions on solids occur on the surface of the catalyst. The often expensive catalyst material is therefore utilized most efficiently by maximising the surface-to-volume ratio, and the active material in an industrial catalyst is thus typically highly dispersed into nanoparticles on a high surface area support. Fundamental research in catalysis has traditionally been conducted on extended surfaces (single crystals), but it has been found that nanoparticles can have significantly different catalytic properties. This motivates the study of nanoparticulate model catalysts to gain a deeper understanding of "real" industrial catalysts.

1.2 Understanding the reactivity of transition metal surfaces

A basic theoretical description of the parameters that govern the reactivity of a surface, will be presented in this section.

The origin of the reactivity of transition metal surface can be understood on the basis of the Newns-Anderson model[2, 3], which can broadly account for what happens when a molecule approaches and binds to a surface and accounts for the differences in reactivity through the transition metals in the periodic table[4, 5].

When a molecule approaches a surface it initially the feels a weak attractive Van der Waals forces and as the molecule approaches further towards the surface the molecule may be chemisorbed when the electronic wave functions of the molecule and the metal interact and if a rearrangement of the electronic configuration occurs. This is shown schematically in Figure 1.2b. Figure 1.2a illustrates the density of states of a transition metal which consist of a broad sp-band and a narrow d-band. The interaction between the electronic states of the molecule and the metal sp-band leads to a broadening and a downshift of the molecular energy levels, contributing to a bonding of the molecule to the surface. The interaction of the bonding and anti-bonding intra-molecular energy levels with the narrow d-band leads to a splitting

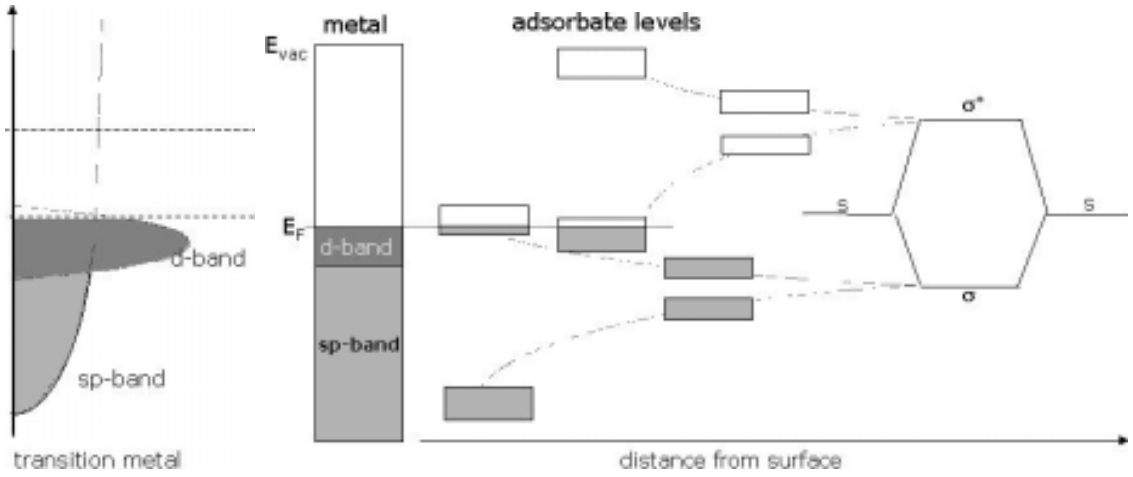

Figure 1.2: (a) Schematic drawing of the density of states of transition metals. Note the broad sp-band and the narrow d-band. (b) Molecule with a bonding σ orbital and an antibonding σ^* orbital interacting with the sp-band and d-band of the transition metal. Both adapted from [1].

of these levels which constitute the bonding and anti-bonding orbitals between the molecule and the metal. The bonding orbitals between the molecule and metal move down in energy and contribute to the bonding of the molecule, whereas the anti-bonding orbitals between the molecule and metal moves up in energy and weakens the bonding. The energy levels that fall below the metal Fermi energy will be filled and any filling of the intra-molecular anti-bonding orbital weakens the intra-molecular bond which may lead to dissociation of the molecule while simultaneously strengthens the bonding of the molecule to the surface. This is the essence of how a catalyst facilitates the dissociation of a molecule. The important conclusion is that the interaction with sp-band primarily contributes to the bonding of the molecule to the surface whereas the interaction between the metal d-band and anti-bonding molecular orbital determines whether the adsorbed molecule dissociates. It is the position of the d-band center that determines the degree of filling of anti-bonding molecular orbital and therefore in-turn the reactivity of a transition metal surface. The position of the d-band center is therefore a crucial parameter for understanding the variations in reactivity through the transition metals.

The catalytic activity of a surface is, however, not only a matter of minimizing the activation energy. If the surface is too reactive the molecules will easily dissociate, but the reactants, reaction intermediates or products will bind too strongly to the surface and block the surface to further reaction turn-overs. The optimal catalyst for a given reaction is therefore always subjected to a compromise between a low activation barrier and intermediate bonding of adsorbates. This concept is called

Sabatier's principle. Sabatier's principle gives rise to volcano shaped curves as shown in Figure 1.3 for ammonia synthesis. The figure nicely illustrates the fact that metals to the left in the periodic table are capable of dissociating N_2 but bind the adsorbed N-atoms too strongly whereas metals to the right are incapable of dissociating N_2, leading to a maximum activity for the metals with the best compromise.

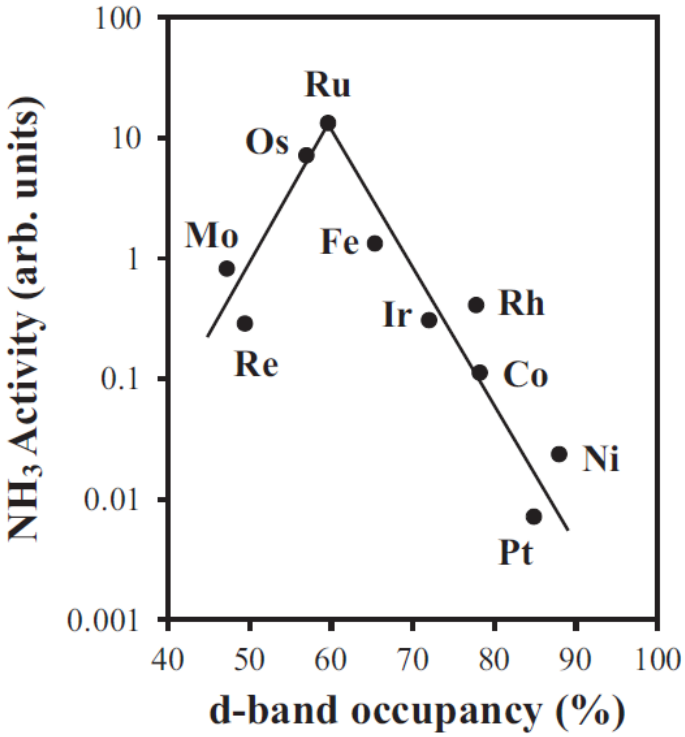

Figure 1.3: Volcano curve of the catalytic activity of various supported metals for ammonia synthesis as a function of the d-band occupancy of the metal. Adapted from [1], originally from [6].

1.3 Tailoring the reactivity

As explained in the previous section, the position of the d-band center determines the reactivity of a given surface. Finding a way to shift the d-band center for a given metal will therefore be a tool to tune or tailor the reactivity of that metal.

1.3.1 Stress or strain

For a given metal, the overlap between the electron orbitals of the surface atoms can be changed by introducing stress or strain in the surface, i.e. effectively compressing or expanding the lattice distance. This can also be seen as respectively increasing or

decreasing the average coordination of the surface atoms. A change in the overlap of the electron orbitals between the surface atoms will change the width of the d-band, and to maintain its filling degree the d-band center will have to move either up or down. This will alter the electronic properties of the surface and thereby also the reactivity. A compressed surface will be less reactive than a strained surface. Such stress or strain can be introduced by epitaxially growing a thin metal layer on top of another metal with a slight lattice mismatch. This can be done both on single crystals or in the form of core-shell nanoparticles.

1.3.2 Modifying the structure

The coordination number of surface atoms differ from one crystal facet to another. More open surfaces have a lower average coordination number than closed surfaces and are therefore generally more reactive. The same applies to under-coordinated surface atoms such as steps and kinks. As an example, the step sites (so-called B5 sites) on Ru(0001) were found to be nine orders of magnitude more active for N_2 dissociation (the rate limiting step in ammonia synthesis) than the facets [7, 8]. The B5-step sites are hereby completely dominating as active sites for ammonia synthesis compared to the close packed Ru(0001) surface. The dominating effect of under-coordinated adsorption sites emphasise the importance of controlling/predicting the atomic structure of the catalyst. This is also highly relevant for nanoparticles as they expose various crystal facets along with under-coordinated sites such as steps, kinks, edges and corners. The abundance of specific active sites is determined by the size and morphology of the nanoparticles, which hereby determines the catalytic properties of the catalyst. The ability to control or predict the size and morphology of supported nanoparticles is therefore essential when developing new catalysts.

1.4 Nanoparticle morphology

The equilibrium shape of a nanoparticle is determined by the surface free energy of the crystal facets as the shape that minimizes the total surface energy at constant volume. The shape can be found with good approximation by calculating the Wulff construction based on the Wulff theorem from 1901[9]. The theorem states that the normal distance h_{hkl} from a specific facet (hkl) to the center of the particle is proportional to the surface free energy γ_{hkl} of that facet, with a common proportionality factor. Knowing the surface free energy for a sufficient number of low energy facets, it is possible to construct the particle shape, as shown in Figure 1.4a, by the equa-

tion, $\frac{h_{111}}{\gamma_{111}} = \frac{h_{100}}{\gamma_{100}} = ... = \frac{h_{hkl}}{\gamma_{hkl}}$. This leads to a faceted particles that predominately expose facets with lowest surface energy. A Ru particle found by Wulff construction based on surface free energies calculated by density functional theory is shown in Figure 1.4b[10]. When the particle is supported on a substrate, the adhesion energy β between the particle and the substrate will cause the particle to wet the substrate as seen in the bottom of Figure 1.4a. Strong adhesion will cause a high degree of wetting whereas weak adhesion will almost will preserve the unsupported shape.

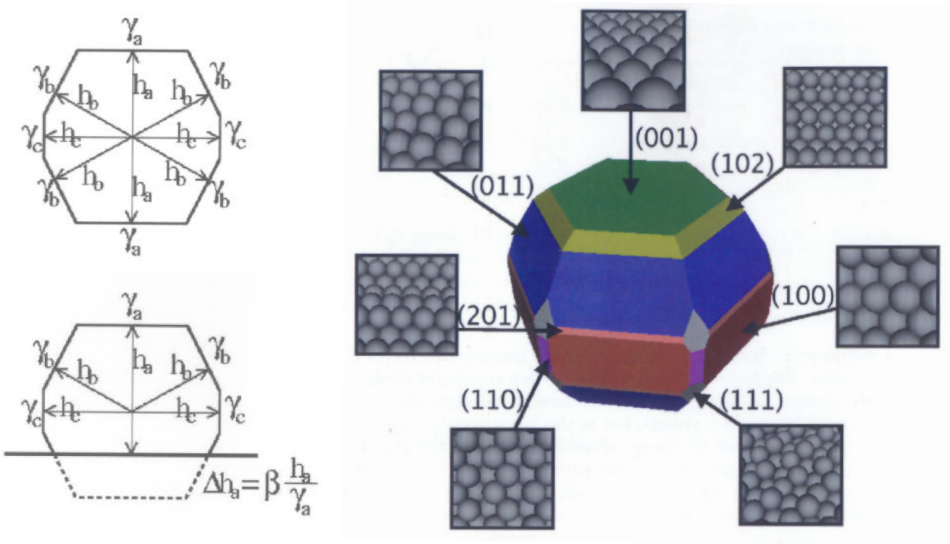

(a) (b)

Figure 1.4: Wulff construction. (a) A 2D schematic of the Wulff construction. Top: Unsupported particle. Bottom: Particle adhered to a substrate. γ is the surface free energy, h is the distance from the center to the facet and β is the adhesion energy. (b) Ru particle calculated by Wulff construction. Both adapted from [10].

Of course, the Wulff construction does not take into account energy associated with the formation of under-coordinated sites such as edges and corners. In reality, edges and corners may be reconstructed if it is energetically favourable so the Wulff construction can not be used to gain detailed structure information about the catalytically important under-coordinated sites.

1.5 Modelling the "real" catalyst

The surface science approach to catalyst research is to build simplified model systems that mimic the catalytically active surface of the real industrial catalyst, and employ surface science techniques to study the model system. The often large dif-

ferences between the model catalyst and the industrial catalyst present a barrier when relating the information gained from model studies to the working catalytic converters.

A typical industrial metal catalyst consist of highly dispersed metal nanoparticles on high surface area oxide supports such as Al_2O_3, TiO_2 and SiO_2 or carbon, where the metal nanoparticles are the active surface. The activity, selectivity and stability of such catalysts for a given reaction are governed by factors such as the metal element, particle size, particle atomic structure and support effects such as particle-support interactions.

Model systems based on metal single crystals have been developed to mimic the active metal surface. Single crystals can be carefully cleaned under UHV conditions so that they expose a well-defined crystal facet termination. Single crystal model catalysts can be used to study the catalytic properties of a metal facet with a specific orientation, including the effect of steps. Using microscopy and surface sensitive spectroscopy techniques, these systems have been characterised at the atomic level and gas adsorption/desorption, surface reactions and adsorbate-adsorbate interactions have been studied in great detail and correlated to the surface structure. Keeping in mind that real catalysts are supported nanoparticles, such single crystal experiments can not be used to investigate particle size effects or support effects.

To overcome this discrepancy, called "the material gap", model systems consisting of metal nanoparticles supported on well-defined planar oxide or carbon surfaces has been created. These model systems constitute a better replica of a real catalyst while still compatible with currently developed surface science techniques, enabling investigations of particle size effects and support effects. Going from single crystals to supported nanoparticles increases the complexity of the model system, which become less well characterised. It is especially challenging to gain atomic scale structure information of the supported nanoparticles whereas the support can be very well characterised. Almost all the experimental methods used for surface characterisation (except microscopy) such as x-ray photoelectron spectroscopy, when studying gas adsorption/desorption and when measuring reaction rates are integral (area-averaging) methods, probing the entire ensemble of nanoparticles. Deriving particle size effects from such experiments will thus require samples with a narrow particle size distribution.

In this project, the approach to study correlations between particle size/structure and the reactivity has been to deposit mass selected nanoparticles onto planar supports under UHV conditions. The nanoparticles were produced in a clean UHV

environment from high purity metal targets without any need for cleaning or pre-treatment procedures. This is in contrast to chemical synthesis methods where precursors or polymers must be removed before characterisation or catalyst testing. The model system hereby contain supported particles with a narrow size distribution and any observed size effects can readily be deduced by comparing results from samples with different size particles. It is important to note that the mass selection does not ensure a particular structure of the deposited particles, nor does it ensure that the ensemble of particles adopt the same structure. The particle structure must be investigated by microscopy, e.g. by transmission electron microscopy.

Industrial catalysts are often working under reaction conditions at elevated pressure and temperature, but a majority of surface science techniques require UHV conditions to operate. The large pressure gap induces a barrier for transferring results found under UHV conditions to the catalyst under operating conditions. The catalyst particles may dynamically change shape in response to changes in the gaseous environment[11] and metal oxide or carbide phases may form under reaction conditions[12], which in both cases will alter the catalytic properties. For the purpose of studying catalysts under (or close to) reaction conditions, experimental setups has been developed with in-situ cells in particular at synchrotron facilities using x-ray scattering and spectroscopy techniques at ambient pressure[13] as well as x-ray photoelectron spectroscopy under mbar range pressure[14, 15]. Environmental transmission electron microscopy and high pressure scanning tunnelling microscopy also serve as tools to study model catalysts at elevated pressures[16].

As an attempt to narrow the pressure gap a UHV compatible high pressure cell has been mounted on the existing UHV system, which allows direct transfer of samples under UHV, between the high pressure cell and the UHV chamber. The high pressure cell can be used for high pressure dosing and as a batch reactor since the gas composition inside the cell can be continuously probed by a quadrupole mass spectrometer. With this configuration, the sample can be prepared and characterised under UHV conditions before and after reaction or high pressure exposure, without exposing the sample to open air, but can not be studied in-situ during reaction.

1.6 Thesis outline

Chapter 1 was an general introduction to heterogeneous catalysis along with a basic description for understanding the origin of structure sensitivity

Chapter 2 describes the experimental setup and the experimental methods that have been used throughout this project, with most emphasis on less well known techniques such as the nanoparticle generation method.

Chapter 3 addresses the structure sensitivity and particle size dependence of the dissociation of CO on ruthenium nanoparticles, with a model catalyst consisting of mass selected Ru nanoparticles supported on Highly Oriented Pyrolytic Graphite. Additionally, we have investigated the materials gap between single crystal and nanoparticulate systems. The chapter starts with an introduction to this subject.

Chapter 4 addresses the topic of adsorbate induced surface-structure reconstructions. We have probed CO induced structural changes of mass selected platinum nanoparticles supported on SiO_2/Si by TPD experiments and compared the results to a parallel set of experiments on a Pt(111) single crystal. The chapter starts with an introduction to this subject.

Chapter 5 describes the results from a project involving platinum and platinum-yttrium alloy nanoparticles as a catalyst for the electrochemical oxygen reduction reaction relevant for fuel-cell applications. The structure sensitivity and size dependence of the reaction is addressed both for pure platinum and platinum-yttrium alloy nanoparticles.

Chapter 6 is as general summery and conclusion based on the results presented in the previous chapters.

Chapter 2

Experimental setup and methods

This chapter describes the experimental setup as well as a basic description of the experimental methods used in our studies. Methods that are not well known or methods used in a specialized manner are described in detail whereas well-known methods commonly used in the literature are only briefly described.

2.1 The Ultra High Vacuum System

The Ultra High Vacuum (UHV) system consists of four interconnected chambers which can be isolated from each other by gate valves. The four connected UHV chambers are named as follows; the Analysis chamber, the Preparation chamber, the High Pressure Cell and the Cluster Source. Throughout the project, two different cluster source chambers have been used, they will be referred to as Cluster source I and Cluster source II. The system operates with sample holders that can be introduced the vacuum system via a loadlock, and transferred between the analysis chamber, the preparation chamber and the high pressure cell by the use of linear transfer arms and wobble sticks.

2.1.1 Analysis Chamber

The analysis chamber is an Omicron Multiscan Lab equipped with a Scanning Electron Microscope (SEM) and a Scanning Tunneling Microscope (STM). The SEM is a UHV Gemini column with an optimum lateral resolution of 3 nm and is foremost used for overview imaging of samples, i.e. checking for homogeneity of the nanoparticle coverage and for sintering. The STM is capable of achieving atomic resolution, but for nanoparticulate samples this has been extremely difficult to achieve due

to the unfavourable morphology of the particles and the extreme height variations across the particles. The STM is on the other hand excellent for nanoparticle height measurements. For surface characterisation and compositional analysis the chamber is also equipped with a fixed x-ray source (Mg and Al anodes) for X-ray Photoelectron Spectroscopy (XPS), and the SEM column is used as electron source for Auger Electron Spectroscopy (AES). Furthermore a differentially pumped focused ion-gun with He is used for Ion Scattering Spectroscopy (ISS), which complements XPS and AES by only probing the outermost atomic layer. The spectroscopic energy analysis is conducted with a Hemispherical Energy Analyser (HEA) capable of analysing both electrons and positive ions up to 2000 eV. The chamber is pumped by a Varian ion getter pump as well as a Pfeiffer turbo molecular pump which can be isolated by a gate valve. The base pressure is typically in the 10^{-11} mbar range.

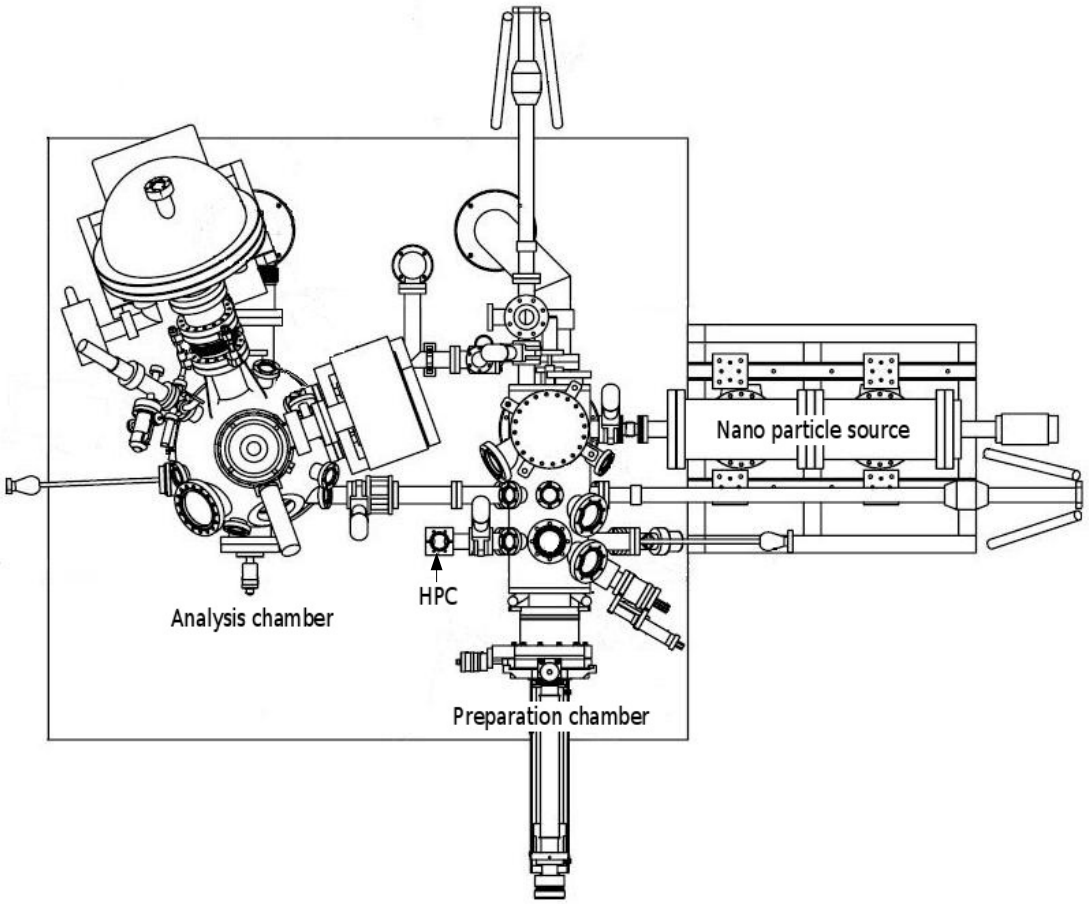

Figure 2.1: A diagram showing the total experimental setup. On the left is the Analysis chamber, in the middle is the Preparation chamber with the High Pressure Cell attached and to the right is the Cluster source.

2.1.2 Preparation Chamber

The preparation chamber is used for sample preparation which typically involves sample de-gassing, sputter cleaning of substrates and the deposition of nanoparticles from the cluster source. The chamber is also equipped with a differentially pumped Balzers QMA 125 Quadruple Mass Spectrometer (QMS) for the purpose of performing Temperature Programmed Desorption (TPD) experiments. The chamber is pumped by a Varian ion getter pump as well as a Pfeiffer turbo molecular pump which can be isolated by a gate valve. The base pressure is typically below 10^{-10} mbar. The sample receptor stage is mounted on the end of a linear transfer arm to move the sample to various positions in the chamber. The stage incorporates a Pyrolytic Boron Nitride (PBN) heating element capable of heating the entire sample holder to ~ 800°C.

2.2 Sample holder and sample substrates

The sample holder itself (Omicron VT) is depicted in Figure 2.2(a)-(d) and comes in two types: Type (a) incorporates a PBN heater and is typically used with HOPG substrates (7 mm×7 mm, SPI 1-grade). The temperature is measured by pressing a C-type (W5%Re/W26%Re) thermocouple junction into the backside of the HOPG substrate. Type (b) does not contain a heating element and is used with SiO_2/Si-RTD substrates which can be heated by passing a DC current directly through the wafer. The temperature is measured by the integrated resistance temperature detector (RTD) which is contacted by molybdenum foils attached to the top plate (see the following section for more details about the Si substrates with integrated RTD). A third sample holder, machined from a molybdenum block, was made in-house to carry the glassy carbon disks that were used as substrates for Pt and Pt-Y alloy nanoparticles. The glassy carbon disks were used as working electrodes in the electrochemical cell when measuring the activity of the mass-selected particles for the oxygen reduction reaction.

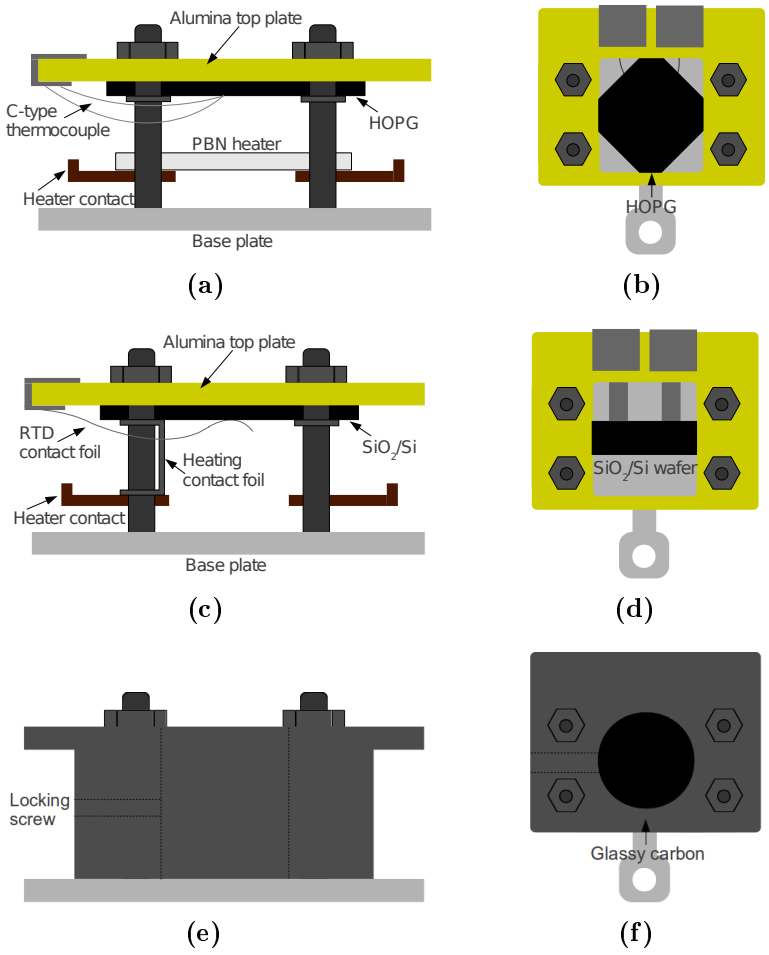

Figure 2.2: (a) Omicron VT sample holder with incorporated PBN heater located just under the sample. This holder is typically used for HOPG substrates. (b) Top view of sample holder used for HOPG substrates. (c) Omicron VT sample holder without heating element is used for the Si/SiO_2-RTD substrates which are heated by passing a DC current through the wafer. (d) Top view of sample holder used for Si/SiO_2-RTD substrates. (e) Sample holder made for glassy carbon disks used as electrode in the electrochemical cell for the oxygen reduction reaction. (f) Top view of the glassy carbon sample holder.

2.2.1 Si/SiO_2 substrates with incorporated RTD

A planar substrate exposing a Si$O2$ surface on the front-side was designed and fabricated with an integrated platinum resistance-temperature device (RTD) on the back-side, as a support for mass selected nanoparticles. The substrate facilitates a highly responsive and accurate measurement of the sample temperature which is desirable for temperature programmed desorption (TPD) experiments. Generally it is a difficult task to achieve a precise temperature measurement of a non-metal substrate under vacuum conditions. Typically thermocouples are used to measure the sample temperature in a UHV setup but it can be difficult to achieve a good and reproducible thermal contact to an oxide substrate. In the case of a metal single crystal, the thermocouple is often spot-welded to the crystal which ensure good thermal contact. I our case, new oxide substrates were used for each particle deposition, so good reproducibility was essential, and difficult to achieve by pressing or glueing a thermocouple onto the substrate.

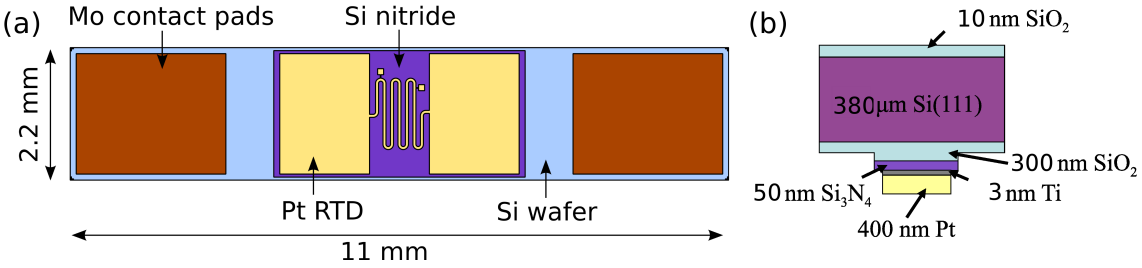

Figure 2.3: Schematic drawings of the device (a) Top view of the back side of the device showing the RTD design. (b) Side-view of the device showing the layered structure. The front side of the chip is where nanoparticles are deposited and the surface studies are performed. See text for a description of the fabrication process. The devices are fabricated by Thomas Pedersen at the clean-room facilities at DTU Nanotech.

A schematic drawings of the backside and side-view of the device are shown in Figure 2.3(a) and (b), respectively. The substrates incorporate a platinum resistance-temperature device (RTD) on the backside and expose a thin layer of SiO_2 grown by wet oxidation on top of the Si(111) wafer on the top side. The substrates were made by micro-fabrication techniques in the clean-room facilities at DTU-nanotech. For TPD experiments, substrates with 100 nm SiO_2 were used. The samples were heated by passing a direct current through the wafer, and the resistance across the wafers were 12.5 Ω.

The chips are fabricated on 111 oriented, 380 μm thick, double side polished silicon wafers. Each wafer contains 239 chips. The resistivity of the wafer is about 6 ohm-cm. Since the chip is resistively heated it is preferable to have a resistance across

the chip of about 10 Ω, so the first step of the fabrication is to diffuse phosphorous into the wafer to change the sheet resistance. A phosphorous pre deposition is made in a $POCl_3$ atmosphere at 1000 °C for 30 min, this lowers the sheet resistance and gives a resistance across each chip of ∼14 Ω. Next, a 300 nm oxide film is grown and on top of the oxide a 50 nm nitride film is deposited. The insulator stack is used to insulate the RTD from the bulk silicon. The oxide and nitride layers are patterned using a standard UV lithography process. The nitride is etched away on the frontside of the wafer and in the pattern defined by the resist on the backside in a reactive ion etch system. The silicon oxide film is etched using buffered hydroflouric acid (BHF). Following the definition of the insulator stack a 10 nm thick silicon oxide is grown on the frontside of the chip. The RTD and the contacts are defined using a lift off process. Next, the metal is deposited using an E-beam evaporator and finally it is lifted off in acetone leaving a metal pattern as defined during the lithography process. Before dicing the wafer into individual chips the surface of the wafer is protected with a 1.5 μm thick resist layer on each side. This will leave the surface free of particles otherwise deposited during the dicing process.

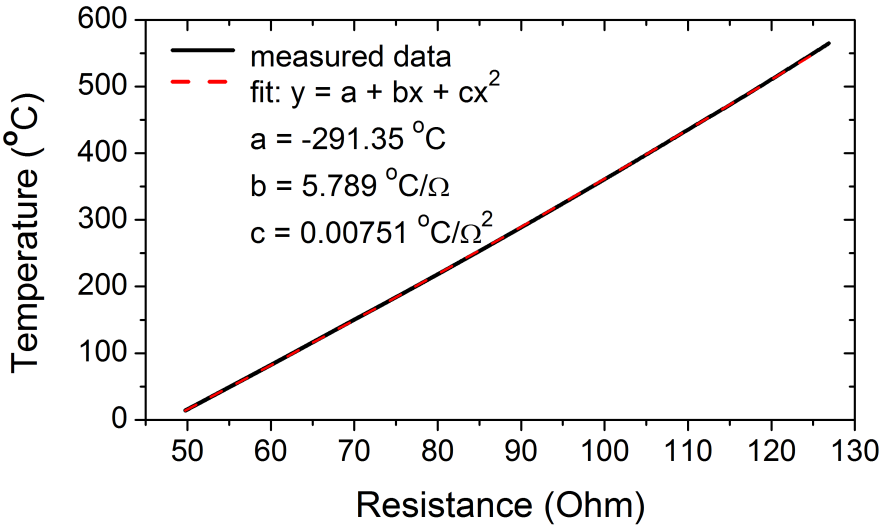

Figure 2.4: The resistance vs. temperature behaviour of the RTD, measured in a tube furnace in a flow of Ar.

The resistance-temperature behaviour of the RTDs was measured in a tube furnace in a flow of Ar. The result is shown in Figure 2.4 and it is seen that the resistance vs. temperature response of the RTD can be perfectly fitted with 2. order polynomial. During the first heating ramp to ∼650 °C the Pt RTD anneals out but after the first annealing the temperature coefficients of the resistance remains constant if the temperature is kept below the annealing temperature.

When the substrates are used in the vacuum chamber they are mounted in the

sample holder as shown in Figure 2.2(c) and (d). Differences in contact resistances proved not to be a problem, as TPD spectra were observed to be very reproducible between samples.

2.3 High Pressure Cell

The High Pressure Cell (HPC) itself is manufactured of Ni-free steel (W no. 1.2510) to prevent the formation of Ni carbonyls and has six CF70 flange connections. The HPC is capable of handling pressures up to 1 bar and is equipped with a MKS 121A Baratron® capacitance gas independent pressure sensor with 1000 mbar full range and 0.1 mbar resolution. The cell is attached to the preparation chamber via a gate valve, which enables in-vacuum transfer of the sample, and makes it possible to have up to 1 bar in the HPC while maintaining UHV in the preparation chamber. The sample receptor stage and electrical contacts for sample heating and temperature measurements are identical to the design in the preparation chamber but without any heating elements in the sample stage itself. The HPC is connected to a gas handling system where the feed gas supply can be controlled and additional gas cleaning can be done before filling the HPC. The HPC and the gas handling system are fully UHV compatible and bakeable to at least 150 °C. A schematic drawing of the HPC and a diagram of the gas handling system is shown in Figure 2.5. The

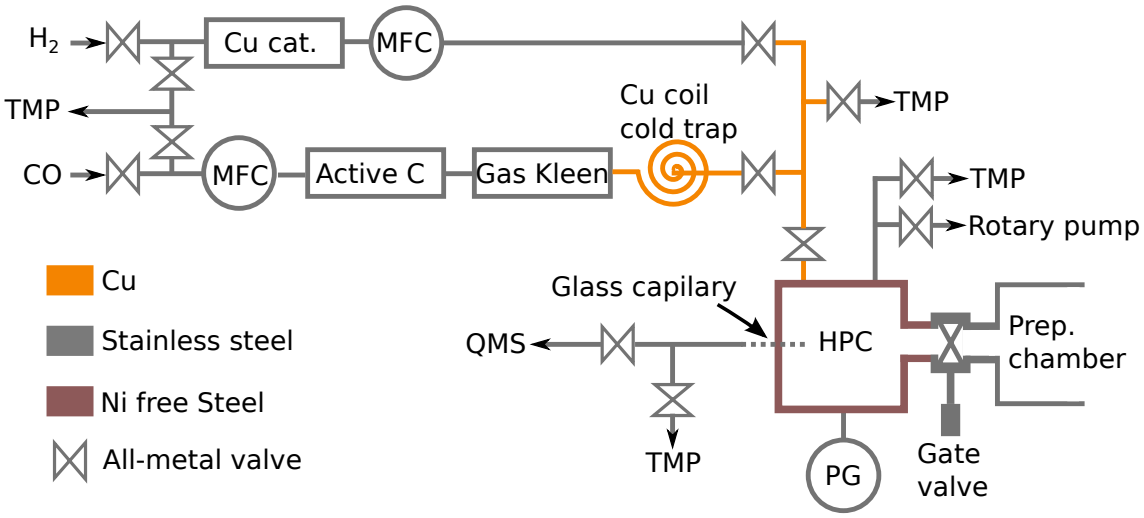

Figure 2.5: A schematic drawing of the high pressure cell and a diagram of the accompanying gas handling system. Only the relevant H_2 and CO lines are shown. The color coding indicates the material as noted in the figure. Abbreviations: TMP = turbo molecular pump, Cu cat. = copper catalyst filter, Active C = active carbon filter, MFC = mass flow controller, QMS = quadrupole mass spectrometer, PG = Baratron absolute pressure gauge.

cell is connected directly to the ionization chamber of the QMS mounted on to the preparation chamber via a glass capillary that reduces the pressure by a factor of $\sim 10^9$. This arrangement makes it possible to probe the gas composition inside the cell and hereby use it as a batch reactor. The cell is pressurized from the gas handling system through the inlet valve, which is closed when the desired pressure has been achieved. The cell is evacuated through the outlet valve either to the fore-vacuum pump or directly into the turbomolecular pump on the gas handling system, depending on the pressure.

The CO feed line on the gas handling system differs from the other lines as it contains a series of filters to remove trace amounts of nickel-carbonyl species, $Ni(CO)_4$, contained in the CO feed gas. Nickel-carbonyls are formed by CO at high pressure reacting with nickel contained in the steel tubing. The first filter contains activated carbon, followed by a commercial filter (Mini Gaskleen, Pall Corporation) to absorb impurities such as O_2, H_2O, CO_2 and $Ni(CO)_4$. The third stage is a cold trap made of a coiled up 1/4" copper tube submerged into a ethanol slurry bath cooled by liquid N_2, to condense out any residual nickel-carbonyls. To avoid any nickel-carbonyl formation after the filters, all tubing to the HPC is made from copper.

2.4 Cluster Source

Two different cluster sources have been used throughout this project, both with mass selection capability. Both sources use the magnetron sputtering inert gas aggregation principle for the cluster formation but differ on the mass selection principle. Cluster source I uses a quadrupole mass filter whereas cluster source II makes use of a lateral time-of-flight (TOF) principle for the mass selection. Cluster source I is supplied by Mantis Deposition Ltd[17] and consists of the Nanogen 50 nanoparticle source with the MesoQ mass filter. Cluster source II was supplied by Birmingham Instruments in the fall 2011 and the instrument is called Nanobeam 2011. Commissioning of cluster source II and the development of the methods to measure the cluster current/deposition rate have been conducted in the course of this project.

Both sources are fully UHV compatible and bakeable to at least 150°C and a base pressure of $2{\cdot}10^{-10}$ mbar is typically achieved. A good vacuum has proven to be essential for producing clean metal nanoparticles as highly reactive transition metals such as ruthenium, platinum and yttrium are especially sensitive to contaminations. As the sources are operated with mbar range pressures of Ar and He the gas purity is

of great importance. For that reason the Ar and He gasses are of N60 purity and in order to increase the purity even further, the gasses are passed through gas cleaning filters consisting of stainless steel tube filled with a reduced iron based catalyst, that adsorb trace amounts of O_2, H_2O and CO.

Cluster source I was used to produce the Ru nanoparticles for the CO dissociation investigations (Chapter 3) and to produce Pt nanoparticles for the study of CO induced surface reconstruction (Chapter 4) and of the size dependence of the activity for electrochemical oxygen reduction reaction (Chapter 5). Cluster source II was used for producing Pt-Y alloy nanoparticles for electrochemical oxygen reduction reaction (Chapter 5).

2.4.1 Cluster formation principle

The cluster formation principle is based on the nanoparticle source described by Haberland in ref [18]. A schematic drawing of cluster source I is shown in Figure 2.6 and the condensation chamber (left part) is representative for both cluster source I and II. The nanoparticles are formed by gas-phase condensation of metal atoms sputtered from a metal target mounted on a magnetron sputter head (B). The magnetron head is located inside a liquid nitrogen cooled condensation (or aggregation) chamber(C) with a small exit aperture and inlet gas lines for supply of Ar and He gases which are controlled by mass flow controllers. The metal target is biased by ∼200 V which ionizes the Ar gas that is introduced locally above the metal. A strong magnetic field created by permanent magnets behind the target traps electrons in front of the target enhancing the ionizing probability and an Ar plasma can be ignited and sustained in front of the target. The intense sputtering produces a dense vapour of metal atoms inside the condensation chamber and the cooled Ar and He gas facilitate the condensation process by cooling the metal atoms and clusters through collisions. The Ar and He also serves the purpose of carrier gas sweeping the metal atoms and clusters through the condensation zone. The condensation process starts by a dimer formation through a three-body collision with two metal atoms and one Ar atom[18]. The clusters can now grow into nanoparticles by ad-atom growth or by cluster-cluster coagulation[19]. The dominating growth process will play a determining factor for the final shape and structure of the nanoparticles that will be deposited.

The gas exiting the condensation chamber is expanded through the exit aperture followed by a conical shaped skimmer (L), with differential pumping of the volume between. After this stage no further cluster growth is taking place. About 30% to

80% of the particles are charged[18], which makes it possible to do mass filtering according to the mass-to-charge (m/z) ratio. After the expansion the particle beam is now guided into the quadrupole or lateral time-of-flight mass filter for cluster source I and II, respectively, which are described in the following sections.

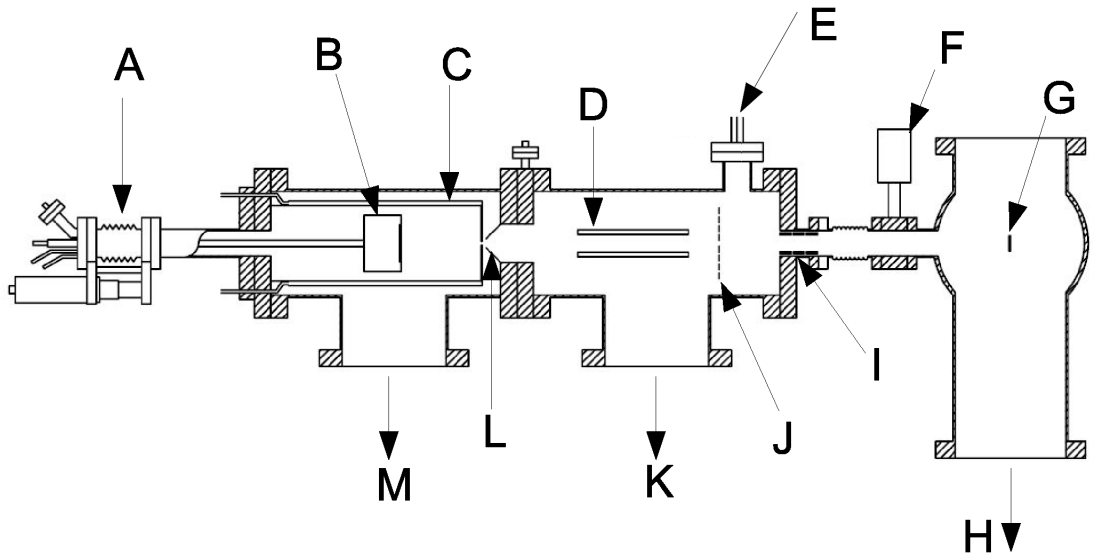

Figure 2.6: Schematic of the nanoparticle source: A. Linear translator for the magnetron sputter head, B. Magnetron sputter head, C. Cooling shroud, D. Quadropole Mass Filter (QMF), E. Ion Gauge, F. Gate valve between NP source and prep. chamber, G. Sample holder, H. Prep. chamber pumping, I. Einzel lenz consisting of three stainless steel rings, J. Insertable plate for measuring NP ion current, K. Pumping for QMF-zone by turbo molecular pump, L. Skimmer for super sonic expansion and differential pumping of gas stream, M. Pumping for gas aggregation zone by turbo molecular pump. Adapted from [20].

The size or mass distribution of the particles exit the condensation chamber will be determined by a number of factors including **residence time** in the condensation zone, **Ar and He pressure**, **metal vapour pressure** and the **temperature** of the condensation chamber walls. In the following it will be described how these factors can be controlled and trends on how changes will affect the particle size distribution. The growth mechanism is a complicated process which is not understood in detail so exceptions to these trends may very well occur.

The residence time inside the aggregation zone determines the growth time so the particle size is proportional to the residence time. The residence time can be controlled by varying the position of the sputter head relative to the exit aperture,

effectively changing the length of the condensation zone. Varying the Ar/He flow into the condensation chamber will affect both the residence time, due to changes in the carrier gas flow rate through the aggregation chamber, and the Ar/He pressure. With a fixed exit aperture (as on cluster source I) the gas Ar/He flow-rate and Ar/He pressure can not be controlled independently. Cluster source II is equipped with an adjustable exit aperture which decouples these two parameters. For a fixed exit aperture, the Ar and He flow rate will in general be inversely proportional to the particle size, giving smaller particles with higher flow rates. The Ar/He pressure will determine the number of collisions between the cool Ar and He molecules so for a fixed Ar/He flow-rate, increasing the pressure by closing the exit aperture will result in larger particles. The sputter power will determine the metal vapour pressure and in general higher sputter power should give larger particles, but during the experiments making Pt particles we found that low sputter power was also successful in producing large ∼10 nm particles. The temperature of the aggregation chamber in general affects the size distribution such that it is necessary to cool with liquid nitrogen to produce particles above ∼2 nm, but this has been proven to be very much dependent on the metal.

There has not been conducted a proper systematic study of how these parameters affect the size distribution. In practice it has proven to be sufficiently easy to find the source parameters that produce the particle sizes of interest utilizing the general trend described above combined with trial and error. An example of how the particle mass distribution depend on the Ar flow/pressure is shown in Figure 2.11(a), where it is seen that the average Ru particle size decreases with increasing Ar flow/pressure.

2.4.2 Quadrupole mass filter (Cluster source I)

The mass filter on cluster source I is a quadrupole mass filter with an ultimate resolution of m/Δm = 50 and it is specified to filter particles in the mass range from 350 amu to 10^6 amu[17]. The quadrupole principle is illustrated in Figure 2.7 and it consist of four rods sitting in a square arrangement as shown. The four rods are pair-wise electrically connected as shown and one pair is biased by AC voltage V with an angular frequency ω on top of a DC voltage offset U ($U + Vcos(\omega t)$) and the same bias with opposite sign is applied to the other pair. Ions travelling inside the quadrupole can only be transmitted (have stable trajectories) if the ratio U/V is less than 0.168. Below this value, the ratio U/V defines the mass resolution and corresponding values for the instrument are listed in Table 2.1. The choice of U/V ratio is always a compromise between resolution and cluster flux. The mean

mass-to-charge ratio that is allowed to be transmitted through the quadrupole is defined by the angular frequency ω when the amplitude V is held constant.

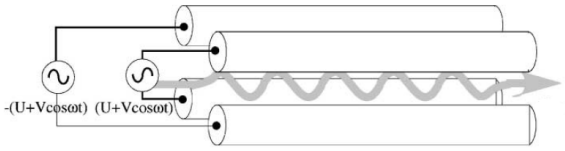

Figure 2.7: Schematic drawing of a quadrupole. Adapted from [21].

The full cluster source I setup is shown in Figure 2.6 with the sputter aggregation chamber on the left, the quadrupole mass filter in the middle and the preparation chamber with the sample on the right. After the cluster beam has expanded through the skimmer it enters the mass filter where the charged particles are filtered, and guided into the preparation chamber and onto the sample by electrostatic (Einzel) lenses. The uncharged fraction of the clusters are unaffected by the filter. Despite the sample being in line-of-sight with the magnetron, the contribution of uncharged particles deposited onto the sample has been shown by microscopy and reference experiments to be negligible.

U/V ratio	Resolution = $m/\Delta m$
0.05	1.7
0.10	3.5
0.12	5.6
0.15	28.7

Table 2.1

2.4.3 Lateral time-of-flight (Cluster source II)

This mass filtering technique, called lateral time-of-flight, was first described by von Issendorff and Palmer in ref. [22] and a full description can be found therein. Briefly described, the technique is based on the time-of-flight (TOF) principle, using time-limited high voltage pulses to displace the cluster beam laterally, without changing the direction or shape of the beam. A great advantage of this principle is that the displacement of the clusters perpendicular to their original beam direction is independent of their forward velocity, thus the mass resolution and the absolute value of the filtered mass does not depend on the cluster beam energy. In our system a mass resolution of $\frac{m}{\Delta m} = 20$ to 160 can be achieved with a transmission up to 44 %, both independent of the selected mass. Choosing the mass resolution is always a compromise between a narrow mass distribution and high throughput,

and a mass resolution of 20 has typically been used. A schematic of the system is shown in Figure 2.8.

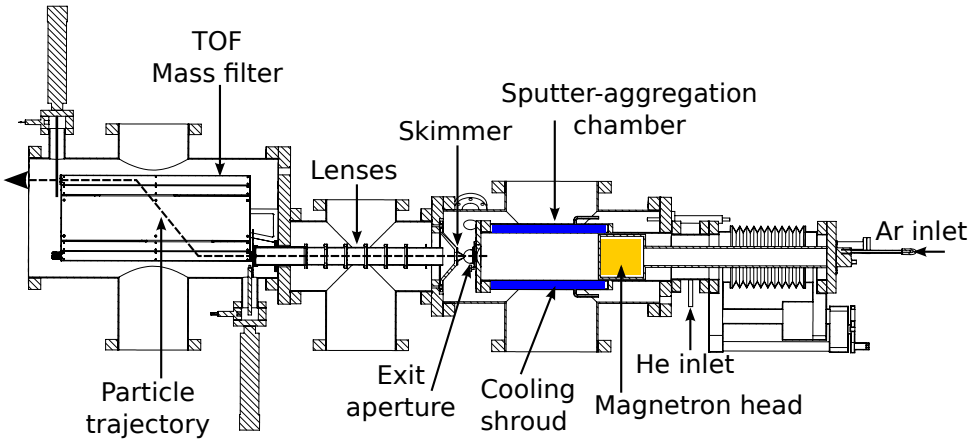

Figure 2.8: Side view drawing of cluster source II.

A schematic drawing of the lateral TOF mass filter is shown in Figure 2.9(a). The unfiltered cluster beam enters through a slit at the bottom left and is focussed into a small spot at the far end as shown on the figure. The beam is pulsed upwards, perpendicular to its original direction by a voltage pulse applied to plate 1. The beam drifts upwards for some time until an identical voltage pulse is applied to plate 4 which stops the upward motion while the beam continues to travel in the original direction. All clusters gain the same momentum perpendicular to the beam direction and clusters with the same mass will therefore gain the same velocity. When the upwards motion is stopped by the second pulse, light clusters have travelled a longer distance than heavy clusters. The timing of the two voltage pulses thus defines the mass of the clusters that exit the slit at the upper right. The exit slit cuts out a certain range of masses of the cluster beam, with the masses dispersed laterally, and the width of the slit thus defines the resolution.

A schematic drawing of the voltage pulse timing is shown in Figure 2.9(b). τ_p is the pulse width which is time needed for the clusters to travel the distance a on Figure 2.9(a). τ_d is the delay time between the acceleration pulse and the de-acceleration pulse which is the time needed for the clusters to travel the distance b. τ_w is the wait time between the acceleration pulses which is the time necessary for a new section of the beam to fill the bottom of the chamber.

The mass resolution of the filter can be calculated by considering the mass dependence of the lateral displacement, and it can be shown that the best achievable

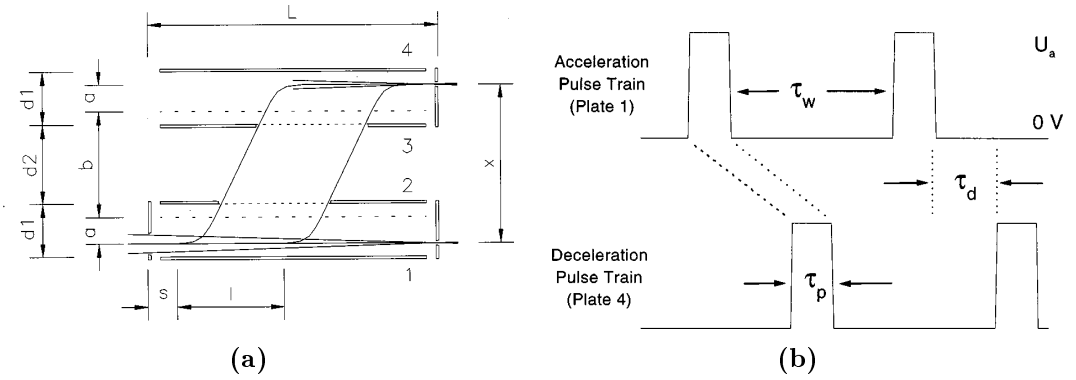

Figure 2.9: (a) Schematic of the lateral TOF. l = length of the ion beam package displacement, x = total displacement, a = beam displacement during the high voltage pulse, b = length of field free region, d1 and d2 = plate separations, s = length of discarded ion beam, L = total TOF chamber length. (b) Schematic drawing of the high voltage pulse timing. Identical pulse-trains, displaced in time, are applied to plates 1 and 4 shown in (a). τ_p = pulse length, τ_d = drift time between acceleration and deceleration pulse, τ_w = time between consecutive acceleration pulses. Both adapted from [22].

resolution is given by the ratio between the distance x and the slit opening.[22]

$$\frac{m}{\Delta m} = \frac{x}{\Delta x} \tag{2.1}$$

where m is the filtered mass, Δm is the full width half maximum (FWHM) of the mass distribution, x is the lateral displacement and Δx is the FWHM of the convolution of the exit slit opening and the beam profile width.

2.4.4 Measuring particle deposition rate

Two ways have been implemented of measuring the nanoparticle deposition rate. The first method is based on measuring the nanoparticle current with an ammeter, i.e. the amount of ions hitting the sample. Assuming that all the particles deposited onto the sample carry a single charge, the measured electrical current is equal to the rate of particles hitting the sample. The second method is based on measuring the deposited mass with a Quartz Crystal Microbalance (QCM). During deposition the sample is positioned behind a mask which contains three circular apertures with varying diameters and the QCM housing, see Figure 2.10. The mask is mounted on a linear drive for selection of aperture size or QCM measurement and the entire mask is electrically floated and grounded through an ammeter, with an option of biasing the mask up to ±48 V by the use of batteries. The sample including the sample stage is also floating and grounded through an ammeter, also with the option of applying up to ±48 V bias. The deposition current can be measured on the mask and on the

sample simultaneously, making it possible to estimate how focussed the nanoparticle beam is. The particles were in any case soft-landed, with a kinetic energy less than 0.1 eV/atom, onto the support surface[23]. By doing so, the nanoparticles are not deformed upon impact with the substrate which has been observed at much larger biases[24].

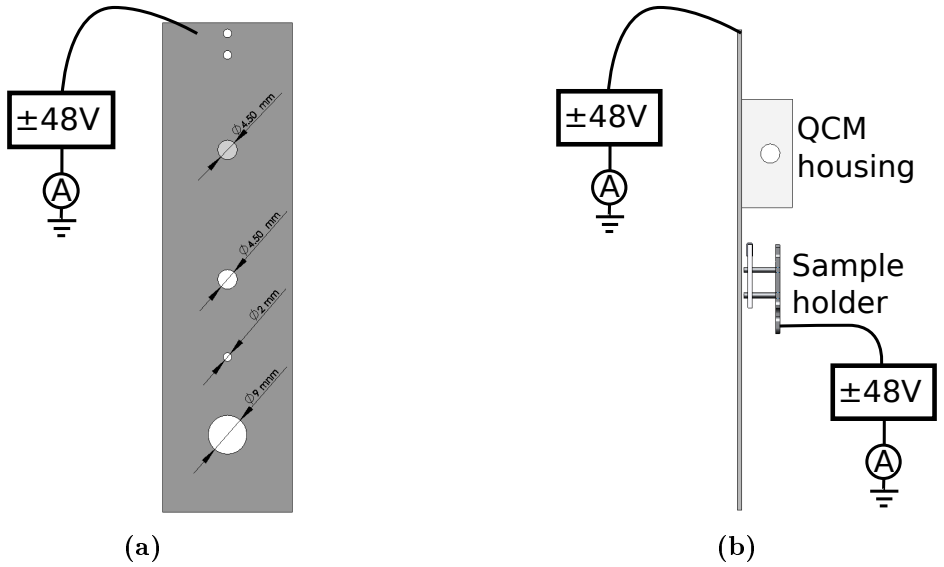

Figure 2.10: The deposition mask with various size apertures and integrated QCM is shown in (a) front view and (b) side view with the sample in place behind the 4.5 mm aperture. The wiring for measuring the cluster current through ammeters is also shown along with the option of applying ± 48 V bias to the mask and sample using batteries.

Before starting the deposition of particles, the mass filter in the cluster source is set to scan the filtered mass in a predefined range while simultaneously measuring the particle current, resulting in a mass spectrum as shown in Figure 2.11. When the appropriate mass distribution of the cluster source has been realised, the mass filter is set to filter particles of the desired mass. For depositing nanoparticles onto a sample, the sample is positioned behind the selected aperture in the mask and the deposition rate can be calculated from the measured cluster current and monitored throughout the deposition.

In order to calculate the ORR mass activity of the mass-selected nanoparticles it is paramount that we have an accurate measure of the total deposited mass. The total deposited mass can be calculated from the cluster current when knowing the individual particle mass, but due to the importance of knowing the deposited mass, the deposition rate was also measured on the QCM prior to deposition. Assuming that the deposition rate is constant throughout deposition, the total mass of nanoparticles deposited onto the sample can be calculated. As the QCM measures

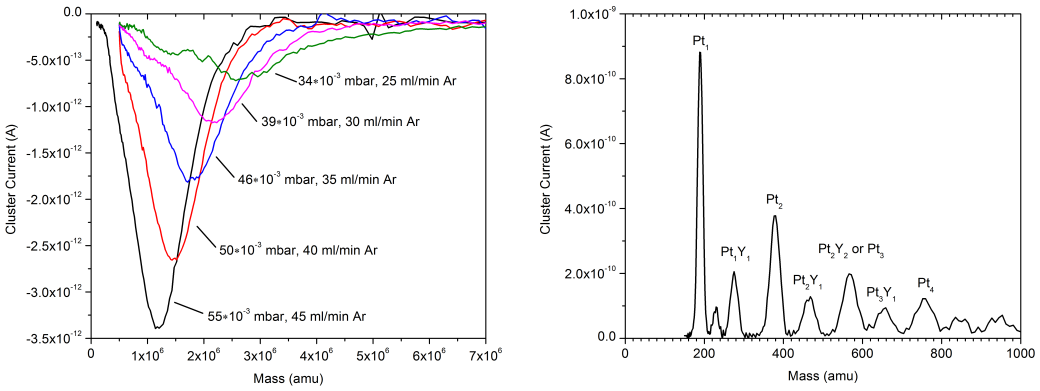

(a) **(b)**

Figure 2.11: (a) Multiple nanoparticle mass scans from a ruthenium target showing how the particle mass distribution of negatively charged Ru nanoparticles that exit the aggregation chamber aperture change with different Ar flow rates (or Ar pressure). The aggregation chamber aperture size was fixed, the sputter power was 10 W and no He was used. (b) Mass scan obtained from a Pt_9Y target illustrating the capability of the TOF mass filter to select positively charged clusters with countable atoms. Both spectra were obtained from Cluster Source II.

the deposited mass in a more direct manner, such measurement gives strong evidence for the deposited mass. The deposition rate can be measured on the QCM by positioning the quartz crystal in line of sight of the beam. Briefly, the QCM works in the following way. When mass is added to the face of the resonating quartz crystal, the frequency of these resonances change which can be related to the change in added mass by the Sauerbrey equation,

$$\Delta f = \frac{2f_0^2}{A\sqrt{\rho_q \mu_q}} \Delta m \tag{2.2}$$

where Δf is the frequency change (Hz), f_0 is the resonant frequency (Hz) of the uncoated crystal, Δm is the mass change (g), A is the piezoelectrically active crystal area (cm^2), ρ_q is the density of quartz (= 2.648 g/cm^3) and μ_q is the shear modulus of quartz (= 2.947x1011 $g/cm{\cdot}s^{-2}$). The Sauerbrey equation is valid for small amounts of deposited material corresponding to $\Delta f < 0.02 f_0$, which was complied with.

2.5 X-ray Photoelectron Spectroscopy

X-ray Photoelectron Spectroscopy (XPS) utilizes the photoelectric effect to give elemental composition and chemical state information about the sample surface. A

valence or core electron can be emitted from an atom when the energy from an incident photon is absorbed. The photo emission process is illustrated in Figure 2.12(a).

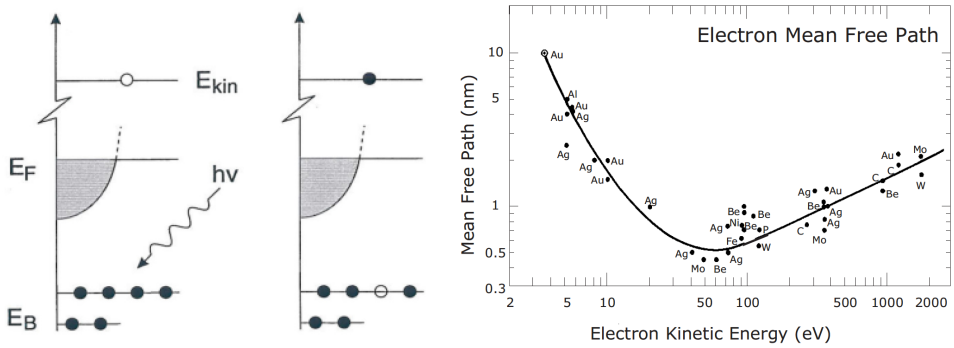

(a) **(b)**

Figure 2.12: (a) An illustration of the x-ray induced photo emission process. An incident electron is absorbed and an electron is emitted. E_B is the binding energy, E_F is the Fermi level, E_{kin} is the kinetic energy and $h\nu$ is the photon energy. Adapted from [25]. (b) A plot of the electron mean free path in metals as a function of kinetic energy. Originally from [26].

The maximum kinetic energy E_{kin} of an emitted electron with binding energy E_b can be expressed as[1]

$$E_{kin} = h\nu - E_b - \varphi \tag{2.3}$$

where h is planck's constant, ν is the frequency of the incident radiation and φ is the work function of the energy analyser. In XPS the intensity of the emitted electrons is measured as a function of the kinetic energy, which is done by the hemispherical energy analyser on this setup. Each element gives rise to a characteristic set of XPS peaks that correspond to the electronic configuration of the atom, and it is hereby possible to identify the elemental composition of the sample. Additional peaks from Auger electrons will also be present in the spectrum which can be identified by switching anode because Auger electrons have fixed kinetic energy independent of the photon energy. Furthermore, less intense extra peaks might be present in an XPS spectrum such as satellite peaks generated by other transitions in the x-ray source anode and ghost peaks originating due to photons emitted from the unused anode.

The x-ray source on the chamber has two anodes which can produce either Mg K_α (1253.6 eV) or Al K_α (1486.3 eV) lines. Even though the penetration depth of the generated x-rays is in the micrometer range, XPS is a surface sensitive technique due to the short mean free path of the emitted electrons, which have kinetic energies in

the 0-1000 eV range. Figure 2.12(b) shows the electron mean free path as a function of kinetic energy in metals and it is seen that the mean free path is 0.5 - 2 nm in the relevant region from 10 eV to 1300 eV.

2.5.1 Quantitative XPS

It is possible to quantify the composition of a surface with XPS by taking into account the cross section, the electron mean free path and the analyser transmission function. These factors are often collected into a sensitivity factor S_{xk} for an element x and electron shell k. The intensity of the XPS peak, given as the area under the peak, from shell k of element x can be written as [25]

$$I_{xk} = S_{xk} N_x F_{h\nu} \tag{2.4}$$

where N_x is the atomic density of element x and $F_{h\nu}$ is the number of photons with energy $h\nu$. Assuming that the concentration is homogeneous in depth, the atomic concentration of each element can then be estimated as [25]

$$C_x = \frac{\frac{I_{xk}}{S_{xk}}}{\sum_{i=1}^{n} \frac{I_i}{S_i}} \tag{2.5}$$

where i refers to one shell in any of the other observed elements. If the compound is not homogeneous, it is necessary to gain structural information to estimate the elemental composition.

2.6 Auger Electron Spectroscopy

The auger process is a three step transition: A high energy incident electron creates a hole in a core level. An electron from an outer level fills in the core hole and the transition energy is imparted to another outer level electron which is emitted, see Figure 2.13.

The kinetic energy of the emitted electrons can be approximated as [25]

$$E_{kin} = E^{initial}_{Core\ state} - E^{final1}_{1st\ outer} - E^{final2}_{2nd\ outer} \tag{2.6}$$

where $E_{Core\ state}$, $E_{1st\ outer}$ and $E_{2nd\ outer}$ are the energies of and the core state and the 1st and 2nd outer electronic levels, respectively. The kinetic energy of the emitted electrons reflects the electronic structure of the atom, and since that is unique for an atom of a specific element, the recorded energy spectrum can be used to

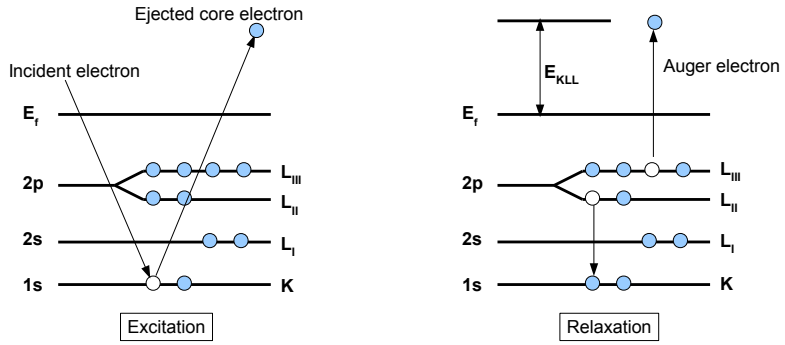

Figure 2.13: Diagram of the Auger process with electron energy levels indicated: The left diagram shows the excitation process and the right diagram shows the relaxation process.

identify the elemental composition. The energy analysis of the emitted electrons is performed by the hemispherical analyser. On this setup, the SEM column generates the incident electron beam with kinetic energies of 3-10 keV and 1-3 nA probe current. The high resolution of the SEM column provides the possibility of high resolution Scanning Auger Microscopy, producing a spatially resolved 2D image of the surface chemical composition. The emitted electrons have an energy range from ∼10 eV to ∼2000 eV corresponding to the mean free path minimum, see Fig. 2.12(b). This makes AES a surface sensitive method.

2.7 Ion Scattering Spectroscopy

In Ion Scattering Spectroscopy (ISS) low energy He^+ ions of 1 keV are focused onto the sample with an ion gun and the He^+ ions scatter from the surface in an almost perfect binary collision interaction, as illustrated in Figure 2.14.

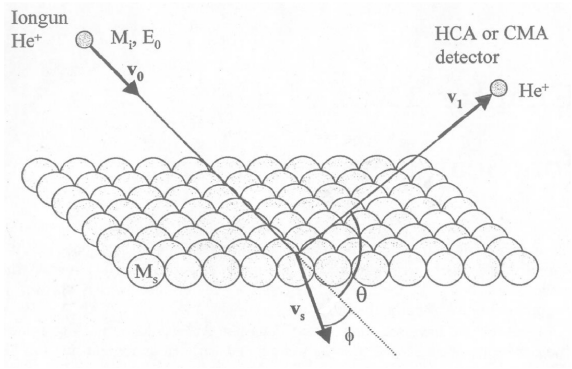

Figure 2.14: Schematic of the ion scattering process. Adapted from [25]

The energy of the scattered He^+ ions, E_1, is measured by the hemispherical energy analyser, resulting in an energy spectrum. Knowing the mass of the incoming ion

M_i, the energy of the incoming ion E_0 and the scattering angle θ, the mass of the surface atom can be calculated by the following equation[1]

$$\frac{E_1}{E_0} = \left[\frac{\sqrt{M_s^2 - M_i^2 sin^2(\theta)} + M_i cos(\theta)}{M_s + M_i}\right] \tag{2.7}$$

In the setup, the scattering angle Θ between the ion gun and the analyser is 146.7°, and the ISS experiments were done with the sample in the STM stage tilted 25° towards the hemispherical energy analyser.

The method is extremely surface sensitive because of the high scattering cross section, and particularly because any ions that penetrate the surface will with a very high probability be neutralized before exiting the surface again. ISS is a destructive method due to the sputter effect of the incident ions, but this effect can be minimized by using a low ion current and light ions like He. By increasing the sputter current, the sputtering effect can also be utilized for depth profiling. Intense He^+ sputtering will remove atoms from the outermost layer, and subsequent ISS and XPS spectra will give compositional information about interior of the sample. This approach has been used for compositional analysis of the Pt-Y alloy nanoparticles in Chapter 5.

2.8 Temperature Programmed Desorption

Temperature Programmed Desorption (TPD) is a simple but powerful surface science technique to probe the binding and desorption of molecules adsorbed onto surfaces. The sample is exposed to the probe gas, which is dosed into the UHV chamber, and the molecules adsorb onto the sample. The temperature of the sample is then ramped linearly in time at a fixed heating rate and the adsorbed molecules desorb at distinct temperatures. During the temperature ramp, the composition of the desorbing molecules is monitored by a quadrupole mass spectrometer (QMS) as a function of temperature.

Before dosing gas, the sample surface must be clean and free of adsorbates, which is normally ensured by degassing or cleaning procedures. It is also essential to maintain a good vacuum preferably $< 10^{-10}$ mbar to avoid adsorption of unwanted molecules such as CO, H_2O and O_2. The standard sample preparation procedure in this thesis include several hours degassing of the sample holder and substrate at ∼500°C followed by nanoparticle deposition. The nanoparticles does not need cleaning as they are produced in vacuum. The QMS is equipped with an oxygen-free high conductivity copper sniffer tip with a 1 mm diameter aper-

ture, positioned within 0.5 mm of the sample surface as showed in Figure 2.15. This arrangement allows the local gas composition above the sample surface to be measured with negligible contribution from the sample holder or surroundings.

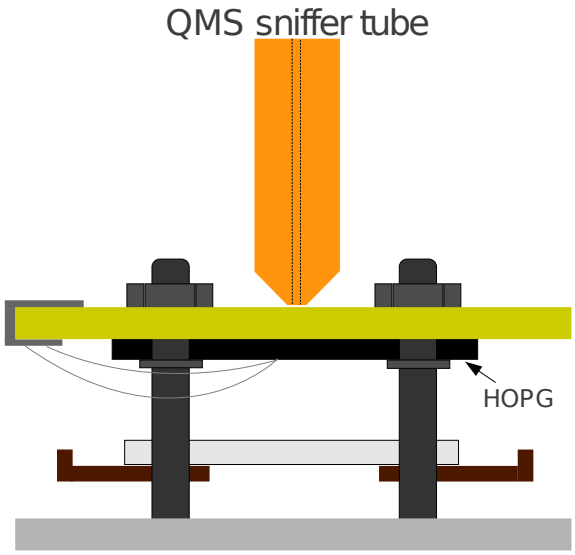

Figure 2.15: Schematic drawing of the sniffer placed above the sample for TPD experiments.

Much information is contained in a TPD spectrum. Firstly, the area under the TPD curve is proportional to the initial adsorbate coverage, and with a known reference coverage, the initial coverage can be found from a TPD spectrum. Secondly, the desorption temperature reflects how strong the adsorbate is bound to the surface, and as discussed in Section 1.2, the interaction (bonding) between the surface and adsorbate is dependent on the nature of the adsorption site. If the structure dependence of the adsorption energy is sufficiently large, the presence of various adsorption sites will show up in a TPD spectrum as shifted desorption temperatures. Combined with structural information from microscopy or LEED, TPD makes a powerful tool to identify and quantify the presence of various adsorption sites. Furthermore, the desorption energy may depends on adsorbate coverage due to interactions between the adsorbed molecules, thus, such interactions can also be probed by TPD experiments.

The dissociation of molecules adsorbed on a model catalyst can be probed by the use of isotopic labeled gasses. The technique was used in this project investigating the dissociation of CO on ruthenium. By simultaneous dosing of $^{13}C^{16}O$ and $^{12}C^{18}O$ the ruthenium surface will be covered by these molecules, randomly mixed. Any detection of the scrambling products $^{12}C^{16}O$ and $^{13}C^{18}O$ in a subsequent TPD spectrum can only be a consequence of CO dissociation events followed by scrambling, recombination and desorption. In this way, the part of the ruthenium nanoparticles active for CO dissociation can be quantified as well as the desorption temperature.

2.9 Microscopy

Several microscopy methods has been used to image the nanoparticles, including Scanning Electron Microscopy (SEM), Scanning Tunneling Microscopy (STM) and Transmission Electron Microscopy (TEM). As the SEM and STM are located inside the vacuum chamber these techniques can image the samples without air exposure. The TEM is located at CEN-DTU in the neighbouring building, thus all samples imaged by TEM have been exposed to air.

2.9.1 Scanning Electron Microscopy

The SEM works by scanning a focused beam of electrons across the sample, and the scattered electrons are then collected to make up an image of the sample.

The microscope is a Zeiss Supra 55VP SEM. The primary electrons are emitted from a field emission tip (ZrO/W-cathode) and a high voltage (1000 V - 20 kV) accelerates the electrons towards the sample. The lens system focuses the electron beam to small spot and the scan coils raster the beam across the sample. The interaction of the primary electrons and the sample creates numerous products such as secondary electrons and backscattered electrons. The secondary electrons come from the ionization of surface atoms through inelastic collisions with primary electrons and has a low energy $<$50 eV. These electrons are detected by the In-Lens Secondary Electron Detector and gives a good surface sensitivity and topographic contrast. Backscattered electrons (BSE's), which are not detected, are primary beam electrons that have undergone multiple elastic collisions in the sample before exiting the surface. They have a higher energy ($>$50 eV) and are generated from a deeper range in the interaction volume and therefore carry depth information. The SEM micrograph is a 2D map of the intensity of the detected signal being emitted as the beam scans across the sample, and the best achievable resolution with this microscope is about 3nm

The SEM has mainly been used for overview imaging to check for homogeneity of the nanoparticle coverage as well as agglomeration. To achieve the highest resolution, all turbo pumps must be turned off to eliminate vibrations.

2.9.2 Scanning Tunneling Microscopy

The microscope is an Omicron Multiscan Variable Temperature STM which can operate in the temperature range from 70K to 1000K. The STM is positioned under the SEM column and by operating the SEM and STM simultaneously, the SEM can provide accurate positioning of the STM tip. The simultaneous SEM-STM operation capability requires a fixed sample-to-SEM column distance, so the STM is fastened directly onto the chamber with Viton rubber rings providing the only vibrational damping. This STM is therefore more susceptible to external vibrations compared to a STM hung in a spring system. The entire UHV system is therefore carried on air suspension damping legs.

The STM is operated, by applying a voltage bias between the sharp tip and the sample. The tip is scanned across the sample surface with a sub-nm tip-to-sample separation without contact. Due to the quantum mechanical tunneling effect (overlap of electronic wavefunctions from tip and surface) electrons tunnel from occupied states in the tip into the lowest unoccupied states in the sample when the sample is positively biased with respect to the tip, and from the highest occupied states in the sample into unoccupied states in the tip when the bias voltage is reversed[27]. The tip (x,y,z)-movement is controlled by piezo electric elements, that provide sub-angstrom movement capability. The STM was operated in constant current mode, where an electronic feed-back loop moves the tip towards or away from the sample such that the tunnel current is held constant during the lateral scan. The x, y and z-motion of the tip is then converted into a 3D image of the scanned surface. The piezo scanner has a lateral resolution of 0.1 Å and height resolution of 0.01 Å. The voltage bias between the tip and the sample was typically between $\pm$100 mV and $\pm$1.5 V. The actual tunnel parameters used are stated with the presented STM images. A quantum mechanical treatment of the problem is given elsewhere[27].

2.9.3 Imaging nanoparticles

Imaging a flat surface "only" requires an atomically sharp tip, meaning that one atom of the tip must be closer to the surface than all the others. The radius of the tip apex is not crucial. When imaging nanoparticles the sharpness of the tip apex is very important if the particles are to be imaged correctly. If the tip apex is significantly bigger than the NP to be imaged, the NP will image the tip just as the tip images the NP (Figure 2.16(a)+(b)). In the intermediate range where the tip

apex and the NP are comparable in size the STM image will be a convolution of the tip shape and the NP shape. The tips used here are made of tungsten and a good tip is estimated to have an apex radius of about 5 nm to 10 nm. Thus in practice it is a very difficult task to image the correct shape of NP's with high aspect ratio. Particularly the side facets are hard to resolve. The top facet should be possible to resolve, because when the tip is on the top facet it resembles a flat surface and the tip radius becomes less important. This means that it is possible to resolve the height of the particle while the lateral shape is poorly resolved and the diameter is often overestimated[28], as illustrated in Figure 2.16(c).

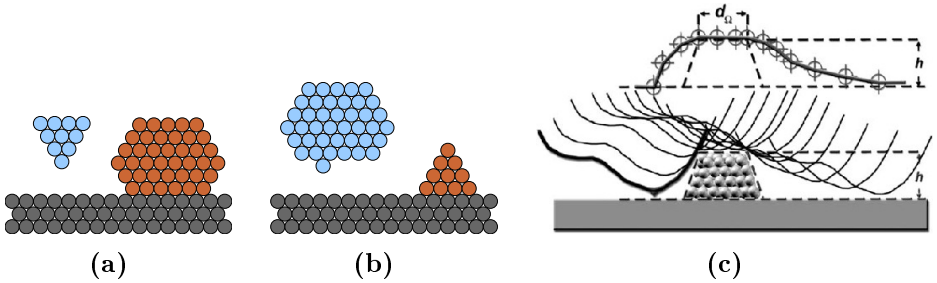

Figure 2.16: Imaging nanoparticles by STM: (a) Small tip and big nanoparticle, (b) Big tip and small nanoparticle, (c) Bottom: Illustration of a tip scanning across a nanoparticle., Top: The resulting line profile of the tip z-movement. It is seen that the height is recorded correctly whereas the diameter is overestimated. (c) is reprinted from[28].

2.9.4 Transmission Electron Microscopy

TEM works by transmitting a beam of high energy electrons through a thin sample and utilizes the wave nature of electrons. The transmitted electrons are collected by a fluorescent screen or a CCD camera.

The formation of contrast in TEM images depends on the image mode used. Working in bright field mode the contrast is formed simply by absorption of electrons, also called Mass-Thickness contrast. This means that the contrast changes with thickness (thick=dark) and atomic number (high atomic number=dark), and the image will be a two dimensional projection of the sample. When imaging in bright field mode the objective aperture is inserted, blocking any of the diffracted electrons. Working in High Resolution (HR) mode, a contribution to the image contrast comes from phase contrast. The objective aperture is set (or removed) to allow both the direct transmitted beam and the Bragg diffracted beams. The phase contrast relies on differences in phase between electrons that have been scattered

by crystal planes and corresponds to the interference pattern of the beams. HR mode thus only works on crystalline areas on the sample. Working in HR mode sets high demands to the absence of aberrations in the lens system and coherence of the incident electron beam. The images are not easily interpreted because the image contrast can come from multiple diffracting crystal planes.

The microscope used in this project is the FEI Technai T20 at the DTU Center for Electron Nanoscopy (DTU-CEN). The microscope has a point resolution of 2.4 Å, and line resolution of 1.5 Å.

Chapter 3

CO dissociation on Ruthenium nanoparticles

This chapter addresses the structure sensitivity and particle size dependence of the dissociation of CO on ruthenium nanoparticles. The model catalyst consists of mass selected Ru nanoparticles supported on Highly Oriented Pyrolytic Graphite. Additionally, we have investigated the materials gap between a single crystal and nanoparticulate system.

3.1 Introduction

The dissociation of CO on transition metal catalysts is a key reaction step in reactions involving syn-gas (CO and H_2), such as Fischer-Tropsch synthesis and the methanation reaction, where it is believed to be the rate limiting step[29, 30]. Ruthenium has also been found to be a very active catalyst for steam reforming, where methane and steam is converted to CO and H_2 [31]. Ruthenium has also been found to be active for ammonia decomposition[32] and proposed as catalyst for ammonia synthesis[33–35], where the dissociation of N_2 is the rate limiting step.

As mentioned in Chapter 1, industrial catalysts are predominantly nano-sized metal particles supported on high surface area oxide supports. The catalytic activity has in many cases been observed to be highly dependent on the particle size[36–41], but the origin of these observations are not very well understood. Investigations of particle size effects along with any support interaction effects can not be conducted using single crystal model systems, but model systems consisting of mass selected nanoparticles supported on planar supports are well suited. Aside from more closely mimicking the industrial catalyst such systems carry the advantage of compatibility

with existing surface science techniques as opposed to high surface area powder catalysts. For the purpose of studying the particles size effect, it is furthermore essential to achieve samples with mono-dispersed particles. The combination of a gas-aggregation particle source and a mass filter is well suited for the production of nanoparticles with a narrow size distribution. Several examples exist where this type of nanoparticulate model system has successfully been used to study a size dependence of catalytic reactions. A study of low temperature CO oxidation on gold nanoparticles supported on TiO_2, revealed a strong size dependence with a sharp increase in turnover frequency when the particle diameter was decreased below ~5 nm[42, 43], with a maximum at 2-3 nm[44]. The opposite effect was seen for CO oxidation over supported Ru nanoparticles where the activity was observed to increase with increasing particle size from 2 to 6 nm[45]. A similar effect was observed for Fischer-Tropsch synthesis over supported Co nanoparticles where the activity was shown to drop when the particle size was decreased below 6-8 nm[46].

The ability to gain structural information about the nanoparticles is naturally essential when correlating morphology to catalytic properties. The adsorption of CO on Ru single crystal surfaces has been studied extensively, and it is known that CO bound to different adsorption sites, such as facets and steps, can be distinguished as different desorption features in a TPD spectrum[47–70]. As the structural dependence of the desorption features from Ru single crystal surfaces are very well understood it can be used as the basis when interpreting the TPD spectra obtained from supported nanoparticles. Structural information from the nanoparticles can hereby be derived from recorded TPD spectra. Obtaining detailed structural information at the atomic scale by microscopy, such as STM and TEM, is a very challenging task even from a single nanoparticle[71]. For such structural information from TEM and STM to be representative of the whole ensemble of nanoparticles, the investigation of large number of particles is needed, which is even more cumbersome. For the purpose of gaining average structural information of the entire sample, TPD experiments serves as a relatively accessible method.

The dissociation of CO has also previously been studied on Ru single crystal surfaces by thermal desorption studies, e.g. using isotopically labled CO. Studies on close packed Ru single crystals have shown that the Ru(001) terrace sites are inactive for CO dissociation whereas step sites are active[47, 52, 54, 55]. Other studies have shown that more open Ru single crystal facets are active for CO dissociation[70, 72]. The CO dissociation reaction step is therefore concluded to be highly structure sensitive on ruthenium. The activity of supported Ru nanoparticles to dissociate CO is, due to the structure sensitivity of the reaction, believed to be correlated to the particle morphology and in particular to the abundance of under-coordinated

sites and open surfaces.

In this chapter the CO dissociation properties of mass selected Ru nanoparticles supported on HOPG will be investigated and correlated to the size and structure of the particles. The CO dissociation activity has been probed by TPD experiments using isotopically labled CO and structural information has been obtained by TEM and TPD spectrum analysis. In an effort to investigate the materials gap between single crystals and supported nanoparticles, the CO desorption properties of the HOPG supported Ru nanoparticles will be compared to that of a Ru single crystal by a method that allowed us to follow the gradual change from single crystal like behaviour to nanoparticle like behaviour and vice versa.

3.2 Nanoparticle deposition

The HOPG substrate was a 7 mm×7 mm × 1 mm HOPG (SPI-1) mounted in the sample holder described in Section 2.2. The HOPG substrate was freshly cleaved using adhesive tape before it was loaded into the preparation chamber. The entire sample holder was degassed for at least 5 hours at ∼500 °C in UHV before depositing nanoparticles. To examine the effect of graphitization, selected HOPG samples were sputtered with 500 eV Ar^+ ions for 15 min with a sputter current density of ∼1 $\mu A/cm^2$ and subsequently heated to ∼527 °C for 15 min to desorb implanted Ar atoms. Mass selected, negatively charged, Ru nanoparticles from 3 nm to 15 nm in diameter were then deposited using cluster source I (see Section 2.4.2) with the quadrupole mass filter set to a diameter resolution of (Δd/d) ±6 %, until 10-40% of the substrate was covered with particles. The substrate was biased +36 V to attract the particles while ensuring the particles are soft landed with kinetic energy <0.1 eV per atom, to avoid particle deformation at impact. After deposition these samples were investigated by TPD experiments using isotopically labled CO which is described later.

Duplicate samples were also prepared for TEM imaging, for characterising the particle morphology and measuring the actual size distribution for each selected size. When preparing the TEM grids, the particles were deposited directly onto standard lacey or holey carbon on copper mesh TEM grids. These results are presented in the following section.

3.3 Particle size distribution and morphology

The particle morphology and the particle size distribution were investigated for six selected particle sizes within a range of 3-15 nm in diameter by TEM. A typical TEM image used for measuring the particle size distribution is shown in Figure 3.1(a) and the measured size distributions for all the selected sizes are presented in Figure 3.1(b). The size distribution histograms were fitted with a Gaussian function to find the mean diameter and the standard deviation, σ. The obtained diameter resolution ($d/\Delta d$) lies within 10-20% if Δd is defined as 1σ. The size distributions were found by TEM image analysis which compute the projected area of the individual particles. The diameter distribution is then found from the measured projected areas by the spherical approximation where, projected area $= \pi(d/2)^2$. The particles are not perfect spheres but predominantly the aspect ratio is close to one which makes a diameter a good description of the particle size. The size distributions are broader than the mass filter setting should allow. This is suggested to be due to imperfections in the mass filter and due to the variety of particles shapes which in the image analysis would result in a broadening of the measured size distributions.

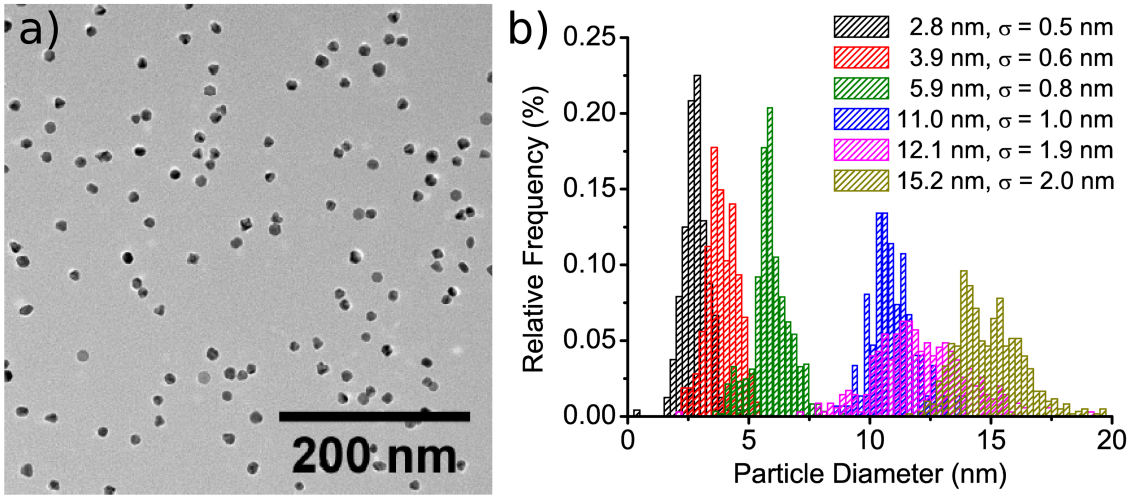

Figure 3.1: (a) TEM image of 11.0 nm Ru nanoparticles on carbon of low resolution, typically used for size distribution analysis. (b) Size distributions based on TEM images of samples with mass selected Ru nanoparticles. The TEM grid samples for each size were prepared similar to the HOPG samples used for the TPD experiments. Adapted from [73].

Detailed structural information was obtained by high resolution TEM, and selected images from samples with 2.8 nm, 6.3 nm and 15.1 nm particles are presented in Figure 3.2. The atomic structure show hexagonal symmetry and the lattice fringes periodicity was found to match the (100) interplanar distance. These findings suggest that the crystal structure of the particles is equivalent with Ru bulk hcp

structure. Further details of the structural study can be found in ref [20]. It was not possible to extract quantitative information on the atomic structure at the surface of the particles but the overall shape of the particles could be determined from the high resolution TEM images. The shape of the small particles appear predominantly to be close to the truncated hexagonal bypyramid equilibrium structure (see Chapter 1) whereas the proportion of particles that diverge from the equilibrium Wulff structure becomes larger as the particle size is increased. A large proportion of the non-equilibrium particles appear to be constructed as an agglomeration of smaller particles. In general, the large particles are non-equilibrium shaped, less faceted and show a higher degree of surface roughness than the small particles, which are closer to equilibrium and the large particles are therefore likely to contain a higher proportion of under-coordinated surface atoms than the small particles.

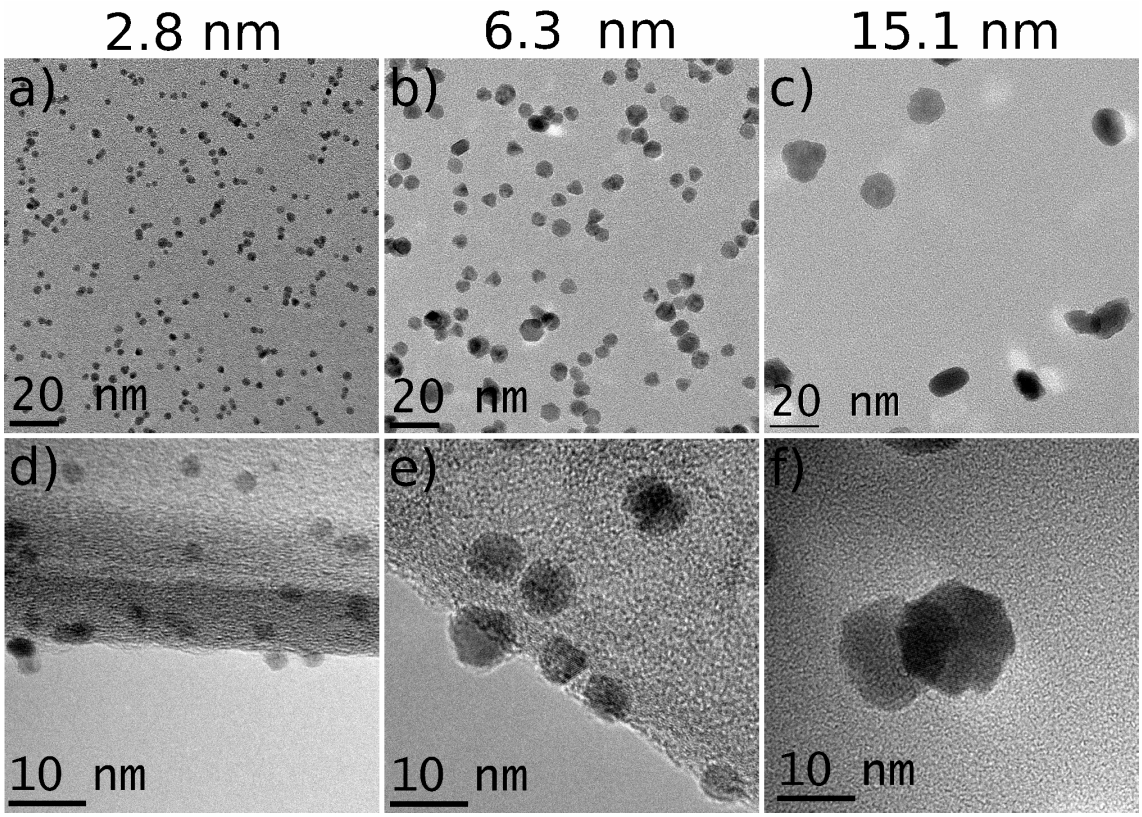

Figure 3.2: TEM images and High resolution TEM images of Ru nanoparticles from samples with a mean particles diameter of 2.8 nm, 6.3 nm and 15.1 nm. Adapted from [73].

3.4 CO scrambling

The CO desorption behaviour and the active sites for CO dissociation were probed by TPD experiments using isotopically labled CO. The TPD experiments were performed in the preparation chamber (see Section 2.1.2 and Section 2.8) immediately after nanoparticle deposition. Isotopically labled $^{13}C^{16}O$ (CIL, 99% ^{13}C, <10% ^{18}O) and $^{12}C^{18}O$ (CIL, <2% ^{16}O) were dosed simultaneously in a 1:1 ratio at 2×10^{-8} mbar for 10 min, corresponding to 9 Langmuir, sufficient to obtain a saturated CO coverage. During dosing, the sample was held at room temperature and the ratio of $^{13}C^{16}O$ and $^{12}C^{18}O$ was monitored with the mass spectrometer. When performing the TPD experiment, the temperature was ramped linearly at 1 K/s while monitoring the desorption products at mass 28, 29, 30 and 31 amu. The sample was placed within a distance of 0.5 mm to the QMS sniffer tip which ensures a local measurement of the gas composition with negligible contribution from the sample holder.

It is assumed that the dose gases, $^{13}C^{16}O$ and $^{12}C^{18}O$, adsorb randomly onto the surface of the nanoparticles. If the adsorbed $^{13}C^{16}O$ and $^{12}C^{18}O$ molecules dissociate, the dissociated ^{12}C, ^{13}C, ^{16}O and ^{18}O species will recombine and desorb during a TPD experiment. The dissociated species may be mobile on the surface and scramble and subsequently recombine into the four possible combinations, $^{12}C^{16}O$, $^{13}C^{16}O$, $^{12}C^{18}O$ and $^{13}C^{18}O$. Any formation of $^{12}C^{16}O$ and $^{13}C^{18}O$ is therefore a consequence of CO dissociation events, and the detection of scrambled CO molecules will be a measure of the concentration of active sites.

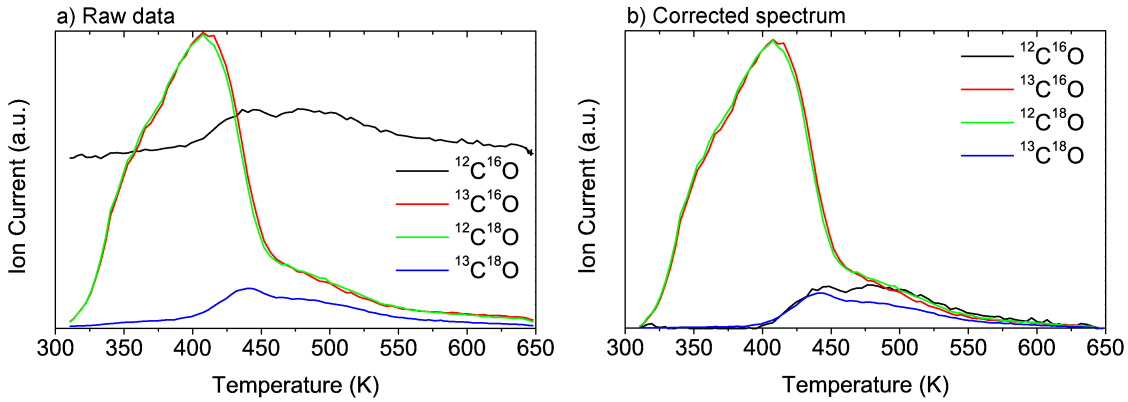

Figure 3.3: CO TPD spectrum obtained after dosing 9L of a 1:1 mixture of $^{13}C^{16}O$ and $^{12}C^{18}O$ onto 11.0 nm Ru particles on un-sputtered HOPG. Heating rate was 1 K s^{-1}. (a) Raw data measured by the QMS showing mass 28 amu (black), 29 amu (red), 30 amu (green) and 31 amu (blue). Note the high background of $^{12}C^{16}O$. (b) Corrected TPD spectrum obtained from the raw QMS data as described in the text for a better representation of the desorption. Adapted from [73].

The raw mass spectrometer data acquired during a TPD from 11.0 nm Ru nanoparticles supported on un-sputtered HOPG is shown in Figure 3.3a. The high intensity signals (red and blue curves) are recorded at mass 29 amu and 30 amu originating from the dosed $^{13}C^{16}O$ and $^{12}C^{18}O$, respectively. The black and blue curves are recorded at mass 28 amu and 31 amu which originate from scrambling into $^{12}C^{16}O$ and $^{13}C^{18}O$, respectively. The relatively high background of $^{12}C^{16}O$ is due to an unavoidable presence of CO in UHV chambers and in the mass spectrometer due to hot filaments and hence not desorption from the sample. TPD spectra that represent the samples quantitatively has been achieved by a background subtraction of each mass and by subtracting contributions from trace $^{12}C^{16}O$ and $^{13}C^{18}O$ impurities in the dosed gases. The corrected spectrum is shown in Figure 3.3b.

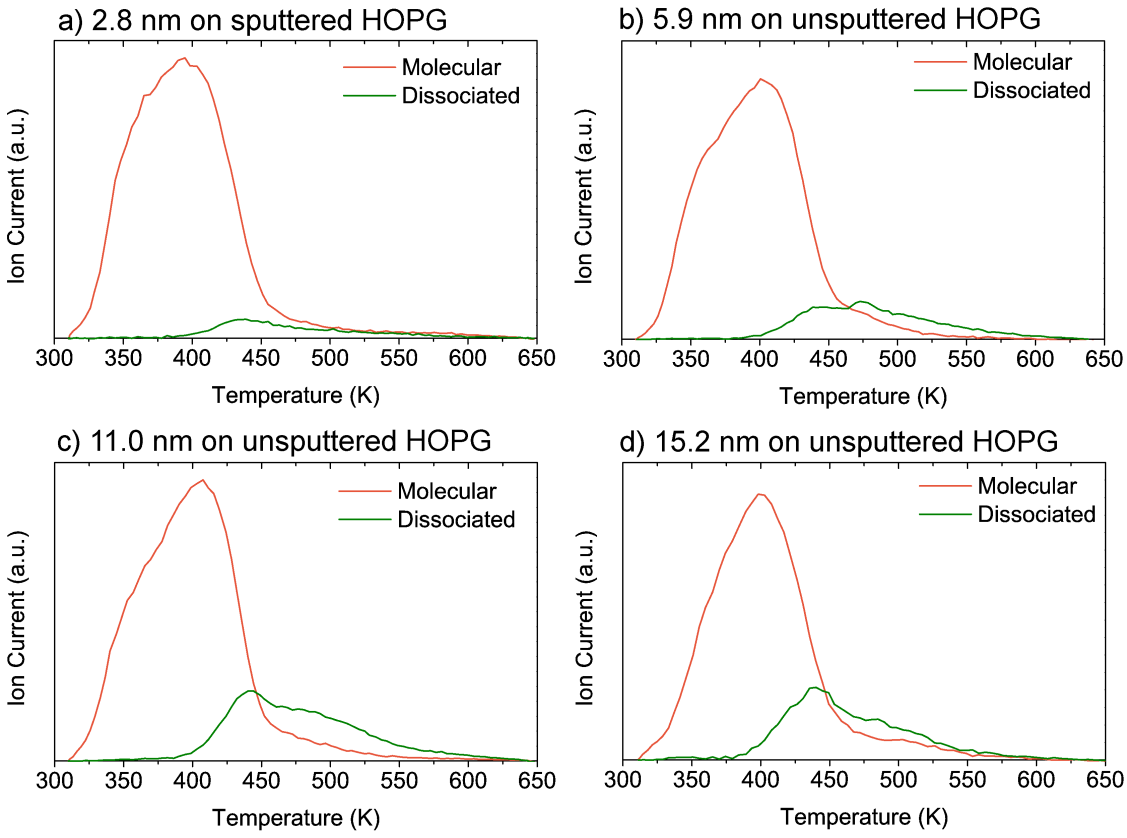

Figure 3.4: TPD spectra from samples with various size Ru particles on HOPG showing the CO desorption separated into the components originating from molecular adsorbed CO and CO that has been dissociated. Adapted from [73].

It is possible to construct TPD spectra where the desorption products are separated into signals originating from non-dissociated CO and from CO that has been dissociated (scrambling products). The resulting spectra are shown in Figure 3.4. Assuming equal probability for scrambling into each of the four possible products, the intensity of the $^{13}C^{18}O$ signal represents the scrambling into each of the four

possible isotopologues. The $^{13}C^{18}O$ signal hereby also constitute 1/4 of the total amount of scrambling products. The TPD spectrum of the total amount of scrambling products is therefore equal to four times the intensity of the $^{13}C^{18}O$ signal (green curve). The TPD spectrum originating from molecularly adsorbed CO can be found by adding the intensity from $^{13}C^{16}O$ and $^{12}C^{18}O$ and hereafter subtracting two times the $^{13}C^{18}O$ signal to account for the self-scrambling of $^{13}C^{16}O$ and $^{12}C^{18}O$ into $^{13}C^{16}O$ and $^{12}C^{18}O$ (orange curve). Figure 3.4 shows the desorption spectra separated into the molecular and dissociated components from samples with 2.8 nm, 5.9 nm, 11.0 nm and 15.2 nm nanoparticles on sputtered and un-sputtered HOPG. From Figure 3.4 it is seen that molecular adsorbed CO has a desorption peak at ∼410 K and the associative desorption from dissociated CO results in a broad feature at 400-600 K with two main peaks at ∼440 K and ∼475 K. The differences in desorption temperature indicate that the adsorption sites active for CO dissociation bind CO stronger than the inactive sites, as expected.

The shape of the TPD spectra is qualitatively the same across particle size, whereas the amount of dissociated CO relative to the total amount of adsorbed CO varies greatly as a function of particle size. The relative amount of dissociated CO has been calculated as the integrated desorption signal from dissociated CO normalised by the total CO desorption, for each particle size and the results are presented in Figure 3.5. The results show that the activity for CO dissociation increases with size indicating an increasing abundance of active sites with particle size. The sample with 11.0 nm particles showed the highest activity where ∼25 % of the adsorbed CO was dissociated.

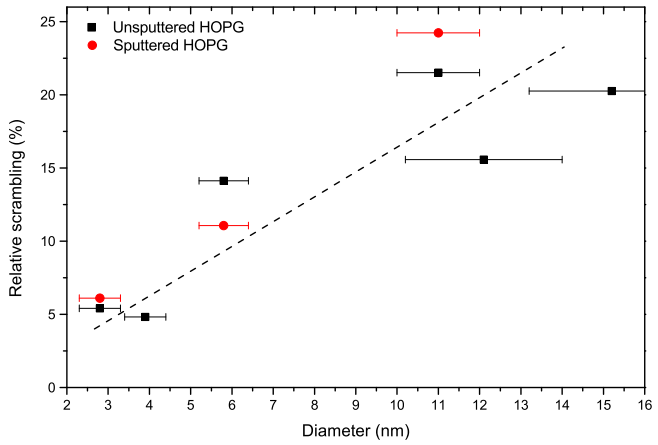

Figure 3.5: The amount of scrambled CO, i.e. CO that has been dissociated, relative to the total amount of CO as a function of particle size. The dashed line is drawn to guide the eye. Adapted from [73].

3.5 Linking nanoparticles to single crystal

The interaction of CO with Ru single crystal surfaces has been studied in great detail. The studies carry the advantage of using very simplified and well defined model systems. The study presented in this chapter builds upon the understanding provided by these single crystal studies. Providing a direct link between a nanoparticulate and a single crystal model system is therefore valuable when comparing results between these two systems.
In this section, results will be presented that demonstrate that CO desorption from Ru surfaces can be switched from that typical of single crystal surfaces to one more characteristic of supported nanoparticles and vice versa.

3.5.1 Nanoparticluate sample

A 50 Å Ru thin-film was thermally evaporated by electron-beam bombardment of a Ru rod (99.99% purity, Goodfellow) onto a freshly cleaved and degassed HOPG substrate. A STM image of such a freshly prepared sample is shown in Figure 3.6(a). The surface consist of 6 nm ± 2 nm particles in a coherent film fully covering the substrate.

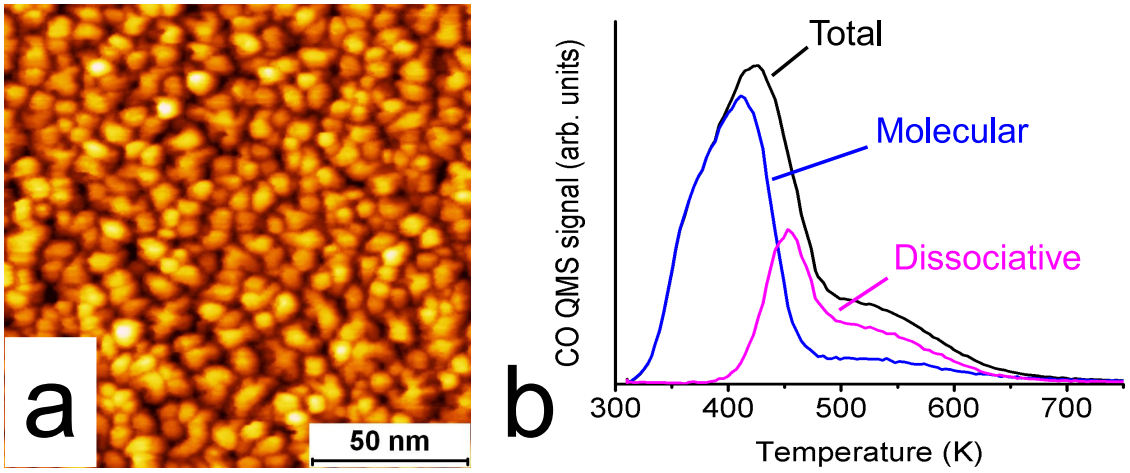

Figure 3.6: (a) STM image of a freshly prepared 50 Å Ru film on HOPG. (b) Corresponding CO TPD spectrum showing the total desorption of CO as well as the components originating from molecularly adsorbed and dissociatively adsorbed CO. Adapted from [74].

The corresponding CO TPD is shown in Figure 3.6(b) with the molecularly- and dissociatively adsorbed CO (blue and magenta curves) components separated along with the total CO desorption signal (black curve). The molecularly adsorbed CO show a desorption peak at ∼410 K and the dissociatively adsorbed CO peaks at

~450 K with a shoulder extending to ~650 K, very similar to the CO TPD from the mass selected particles. The relative amount of CO scrambling is ~33 % which is higher than the most active particles made by gas aggregation.
The film was subsequently annealed to 900 K for 10 min and the morphology of the film was imaged by STM and shown in Figure 3.7(a). After annealing, the film exposes flat terraces separated by monoatomic steps. The film is most likely polycrystalline with terraces being Ru(001) facets, as it has the lowest surface free energy. The corresponding CO TPD spectra is shown in Figure 3.7(b), and displays two desorption features at ~390 K and ~450 K. An additional, smaller peak can be seen at ~530 K. This spectrum is in good agreement with a typical desorption spectrum obtained from the Ru(001) facet[51, 55, 63–65]. The two first high-intensity peaks can be attributed to desorption of molecularly adsorbed CO from the terraces (α peaks), while the smaller peak can be attributed to desorption of dissociatively adsorbed CO from step sites (β peak)[55].

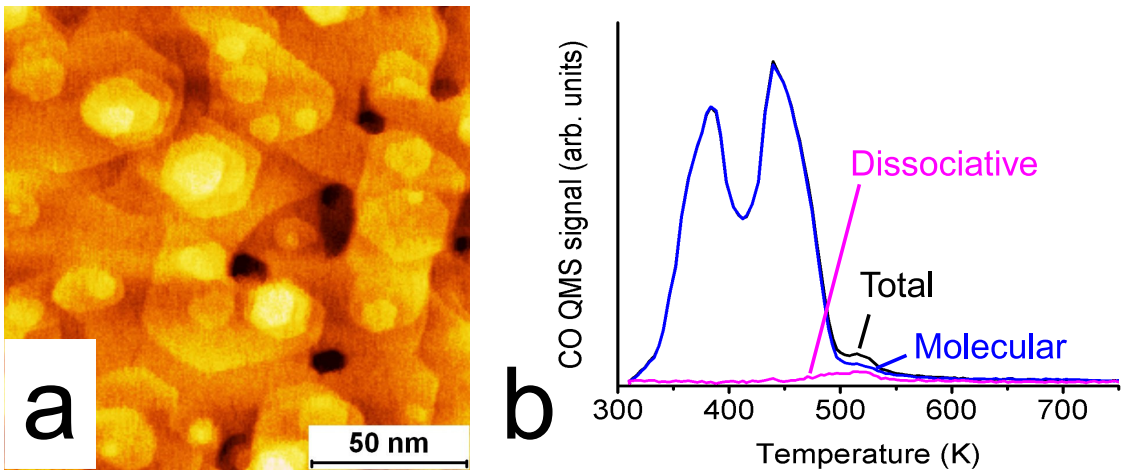

Figure 3.7: (a) STM image of a 50 Å Ru film on HOPG annealed to 900 K in vacuum for 10 min. (b) Corresponding CO TPD spectrum showing the total desorption of CO as well as the components originating from molecularly adsorbed and dissociatively adsorbed CO. Adapted from [74].

3.5.2 Ru(0 1 54) Single crystal

The single crystal studies presented in this section were performed on two Ru(0 1 54) single crystals (Matek GmbH) involving two other separate UHV setups. One crystal was mounted in a UHV setup with STM, TPD, ISS and XPS capabilities, primarily responsible for the STM results. The other crystal was mounted in a UHV setup with TPD, AES and ISS capabilities, primarily responsible for the TPD results. The Ru(0 1 54) surface exposes 27 atom wide (001) terraces on average, separated by

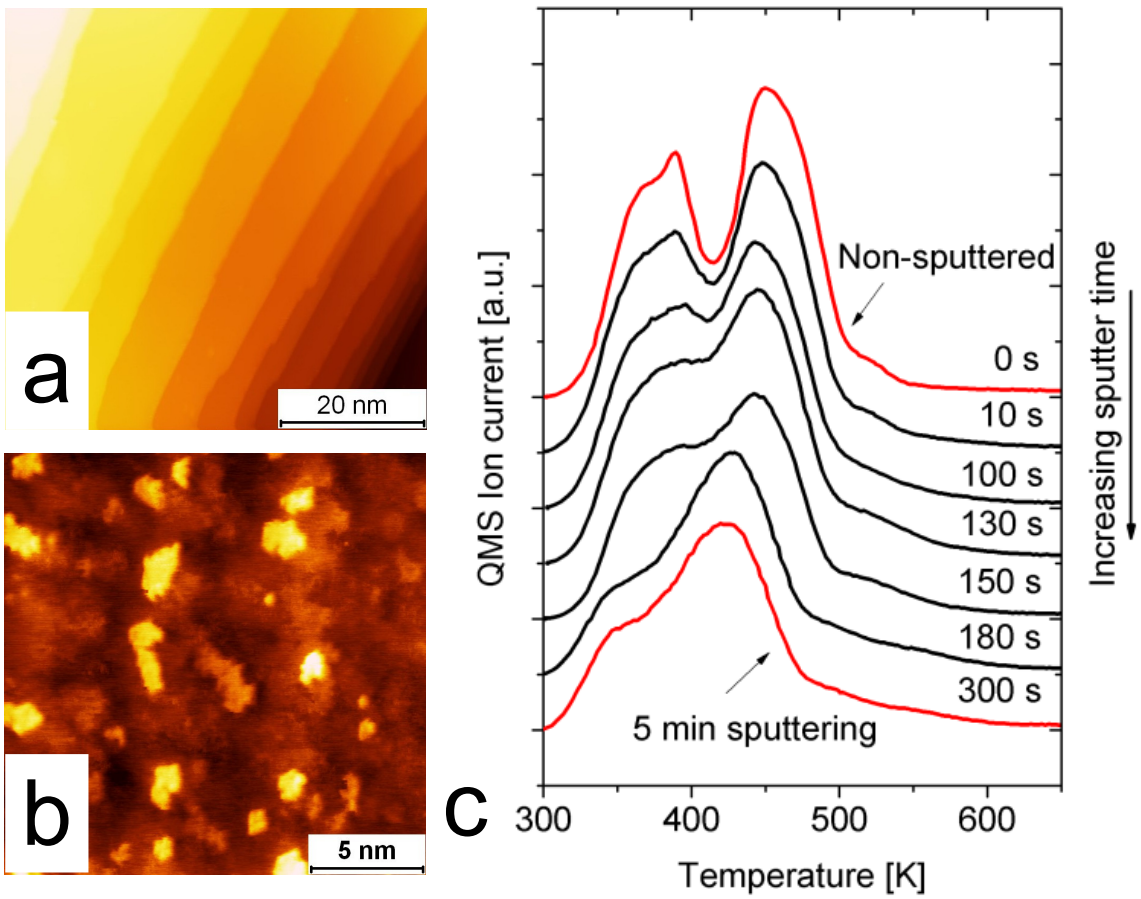

Figure 3.8: (a) STM image of a cleaned and non-sputtered Ru(0 1 54) surface. (b) STM image of a cleaned and subsequently sputtered with 1 keV Ar^+ ions for 5 min with a current density of 18 μA cm^2. c) Sequence of CO TPD spectra obtained after increasing time of Ar^+ ion sputtering. The STM experiments on the single crystal were performed by Yann Tison and Kenneth Nielsen and the TPD experiments on the single crystal were performed by Søren Vendelbo and Christian Conradsen. Adapted from [74].

monoatomic steps. Due to the hexagonal crystal structure, the steps separating the close packed (001) terraces are alternating between two step configurations. One with three-fold symmetry containing the so-called B5 sites and one with four-fold symmetry containing the so-called A5 sites[65, 75, 76]. Both samples were cleaned before experiments by cycles of sputtering with 1 keV Ar^+ ions at 800 K for 30 min followed by oxidation in 10^{-7} mbar O_2 at 1100 K for 10 min, reduction in 10^{-6} mbar H_2 at 500 K for 30 min and finally annealing at 1200 K for 1 min. The cleanliness of the samples was checked by AES or XPS after the cleaning procedure.

The TPD experiments were performed at a linear temperature ramp of 2 K s^{-1} after dosing CO at 10^{-7} Torr for 7 min, obtaining a saturation coverage of CO. A sequence of CO TPD spectra were obtained after increasing sputtering time with 1 keV Ar^+ ions at a current density of 18 μA cm^2, and the results are presented in Figure

3.8(c).The STM images shown in Figure 3.8(a) and (b) were recorded from the non-sputtered Ru(0 1 54) surface as well as after 5 min Ar^+ ion sputtering, corresponding to the surfaces responsible for the top and bottom TPD in Figure 3.8(c), respectively. The non-sputtered surface displays atomically flat terraces with an average with of 6.5 nm (corresponding to 27 atoms) separated by straight monoatomic steps. In comparison, the sputtered surface display terraces with small island patches and a high degree of surface roughness produced by the sputtering process. The TPD spectra from the non-sputtered surface displays a double peak feature at 390 K and 460 K (α_1- and α_2 peaks) followed by a small high temperature shoulder at ∼535 K (β peak), characteristic for a stepped Ru(001) surface. With increasing sputtering, the double peak feature is gradually diminished and replaced by a spectrum in close resemblance to a CO TPD from nanoparticles with a main peak at 420 K, a low temperature shoulder at 390 K and an increased high temperature feature (β peak) extending from approximately 480 K to 650 K.

3.6 Discussion

The desorption of CO from various Ru single crystal surfaces has previously been studied extensively, including Ru(001)[48], Ru(109)[55], Ru (0 1 54)[65] which essentially are Ru(001) surfaces with varying step density along with more open surfaces such as Ru(11$\bar{2}$0)[70] and Ru(11$\bar{2}$1)[77]. Each surface results in different desorption spectra. In a simple model based on the Wulff construction, supported Ru nanoparticles are comprised primarily of (001), (101) and (100) facets along with edge and corner atoms. CO desorption spectra from such idealised particles should thus for large particles primarily contain contributions from these facets, whereas contributions from the under-coordinated edge and corner atoms become increasingly dominant for smaller particles. The mass selected Ru particles produced in the project, imaged by TEM in Figure 3.2, are seen to deviate from the equilibrium shape predicted by the Wulff construction, so the resulting CO desorption is presumably more complex than a superposition of desorption from low surface energy facets.

The transformation of the well-ordered Ru(0 1 54) surface into a highly defected surface induced by Ar^+ sputtering, is clearly seen from the STM images in Figure 3.8(a) and (b), resulted in a gradual change in the CO desorption behaviour from that of stepped Ru(001) surface to that of the mass selected nanoparticles (see Figure 3.8(c)). The reverse transformation from nanoparticulate film to presumably polycrystalline film exposing Ru(001) facets, induced by annealing, resulted in a similar

but reverse transformation. These two results combined gives strong confidence for the TPD spectra obtained from the mass selected nanoparticles not to be influenced by contaminants such as O_2, but directly correlated to the surface structure. The characteristic double peak (α_1 and α_2) feature seen in the TPD spectra from the non-sputtered Ru(0 1 54) and the annealed 50 Å film, arise due the formation of an ordered $\sqrt{3}$x$\sqrt{3}$R30° CO overlayer at 1/3 monolayer coverage[59, 61]. This double feature has been observed to disappear when the (001) terrace width becomes sufficiently small and is also absent from the nanoparticles. The double peak has been observed to be fully present from Ru(0 1 54) with 27-atom wide terraces [65] and transformed into one main peak with a low temperature shoulder from Ru(109) with ∼10-atom wide terraces [55]. Two explanations have been suggested to account for this observation. 1) Narrow or disordered terraces can not sustain the ordered CO overlayer due to the lack of long range order. 2) Compressed lattice strain (observed by STM) localised at the upper (001) terrace extending 1-2 nm from a step edge[62], which can alter the CO desorption behaviour from these areas. Both of these phenomena may affect the CO desorption from nanoparticles but it has not been possible to verify.

The CO scrambling experiment TPD spectra from the mass selected nanoparticles presented in Figure 3.4 show that molecular adsorbed CO has a desorption peak at ∼410 K and the associative desorption from dissociated CO results in a broad feature at 400-600 K with two main peaks at ∼440 K and ∼475 K. The molecularly adsorbed CO desorbs at a lower temperature (peak at ∼410 K) than dissociated CO (from 400 K to 600 K), which shows that the sites active for CO dissociation bind CO more strongly than the inactive sites, as expected. It is known from the work by Zubkov et al. that step sites on Ru(109) are active for CO dissociation whereas the (001) facets are inactive[54, 55], which was confirmed by Vendelbo et al by studying a Ru(0 1 54) single crystal[65]. In the aforementioned study by Zubkov et al., it was found that by a combination of infrared spectroscopy and TPD experiments that CO dissociates at 450-500 K followed by recombination and desorption at 500-550 K. A STM study of a Ru(0 1 54) single crystal supported by DFT calculations determined that only the B5-site with 4-fold symmetry is active for CO dissociation. A study by Wang et al. indicates from high resolution electron energy loss spectroscopy (HREELS) that CO dissociates on the open Ru(11$\bar{2}$0) surface already from 300 K followed by recombination and desorption starting at 450 K with peaks at 500 K and 540 K[70]. It was furthermore concluded that both terrace and defect sites were active. The low onset temperature at ∼400 K, from dissociated CO in the present study, suggests that active sites similar to the open Ru(11$\bar{2}$0) surface are present and the broad desorption feature suggests that there exist several sites that

are active for CO dissociation. This is in good agreement with the high proportion of non-equilibrium shaped nanoparticles observed by TEM, where the surface exhibits a high degree of roughness, hereby exposing a large variety of under-coordinated surface atoms.

The relative amount of CO scrambling as a function of particle size presented in Figure 3.5 shows that larger particles contain relatively more active sites for CO dissociation than smaller particles. For equilibrium shaped nanoparticles the optimal particle size is by DFT calculations shown to be ∼3 nm for N_2 dissociation as this size exposes the highest concentration of active sites[78]. A combination of TPD experiments, STM and DFT calculations has shown that both CO and N_2 preferentially dissociate on the B5 step-site on Ru(001)[7, 65, 76] and DFT calculations suggest geometrically very similar active sites for CO and N_2 dissociation on the corrugated Ru(11$\bar{2}$1), as well. As the active sites for CO and N_2 dissociation on Ru are very similar, it is expected that the optimal particle size for CO dissociation is the same as for N_2. The optimal particle size found in this study deviate from the theoretically predicted as the particle structure deviate from equilibrium. The observed size dependence is believed to be correlated to structural differences when increasing the particle size, due to the formation process inside the aggregation zone of the cluster source, where the particle growth mechanism can be dominated by either ad-atom growth or growth by cluster-cluster agglomeration. The hypothesis is that small particles are predominately formed by ad-atom growth leading to a particle shape close to equilibrium, whereas the large particles are predominately formed by gas phase cluster-cluster coagulation leading to highly non-equilibrium shaped nanoparticles, with a high degree of surface roughness. Such a growth mechanism has previously been observed for PtFe particles[79] and for Pt particles where particles larger than 2.5 nm resulted in ramified structures, which showed evidence for cluster-cluster coagulation in the growth kinetics[80]. The conditions in the aggregation chamber (gas pressure, sputter power, residence time) will affect the growth mechanism so it is likely that there exist a set of conditions that will produce large particles dominated by ad-atom growth and thus result in particles with structures close to equilibrium.

3.7 Conclusion

Mass selected Ru nanoparticles from 3-15 nm in diameter were deposited on HOPG and the active sites for CO dissociation were probed by TPD experiments using isotopically labled CO as a function of particle size. From the TPD experiments it

was shown that molecularly adsorbed CO desorbs in a broad peak with a maximum at 410 K and dissociatively adsorbed CO, recombines, and desorbs from 400 K to 600 K with two main peaks at ∼440 K and ∼475 K, suggesting that the particles expose several types of active sites. The relative number of active sites was quantified for each particle size and shown to increase for increasing particle size. The maximum amount of CO scrambling was measured from ∼11 nm particles to be ∼25 %. The observed size dependence is suggested to be correlated to the increasing surface roughness for larger particles. We have provided a link in the CO desorption behaviour from Ru single crystal model catalysts to nanoparticulate model catalyst, in order to narrow the materials gap. A nanoparticulate Ru film grown on HOPG by physical vapour deposition, showed a CO desorption behaviour like the mass selected nanoparticles. By thermal annealing the film structure changed and the CO desorption behaviour transformed to that comparable with a single crystal surface. The reverse transformation in CO desorption behaviour was demonstrated by Ar^+ sputtering a stepped Ru(001) single crystal for an increasing amount of time, hereby gradually changing the surface into a highly defected structure.

Chapter 4

High pressure CO induced surface reconstruction on Platinum nanoparticles

This chapter addresses the topic of adsorbate induced surface reconstructions. We have probed CO induced structural changes of mass selected platinum nanoparticles supported on SiO_2/Si by TPD experiments and compared the results to a parallel set of experiments on a Pt(111) single crystal.

4.1 Introduction

A catalyst is working in the presence of the reactant gas and molecules are adsorbed on the surface. The ability for a catalytically active surface to reconstruct induced by the presences of adsorbed species will play a crucial role for the catalytic properties under working conditions because the activity is often strongly dependent on the atomic arrangement of the atoms that constitute the active sites. Other surface dynamics phenomena such as particle sintering, changes in oxidation state and changes in elemental composition in alloy nanoparticles, can also be driven by adsorbate induced interactions and are relevant for the catalytic properties. Experiments that contribute to the understanding of adsorbate induced surface reconstructions are therefore necessary to understand the origin of the catalytic properties of a catalyst under reaction conditions, which may lead to the design of new and better catalysts.

There is profound interest in platinum as a catalyst on the electrodes in polymer electrolyte membrane fuel-cells (PEMFCs) due to its high activity for the electro-

chemical oxygen reduction reaction, and for methanol oxidation which is relevant for direct methanol fuel cells (DMFCs). The noble properties of Pt are especially important to avoid corrosion under the acidic conditions and electrochemical potentials. Pt is also used as an oxidation catalyst in catalytic converters for cleaning soot and hydrocarbon species in engine exhaust gas. It is therefore highly relevant to gain knowledge about structural modifications of platinum nanoparticles when exposed to various gaseous environments.

Structural modifications of nanoparticle model catalysts due to adsorbate-surface interactions and variations in temperature can presently be studied near reaction conditions by several techniques such as environmental transmission electron microscopy (E-TEM), high pressure x-ray photoelectron spectroscopy (HP-XPS) and other x-ray techniques such as Extended X-ray absorption fine structure (EXAFS). Dynamic and reversible shape changes of supported copper nanoparticles in response to changes in the gaseous environment were observed by Hansen et al. using ETEM[11]. A similar study by Yoshida et al. showed that the morphology of Pt nanoparticles on CeO_2 changed from faceted in vacuum, to rounded in 1 mbar CO at room temperature.

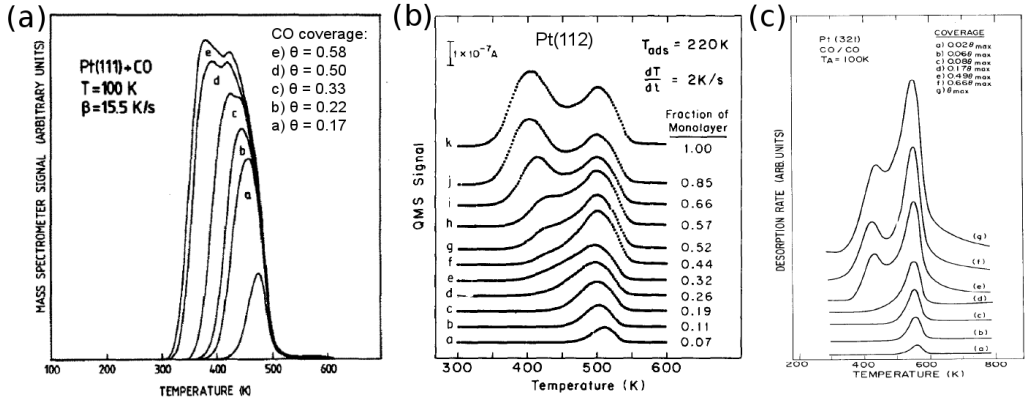

Figure 4.1: (a) CO TPD from Pt(111) at various CO coverages. The heating rate was 15.5 K/s and CO was dosed at 100 K. Adapted from [81]. (b) CO TPD from Pt(112) at various CO coverages. The heating rate was 2 K/s and CO was dosed at 220 K. Adapted from [82]. (c) CO TPD from Pt(321) at various CO coverages. The heating rate was 10 K/s and CO was dosed at 100 K. Adapted from [83].

In contrast to the techniques mentioned above, which are expensive (the x-ray techniques require synchrotron radiation facilities) and often difficult to access, a comparatively simple way of probing the surface structure is by the use of gas adsorption followed by temperature programmed desorption. It is well known that the desorption profile from single crystal surfaces reflects the surface structure due to the dependence of the adsorption energy on the coordination number of the surface

atoms that constitute the adsorption site[82, 84, 85]. Chemisorbed adsorbates are bound more strongly at under-coordinated (step) sites than at terrace sites and the desorption temperature from step sites is therefore higher than from terrace sites. For CO on Pt it has been shown by DFT-calculations that the CO binding energy is highly dependent on coordination number and that the binding energy scales inversely with coordination number (higher binding energy for lower coordination number)[86]. Three examples from literature of temperature programmed desorption (TPD) spectra from CO adsorbed on various platinum single crystal terminations are shown in Figure 4.1, and a comparison of the spectra nicely illustrates that the differences in desorption characteristics reflect the difference in surface structure. Figure 4.1(a) is from a Pt(111)[81], Figure 4.1(b) is from a Pt(112)[82] which consists of 3 atom wide (111) terraces separated by monoatomic (100) steps and Figure 4.1(c) is from a Pt(321) which consists of 3 atom wide (111) terraces separated by kinked monoatomic $(31\bar{1})$ steps. It is clearly seen that desorption from the (111) terraces and the steps present on the Pt(112) can be distinguished and give rise to a low- and high-temperature peak, respectively. It can also be seen that CO adsorbed at the kinked step sites on Pt(321) desorb at slightly higher temperatures than the CO adsorbed at the step sites on Pt(112), in good agreement with the coordination dependent adsorption energy mentioned above.

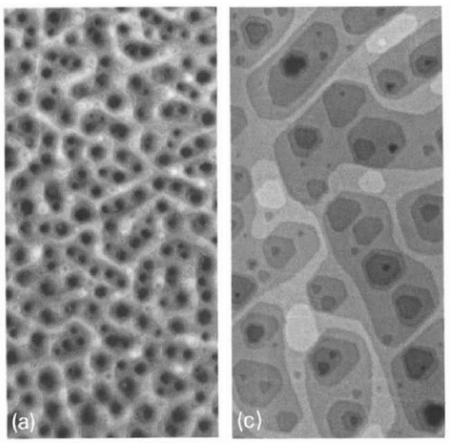

Figure 4.2: Two STM images (1650 Å× 3300 Å) of a Pt(111) single crystal after sputtering at two different temperatures: (a) 625 K and (c) 735 K. Adapted from [87].

The well-defined single crystal surfaces are often achieved by sputter and annealing cycles. Sputtering removes the top layer atoms and thereby cleans the surface from impurities. The defected surface created by the sputtering is then healed again by annealing the crystal to very high temperatures. The effect of sputtering at various temperatures has been studied by Michely et al. where at Pt(111) surface was sputtered at various temperatures and subsequently imaged by STM[87]. The sur-

face morphologies that were obtained after sputtering at 625 K and 735 K are shown in Figure 4.2. The STM images show that sputtering gives rise to pit formation and by varying the sputter temperature the pits size and corresponding step density can be controlled.

The main purpose of this chapter is to investigate CO induced structural changes on mass selected Pt nanoparticles supported on SiO_2/Si, and provide important information about the concentration of different types of surface sites (facet, steps, corners etc.) at various pressures of CO. Such information is relevant for modelling structure sensitive reactions involving CO, e.g. synthesis gas, under reaction conditions. The work is also inspired by STM investigations which have shown surface reconstructions of Pt crystal surfaces induced by various pressures of CO from high vacuum to near atmospheric pressure[14, 88–91]. For the purpose of establishing CO TPD experiments as a technique to quantify the concentration of different types of surface sites, low pressure CO TPD spectra acquired from nanoparticulate samples and a Pt(111) single crystal (annealed or sputtered) are compared, and we establish a link between under-coordinated sites of the two systems. The samples are then exposed to mbar pressures of CO at elevated temperatures and modifications in the desorption spectra are observed, and the changes induced by CO are interpreted as a promotion of annealing out the single crystal versus a roughening of the nanoparticle surface. We furthermore observed a size dependence of nanoparticle roughening suggested to be determined by the size of the low index facets.

4.2 Sample preparation

The samples were prepared by depositing mass selected Pt nanoparticles produced by Cluster Source I onto SiO_2/Si substrates with an incorporate platinum resistance-temperature device (RTD) on the backside (see Section 2.2.1 for details). The substrates were cleaned prior to particle deposition by heating the entire sample holder to ∼600°C for $>$ 12 hours using the PBN-heater incorporated in the manipulator head. The wafer alone was then heated, by passing a current directly through the wafer, to 500°C for 30 min in 10^{-6} mbar O_2 to oxidise any hydrocarbon contaminants present on the SiO_2 surface. The cleanliness of the substrate was confirmed by ISS with 980 eV He^+ ions after the cleaning procedure and after nanoparticle deposition.

4.3 Particle morphology

The particle morphology and size distribution were investigated by TEM for particles with a mean diameter of 3 nm, 6 nm and 11 nm. Particles were deposited directly onto TEM-grids with carbon or SiO_2 films and imaged as deposited without further treatment. The cluster source conditions used to produce the TEM-grids and the samples for TPD experiments were identical. The results presented in Figure 4.3 show both size distribution histograms along with TEM images of particles representative of the samples.

The size distributions in Figure 4.3(a), (b) and (c) were determined by analysing TEM images finding the projected area of a number of individual particles. The particle diameter distributions were then found assuming spherical morphologies. The (d) 3 nm and (e) 6 nm particles showed near-spherical cross sections whereas the (f) 11 nm particle projections showed more faceted particles with well-defined edges that are consistent with octahedron and cuboctahedron morphologies. High resolution images with visible lattice fringes, were always found to match the lattice periodicity consistent with the bulk Pt fcc structure. In general, the particle morphologies are not perfect Wulff constructions but all the imaged particles appeared to be monolithic and crystalline.

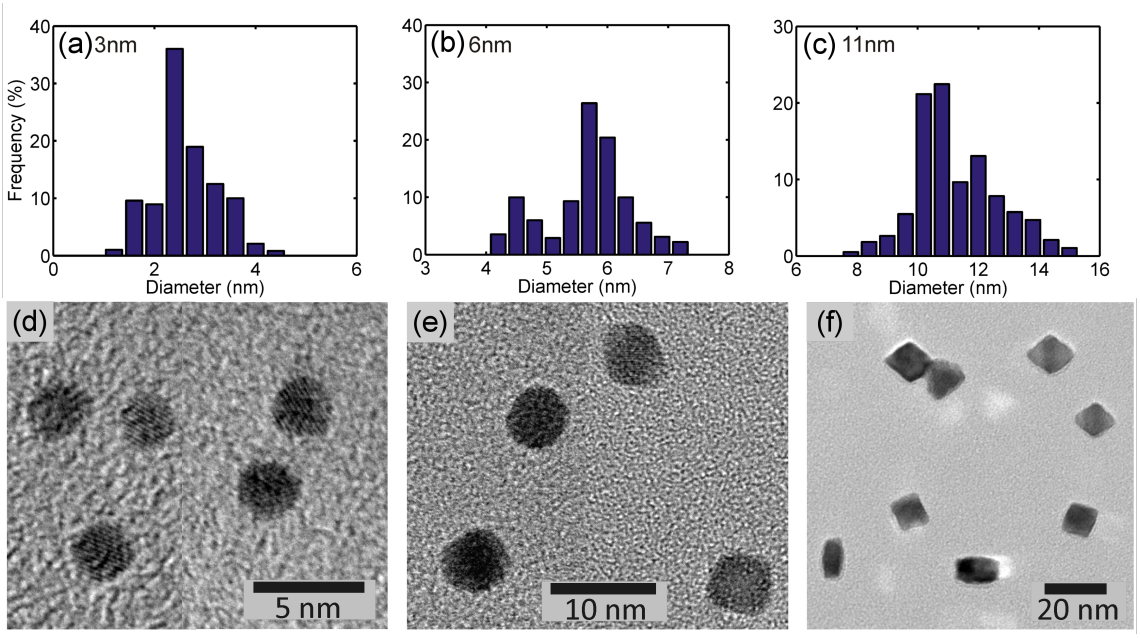

Figure 4.3: Size distribution histograms (a)-(c) and corresponding TEM-images (d)-(f) from samples with 3 nm, 6 nm and 11 nm mass selected Pt nanoparticles. The different particle sizes were prepared with different cluster source conditions. Adapted from [92].

4.4 Low pressure CO

Figure 4.4 shows TPD spectra from 3 nm, 6 nm and 11 nm Pt particles supported on SiO_2: (a) shows the first TPD experiment from as-deposited particles and (b) shows the second TPD and therefore from samples that have been heated to 700 K. Prior to the TPD experiments, the samples were dosed with $^{12}C^{18}O$ through a leak valve at 10^{-7} mbar for 10 min corresponding to 60 Langmuir, sufficient to saturate the surface. During the TPD experiments, the temperature was ramped at 1 K/s from 298 K to 700 K by heating the wafer directly, while simultaneously recording the quadrupole mass spectrometer (QMS) signal at mass 30 amu with the sniffer tip placed within a distance of 0.5 mm to the sample. In Figure 4.4 the spectra are normalized to maximum intensity of the QMS ion signal, to make a comparison of the desorption features from the different size particles more straightforward.

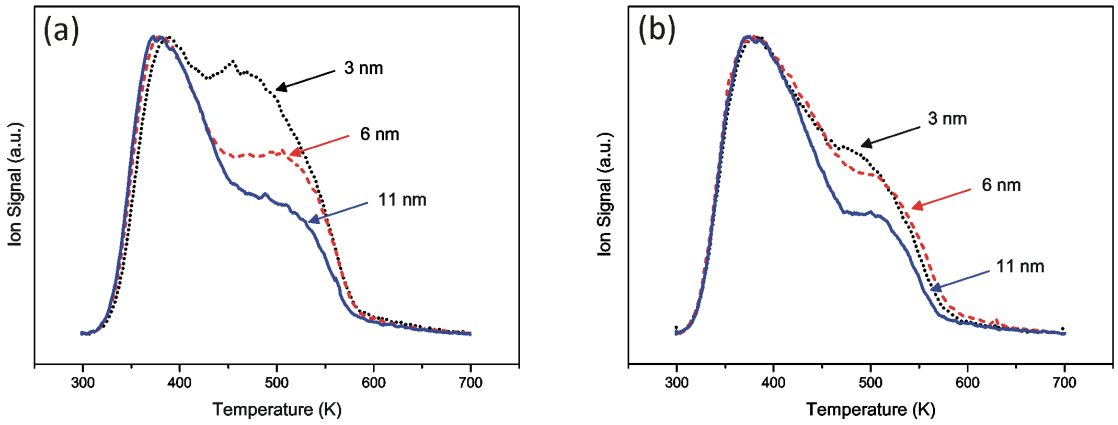

Figure 4.4: CO TPD spectra from mass selected Pt nanoparticles of 3, 6 and 11 nm. (a) first TPD of as deposited particles, (b) second TPD. The temperature ramp rate was 1 K/s. Adapted from [92].

All the desorption spectra presented in Figure 4.4 show a low temperature peak at 390 K and a high temperature peak/shoulder at ~475 K that extends to 575 K. The apparent difference when reducing the particle size from 11 nm to 6 nm to 3 nm is the increased intensity of the high temperature feature. The observed trend is consistent with particles exposing an increasing proportion of under-coordinated sites when decreasing the particle size. Similarly, when comparing the first TPD to the second TPD it is evident that the high temperature feature is reduced after the particles have been heated briefly to 700 K. This observation is consistent with a surface reconstruction of the particles where an initial roughness of the particles is removed by the annealing during the first TPD. A third TPD was performed on selected samples (not shown) which proved to be identical to the previous TPD, supporting the idea of a minor surface reconstruction, and showing that the particles

have attained a stable structure after the second TPD.

4.5 High pressure CO

After the samples were subjected to the two low pressure TPD experiments presented above, they were transferred into the high pressure cell and annealed at 573 K in ∼5 mbar CO for 10 min. The samples were then cooled down to 300 K in the CO atmosphere after which the cell was evacuated. The samples were then transferred back into the vacuum chamber and placed under the QMS sniffer tip, where a TPD experiment was performed immediately. The resulting TPD spectra are shown in Figure 4.5(a) as the dashed red line along with the previous low pressure TPD represented by the black line.

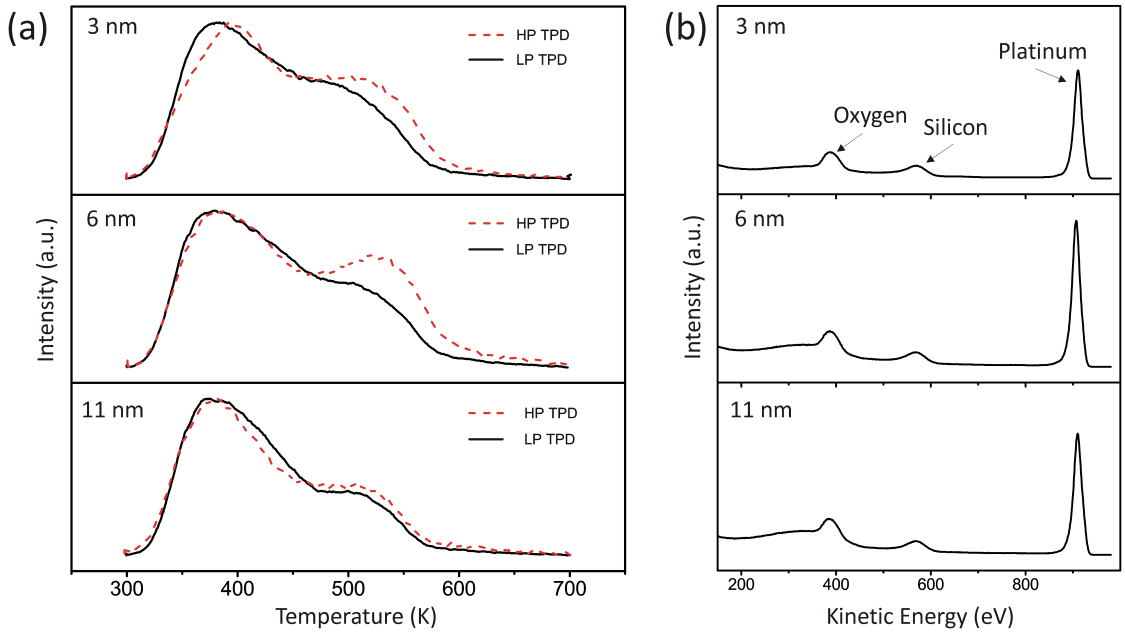

Figure 4.5: (a) CO desorption spectra from samples with 3, 6 and 11 nm Pt nanoparticles on SiO_2/Si. The black lines are from the second low pressure TPD as presented in Figure 4.4(b) and the dashed red lines are the CO TPDs after the subsequent annealing of the samples at 573 K in ∼5 mbar CO. (b) ISS spectra from the corresponding samples acquired after the high pressure TPD experiments. Adapted from [92].

For the 3 nm particles, the high pressure CO annealing increases the high temperature desorption feature and the desorption now extends beyond 550 K. This increase of the high temperature desorption feature is even more pronounced for the 6 nm particles, whereas the desorption behaviour of the 11 nm particles basically remains unaffected when comparing the low and high pressure CO dose.

ISS was performed after the high pressure annealing and subsequent TPD experiments with the purpose to check for nickel contamination. Nickel is a well-known source of contamination when working with high pressure CO dosing. CO under high pressure reacts with nickel contained in stainless steel tubing and containers to form nickel-carbonyl species. If nickel-carbonyls are present in the dosing gas they will decompose on the catalyst surface and deposit nickel. A suitable cleaning of the CO feed gas, as described in Section 2.3, will remove the trace amounts of impurities. The ISS spectra presented in Figure 4.5(b) show no indication of nickel contamination, only the expected oxygen, silicon and platinum peaks are present as indicated in the figure.

4.6 Comparative study on Pt(111)

A comparative study on a Pt(111) single crystal was conducted in parallel to the study of the nanoparticle model system. The aim was to investigate the CO desorption from an annealed Pt(111) surface containing very few step sites and after introducing a rougher surface topography by Ar^+ sputtering. From these experiments, a close link between the CO desorption temperature and the coordination number of the adsorption site can be made and hereby establish CO TPD experiments as a tool to investigate the surface structure. The CO desorption was investigated after dosing at low pressure, and by transferring the crystal into the attached high pressure cell the effect of annealing in a high pressure of CO was also studied. The experiments were conducted at a different UHV setup at CINF with XPS, ISS, TPD and Low Energy Electron Diffraction (LEED) capabilities.

4.6.1 Low pressure CO

Figure 4.6(a) show CO TPD spectra from the Pt(111) crystal in the annealed state and after various sputter treatments: Annealed to 1273 K, sputtered at 373 K, sputtered at 573 K and sputtered at 673 K. All sputter treatments were performed with 1.2 keV Ar^+ ions after a standard cleaning procedure involving cycles of sputtering at room temperature, annealing to 1273 K and sputtering at 1273 K. The cleanliness of the crystal was checked with LEED, XPS and ISS. The CO dosing was done at 2×10^{-7} mbar for 10 min while the cooling down the crystal from the sputtering temperature to room temperature and the TPD was acquired with a heating rate of 2 K/s. The four spectra shown in the figure are normalised to the maximum intensity to enhance the sputter dependent high temperature feature. The TPD spectrum

from the annealed crystal show only a single broad desorption peak from 300 K to 500 K, consistent with the results from Steininger et al. [81]. When the crystal is sputtered, the main desorption peak becomes narrower and a high temperature feature emerges from 475 K to 550 K. It is furthermore seen that the high temperature feature becomes more pronounced when lowering the sputter temperature.

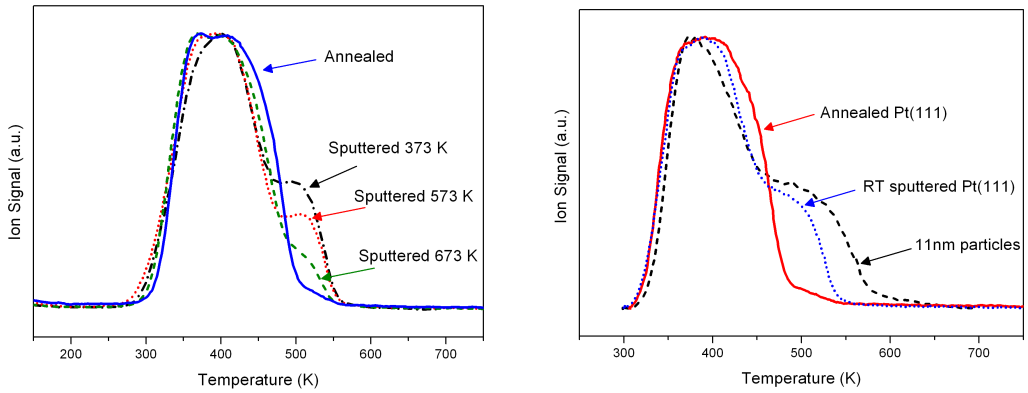

Figure 4.6: (a) CO TPD spectra from the Pt(111) single crystal after different sputter temperatures. The crystal was cooled to room temperature in a background of CO at 10^{-7} mbar for 10 min. The heating rate was 2 K/s. (b) A comparison of TPD spectra from the annealed Pt(111), the Pt(111) sputtered at room temperature and from a sample with 11 nm Pt particles on SiO_2/Si. The samples were dosed at 300 K in 10^{-7} mbar CO for 10 min. The experiments involving the Pt(111) crystal were conducted by Tobias Johansson and Angela den Dunnen. Both adapted from [92].

The STM study by Michely et al. showed that low temperature sputtering results in a rougher surface topography with more step sites than high temperature sputtering[20, 87], as mentioned in the introduction. The change in surface structure, i.e. in the amount of step sites, is clearly observed in the CO TPDs shown in Figure 4.6 as a change in the amount of CO desorbing at high temperatures (i.e. CO bound to step sites) relative to CO desorbing at low temperature (i.e. CO bound at terrace sites). This demonstrates CO TPDs as a useful tool to probe the surface structure of nanoparticles (this is further elaborated in the discussion below).

In Figure 4.6(b), CO desorption spectra from the annealed Pt(111), room temperature sputtered Pt(111) and 11 nm mass selected Pt particles on SiO_2 are shown, and normalised to the maximum intensity for easy comparison. The single crystal and nanoparticle sample experiments were performed in two different UHV systems but the CO dosing and TPD conditions were kept as similar as possible. The dosing was done with freshly prepared samples at room temperature in 10^{-7} mbar CO for 10 min and the TPD heating rate was 1 K/s in both cases. Comparing the TPD

from the 11 nm particles to the sputtered single crystal a similar desorption behaviour is observed with small differences. In both cases, the desorption kicks off at ∼300 K followed by a narrow main desorption peak and a high temperature shoulder. The apparent differences include the main peak of the nanoparticle spectrum being slightly more narrow and centred at 390 K as well as the high temperature feature extending further until ∼575 K. For comparison, CO from the sputtered single crystal is fully desorbed at ∼540 K.

4.6.2 High pressure CO

In the previous section we established the use of CO TPD as tool to probe surface structure of Pt nanoparticles. In this section the effect of annealing in a high pressure of CO on the surface structure is investigated using CO TPD experiments. A series of comparative experiments were performed where the effect of annealing in either vacuum or 10 mbar CO were investigated. The Pt(111) crystal was sputtered at 373 K and subsequently annealed in either vacuum or 11 mbar CO at 373 for 10 min. The CO TPD spectra after these sets of treatments are showed in the bottom section of Figure 4.7(a) along with a CO TPD from the annealed crystal (top section) for comparison. In Figure 4.7(b) the results are presented from a comparable set of experiments with the sputter and annealing temperature set to 573 K. Prior to the TPD experiments, the vacuum annealed samples were dosed with CO at 10^{-7} mbar for 10 min at room temperature, whereas the samples annealed in CO were cooled down to 300 K, at which point the CO was evacuated.

When comparing the CO desorption spectra after annealing in vacuum (red line) and in 11 mbar CO (black line) in Figure 4.7(a), it is evident that the presence of CO only has a minor annealing effect on the surface structure at 373 K. Alternatively, as shown in Figure 4.7(b), annealing to 573 K in 11 mbar of CO produces a large annealing effect compared to vacuum annealing. The same annealing effect was also observed when annealing in 3 mbar CO at 573 K (data not shown). From these experiments it is evident that the presence of CO adsorbed on the surface enhances the rate of a surface restructuring where the sputter induced steps are annealed out.

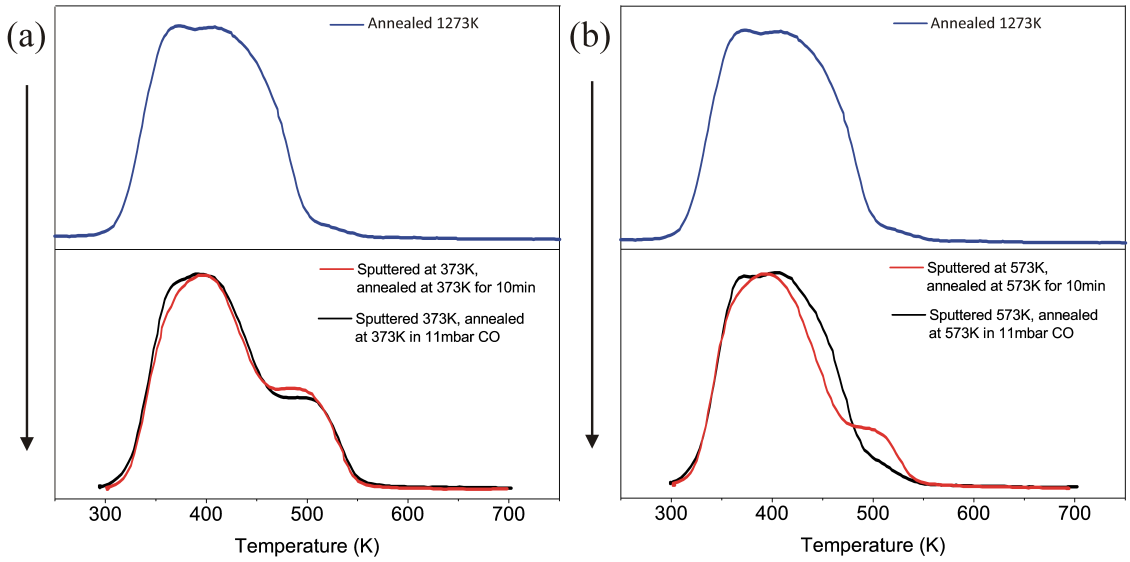

Figure 4.7: CO TPD spectra from the Pt(111) crystal after sputtering and vacuum annealing at (a) 373 K and (b) 573 K (red lines), after sputtering and annealing in 11 mbar CO at (a) 373 K and (b) 573 K (black lines) and in the fully annealed state (blue lines) for comparison. The experiments were conducted by Tobias Johansson and Angela den Dunnen. Adapted from [92].

4.7 Discussion

The structure of nanoparticles is not easily characterised experimentally. Single crystal surfaces, on the other hand, are well defined and relatively easy to characterise. The adsorption and desorption behaviour of CO from various surface terminations of the Pt single crystal has previously been studied and the desorption temperature has been proven to be very dependent on the structure of the adsorption site[81–83]. DFT calculations have also shown that the binding energy of CO on Pt is highly structure sensitive[86] and correlated to the coordination of the surface atoms[88]. By correlating the surface morphology of Pt single crystals determined by e.g. STM or LEED to the desorption behaviour, desorption spectroscopy can be used as a tool to probe the surface structure. Nanoparticles can be more or less crystalline and attain shapes close to equilibrium exposing various facet terminations or adopt shapes far from equilibrium exposing very rough surfaces. With the single crystal desorption results in hand, temperature programmed desorption can be used to probe the surface structural composition of nanoparticles.

4.7.1 Correlating low pressure CO TPD to surface structure

The STM study, mentioned in the introduction, by Michely et al. of the Pt(111) surface after Ar^+ sputter treatments at various temperatures showed that sputtering leads to pit formation and that the step-density increases when lowering the sputtering temperature. Comparing the CO TPD spectrum from Pt(111) in the annealed state to those after sputtering at increasing temperatures (Figure 4.6(a)), clearly indicate that the high temperature feature from 475 - 550 K originates from CO bound to step sites and the main peak from 300 K to 500 K originates from CO bound to terraces. This is also consistent with results from stepped Pt single crystals such as the Pt(112)[82]. The increasing intensity of the high temperature feature is furthermore consistent with the increasing step density created when decreasing the sputter temperature. Having established a correlation between that structure and CO desorption behaviour, the CO TPD results from the nanoparticulate samples can be correlated to the particle structure. In Figure 4.6(b) the TPD from 11 nm particles on SiO_2 is compared to that of an annealed and sputtered Pt(111). The low temperature peak indicates that the 11 nm particles contain (111)-facets. The high temperature peak from the nanoparticles differs from the sputtered Pt(111) by extending to higher temperatures. This indicates that the nanoparticles contain both step-sites and highly under-coordinated sites such as kinks, edges and corners, consistent with the high temperature CO desorption feature from the kinked Pt(321) surface (containing 60% 6-fold coordinated terrace atoms, 20% 5-fold coordinated step atoms and 20% 4-fold coordinated kink atoms) which extends from 500 K to 600 K.
When comparing the CO desorption from 3 nm, 6 nm and 11 nm Pt particles, it can be seen from Figure 4.4(a) that the high temperature feature is more pronounced from smaller particles along with an increased desorption above 550 K. This trend fits well with the picture that smaller particles exposing a higher surface area fraction of under-coordinated sites. The surface reconstruction upon annealing to 700 K can be observed in Figure 4.4(b) where a loss of the initial surface roughness results in an intensity drop of the high temperature feature. Due to the particle formation process inside the aggregation zone of the cluster source, the particle morphology is not expected to be in equilibrium so some degree of surface reconstruction upon annealing is expected.

The discussion above displays that the binding energy of CO to Pt is dependent on the coordination of the surface sites, which in turn is correlated to the particle size. Another particle size effect which could come into play are finite size effects including lattice stain and electronic effects when decreasing the particle size below

∼5-3 nm. A TEM study of 3-5 nm gold particles suggest that the surface atoms are contracted and that the contraction is coordination dependent, dominated by edge atoms and atoms on (100) facets[93]. A concern in this study is the presence of adsorbates which are unaccounted for, but most likely present in the relatively poor vacuum in a TEM. DFT calculations on adsorption energies of O and CO on unsupported gold nanoparticles by Kleis et al. have shown that gold particles below 2.7 nm exhibit clear finite size effects, with the general trend that the adsorption of O and CO becomes stronger as the particle becomes smaller[94]. Above 2.7 nm, the particles have chemical properties similar to extended surfaces. Recent unpublished results obtained by Kleis et al. show the same trend for Pt nanoparticles, where the finite size effect appears below ∼2 nm. It is also concluded that the observed changes in adsorption energy with particle size is dominated by electronic effects rather than by lattice strain effects. The opposite effect has been reported in a recent CO TPD study from Pt nanostructures on HOPG where a lower desorption temperature was observed when decreasing the particle size in the size range of a few nanometers, suggesting a decreasing CO binding energy for decreasing particle size[95]. A similar study by microcalorimetry also observed a degrease in CO binding energy with decreasing particles size for Pd nanoparticles on a thin film of Fe_3O_4[96]. Despite the above mentioned observations, our results show no clear indication of any such size effect, as the desorption peaks in Figure 4.4 remain at the same temperature, regardless of particle size. As indicated the DFT studies mentioned above, the absence of this size effect may be due to the size of the investigated particles simply being too large.

4.7.2 High pressure induced surface reconstructions

The enhancement of annealing out the sputtered Pt(111) was clearly observed to be induced by the presence of mbar pressures of CO. We believe that the adsorption of CO enhances the mobility of Pt surface atoms which facilitate the accelerated surface restructuring.

As mentioned above, DFT-calculations have shown that the adsorption energy of CO to Pt strongly depends on the coordination number of the Pt atom, with increasing adsorption energy for lower coordination numbers[88]. The increase in adsorption energy for decreasing coordination numbers is on the order of the energy required to break Pt-Pt nearest neighbour bonds. This mean that the adsorption of CO can spontaneously create low-coordinated Pt atoms and hereby enhance mobility of Pt surface atoms and thus increase the rate of surface reconstructions. Enhanced diffusion of Pt atoms has also been observed by adsorption of hydrogen atoms[97]

Apart from the enhanced mobility observed in this study, the equilibrium structure of a surface can be highly dependent on the presence and on the coverage of adsorbed species. CO-induced surface restructuring has been observed on a number of Pt single crystal terminations. The highly stepped Pt(557) and Pt(332) was shown, by STM and high-pressure XPS, to break up and form nanometer sized clusters on the terraces when exposed to CO pressures above 0.1 Torr[14]. The apparent roughening of the surface structure was through DFT-calculations explained by a mechanism where the increased concentration of under-coordinated Pt edge sites produced by the cluster formation allow the adsorbed CO molecules to tilt away from each other and hereby relieve the strong CO-CO repulsion at high coverage. In a combined STM and DFT study by Thostrup et al.[88, 89] the corrugated Pt(110)-(1×2) surface was exposed to CO pressures from UHV to 1 bar. The fraction of step-atoms was reported to increase dramatically when the CO coverage increased to ∼0.7 followed by a steep decrease in the fraction of step-atoms when the CO coverage was further increased to 1. A temperature of 373 K was sufficient to facilitate the formation of equilibrium structures. The observed equilibrium structures were explained by the difference in CO adsorption energy with Pt coordination number. The surface structure of Pt(111) has also previously been investigated by STM in the presence of CO from 10^{-6} Torr to 760 Torr at room temperature, and no surface reconstruction was observed throughout the pressure range[90], consistent with the equilibrium structure observed in this study. The afore mentioned studies display the vast diversity of possible surface reconstructions in response to CO exposure/adsorption, and that the resulting structure is dependent on the initially exposed crystal facet and the step density. In general, surfaces will adopt the structure that minimises the total energy of the system, corresponding to thermodynamic equilibrium. Based on the previous examples the energy of the system seems to be determined by an interplay of the coordination dependent CO adsorption energy and the energy associated with the CO-CO repulsion in the CO adsorption layer.

Exposing supported Pt nanoparticles to a high pressure of CO at elevated temperatures results in the opposite effect as observed for the Pt(111) single crystal. The amount of CO bound at high temperatures increases for the 3 nm and 6 nm particles which is indicative of a CO induced restructuring of the particle surface to expose a higher concentration of surface sites with low coordination numbers. This is consistent with a recent study by Yoshida et al. where the shape of ∼3.5 nm Pt nanoparticles supported on CeO_2 were investigated in an environmental TEM (ETEM) under vacuum and 1 mbar CO at room temperature[98]. They observed the particle morphology change from faceted (exposing low index facets) under vacuum to round in CO, hereby exposing high index facets and sites with low coordination

numbers. We speculate that the observed surface restructuring of the 3 nm and 6 nm nanoparticles is due to the coordination dependent adsorption energy of CO to Pt-sites hereby promoting a surface morphology with a high concentration of under-coordinated sites. In contrast to the observed roughening of the 3 nm and 6 nm particles, the CO desorption from the 11 nm particles remain virtually unaffected by the presence of the high pressure CO atmosphere. The previously mentioned highly stepped Pt(557) and Pt(332), which were observed to roughen when exposed to mbar pressure of CO, both consist of 6 atom wide (111) terraces separated by monoatomic steps under UHV conditions. The edge length of the (111) facets on a 11 nm Wulff constructed Pt nanoparticle is on the order of 41 atoms, which is considerably larger. Thus, the facet size could be the determining factor for the different reconstructions observed for different particle sizes.

The observed surface reconstructions induced by the presence of adsorbates and the particle size dependence of this phenomena can very likely be expanded to other metal-adsorbate systems and have to be taken into account when describing structure sensitive catalytic reactions, e.g. dissociation reactions that require special under-coordinated sites, as well as the oxygen reduction reaction in fuel cell Pt catalysts where the reaction occurs preferentially on the close-packed (111) facet.

4.8 Conclusion

We have demonstrated the use of temperature programmed desorption experiments as a sensitive probe of the configuration of surface sites and the ability to distinguish between low index facets and under-coordinated Pt atoms on both single crystal and nanoparticle model catalysts. By applying this technique to two model systems, the Pt(111) crystal and mass selected Pt nanoparticles supported on SiO_2, we found good agreement between the surface structure and the corresponding CO desorption characteristics. Comparing the CO desorption characteristics from the annealed Pt(111), the sputtered Pt(111) and the mass selected Pt nanoparticles, showed that the high temperature desorption feature from the nanoparticles was consistent with desorption from step sites available both on the roughened Pt(111) and highly stepped Pt crystal surfaces reported in the literature, along with a minor contribution from sites with even lower coordination numbers (edges, kinks and corners). Reducing the particle size from 11 nm to 6 nm to 3 nm resulted in an increased intensity of the high temperature feature, consistent with a size dependent particle morphology where under-coordinated sites increasingly dominate nanoparticles as the particle size is decreased.

Exposing the roughened Pt(111) crystal to mbar range pressures of CO at elevated temperatures gave rise to a promotion of the annealing process whereas the same treatment of the 3 nm and 6 nm Pt particles induced an apparent surface roughening as indicated by the increase in CO desorption at high temperature. The 11 nm particles showed only a minor increase in high temperature CO desorption. Based on literature, we expect that Pt-Pt nearest neighbour bonds weakens due to adsorption of CO which gives rise to enhanced mobility of Pt surface atoms and thereby promotes the surface restructuring into a more thermodynamically favourable structure. It is known from literature, that Pt surfaces may reconstruct into various structures dependent on the CO coverages and crystal termination, which is proposed to be due to the coordination dependent CO adsorption energy and CO-CO repulsion at high coverages. Highly stepped and corrugated Pt surfaces reconstruct whereas Pt(111) does not reconstruct. We speculate that the differences in CO induced surface reconstruction with particle size is related to the facets size and the distribution of surface atoms with low coordination number.

Chapter 5

Pt and Pt-Y alloys for Oxygen Reduction Reaction

In this chapter we establish a size and structural dependence of platinum nanoparticles for the electrochemical oxygen reduction reaction (ORR). We expand the study to platinum-yttrium alloy nanoparticles which show an improved activity for the ORR.

The electrochemical measurements were performed in the electrochemical lab at CINF and the people involved were Francisco J. Perez-Alonso, Patricia Hernandez-Fernandez and Ifan E. L. Stephens.

5.1 Introduction

Studying the size and structural dependence of Pt for the ORR is motivated by the use of Pt in low temperature polymer electrolyte membrane fuel cells (PEMFCs). Pt is used in state-of-the art PEMFCs, but due to the slow kinetics of the oxygen reduction reaction (despite the use of Pt), a high Pt loading is required at the cathode. Pt is scarce and expensive so the required high Pt loading at the cathode is the main obstacle for making PEMFCs economically viable[99]. In order to improve the reaction kinetics, a fundamental understanding of the factors that control the ORR activity of Pt is needed. Especially the size and structural dependence as well as the nature of the active site are important factors to understand. Numerous studies have been reported on this subject and most articles report an increase in specific activity (activity per Pt surface area) with increasing particle size. The observed trend was rationalised by Nørskov, Rossmeisl and co-workers through density functional theory (DFT) calculations, and they proposed that the terrace sites are the active

sites and that under-coordinated sites bind the reaction intermediates (O*, HO*, HOO*) too strongly[100, 101]. Recently, Arenz and co-workers have questioned the validity of the aforementioned experimental studies of the ORR activity measured on Pt nanoparticles on high surface area supports, due to the influence of uncompensated resistance and support capacitance[102]. The arisen controversy strongly motivates model studies with good control of particle size and dispersion and by using a planar support, capacitance effects can be neglected. The existing UHV setup with attached cluster source is well suited for the purpose of preparing such model catalysts, due to the capability of depositing mass selected Pt nanoparticles directly onto a planar glassy carbon support which is compatible with the rotating ring disc electrode (RRDE) assembly. It is furthermore an advantage that the nanoparticles generated by the gas aggregation technique does not contain surfactant molecules that would be present on particles produced by chemical synthesis, and as the model catalysts are prepared in vacuum, surface science characterisation techniques can readily be employed.

The overall reaction in a PEMFC is $2H_2 + O_2 \rightleftharpoons H_2O$. On the anode side, the Hydrogen Oxidation Reaction (HOR) takes place, and the protons are conducted through the proton exchange membrane (often made of Nafion) to the cathode while the electron goes through an external circuit. On the cathode side the protons and electrons react with oxygen to give water, which is called the Oxygen Reduction Reaction (ORR).

$$O_2 + 4H^+ + 4e^- \rightleftharpoons 2H_2O \tag{5.1}$$

The thermodynamic potential for the overall reaction at 80°C is 1.17 V which would be the potential over the PEMFC if no losses were present. A measured polarisation curve of a state-of-the art PEMFC is shown in the red curve in Figure 5.1. As the current density increases, losses in the cell from ohmic resistance, mass transport limitations and from poor kinetics of the half-cell reactions gives rise to a potential drop (overpotential η) over the cell. The blue curve in Figure 5.1 represents the contribution to the overpotential from the ORR, η_{ORR}, which clearly shows that the poor kinetics (large reaction barrier) of the ORR is the main contributor to the overpotential. A more active catalyst for the ORR would result in a higher current density at a given cell potential.

The reaction mechanism for the oxygen reduction reaction involve four proton and four electron transfers to each O_2 molecule (see Equation 5.1) and several intermediate species are bound to the surface i.e. O*, HO* and HOO*. The exact reaction mechanism is controversial as it is difficult to probe the intermediates *in*

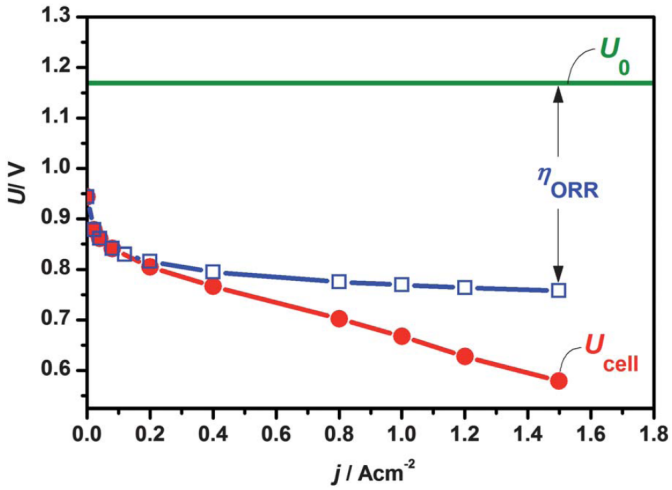

Figure 5.1: Polarisation curve of a state-of-the are PEMFC, using a platinum catalyst. The cell is operated at 80°C at a total pressure of 1.5 bar H_2/O_2. Adapted from [103], originally from [99].

situ experimentally. Considering the reaction mechanism depicted in Figure 5.2, theoretical models developed by Rossmeisl, Nørskov and co-workers through DFT calculations can successfully account for the overall trends, and by including the adsorption energies of the different ORR intermediates, i.e. O*, HO* and HOO* in the model, the full free energy pathway for the reaction as a function of potential can be calculated[104, 105]. Figure 5.2(a) shows the free energy diagram of the ORR at 0.9 V on Pt(111) and the stepped Pt(211). Any reaction step that is uphill in energy, such as ΔG_1 and ΔG_2 will slow down the reaction and give rise to an overpotential, and the reaction step that is most uphill is the potential determining step. By increasing the overpotential, the driving force for each reaction step is increased (i.e. ΔG_1 and ΔG_2 are decreased), until all the reaction steps are downhill in free energy the current density will exponential increase. A catalyst that binds HO* stronger as well as HOO* weaker will according to Figure 5.2(a) decrease the overpotential and thereby increase the activity. Unfortunately, it has been found that the adsorption energies of HO* and HOO* are linearly dependent on metal surfaces[106] and the optimal catalyst therefore bind each of the four intermediately moderately such that ΔG_1 and ΔG_2 are equal. Figure 5.2(a) furthermore show that the close-packed Pt(111) surface is much more active that Pt step sites as the reaction intermediates are simply bound too strongly to the step sites (ΔG_2 step sites » ΔG_2 terrace sites).

Pt is the most active pure metal, but from the volcano curve shown in Figure 5.2(b) it can be seen that the optimal catalyst for the ORR, should have an O binding energy of 0.2 eV weaker than pure Pt. Due to the linear scaling between the adsorption energy of the reaction intermediates, the trends in ORR activity on

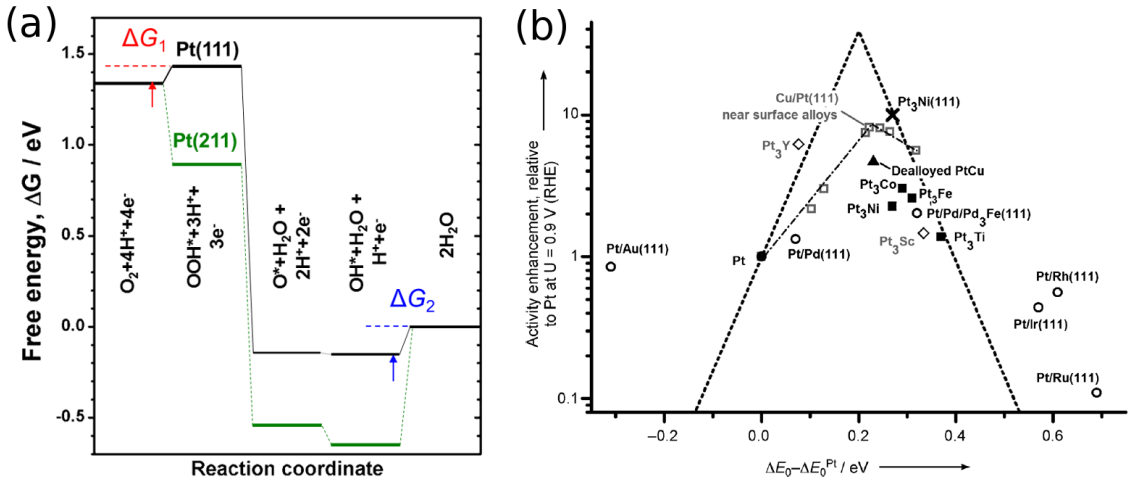

Figure 5.2: (a) Free energy diagram of Pt(111) and Pt(211). Data in the figure are from [100, 105]. (b) Volcano plot for different Pt alloy catalysts with Pt overlayers, showing experimental ORR activity enhancement as a function of oxygen binding energy ΔE_O, both relative to pure Pt. All data are at 0.9 V (RHE). Adapted from [107]

different metal surfaces can be related to one "descriptor"; the O binding energy. This is what gives rise to a volcano-type curve as shown in Figure 5.2(b), where experimental ORR activity enhancement relative to Pt is plotted as a function of the calculated oxygen binding energy relative to Pt, for a number Pt alloy catalysts with Pt overlayers[107]. On the weak binding side of the volcano (right side), OOH^* formation is the potential determining step and on the strong binding side of the volcano (left side), OH^* removal is the potential determining step. One route to reduce the Pt loading in PEMFCs is to increase the activity of Pt by alloying with other metals. A number of alloys of Pt and late transition metals have been studied and tested and the achieved activity enhancements are shown as data points in Figure 5.2(b). All the Pt alloys in Figure 5.2(b) has a pure Pt overlayer and the result of alloying is a modified electronic properties of the Pt overlayer that weakens the adsorption energy of the ORR intermediates relative to pure Pt. This modification can be obtained by two effects: ligand effect or strain effect. The ligand effect is due to the *solute* metal in the subsurface layer which change the electronic properties of the Pt overlayer. The strain effect is present when the Pt surface-layer is compressed laterally induced by a slight lattice mismatch between Pt and the underlying alloy structure. The compressed Pt overlayer exhibit a downshift in the d-band center which makes it less reactive (see Section 1.3.1). The mutual importance of the two effects are in general difficult to distinguish. When alloying Pt with a less noble metals such as Cu, Co, Ni, Fe or Y, the solute metal is not stable under acidic condition and high potentials and the solute metal is therefore dissolved in solution leaving behind a pure Pt overlayer[99, 108–114]. This Pt overlayer is stable and

act as a kinetic barrier for further de-alloying. Pt alloy catalysts such as $PtNi_x$, $PtCo_x$, $PtFe_x$ and $PtCu_x$ have been tested in PEMFCs and they tend to degrade over time[99, 109, 111, 113], due to segregation of the solute metal into the surface layer and further dissolution into the electrolyte. The susceptibility for de-alloying is not surprising, as the alloying energy is negligible[115].

Motivated by reported activity enhancements of Pt alloy catalysts for the ORR we have studied model catalysts consisting of Pt-Y alloy nanoparticles for the ORR, and the results are presented in the second part of this chapter. The Pt-Y alloy was originally proposed as a result of a computational screening study conducted at CAMD, DTU Physics by Greeley et al. where they investigated a number of different Pt-alloys and the results indicated that Pt_3Y was both thermodynamically extremely stable (very negative alloying energy) and active for ORR[115]. In the same study, the Pt_3Y alloy was also tested experimentally (at CINF) for the ORR in the form of a polycrystalline disc and the results showed a 6-10 times enhancement in the ORR activity relative to Pt depending of the potential, which is the highest ORR activity recorded from a polycrystalline sample[116]. In a recent study from our group by Stephens et al. a number of Pt alloys with early transition metals in the polycrystalline form was tested for the ORR and the results showed that Pt_5Y was also very active (see Figure 5.3(a))[107].

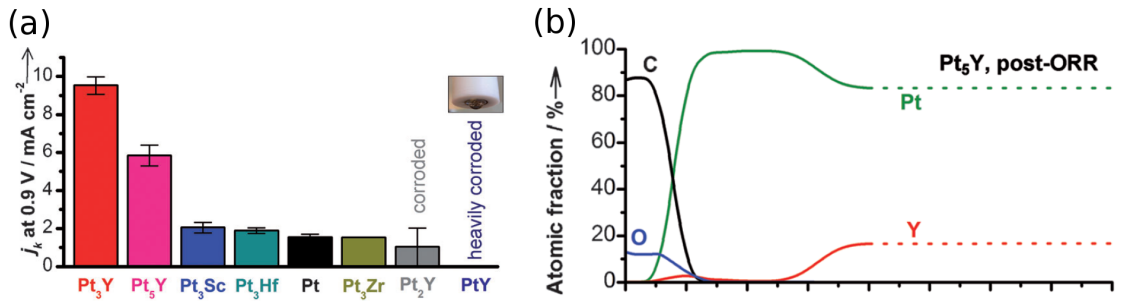

Figure 5.3: (a) Kinetic current density j_k at 0.9 V and 23°C for all catalysts. The current density is normalised to the geometric surface area. (b) Angle-resolved XPS profiles of Pt_5Y acquired after the ORR measurements had been conducted. The dotted lines represent the assumed bulk composition of Pt_5Y. Both adapted from [107]

The original computational screening study by Greeley et al. predicted the high activity of Pt_3Y on the basis of a structure with a monolayer thick Pt skin. Interestingly, the angle-resolved XPS (AR-XPS) measurements performed on the Pt_5Y electrode after the ORR test showed an approximate depth profile with a 10 - 15 Å thick pure Pt surface layer on top of the Pt_5Y bulk, see Figure 5.3(b). A similar Pt surface layer thickness can be expected on the Pt_3Y polycrystalline sample under ORR conditions. Another interesting result from that study is that the catalysts

with high Y content, such as PtY and Pt_2Y, proved to be unstable and the dissolution of Y continued to penetrate deep into the sample. PtY and Pt_2Y nanoparticles are therefore also believed to be unstable.

In order to achieve a better understanding of the nature of the active sites of these Pt-Y catalysts, a parallel study was performed at CINF[117]. The results are unpublished and will be summarised in the following. A Pt-Y model system was prepared by depositing 88 Å Y on top of a Pt(111) single crystal in UHV at 1173 K. By annealing the Y/Pt(111) system an alloy surface-region was formed with a thickness sufficient for the surface properties to be the same as bulk Pt_xY. The results were obtained under UHV conditions and under ORR conditions and are summarized in Figure 5.4. Combining the angle-resolved XPS results (AR-XPS) in Figure 5.4(d) with those obtained by ISS in Figure 5.4(a), suggests that the sample consists of a Pt overlayer on top of some Pt_xY structure. Assuming that the structure is composed of a single Pt monolayer on top of a Pt_xY alloy, x was calculated to be 5.7 on the basis of XPS experiments. The Low-energy electron diffraction (LEED) pattern recorded from the UHV prepared Y/Pt(111) is proposed to correspond to a 2×2 R30° Pt overlayer structure under 6% compressive strain relative to Pt(111) (Figure 5.4(b)). CO TPD spectra from the Y/Pt(111) show that CO is bound weaker than to Pt(111) which is consistent with compressively strained surface (Figure 5.4(c)). Before measuring the ORR activity of the model catalyst, AR-XPS depth profile was carried out (Figure 5.4(d)). The initial 5 Å are attributable to C and O atoms (adventitious contamination) together with a small amount of yttrium oxide. Underneath, there is a Pt overlayer and then the bulk of the sample, which has been fixed to be Pt_5Y on the basis of the XPS results and because this structure is the most Pt rich stable Pt-Y phase[118]. According to recent DFT calculations, the most reliable structure of Y/Pt(111) is the Pt_5Y structure with monolayer Pt on-top which under 5% compressive strain, as shown in the model in Figure 5.4(d). The ORR activity of the Y/Pt(111) model catalyst is significant higher than polycrystalline Pt and comparable to that of polycrystalline Pt_3Y prepared by sputter-cleaned (Figure 5.4(e)). The AR-XPS depth profile performed after electrochemical testing on the model catalyst is significantly different to the one before electrochemical testing (Figure 5.4(f)). The Pt overlayer has become much thicker as a result of Y leaching out from the underlying layers.

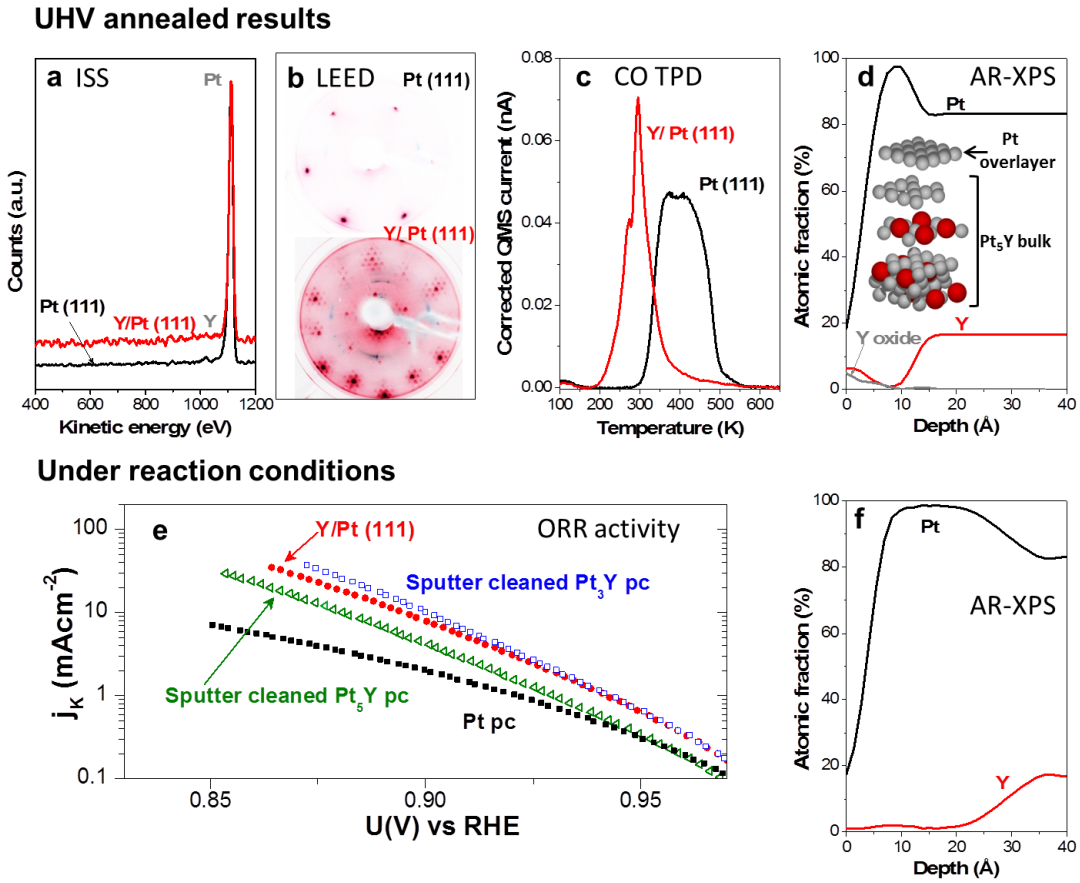

Figure 5.4: Surface characterization of the Y/Pt(111) single crystal under UHV conditions and after ORR activity measurements. (a) ISS spectrum of Pt(111) before (black) and after (red) Y deposition at 1173 K. (b) LEED patterns for Pt(111) and Y/Pt(111). (c) CO TPD from Pt(111) (black) and Y/Pt(111) (red). (d) AR-XPS depth profile of the Y/Pt(111). The inset represents the calculated structure. (e) Kinetic current density as a function of the potential for Pt pc (black), sputter cleaned Pt_5Y (green) and Pt_3Y (blue) and Y/Pt(111) (red). The measurements were recorded at $50 mVs^{-1}$, 1600 rpm and $60 \pm 1°C$ in O_2-saturated 0.1 M $HClO_4$ electrolyte. (f) AR-XPS depth profile of the Y/Pt(111) after ORR activity measurements.

In conclusion, this study suggests that the active surface of Pt_5Y during ORR activity measurements consist of a 10 - 15 Å thick Pt overlayer on top of the Pt_5Y structure, and the surface is most likely terminated by a compressively strained Pt(111) surface. A compressively strained Pt(111) surface will bind oxygen weaker, which correspond to moving to the right on the volcano curve in Figure 5.2(b), and according to DFT calculations a Pt(111) under 2% compressive strain will shift the oxygen binding energy ∼0.2 eV to the top of the volcano[119]. The LEED experiments and DFT calculations suggest that the UHV prepared Y/Pt(111) surface is under 5% to 6% compressive strain, which would weaken the oxygen binding energy too much and result in a activity than pure Pt, in contradiction with the experimental results. However, under the ORR conditions, the thickness of the Pt overlayer increase which is likely to induce some strain relaxation. The strain of the surface under ORR conditions will thereby be significantly lower than the 6%, and the oxygen binding energy will shift towards the top of the volcano, and give rise to the high measured ORR activity. In order to quantify the strain relaxation in the Pt overlayer, in-situ surface X-ray scattering experiments on the Y/Pt(111) overlayer in the electrochemical cell are planed in near future.

5.2 Pt nanoparticles for ORR

In this section, a study of the activity of Pt nanoparticles for electrochemical ORR as a function of particle size is presented. The measured ORR activity is correlated to the fraction of terraces sites which is obtained by CO TPD measurements. The results are furthermore compared to recent theoretical predictions which form a coherent picture of the origin of the ORR activity.

5.2.1 Sample preparation

Two sets of identical samples were prepared with mass selected Pt nanoparticles; one set for electrochemical measurements and one set for CO TPD characterisation[1]. The substrates used for electrochemical measurements were polished glassy carbon (GC) discs, 5 mm in diameter, which were mounted in the sample holder show in Figure 2.2(e)+(f). After a GC substrate was loaded into the UHV chamber it was degassed up to 500°C for a few hours, then cooled down and Pt nanoparticles were hereafter deposited onto the GC disc using Cluster Source I until maximum 10 % of the substrate was covered with nanoparticles. GC discs were prepared with particles of 2, 3, 4, 6, 7.7 and 11 nm in diameter. The particle coverage was determined by integrating the cluster current (see description in Section 2.4.4). The total Pt surface area was also measured electrochemically by CO stripping and compared to the Pt surface area predicted by integrating the cluster current (results presented in a later section). The samples for CO TPD characterisation consisted of SiO_2/Si substrates with mass selected Pt nanoparticles, prepared with cluster source conditions identical to the samples for electrochemistry. The sample preparation and CO TPD procedure for theses samples has already been described in the previous chapter (Chapter 4) and the samples and CO TPD results are the same as presented in the previous chapter.
A set of TEM grids with a range of particle sizes were also prepared using identical cluster source conditions for studying the morphology of different particle sizes.

5.2.2 Morphology

The morphology of different particle sizes were determined by TEM and by CO TPD experiments in the same manner as described in Chapter 4. Representative

[1]The set of samples used for CO TPD characterisation are the same samples as presented in Chapter 4

TEM images, size distributions and CO TPD spectra including fits are shown in Figure 5.5. The CO desorption characteristics reflect the particle morphology as the CO desorption temperature is dependent on the geometry of the adsorption site, as discussed in the previous chapter. For the purpose of quantifying the fraction of terrace sites on the particles from the TPD data, the TPD spectra were deconvoluted and fitted with three Gaussian functions. The fraction of terraces sites presented in the figure were determined as the sum of the area of the first and second Gaussian normalised to the area of all three Gaussians. The fraction of terrace sites increase with particle size.

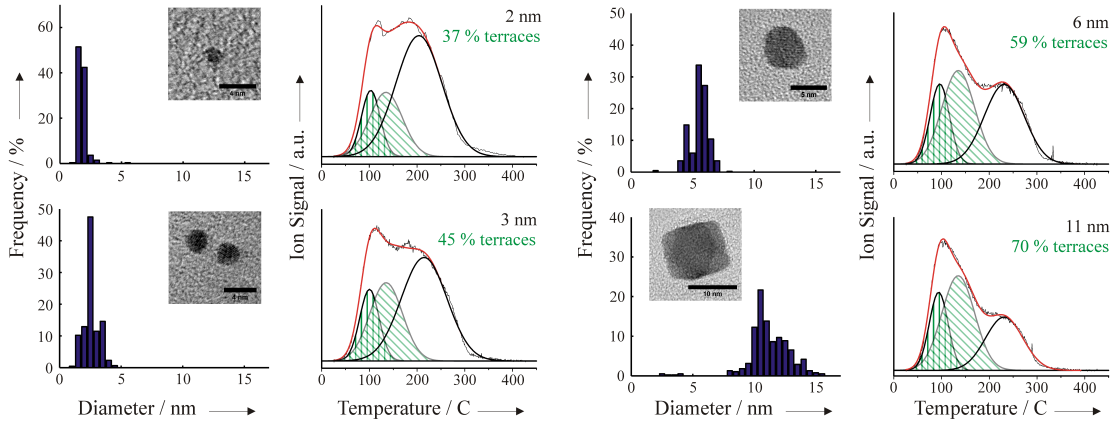

Figure 5.5: Nanoparticle size distributions and the corresponding CO TPD desorption spectra from Pt/SiO_2 samples with 2, 3, 6 and 11 nm particles. Each TPD spectrum has been fitted with three Gaussian functions as described in the text and the fraction of terrace surface area is included. Adapted from [120].

The fitting procedure is rationalized from Pt single crystal studies, where three CO adsorption states have been identified[81–83, 121]: CO bound weakly on terrace sites at high coverage due to CO-CO repulsion, CO bound on terrace sites at low coverage and CO bound strongly at under-coordinated sites. A low temperature peak, corresponding to weakly bound CO on terraces, was fitted without constraints. An intermediate temperature peak, corresponding to strongly bound CO on terraces, was fitted with a fixed center temperature, T_{center} = 410 K, fixed temperature range, T_{range} = 69 K, and without constraints on the area. A high temperature peak, corresponding to CO bound to under-coordinated sites, was fitted without constraints. The 2nd (middle) Gaussian was fixed as we expect the binding of low coverage CO to have a weak dependence on particle size, unlike the CO-CO repulsion effect seen at low desorption temperature and the bonding characteristics to under-coordinated sites. The center position of the 2nd Gaussian was set to match the CO desorption from Pt(111) and the width to ensure the Gaussian decay was

complete near 500 K. A similar method has previously been used for interpreting the coordination dependent binding of oxygen on stepped Pt single crystals[122].

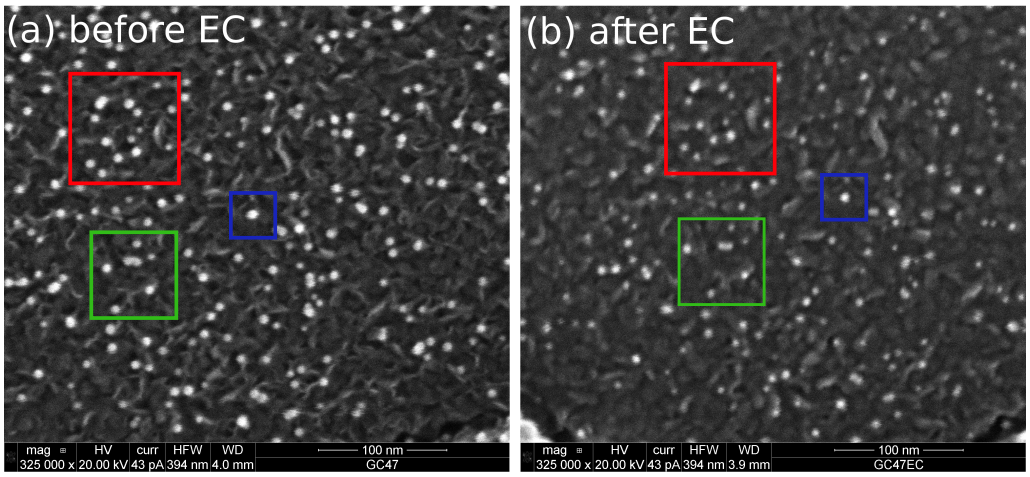

Figure 5.6: Identical location SEM on 5 nm Pt/GC, before and after electrochemical measurements (ORR and CO stripping). Both adapted from [120].

The particle coverage and the homogeneity of the particle coverage was investigated by SEM before and after electrochemical experiments (ORR and CO stripping) at identical locations on selected samples with 5 nm Pt/GC. The result is shown in Figure 5.6 where identical areas are marked. The identical location study shows that a vast majority of the particles are still present after electrochemical measurements and that only small amount of particle agglomeration occurs.

5.2.3 Electrochemical characterisation and ORR activity

All the electrochemical experiments were performed with a potentiostat (Bio-Logic VMP2), a rotating ring disc electrode (RRDE) assembly (Pine Instruments Corporation) and a standard three-compartment glass cell. All glassware was carefully cleaned in 96% H_2SO_4 and 30% H_2O_2 (3:1 v/v) and subsequently sonicated and rinsed several times in Millipore water ($>$18.2 MΩ cm^{-1}, TOC$<$5 ppb). The electrolyte, 0.1 M $HClO_4$ (Merck, Suprapur), was also prepared using Millipore water. The counter electrode was a platinum wire and the reference electrode was Hg/Hg_2SO_4. All potentials are reported with respect to the reversible hydrogen electrode (RHE) and corrected for Ohmic losses. The reference electrode and counter electrode were separated by ceramic frits. The UHV prepared GC electrodes were transferred in air to the electrochemical cell and immersed under potential control at 0.05 V in a N_2 saturated electrolyte.

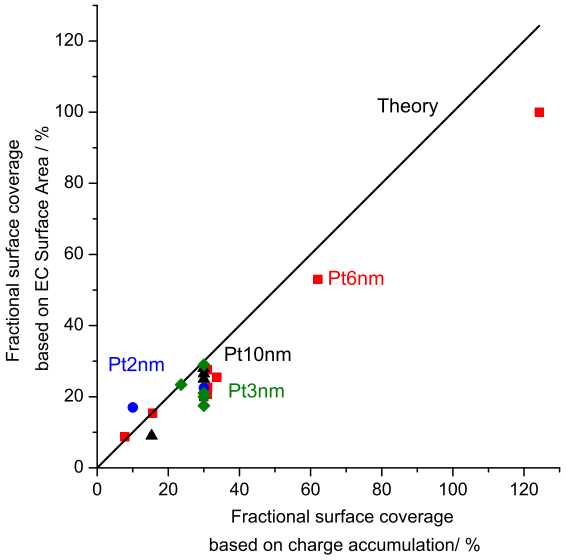

Figure 5.7: Comparison between Pt surface area as a fraction of the GC electrode area on different samples calculated on the basis of CO stripping analysis and on the basis of integrated cluster current and the nanoparticle size. Results from samples with different particle sizes and varying coverages are presented: 2 nm (blue circles), 3 nm (green diamonds), 6 nm (red squares) and 10 nm (black triangles). The black line represents the 1:1 correlation. Adapted from [120] supporting information.

Before measuring the ORR activity the potential was cycled between 0.5 V and 1.15 V until a stable cyclic voltammogram was achieved. The ORR activity measurements were carried out in an O_2 saturated electrolyte by cycling the potential between 0 V and 1 V at 50 mVs^{-1} at 1600 RPM disc rotation speed and 23±1 °C. After the ORR activity measurements, the electrochemical accessible Pt surface area was determined by CO stripping analysis. CO was adsorbed at a constant potential of 0.05 V for 20 min and CO stripping polarization curves were then recorded in a CO free Ar-purged electrolyte solution by scanning the potential until 1.0 V at 50 mVs^{-1}. The active surface area was estimated as the area under the CO stripping peak assuming that CO is bonded linearly on platinum which provides a charge equivalence of 420 $\mu C/cm^2 Pt$[123]. A comparison between the Pt surface area calculated on the basis of the CO stripping analysis and on the basis of the cluster current integration method is shown in Figure 5.7. The results show a good agreement between the two methods with the trend that the CO stripping analysis result in a lower surface area, particularly at high coverages, which is in good agreement with the work by Arenz and co-workers[124]. This can be understood when taking into account a small amount of particle agglomeration which would be most pronounced at high coverages. Furthermore, the electrochemical accessible surface area is expected to be slightly reduced compared to the cluster current integration method due to the particle-support contact area is rendered inaccessible. The fol-

lowing ORR activity results are normalised using the Pt surface area measured by the CO stripping analysis. The kinetic current density, j_k, for the oxygen reduction reaction was corrected for diffusion limitations and calculated as[123]

$$\frac{1}{j_{measured}} = \frac{1}{j_k} + \frac{1}{j_d} \tag{5.2}$$

where $j_{measured}$ is the measured current density and j_d is the diffusion limited current density.

The mass activity, j_m, was established using the total mass of Pt, $mass_{Pt}$, calculated on the basis of the CO stripping analysis by

$$mass_{Pt} = \frac{A_{Pt} \times (\rho_{Pt} \times d_{Pt})}{6} \tag{5.3}$$

where A_{Pt} is the Pt surface area determined by the CO stripping experiments, ρ_{Pt} is the density of Pt and d_{Pt} if the particle diameter. In this way, the mass activity is a measure of the activity if the particles were spherical.

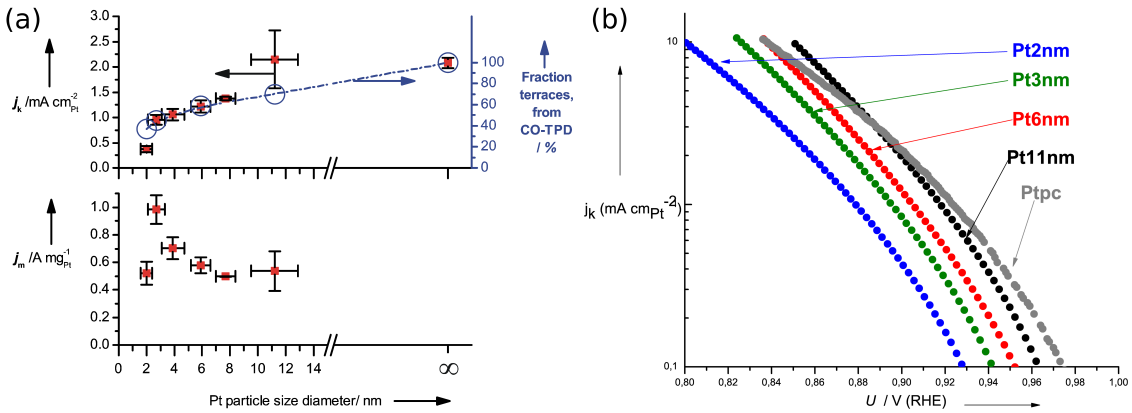

Figure 5.8: (a, top) Specific activity (kinetic current density) and (a, bottom) the mass activity at 0.9 V for the ORR of different particle sizes. The activities are obtained from cyclic voltammograms in an O_2 saturated 0.1 M $HClO_4$ solution at 50 mV/s. The right y-axis and the blue circles represent the fraction of terrace sites obtained by CO TPD experiments. (b) Taffel plot: Specific activity as a function of the electrode potential from Pt nanoparticles of various sizes and from a polycrystalline Pt disc for comparison. Both adapted from [120].

The results of the ORR activity measurements on the different particle sizes are shown as Taffel plots (specific activity vs. potential) in Figure 5.8(b), and it is clearly seen that the specific activity increases with particle size in the whole potential range. In Figure 5.8(a), the specific activities j_k and mass activities j_m at 0.9 V are plotted as a function of the particle diameter which also show that the specific activity increases with size and that the mass activity has a maximum around 3 nm.

The electrochemical ORR activity is related to the fraction of the particle surface comprised of terraces determined by the CO TPD experiments, as shown in the top graph in Figure 5.8(a). It is seen that the fraction of terraces correlates nicely to the specific activity, with two outliers i.e. 2 nm and 11 nm. Given the experimental error bars, the sample with 2 nm particles is the main outlier, which can be explained by a change in surface structure induced by the electrochemical environment. The dissolution of corner and edge atoms will have a relatively large impact on the fraction of active terrace sites on small particles compared to large particles[101] and small particles have been shown to be more susceptible to corrosion[125–127].

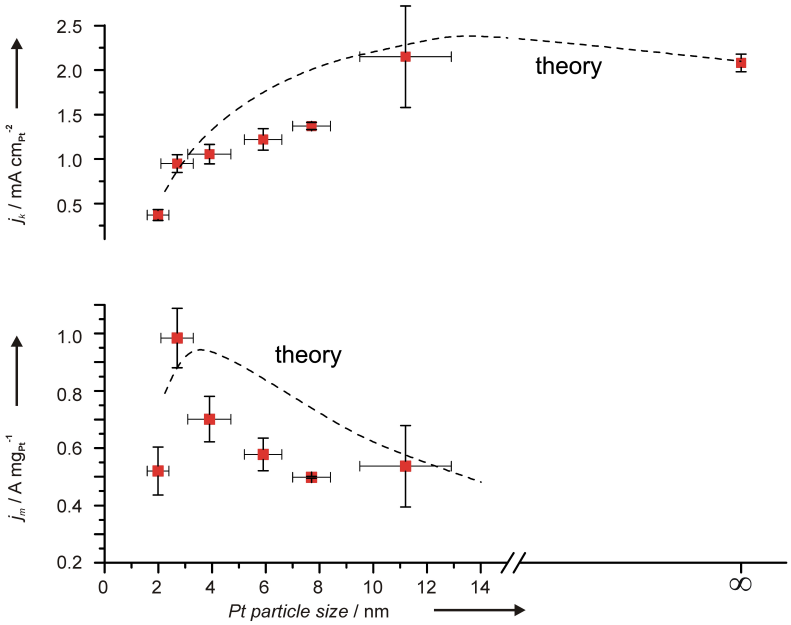

Figure 5.9: (top) The measured specific activity (kinetic current density) and (bottom) mass activity at 0.9 V for the ORR of different particle sizes, plotted along with recent theoretical predictions of the particle size dependence of ORR activity on Pt, which are represented as the dashed line[101]. The experimental ORR activities are obtained from cyclic voltammograms in an O_2 saturated 0.1 M $HClO_4$ solution at 50 mV/s. Adapted from [120] supporting information.

A comparison of the experimentally obtained ORR activities at 0.9 V with recent theoretical predictions by Tritsaris et al. is presented in Figure 5.9[101]. The experimentally obtained ORR specific activities are in good agreement with the theoretical prediction that 11 nm particles have the same activity as extended Pt surfaces and that there is a four-fold increase in the specific activity going from 2 nm to extended surfaces[100, 101]. Furthermore, the maximum in Pt mass activity for the ORR is at ∼3 nm, consistent with previous experimental findings by Gasteiger et al.[99] and the theoretical predictions by Tritsaris et al.[101].

The ORR activities presented in this study are in general, i.e. for all particle sizes, higher than those reported in earlier investigations of commercial catalysts [99, 102, 128]. This is attributed to the employed experimental approach, including the gas aggregation technique for particle formation without use of surfactants and ideal O_2 diffusion conditions during the ORR activity measurements.

5.2.4 Conclusion

It has been shown that the specific activity of Pt for ORR increases with increasing particle size, and that the activity roughly correlates to the fraction of terrace sites, determined by CO TPD experiments. We therefore conclude that the active sites for ORR on Pt are located on the terraces of Pt nanoparticles, in good agreement with earlier theoretical predictions. A maximum in the mass activity has been found for particles with a diameter of $\sim$3 nm.

5.3 Pt-Y alloy nanoparticles for ORR

Motivated by the high ORR activity measured on polycrystalline Pt_3Y and Pt_5Y, as mentioned in the introduction, we set out to study the size dependence of the ORR activity of Pt-Y alloy nanoparticles which are technologically more interesting than extended surfaces. It should be mentioned that the results presented in this section are preliminary and a part of an ongoing study. The study builds upon the results from the pure Pt nanoparticles presented above, and the ORR activity measurements are therefore performed in the same manner. A straight forward comparison of the measured ORR activity can therefore be made between the pure Pt and the Pt-Y alloy nanoparticles.

Much work has been put into tuning and characterising the particle morphology and alloy composition as well as producing samples for the ORR activity measurements. Employing an alloy sputter target in the cluster source has proven to be a challenging task as it opens up a new parameter, i.e. the alloy composition of the formed nanoparticles, which can not be expected to be the same as the sputter target composition.

A previous extended effort to make Pt-Y alloy nanoparticles via a chemical synthesis route had not been successful due to the large difference in standard reduction potentials between the two metals (E^0 = +1.188 V (Pt) and -2.37 V (Y)][129]. Particle synthesis by the sputter aggregation technique proved to be more successful, as it takes place in an oxygen free environment, and with a Pt-Y alloy sputter target with both platinum and yttrium already in the metallic state, metallic Pt-Y alloy nanoparticles could readily be produced.

This section will contain results from Pt-Y nanoparticles with two different Pt:Y ratios which will be presented separately. In the first try to produce Pt_3Y nanoparticles a $Pt_{75}Y_{25}$ sputter target was purchased (99.9% purity, Kurt J Lesker) and mounted in cluster source I. As later explained, the particles produced from this target contained a larger Y content than we wanted, so for the purpose of reducing the Y content in the produced particles a $Pt_{90}Y_{10}$ sputter target was purchased (99.9% purity, Kurt J Lesker) and mounted in cluster source II.

5.3.1 Sample preparation

The samples were prepared in the same manner as the pure Pt nanoparticles, with identical GC substrates for electrochemical measurements and again the particle de-

positions were carried out until 10 % of the substrate was covered with nanoparticles. The particle coverage was determined by integrating the cluster current as well as by depositing onto a quartz crystal microbalance (QCM) prior to depositing particles onto the sample (see description in Section 2.4.4) and a reasonable agreement was found between the two methods. The total electrochemical accessible surface area was measured electrochemically by CO stripping, whereas the total deposited mass of Pt-Y particles on each sample was determined by the QCM measurement prior to the particle deposition. For ISS and XPS characterisation in the UHV setup, both HOPG and glassy carbon substrates were used. TEM grids were also prepared with particles of different size to study the particle morphology.

5.3.2 Nanoparticles from the $Pt_{75}Y_{25}$ sputter target

The results presented in this section are from mass selected Pt-Y particles produced from $Pt_{75}Y_{25}$ sputter target, in an attempt to obtain Pt_3Y nanoparticles and test the electrocatalytic activity for the ORR as a function of particle size. Cluster source I was used to produce the particles.

Morphology and composition

The particle morphology was investigated by TEM and the composition of the Pt_xY nanoparticles were determined by ISS (the X-ray source for XPS was not available at this time).

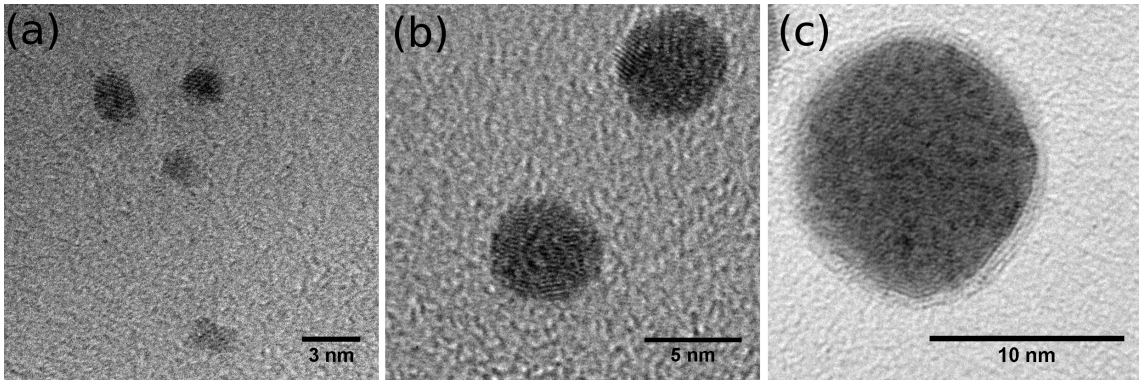

Figure 5.10: TEM images of Pt-Y particles produced from the $Pt_{75}Y_{25}$ sputter target. (a) 3 nm particle on carbon/Cu TEM-grid as deposited. (b) 5 nm particles on carbon/Au TEM-grid dipped in the 0.1 M $HClO_4$ electrolyte. (c) 11 nm particle on carbon/Au TEM-grid as deposited.

TEM images from particles with 3, 5 and 11 nm in diameter are shown in Figure

5.10. From the TEM images in Figure 5.10 it is evident that the small 3 nm particles are crystalline whereas the larger 5 and 11 nm particles are somewhat disordered or polycrystalline. The TEM grid with 5 nm particle imaged in Figure 5.10(b) was dipped into the 0.1 M $HClO_4$ electrolyte, which did not seem the affect the particle morphology. On Figure 5.10(c) a bright shell can be seen around the particle. The shell could consist on yttrium oxide or carbon growth due to the electron beam, but it has not been identified.

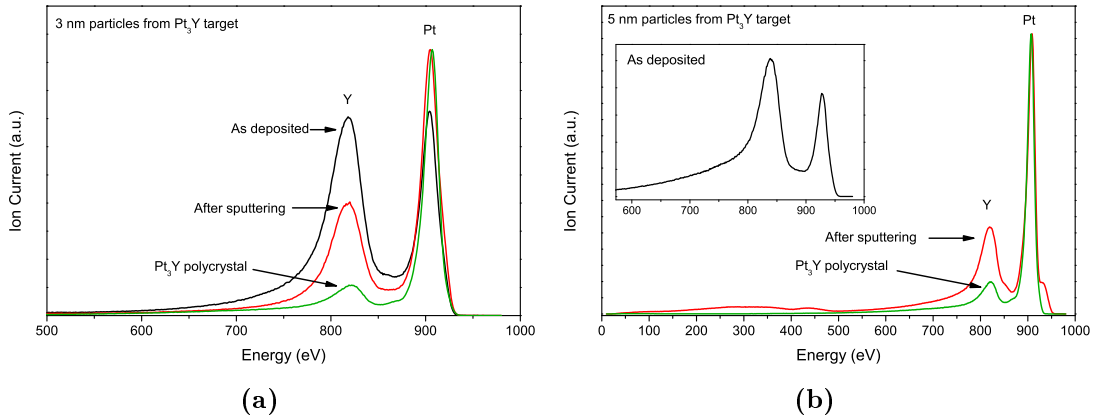

Figure 5.11: ISS spectra from (a) 3 nm and (b) 5 nm Pt-Y alloy nanoparticles from the Pt_3Y sputter target and compared with the Pt_3Y polycrystalline sample. Spectra were acquired from freshly deposited particles and after He sputtering until a stable spectrum was obtained.

The elemental composition of the Pt-Y alloy nanoparticles was probed by ISS. Auger electron spectroscopy was also tried but unsuccessful as the main Pt Auger peak was too low in energy to be detected by the energy analyser. At this time, the setup was not equipped with a X-ray source, so XPS was not possible either. ISS was performed using 1000 eV He ions and the spectra from 3 nm and 5 nm particles on HOPG are shown in Figure 5.11 and compared to a polycrystalline Pt_3Y sample as a reference spectrum (green curve). The polycrystalline Pt_3Y was the same one as used in reference 115. Spectra from (freshly) as deposited 3 and 5 nm particles (black curves) show a high yttrium content on the particle surface compared to the polycrystalline Pt_3Y reference. For the purpose of probing the elemental composition in the bulk of the particles, the He ion current was maximized and used to sputter away surface layers (also called depth profiling). A series of ISS spectra were recorded during the intense He sputtering and initially the yttrium concentration decreased while the platinum concentration increased. With increasing sputter time the elemental composition reached a constant level and the subsequent ISS spectra are shown as the red curves. From these experiments it is evident that the surface of the particles is Y enriched while the core of the particles has a lower Y concentration.

The atomic ratio between Pt and Y was not quantified but it is clearly seen that the particles contain a higher Y content (surface and bulk) than the polycrystalline Pt_3Y reference. It is furthermore noticeable that the particles contain a much higher Y concentration than in the sputter target.

ORR activity

All the electrochemical experiments were performed as described in Section 5.2.3 and the active surface area was also determined by CO stripping analysis. At this point the Pt concentration in the particles was not possible to determine accurately and hence also total mass of Pt on the glassy carbon electrodes, so non of the ORR activities are related to the mass of platinum. Figure 5.12 shows the specific activity at 0.9 V for the ORR from different sizes of Pt_xY nanoparticles (red points) and from pure Pt nanoparticles (black points) for comparison. An activity enhancement relative to Pt is observed especially for the large size particles whereas the 3 nm Pt_xY particles have an activity comparable to pure Pt.

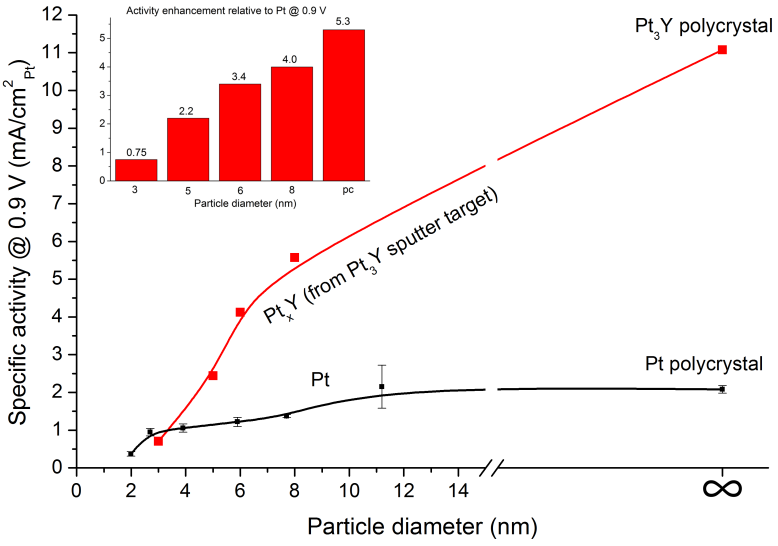

Figure 5.12: Specific activity (current density relative to the platinum surface area) at 0.9 V for the ORR from different sizes of Pt_xY nanoparticles (red) and from pure Pt nanoparticles (black) for comparison. The specific activity from the corresponding polycrystalline (pc) Pt and Pt_3Y are also shown. The insert shows the activity enhancement relative to platinum. All ORR activities were recorded at 50 mVs^{-1}, 1600 rpm and 23±1°C in a O_2 saturated 0.1 M $HClO_4$ electrolyte.

Discussion and conclusion

From the ISS results it is evident that the Y concentration in the particles is higher than in the Pt_3Y polycrystalline sample. It is known from previous experiments on polycrystalline Pt-Y alloy samples that PtY and Pt_2Y corrode in the electrolyte[107],but in spite of the high Y concentration, a significant activity enhancement from the Pt-Y nanoparticles was observed. Some preliminary stability tests were performed by potential cycling from 0 to 1.2 V which showed poor stability, presumably due to the high Y concentration and the high upper limit potential employed. It was decided to try and decrease the Y concentration in the particles by replacing the $Pt_{75}Y_{25}$ sputter target with a $Pt_{90}Y_{10}$ target, and continue the investigations with nanoparticles produced from that target.

5.3.3 Nanoparticles from the $Pt_{90}Y_{10}$ sputter target

In an attempt to produce nanoparticles with a Pt:Y ratio closer to Pt_3Y or Pt_5Y, which in the polycrystalline form are known to be very active for the ORR [107, 115], nanoparticles were produced from a $Pt_{90}Y_{10}$ sputter target. At this time cluster source II was implemented and connected to the remaining UHV chamber, so the $Pt_{90}Y_{10}$ sputter target was therefore mounted herein. The analysis chamber was furthermore equipped with a X-ray source, enabling quantification of the elemental composition by XPS.

The results presented in this section will include TEM investigations on the particle morphology, Pt:Y ratios determined by XPS, ORR activity measurements of a number of particle sizes and stability measurements of the ORR activity.

Morphology and composition

Mass selected Pt_xY particles in a size range from 3 to 9 nm were produced and deposited onto glassy carbon discs (<10% of substrate covered with particles) for electrochemical measurements and on TEM-grids for TEM investigations. Representative TEM images are shown in Figure 5.13 along with corresponding size distributions, and it can be seen that very narrow size distributions have been achieved. It should also be noticed that a minor secondary peak appears at larger sizes. This peak can be assigned to mass selected particles with double mass, which is a consequence of the mass selection principle. The TOF mass filter operates according to the mass-to-charge ratio and double ionised particles with double mass will there-

fore also be transmitted. All particles in the size range appear spherical and the larger 7 and 9 nm particles are polycrystalline with visible smaller crystal domains. The crystallinity of the smaller 3 and 5 nm particles has not yet been determined because of poor resolution in the images. A more thorough investigation of the crystal structure and elemental composition of the particles before and after ORR experiments using the analytical TEM has been planed. The analytical TEM has high resolution scanning transmission electron microscopy (HR-STEM) capabilities which enables chemical mapping across the particle through energy electron loss spectroscopy (EELS).

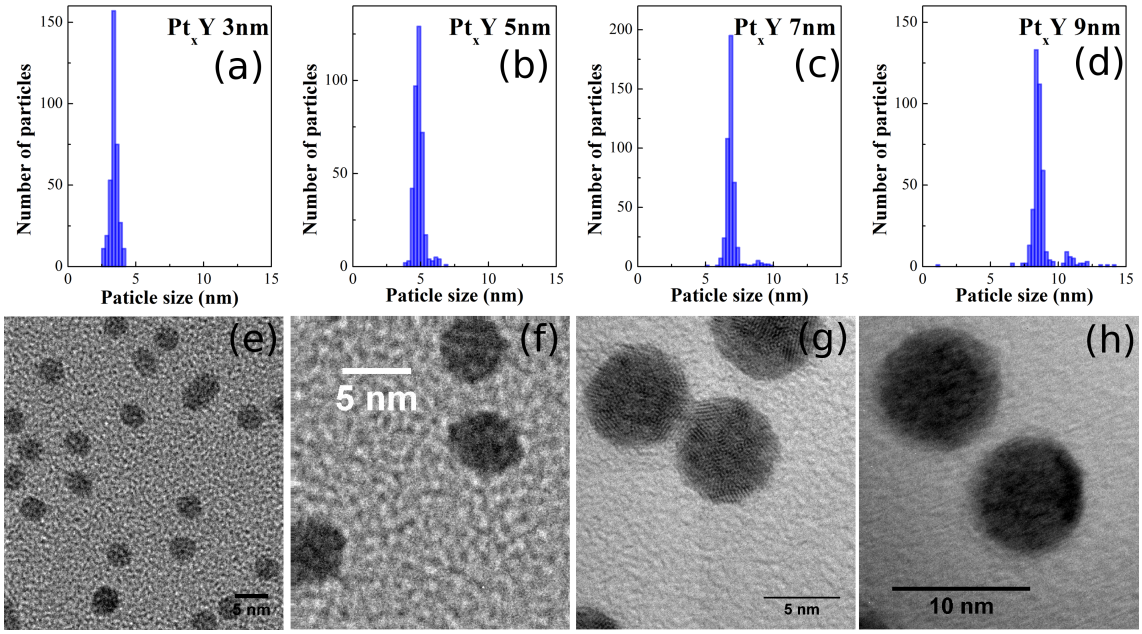

Figure 5.13: (a)-(d) size distributions and (e)-(h) TEM images of 3, 5, 7 and 9 nm Pt-Y particles produced from the $Pt_{90}Y_{10}$ sputter target. The particles were deposited onto carbon/Au TEM-grids, transported in air to the microscope and imaged with further treatment. The stated Pt/Y ratios are quantified by XPS from Pt_xY nanoparticles on glassy carbon before exposed to air.

The elemental composition of the deposited particles have been determined by XPS from all the investigated particle sizes and the Pt/Y atomic ratios are between 4 and 10 as shown in Table 5.1. This is in good agreement with ISS spectra obtained from freshly deposited 9 nm particles which showed slightly smaller amount of Y than the Pt_3Y polycrystalline sample.

A typical XPS spectra from Pt_xY particles deposited on glassy carbon is shown in Figure 5.14, where the observed peaks have been identified. The inserts show high resolution spectra of the Pt4f and Y3d peaks which are used to quantify the Pt/Y atomic ratios. The light blue regions indicate the part of the spectrum used

	3 nm	5 nm	7 nm	9 nm
Pt/Y ratio before ORR	10	5	4	5

Table 5.1: Pt/Y ratio of freshly deposited Pt_xY nanoparticles of various sizes before exposing to air. Quantified by XPS.

in the quantification and the background below the peaks are fitted with a Shirley background. The approximate Pt and Y atomic ratios are calculated on the basis of the area under the peaks which are normalised by atomic-sensitivity-factors (ASF_{Pt} = 4.4 and ASF_Y = 1.57), assuming homogeneous elemental composition. Apart from carbon, platinum and yttrium, small amounts of molybdenum from the sample holder is detected along with small amounts of oxygen and possibly caesium. Oxygen is most likely from adsorbed CO while the origin of Cs is unknown.

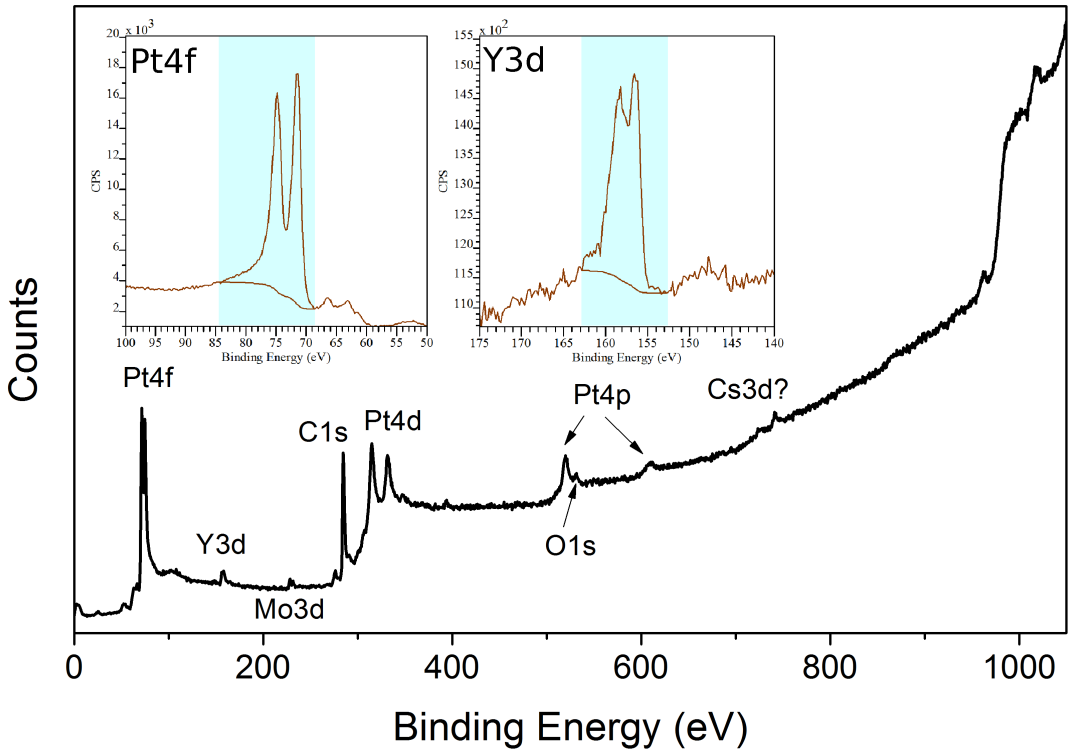

Figure 5.14: Typical XPS spectrum acquired of as-deposited Pt_xY nanoparticles. This spectrum is from 5 nm Pt_5Y nanoparticles and the inserts shown the Pt4f and Y3d peaks that are used to quantify the Pt/Y atomic ratio. Mg anode with a photon energy of 1253.6 eV.

ORR activity and stability

The ORR activity of the glassy carbon-supported Pt_xY nanoparticles has been tested by cyclic voltammetry in a 0.1 M $HClO_4$ electrolyte using a rotating ring disk elec-

trode (RRDE) assembly as described in Section 5.2.3. The specific activity and the mass activity at 0.9 V for the different catalysts are plotted in Figure 5.15. Both the kinetic and the mass current density of the Pt_xY samples (red points) increase with particle size. If we compare the results with those from the pure Pt nanoparticles (black points), a clearly improvement of the ORR activity is observed for the Pt_xY nanoparticles, in line with the previous studies on polycrystalline Pt_3Y and Pt_5Y[107, 115]. Furthermore, the activity of the Pt_xY nanoparticles with the highest diameter, 9nm, is close to that of the corresponding extended Pt_5Y surface.

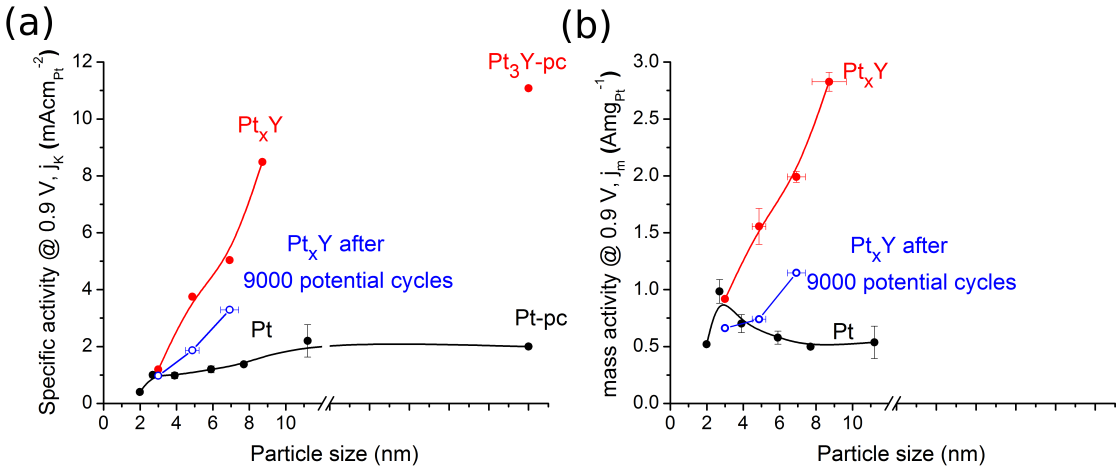

Figure 5.15: (a) Specific activity and (b) mass activity at 0.9 V for the ORR from different Pt_xY particle sizes (red), Pt_xY after 9000 potential cycles (blue) and pure Pt nanoparticles (black) for comparison. The specific activity from the corresponding polycrystalline Pt and Pt_3Y are also shown. All ORR activities were recorded at 50 mVs^{-1}, 1600 rpm and 23±1°C in a O_2 saturated 0.1 M $HClO_4$ electrolyte.

Stability studies were also carried out on the model catalysts. The stability test was performed by cycling the potential between 0.6 and 1 V in O_2 saturated 0.1 M $HClO_4$ electrolyte. After 9000 cycles, the potential window was extended until 0 V and the polarization curves were recorded at 1600 rpm. The active surface area was also measured by CO stripping after the stability test and no significant loss was observed after 9000 cycles (< 10 %). The activity after this test is plotted as a function of particles size represented by the blue points in Figure 5.15. The remaining specific activity at 0.9 V after the stability test for each particle size is quantified in Figure 5.16(b) and it is seen that between 80 and 50 % of the activity remains, relative to the initial activity. Notably, the most part of the activity is lost in the first hundred cycles as is illustrated in Figure 5.16(a), where the kinetic current density as a function of the applied potential is plotted after 30, 650 and 9000 potential cycles for 7 nm Pt_xY. The Pt/Y atomic ratio of 7 nm Pt_xY model catalysts was quantified by XPS before ORR activity test, after ORR activity test

(30 potential cycles) and after stability test (9000 potential cycles). The initial Pt/Y XPS atomic ratio for that catalyst increases from 4 to 14 after the activity test and up to 22 after the stability test. This suggest that the most part of the yttrium is leaching out from the nanoparticles already after the first few potential cycles, followed by a slower dissolution of Y during the following cycles.

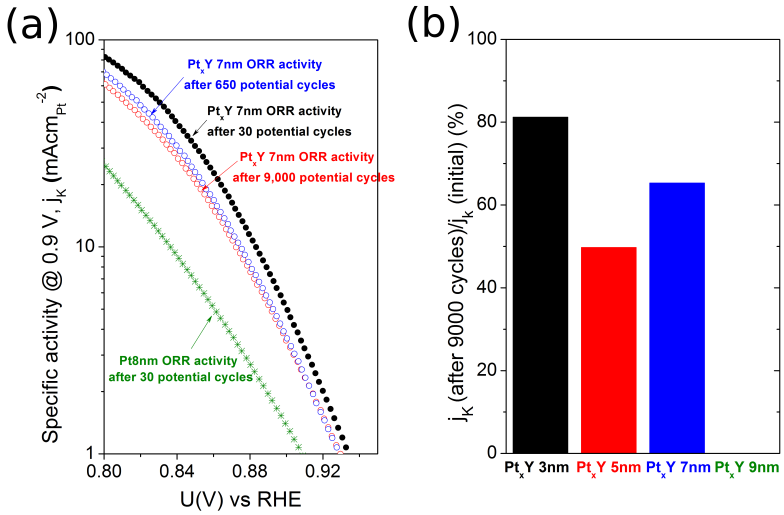

Figure 5.16: (a) Specific activity as a function of the electrolyte potential for 7 nm Pt_4Y nanoparticles: initially (filled black circles), after 650 (open blue circles) and after 9000 (open red circles) potential cycles. (b) Remaining specific activity at 0.9 V after stability test with 9000 potential cycles. All ORR activities were recorded at 50 mVs^{-1}, 1600 rpm and 23±1°C in a O_2 saturated 0.1 M $HClO_4$ electrolyte.

5.4 Discussion

The results from the model catalysts prepared by particle deposition from the $Pt_{90}Y_{10}$ sputter target proved to be a better candidate for an ORR catalyst in terms of activity and stability, than the model catalysts prepared from the $Pt_{75}Y_{25}$ sputter target. The model catalysts prepared from the $Pt_{90}Y_{10}$ sputter target was therefore the most extensively studied and the following discussion will only concern the results from those model catalysts.

The investigated Pt_xY nanoparticles show a clear enhancement of the ORR activity compared to the activity measured from the pure Pt nanoparticles. To the best of our knowledge, the 9 nm Pt_5Y nanoparticles display the highest ORR activity ever measured on supported nanoparticles. The reason for the unprecedented activity is not yet fully understood, but the recent study of the Y/Pt(111) sys-

tem, mentioned in the introduction, suggests that the high activity originates from a compressively strained Pt overlayer formed by Y dissolution into the electrolyte from the outermost atomic layers. The observation of a ∼1 nm Pt overlayer on the Y/Pt(111) system is in good agreement with the observation from the 7 nm Pt_4Y nanoparticulate model catalyst where an increase in the Pt/Y atomic ratio from 4 to 14 was measured by XPS after exposing the catalyst to the ORR environment. When the catalysts were subjected to the stability test, the activity dropped between 20 % and 50 % and XPS measurements on a 7 nm Pt_4Y catalyst showed a further increase in Pt/Y atomic ratio to 22. This suggest that the further de-alloying of the particles is responsible for the observed deactivation. This is not surprising as the dissolution of Y is only kinetically hindered by the protective Pt overlayer because of the very negative reduction potential of Y ($E_{Y \rightarrow Y3+}$ = -2.372 V) or by its high oxygen affinity (ΔH = -1.905 $kJmol^{-1}$). An improved crystallinity of the particles could potentially improve the stability but we have not been successful in that respect. Most attempts of annealing the catalysts to obtain a better particle crystallinity resulted in a decreased ORR activity.

In order to obtain more information about the elemental composition, the crystal structure and the nature of the active site on the Pt_xY nanoparticles, EXAFS experiments has been initiated along with a more detailed investigation by scanning transmission electron microscopy.

5.5 Conclusion

In this chapter, we have established the size dependence of the ORR activity of pure Pt nanoparticles supported on glassy carbon. The specific activity increase with increasing particle size, and correlates to the fraction of terrace sites. We therefore conclude that the active sites for ORR on Pt are located on the terraces of Pt nanoparticles, in good agreement with earlier theoretical predictions. A maximum in the mass activity has been found for particles with a diameter of ∼3 nm.

For the Pt-Y system, we prepared a model catalyst with mass-selected Pt_xY nanoparticles on glassy carbon, where x was ∼5 for the 5 - 9 nm particles and 10 for the 3 nm particles. We observed a clear enhancement of the ORR activity compared to pure Pt nanoparticles, and to the best of our knowledge, the 9 nm Pt_5Y nanoparticles display the highest ORR activity ever measured on supported nanoparticles. The origin of the enhanced activity is speculated to be caused by a compressed Pt overlayer covering a Pt_xY alloy core.

Chapter 6

Summary

In this thesis, the structure and reactivity of mass-selected nanoparticles have been investigated. Important aspects of catalysis, such as structure sensitivity and adsorbate induced surface reconstructions have been illustrated through the experimental investigations of three model systems consisting of mass-selected nanoparticles supported on planar substrates.

Advances in the understanding of catalysis at the molecular level is driven by the developments in surface science and theoretical computational methods. The surface science approach is based on investigations of well-defined model systems that mimic the industrial catalyst as closely as possible but also minimise the complexity. Model catalysts consisting of mass-selected nanoparticles supported on planar oxide or carbon substrates, are well suited for studying the correlation between the structure an reactivity of nanoparticles. Such model catalysts can be characterised by surface science techniques and combined with catalytic testing under operating conditions, in e.g. a high pressure cell, silicon fabricated microreactors or an electrochemical setup as demonstrated in this work. These studies contribute to a better understanding of the factors that govern the activity of nanoparticles and thereby provide valuable information for designing new and improved catalysts.

Two structure sensitive reactions were investigated with very different active sites. The active sites for CO dissociation on Ru consist of under-coordinated sites, whereas the active sites for the electrochemical ORR on Pt are highly-coordinated sites located on the close-packed facets. It was also shown how the reactivity of Pt nanoparticles can be modified by alloying with Y, presumably due to a compressively strained Pt overlayer covering the alloy core. The interplay between theoretical calculations and experiments have played a crucial role for the understanding of the Pt-Y system.

CO dissociation on Ruthenium

Mass-selected Ru nanoparticles were produced by the magnetron sputter gas aggregation technique and the concentration of active sites for CO dissociation was probed by isotopic labled CO TPD experiments. The relative number of active sites was quantified for each particle size and shown to increase for increasing particle size. The maximum fraction of active sites were measured on 11 nm particles to be ∼25%. The observed size dependence is suggested to be correlated to the increasing surface roughness for larger particles. The results suggest that a catalyst consisting of Ru nanoparticles with a similar rough surface structure would be very active where highly under-coordinated sites are called for, such as CO and N_2 dissociation. Such catalyst would only remain highly active if the under-coordinated sites could be made stable or annealing can be avoided.

Platinum and Platinum-Yttrium alloys for electrochemical Oxygen Reduction Reaction

The ORR activity measured from Pt nanoparticles of various sizes was indeed found to correlated to the fraction of terrace sites. The specific activity was therefore found to increase with particles size and a maximum in the mass activity was found for particles with 3 nm in diameter. The results correlate nicely to theoretical predictions by DFT calculations, which confirms that we are starting to build a more coherent picture of the factors that control the activity of nanoparticles for the ORR.
Due to the sluggish kinetics of the oxygen reduction reaction a high Pt loading is required on the cathode on a PEMFC, which is the main obstacle for a vide-spread commercialisation. In an effort to improve the activity of Pt for the ORR, we successfully produced mass-selected Pt_xY nanoparticles which showed an enhanced activity for the ORR. In fact, to the best of our knowledge, the 9 nm Pt_5Y nanoparticles displayed the highest ORR activity ever measured on a nanoparticulate catalysts. The origin of the high activity is speculated to be due to the formation of a compressively strained Pt overlayer. This study elucidate the possibilities of tuning the reactivity of catalysts by alloying and the creation of trained surfaces.

CO induced surface reconstruction of Platinum

Surface reconstructions induced by a high CO pressure were studied on a Pt(111) model catalyst and on a model catalyst consisting of mass-selected Pt nanoparticles supported on SiO_2. We observed that the presence of CO enhanced the annealing of defects on the extended Pt(111) surface, whereas the presence of CO induced an apparent surface roughening of 3 and 6 nm particles. The 11 nm particles showed

only a minor change in surface structure. We speculate that the coordination dependent adsorption energy of CO on Pt and CO-CO repulsion at high coverages induce the observed surface reconstructions and that the facet size and the concentration of under-coordinated surface atoms determines the thermodynamically favourable structure. The observed surface reconstruction highlights the importance of studying the effects of adsorbate induced reconstructions at elevated pressures and the size dependence of the observed reconstruction display the complexity of this phenomena.

Bibliography

[1] I. Chorkendorff and J. W. Niemantsverdriet. *Concepts of Modern Catalysis And Kinetics*. Wiley-VCH Verlag GmbH and Co., 2003.

[2] P. W. Anderson. Localized magnetic states in metals. *Phys. Rev.*, 124:41–53, Oct 1961.

[3] D.M. Newns. Self-Consistent Model of Hydrogen Chemisorption. *Physical Review*, 178(3):1123–1135, 1969.

[4] B Hammer and JK Norskov. Electronic factors determining the reactivity of metal surfaces. *Surface Science*, 343(3):211–220, DEC 10 1995.

[5] B Hammer and JK Norskov. Theoretical surface science and catalysis - Calculations and concepts. In Gates, BC and Knozinger, H, editor, *Advances in catalysis, Vol 45: Impact of Surface Science on Catalysis*, volume 45 of *Advances in Catalysis*, pages 71–129. 2000.

[6] A Ozaki and K Aika. *Catalysis: science and technology*, volume 1. Springer-Verlag, 1981.

[7] S. Dahl, A. Logadottir, R. C. Egeberg, J. H. Larsen, I. Chorkendorff, E. Törnqvist, and J. K. Nørskov. *Physical Review Letters*, 83:1814–1817, 1999.

[8] S. Dahl, E. Törnqvist, and I. Chorkendorff. Dissociative adsorption of n2 on ru(0001): A surface reaction totally dominated by steps. *Journal of Catalysis*, 192(2):381–390, 2000.

[9] G Wulff. Zur Frage der Geschwindigkeit des Wachsturms und der Auflösung der Kristallflächen. *Zeitschrift für Kristallographie* , 34:449–530, 1901.

[10] Jeppe Gavnholt. *The Structure of Individual Nanoparticles and Hot Electron Assisted Chemistry at Surfaces*. PhD thesis, Technical University of Denmark (DTU), 2009.

[11] PL Hansen, JB Wagner, S Helveg, JR Rostrup-Nielsen, BS Clausen, and

H Topsoe. Atom-resolved imaging of dynamic shape changes in supported copper nanocrystals. *Science*, 295(5562):2053–2055, MAR 15 2002.

[12] Fan Zheng, Selim Alayoglu, Jinghua Guo, Vladimir Pushkarev, Yimin Li, Per-Anders Glans, Jeng-lung Chen, and Gabor Somorjai. In-situ X-ray Absorption Study of Evolution of Oxidation States and Structure of Cobalt in Co and CoPt Bimetallic Nanoparticles (4 nm) under Reducing (H-2) and Oxidizing (O-2) Environments. *Nano Letters*, 11(2):847–853, FEB 2011.

[13] JD Grunwaldt, AM Molenbroek, NY Topsoe, H Topsoe, and BS Clausen. In situ investigations of structural changes in Cu/ZnO catalysts. *Journal of Catalysis*, 194(2):452–460, SEP 2000.

[14] Feng Tao, Sefa Dag, Lin-Wang Wang, Zhi Liu, Derek R. Butcher, Hendrik Bluhm, Miquel Salmeron, and Gabor A. Somorjai. Break-Up of Stepped Platinum Catalyst Surfaces by High CO Coverage. *Science*, 327(5967):850–853, FEB 12 2010.

[15] Zhongwei Zhu, Franklin (Feng) Tao, Fan Zheng, Rui Chang, Yimin Li, Lars Heinke, Zhi Liu, Miquel Salmeron, and Gabor A. Somorjai. Formation of Nanometer-Sized Surface Platinum Oxide Clusters on a Stepped Pt(557) Single Crystal Surface Induced by Oxygen: A High-Pressure STM and Ambient-Pressure XPS Study. *Nano Letters*, 12(3):1491–1497, MAR 2012.

[16] S Helveg, C Lopez-Cartes, J Sehested, PL Hansen, BS Clausen, JR Rostrup-Nielsen, F Abild-Pedersen, and JK Norskov. Atomic-scale imaging of carbon nanofibre growth. *Nature*, 427(6973):426–429, JAN 29 2004.

[17] www.mantisdeposition.com.

[18] H. Haberland, M. Karrais, M. Mall, and Y. Thurner. Thin-films from energetic cluster impact - A feasibility study. *Journal of vacuum science and technology a-vacuum surfaces and films*, pages 3266–3271, 1992.

[19] T Hihara and K Sumiyama. Formation and size control of a ni cluster by plasma gas condensation. *Journal of applied physics*, 84(9):5270–5276, 1998.

[20] R. M. Nielsen, S. Murphy, C. Strebel, M. Johansson, I. Chorkendorff, and J. H. Nielsen. *Journal of Nanoparticle Research*, 12:1249–1262, 2010.

[21] C. Binns. Nanoclusters deposited on surfaces. *Surface Science Reports*, 44(1-2):1–49, 2001.

[22] B von Issendorff and RE Palmer. A new high transmission infinite range mass

selector for cluster and nanoparticle beams. *Review of Scientific Instruments*.

[23] M Moseler, H Hakkinen, and U Landman. Supported magnetic nanoclusters: Soft landing of Pd clusters on a MgO surface. *Physical Review Letters*, 89(17), OCT 21 2002.

[24] SJ Carroll, SG Hall, RE Palmer, and R Smith. Energetic impact of size-selected metal cluster ions on graphite. *Physical Review Letters*, 81(17):3715–3718, OCT 26 1998.

[25] I. Chorkendorff. Experimental surface physics: Lecture notes for the experimental surface physics course on dtu. 2003.

[26] G. A. Somorjai. *Chemistry in Two Dimensions, Surfaces*. Cornell University Press, Ithaca, 1981.

[27] C. Julian Chen. *Introduction to Scanning Tunneling Microscopy*. Oxford University Press, second edition, 2008.

[28] H. Hovel and I. Barke. Morphology and electronic structure of gold clusters on graphite: Scanning-tunneling techniques and photoemission. *Progress in Surface Science*, 81(2-3):53–111, 2006.

[29] R. A. Dalla'Betta and M. Shelef. *Journal of Catalysis*, 48:111–119, 1977.

[30] R. J. Madon, S. C. Reyes, and E. Iglesia. *Journal of Physical Chemistry*, 95:7795–7804, 1991.

[31] Glenn Jones, Jon Geest Jakobsen, Signe S. Shim, Jesper Kleis, Martin P. Andersson, Jan Rossmeisl, Frank Abild-Pedersen, Thomas Bligaard, Stig Helveg, Berit Hinnemann, Jens R. Rostrup-Nielsen, Ib Chorkendorff, Jens Sehested, and Jens K. Nørskov. First principles calculations and experimental insight into methane steam reforming over transition metal catalysts. *Journal of Catalysis*, 259(1):147–160, 2008.

[32] A. Klerke, S. K. Klitgaard, and R. Fehrmann. *Catalysis Letters*, 130:541–546, 2009.

[33] Zbigniew Kowalczyk, Slawomir Jodzis, and Jan Sentek. Studies on kinetics of ammonia synthesis over ruthenium catalyst supported on active carbon. *Applied Catalysis A: General*, 138(1):83 –91, 1996.

[34] Z. Song, T. Cai, J. C. Hanson, J. A. Rodriguez, and J. Hrbek. *Journal of the American Chemical Society*, 126:8576–8584, 2004.

[35] K. Honkala, A. Hellman, I. N. Remediakis, A. Logadottir, A. Carlsson, S. Dahl, C. H. Christensen, and J. K. Nørskov. *Science*, 307:555–558, 2005.

[36] R. van Hardeveld and A. van Montfoort. The influence of crystallite size on the adsorption of molecular nitrogen on nickel, palladium and platinum: An infrared and electron-microscopic study. *Surface Science*, 4(4):396–430, 1966.

[37] Geoffrey C. Bond. The origins of particle size effects in heterogeneous catalysis. *Surface Science*, 156, Part 2(0):966–981, 1985.

[38] M Che and C O Bennett. The influence of particle-size on the catalytic properties of supported metals. *Advances in Catalysis*, 36:55–172, 1989.

[39] G C Bond. Supported metal-catalysts - some unsolved problems. *Chemical Society Reviews*, 20(4):441–475, 1991.

[40] Martin Frank and Marcus Baumer. From atoms to crystallites: adsorption on oxide-supported metal particles. *Physical Chemistry Chemical Physics*, 2:3723–3737, 2000.

[41] D.A.J.M. Ligthart, R.A. van Santen, and E.J.M. Hensen. Influence of particle size on the activity and stability in steam methane reforming of supported rh nanoparticles. *Journal of Catalysis*, 280(2):206–220, 2011.

[42] M. Haruta, N. Yamada, T. Kobayashi, and S. Iijima. Gold catalysts prepared by coprecipitation for low-temperature oxidation of hydrogen and of carbon monoxide. *Journal of Catalysis*, 115(2):301–309, 1989.

[43] Masatake Haruta. Size- and support-dependency in the catalysis of gold. *Catalysis Today*, 36(1):153–166, 1997.

[44] M. Valden, X. Lai, and D. W. Goodman. Onset of catalytic activity of gold clusters on titania with the appearance of nonmetallic properties. *Science*, 281(5383):1647–1650, 1998.

[45] Sang Hoon Joo, Jeong Y. Park, J. Russell Renzas, Derek R. Butcher, Wenyu Huang, and Gabor A. Somorjai. *Nano Letters*, 10(7):2709–2713, 2010.

[46] G. Leendert Bezemer, Johannes H. Bitter, Herman P. C. E. Kuipers, Heiko Oosterbeek, Johannes E. Holewijn, Xiaoding Xu, Freek Kapteijn, A. Jos van Dillen, and Krijn P. de Jong. Cobalt particle size effects in the fischer-tropsch reaction studied with carbon nanofiber supported catalysts. *Journal of the American Chemical Society*, 128(12):3956–3964, 2006.

[47] E. Shincho, C. Egawa, S. Naito, and K. Tamaru. *Surface Science*, 149:1–16, 1985.

[48] H. Pfnür, P. Feulner, H. A. Engelhardt, and D. Menzel. *The Journal of Physical Chemistry Letters*, 59:481–486, 1978.

[49] P. Feulner, H. A. Engelhardt, and D. Menzel. *Applied Physics*, 15:355–360, 1978.

[50] J. A. Schwarz and S. R. Kelemen. *Surface Science*, 87:510–524, 1979.

[51] H. Pfnür, P. Feulner, and D. Menzel. *Journal of Chemical Physics*, 79:4613–4623, 1983.

[52] T. Yamada, Y. Iwasawa, and K. Tamaru. *Surface Science*, 223:527–550, 1989.

[53] E. D. Westre, D. E. Brown, J. Kutzner, and S. M. George. *Surface Science*, 302:280–294, 1994.

[54] T. Zubkov, G. A. Morgan, and J. T. Yates. *Chemical Physics Letters*, 362:181–184, 2002.

[55] T. Zubkov, G. A. Morgan, J. T. Yates, O. Kühlert, M. Lisowski, R. Schillinger, D. Fick, and H. J. Jänsch. *Surface Science*, 526:57–71, 2003.

[56] T. E. Madey. *Surface Science*, 79:575–588, 1979.

[57] G. E. Thomas and W. H. Weinberg. *Journal of Chemical Physics*, 70:1437–1439, 1979.

[58] H. Pfnür, D. Menzel, F. M. Hoffmann, A. Ortega, and A. M. Bradshaw. *Surface Science.*, 93:431–452, 1980.

[59] Ellen D. Williams and W.H. Weinberg. The geometric structure of carbon monoxide chemisorbed on the ruthenium (001) surface at low temperatures. *Surface Science*, 82(1):93–101, 1979.

[60] G. Michalk, W. Moritz, H. Pfnür, and D. Menzel. *Surface Science*, 129:92–106, 1983.

[61] H. Pfnür and D. Menzel. *Surface Science*, 148:411–438, 1984.

[62] P. Jakob. *Journal of Chemical Physics*, 120:9286–9296, 2004.

[63] S. Kneitz, J. Gemeinhardt, and H. P. Steinrück. *Surface Science*, 440:307–320, 1999.

[64] S. H. Payne, J. S. McEwen, H. J. Kreuzer, and D. Menzel. *Surface Science*, 594:240–262, 2005.

[65] S. B. Vendelbo, M. Johansson, D. J. Mowbray, M. P. Andersson, F. Abild-Pedersen, J. H. Nielsen, J. K. Nørskov, and I. Chorkendorff. *Topics in Catalysis*, 53:357–634, 2010.

[66] P. D. Reed, C. M. Comrie, and R. M. Lambert. *Surface Science*, 59:33–45, 1976.

[67] R. Ku, N. A. Gjostein, and H. P. Bonzel. *Surface Science*, 64:465–483, 1977.

[68] G. Lauth, T. Solomun, W. Hirschwald, and K. Christmann. *Surface Science*, 210:201–224, 1989.

[69] G. Rotaris, A. Baraldi, G. Comelli, M. Kiskinova, and R. Rosei. *Surface Science*, 359:1–9, 1996.

[70] J. Wang, Y. Wang, and K. Jacobi. *Surface Science*, 488:83–89, 2001.

[71] Lionel Cervera Gontard, Lan-Yun Chang, Crispin J. D. Hetherington, Angus I. Kirkland, Dogan Ozkaya, and Rafal E. Dunin-Borkowski. Aberration-corrected imaging of active sites on industrial catalyst nanoparticles. *Angewandte Chemie-International Edition*, 46(20):3683–3685, 2007.

[72] S. Shetty, A. P. J. Jansen, and R. A. van Santen. CO dissociation on the Ru(11-21) surface. *The Journal of Physical Chemistry C*, 112(36):14027–14033, 2008.

[73] Christian Strebel, Shane Murphy, Rasmus M. Nielsen, Jane H. Nielsen, and Ib Chorkendorff. Probing the active sites for co dissociation on ruthenium nanoparticles. *Physical Chemistry Chemical Physics*, 14(22):8005–8012, 2012.

[74] S. Murphy, C. Strebel, S. B. Vendelbo, C. Conradsen, Y. Tison, K. Nielsen, L. Bech, R. M. Nielsen, M. Johansson, I. Chorkendorff, and J. H. Nielsen. *Physical Chemistry Chemical Physics*, 13:10333–10341, 2011.

[75] Søren Bastholm Vendelbo. *Structure Sensitivity of CO Dissociation and the Methanation Reaction on a Ruthenium Single Crystal.* PhD thesis, Technical University of Denmark (DTU), 2010.

[76] Yann Tison, Kenneth Nielsen, Duncan J. Mowbray, Lone Bech, Christian Holse, Federico Calle-Vallejo, Kirsten Andersen, Jens J. Mortensen, Karsten W. Jacobsen, and Jane H. Nielsen. Scanning Tunneling Microscopy Evidence for the Dissociation of Carbon Monoxide on Ruthenium Steps. *Jour-*

nal of Physical Chemistry C, 116(27):14350–14359, JUL 12 2012.

[77] C. Y. Fan, H. P. Bonzel, and K. Jacobi. Co adsorption on the multiple-site ru(11-21) surface: The role of bonding competition. *The Journal of Chemical Physics*, 118(21):9773–9782, 2003.

[78] J. Gavnholt and J. Schiøtz. *Physical Review B*, 77:035404, 2008.

[79] Sonja Stappert, Bernd Rellinghaus, Mehmet Acet, and Eberhard F. Wassermann. Gas-phase preparation of l10 ordered fept nanoparticles. *Journal of Crystal Growth*, 252(1-3):440–450, 2003.

[80] R. Alayan, L. Arnaud, M. Broyer, E. Cottancin, J. Lermé, J. L. Vialle, and M. Pellarin. Morphology and growth of metal clusters in the gas phase: A transition from spherical to ramified structures. *Physical Review B*, 73:125444, Mar 2006.

[81] H Steininger, S Lehwald, and H Ibach. On the adsorption of CO on Pt(111). *Surface Science*, 123(2-3):264–282, 1982.

[82] HR Siddiqui, X Guo, I Chorkendorff, and JT Yates. Co adsorption site exchange between step and terrace sites on Pt(112). *Surface Science*, 191(1-2):L813–L818, NOV 1987.

[83] MR McClellan, JL Gland, and FR McFeeley. Carbon-Monoxide Adsorption on the Kinked Pt(321) Surface. *Surface Science*, 112(1-2):63–77, 1981.

[84] RW Mccabe and LD Schmidt. Binding States of CO on Single-Crystal Planes of Pt. *Surface Science*, 66(1):101–124, 1977.

[85] H Hopster and H Ibach. Adsorption of CO on Pt(111) and Pt 6(111) x (111) Studied by High-Resolution Electron-Energy Loss Spectroscopy and Thermal Desorption Spectroscopy. *Surface Science*, 77(1):109–117, 1978.

[86] B Hammer, OH Nielsen, and JK Norskov. Structure sensitivity in adsorption: CO interaction with stepped and reconstructed Pt surfaces. *Catalysis Letters*, 46(1-2):31–35, 1997.

[87] T Michely and G Comsa. Temperature-dependence of the sputtering morphology of Pt(111). *Surface Science*, 256(3):217–226, OCT 1991.

[88] P Thostrup, E Christoffersen, HT Lorensen, KW Jacobsen, F Besenbacher, and JK Norskov. Adsorption-induced step formation. *Physical Review Letters*, 87(12), SEP 17 2001.

[89] P Thostrup, EK Vestergaard, T An, E Laegsgaard, and F Besenbacher. CO-induced restructuring of Pt(110)-(1x2): Bridging the pressure gap with high-pressure scanning tunneling microscopy. *Journal of Chemical Physics*, 118(8):3724–3730, FEB 22 2003.

[90] SR Longwitz, J Schnadt, EK Vestergaard, RT Vang, E Laegsgaard, I Stensgaard, H Brune, and F Besenbacher. High-coverage structures of carbon monoxide adsorbed on Pt(111) studied by high-pressure scanning tunneling microscopy. *Journal of Physical Chemistry B*, 108(38):14497–14502, SEP 23 2004.

[91] Feng Tao, Sefa Dag, Lin-Wang Wang, Zhi Liu, Derek R. Butcher, Miquel Salmeron, and Gabor A. Somorjai. Restructuring of hex-Pt(100) under CO Gas Environments: Formation of 2-D Nanoclusters. *Nano Letters*, 9(5):2167–2171, MAY 2009.

[92] D. N. McCarthy, C. E. Strebel, T. P. Johansson, A. den Dunnen, A. Nierhoff, J. H. Nielsen, and Ib Chorkendorff. Structural Modification of Platinum Model Systems under High Pressure CO Annealing. *Journal of Physical Chemistry C*, 116(29):15353–15360, JUL 26 2012.

[93] W. J. Huang, R. Sun, J. Tao, L. D. Menard, R. G. Nuzzo, and J. M. Zuo. Coordination-dependent surface atomic contraction in nanocrystals revealed by coherent diffraction. *Nature Materials*, 7(4):308–313, MAR 2008.

[94] J. Kleis, J. Greeley, N. A. Romero, V. A. Morozov, H. Falsig, A. H. Larsen, J. Lu, J. J. Mortensen, M. Dulak, K. S. Thygesen, J. K. Norskov, and K. W. Jacobsen. Finite Size Effects in Chemical Bonding: From Small Clusters to Solids. *Catalysis Letters*, 141(8):1067–1071, AUG 2011.

[95] A. Julukian, T. Fadnes, S. Raaen, and M. Balci. Size effect on thermal desorption of CO from Pt nanostructures on graphite. *Journal of Applied Physics*, 109(12), JUN 15 2011.

[96] J. M. Flores-Camacho, J. H. Fischer-Wolfarth, M. Peter, C. T. Campbell, S. Schauermann, and H. J. Freund. Adsorption energetics of CO on supported Pd nanoparticles as a function of particle size by single crystal microcalorimetry. *Physical Chemistry Chemical Physics*, 13(37):16800–16810, 2011.

[97] S Horch, HT Lorensen, S Helveg, E Laegsgaard, I Stensgaard, KW Jacobsen, JK Norskov, and F Besenbacher. Enhancement of surface self-diffusion of platinum atoms by adsorbed hydrogen. *Nature*, 398(6723):134–136, MAR 11

1999.

[98] Hideto Yoshida, Koji Matsuura, Yasufumi Kuwauchi, Hideo Kohno, Satoshi Shimada, Masatake Haruta, and Seiji Takeda. Temperature-Dependent Change in Shape of Platinum Nanoparticles Supported on CeO(2) during Catalytic Reactions. *Applied Physics Express*, 4(6), JUN 2011.

[99] Hubert A. Gasteiger, Shyam S. Kocha, Bhaskar Sompalli, and Frederick T. Wagner. Activity benchmarks and requirements for pt, pt-alloy, and non-pt oxygen reduction catalysts for pemfcs. *Applied Catalysis B: Environmental*, 56(1–2):9–35, 2005.

[100] J. Greeley, J. Rossmeisl, A. Hellman, and J. K. Norskov. Theoretical trends in particle size effects for the oxygen reduction reaction. *Zeitschrift Fur Physikalische Chemie-international Journal of Research In Physical Chemistry & Chemical Physics*, 221(9-10):1209–1220, 2007.

[101] G. A. Tritsaris, J. Greeley, J. Rossmeisl, and J. K. Norskov. Atomic-Scale Modeling of Particle Size Effects for the Oxygen Reduction Reaction on Pt. *Catalysis Letters*, 141(7):909–913, JUL 2011.

[102] Markus Nesselberger, Sean Ashton, Josef C. Meier, Ioannis Katsounaros, Karl J. J. Mayrhofer, and Matthias Arenz. The particle size effect on the oxygen reduction reaction activity of pt catalysts: Influence of electrolyte and relation to single crystal models. *Journal of the American Chemical Society*, 133(43):17428–17433, 2011.

[103] Ifan E. L. Stephens, Alexander S. Bondarenko, Ulrik Gronbjerg, Jan Rossmeisl, and Ib Chorkendorff. Understanding the electrocatalysis of oxygen reduction on platinum and its alloys. *Energy & Environmental Science*, 5(5):6744–6762, May 2012.

[104] J. K. Nørskov, J. Rossmeisl, A. Logadottir, L. Lindqvist, J. R. Kitchin, T. Bligaard, and H. Jónsson. Origin of the overpotential for oxygen reduction at a fuel-cell cathode. *The Journal of Physical Chemistry B*, 108(46):17886–17892, 2004.

[105] Jan Rossmeisl, Gustav S. Karlberg, Thomas Jaramillo, and Jens K. Nørskov. Steady state oxygen reduction and cyclic voltammetry. *Faraday Discussions*, 140:337–346, 2008. Conference on Electrocatalysis Theory and Experiment at the Interface, Univ Southampton, Southampton, England, JUL 07-09, 2008.

[106] J Rossmeisl, A Logadottir, and JK Nørskov. Electrolysis of water on (oxidized)

metal surfaces. *Chemical Physics*, 319(1-3, SI):178–184, DEC 7 2005.

[107] Ifan E. L. Stephens, Alexander S. Bondarenko, Lone Bech, and Ib Chorkendorff. Oxygen Electroreduction Activity and X-Ray Photoelectron Spectroscopy of Platinum and Early Transition Metal Alloys. *CHEMCATCHEM*, 4(3):341–349, MAR 2012.

[108] Masahiro Watanabe, Kazunori Tsurumi, Takayuki Mizukami, Toshihide Nakamura, and Paul Stonehart. Activity and stability of ordered and disordered Co-Pt alloys for phosphoric-acid fuel-cells. *Journal of The Electrochemical Society*, 141(10):2659–2668, OCT 1994.

[109] Sanjeev Mukerjee, Supramaniam Srinivasan, Manuel P. Soriaga, and James McBreen. Role of structural and electronic-properties of Pt and Pt alloys on electrocatalysis of oxygen reduction - An in-situ XANES and EXAFS investigation. *Journal of The Electrochemical Society*, 142(5):1409–1422, MAY 1995.

[110] S. C. Ball, S. L. Hudson, B. R. C. Theobald, and D. Thompsett. PtCo, a Durable Catalyst for Automotive PEMFC. *ECS Transactions*, 11(1):1267–1278, 2007.

[111] K. C. Neyerlin, Ratndeep Srivastava, Chengfei Yu, and Peter Strasser. Electrochemical activity and stability of dealloyed Pt-Cu and Pt-Cu-Co electrocatalysts for the oxygen reduction reaction (ORR). *Journal of Power Sources*, 186(2):261–267, JAN 15 2009.

[112] Karl J. J. Mayrhofer, Viktorija Juhart, Katrin Hartl, Marianne Hanzlik, and Matthias Arenz. Adsorbate-Induced Surface Segregation for Core-Shell Nanocatalysts. *Angewandte Chemie-International Edition*, 48(19):3529–3531, 2009.

[113] Shuo Chen, Hubert A. Gasteiger, Katsuichiro Hayakawa, Tomoyuki Tada, and Yang Shao-Horn. Platinum-Alloy Cathode Catalyst Degradation in Proton Exchange Membrane Fuel Cells: Nanometer-Scale Compositional and Morphological Changes. *Journal of The Electrochemical Society*, 157(1):A82–A97, 2010.

[114] F. Maillard, L. Dubau, J. Durst, M. Chatenet, J. Andre, and E. Rossinot. Durability of Pt3Co/C nanoparticles in a proton-exchange membrane fuel cell: Direct evidence of bulk Co segregation to the surface. *Electrochemistry CommunicationsS*, 12(9):1161–1164, SEP 2010.

[115] J. Greeley, I. E. L. Stephens, A. S. Bondarenko, T. P. Johansson, H. A. Hansen, T. F. Jaramillo, J. Rossmeisl, I. Chorkendorff, and J. K. Norskov. Alloys of platinum and early transition metals as oxygen reduction electrocatalysts. *Nature Chemistry*, 1(7):552–556, OCT 2009.

[116] Vojislav R. Stamenkovic, Bongjin Simon Mun, Matthias Arenz, Karl J. J. Mayrhofer, Christopher A. Lucas, Guofeng Wang, Philip N. Ross, and Nenad M. Markovic. Trends in electrocatalysis on extended and nanoscale Pt-bimetallic alloy surfaces. *Nature Materials*, 6(3):241–247, MAR 2007.

[117] Tobias Peter Johansson. *New Materials for Oxygen Reduction Electrodes*. PhD thesis, Technical University of Denmark (DTU), 2012.

[118] B. Predel. *Landolt-Bornstein - Group IV Physical Chemistry: Pt-Y (Platinum-Yttrium)*, volume 5I. Springer-Verlag Berlin Heidelberg, 1998.

[119] Peter Strasser, Shirlaine Koh, Toyli Anniyev, Jeff Greeley, Karren More, Chengfei Yu, Zengcai Liu, Sarp Kaya, Dennis Nordlund, Hirohito Ogasawara, Michael F. Toney, and Anders Nilsson. Lattice-strain control of the activity in dealloyed core-shell fuel cell catalysts. *Nature Chemistry*, 2(6):454–460, JUN 2010.

[120] Francisco J. Perez-Alonso, David N. McCarthy, Anders Nierhoff, Patricia Hernandez-Fernandez, Christian Strebel, Ifan E. L. Stephens, Jane H. Nielsen, and Ib Chorkendorff. The Effect of Size on the Oxygen Electroreduction Activity of Mass-Selected Platinum Nanoparticles. *Angewandte Chemie-International Edition*, 51(19):4641–4643, 2012.

[121] G Ertl, M Neumann, and KM Streit. Chemisorption of CO on Pt(111) Surface. *Surface Science*, 64(2):393–410, 1977.

[122] Maria J. T. C. van der Niet, Angela den Dunnen, Ludo B. F. Juurlink, and Marc T. M. Koper. The influence of step geometry on the desorption characteristics of O-2, D-2, and H2O from stepped Pt surfaces. *Journal of Chemical Physics*, 132(17), MAY 7 2010.

[123] K. J. J. Mayrhofer, D. Strmcnik, B. B. Blizanac, V. Stamenkovic, M. Arenz, and N. M. Markovic. Measurement of oxygen reduction activities via the rotating disc electrode method: From Pt model surfaces to carbon-supported high surface area catalysts. *Electrochimica Acta*, 53(7):3181–3188, FEB 25 2008.

[124] Sebastian Kunz, Katrin Hartl, Markus Nesselberger, Florian F. Schweinberger,

Gihan Kwon, Marianne Hanzlik, Karl J. J. Mayrhofer, Ueli Heiz, and Matthias Arenz. Size-selected clusters as heterogeneous model catalysts under applied reaction conditions. *Physical Chemistry Chemical Physics*, 12(35):10288–10291, 2010.

[125] Edward F. Holby, Wenchao Sheng, Yang Shao-Horn, and Dane Morgan. Pt nanoparticle stability in PEM fuel cells: influence of particle size distribution and crossover hydrogen. *Energy & Environmental Science*, 2(8):865–871, 2009.

[126] Lei Tang, Byungchan Han, Kristin Persson, Cody Friesen, Ting He, Karl Sieradzki, and Gerbrand Ceder. Electrochemical Stability of Nanometer-Scale Pt Particles in Acidic Environments. *Journal of the American Chemical Society*, 132(2):596–600, JAN 20 2010.

[127] Francisco J. Perez-Alonso, Christian F. Elkjaer, Signe S. Shim, Billie L. Abrams, Ifan E. L. Stephens, and Ib Chorkendorff. Identical locations transmission electron microscopy study of Pt/C electrocatalyst degradation during oxygen reduction reaction. *Journal of Power Sources*, 196(15):6085–6091, AUG 1 2011.

[128] KJJ Mayrhofer, BB Blizanac, M Arenz, VR Stamenkovic, PN Ross, and NM Markovic. The impact of geometric and surface electronic properties of Pt-catalysts on the particle size effect in electocatalysis. *Journal of Physical Chemistry B*, 109(30):14433–14440, AUG 4 2005.

[129] M. Pourbaix. *Atlas of Electrochemical Equilibria in Aqueous Solutions*. National Association of Corrosion Engineers, Houston, second edition, 1974.

Included papers

Surface Science 603 (2009) 3420–3430

Contents lists available at ScienceDirect

Surface Science

journal homepage: www.elsevier.com/locate/susc

A comparative STM study of Ru nanoparticles deposited on HOPG by mass-selected gas aggregation versus thermal evaporation

R.M. Nielsen, S. Murphy *, C. Strebel, M. Johansson, J.H. Nielsen, I. Chorkendorff

Center for Individual Nanoparticle Functionality, Technical University of Denmark, 2800 Kongens Lyngby, Denmark

ARTICLE INFO

Article history:
Received 29 July 2009
Accepted for publication 6 October 2009
Available online 14 October 2009

Keywords:
Scanning tunneling microscopy
Nanoparticles
Ruthenium
Graphite

ABSTRACT

Scanning tunneling microscopy was used to compare the morphologies of Ru nanoparticles deposited onto highly-oriented graphite surfaces using two different physical vapour deposition methods; (1) pre-formed mass-selected Ru nanoparticles with diameters between 2 nm and 15 nm were soft-landed onto HOPG surfaces using a gas-aggregation source and (2) nanoparticles were formed by e-beam evaporation of Ru films onto HOPG. The particles generated by the gas-aggregation source are round in shape with evidence of facets resolved on the larger particles. Annealing these nanoparticles when they are supported on unsputtered HOPG resulted in the sintering of smaller nanoparticles, while larger particles remained immobile. Nanoparticles deposited onto sputtered HOPG surfaces were found to be stable against sintering when annealed. The size and shape of nanoparticles deposited by e-beam evaporation depend to a large extent on the state of the graphite support and the temperature. Ru deposition onto unsputtered HOPG is characterised by bimodal growth with large flat particles formed on the substrate terraces and smaller diameter particles aligned along the substrate steps. Evaporation onto sputtered HOPG results in the formation of 2 nm round particles with a narrow size distribution. Finally, thermal deposition onto both sputtered and unsputtered HOPG at 660 °C results in larger particles showing a flat Ru(0001) top facet.

1. Introduction

The structure and morphology of transition metal nanoparticles supported on graphite is of interest to surface scientists and nanotechnologists in a wide range of disciplines. Graphite is a favoured support in many nanoparticle studies because of the small electronic interaction between the particles and the support. The nanoparticles can therefore be mechanically supported, enabling various surface science techniques to be applied, while minimising the influence of the support on the properties being measured. Of course, the pre-treatment of the graphite surface and the method of deposition influence the size, shape and dispersion of the nanoparticles. It is therefore important to characterise how the morphology of the nanoparticles will appear under different preparation conditions, particularly when different methods are used to deposit the nanoparticles onto the surface.

In the present study, we have used scanning tunneling microscopy (STM) to compare the morphology of ruthenium nanoparticles deposited onto highly-oriented pyrolytic graphite (HOPG) using different physical vapour deposition (PVD) methods. Our interest in studying ruthenium is related to its catalytic properties, since it is used as a catalyst in ammonia [1], methane [2] and Fischer–Tropsch synthesis [3], as well as a co-catalyst in direct methanol fuel cells [4]. It has been determined from single crystal surface studies that the ruthenium step sites figure critically in these processes due to their role as active sites for the scission of nitrogen and carbon monoxide molecules, respectively [5–7]. In nanoparticulate form, the number of such active sites and hence the total particle activity, will depend on the shape, structure and size of the ruthenium nanoparticle. For example, models of unsupported ruthenium nanoparticles predict an optimal particle diameter in the range of 2–3 nm for ammonia synthesis [8–10].

The morphology and structure of Ru nanoparticles deposited on HOPG by chemical vapour deposition (CVD) have been previously studied with STM [11]. In that study, Ru nanoparticles were prepared by thermal decomposition of a $Ru_3(CO)_{12}$ precursor on HOPG, which had first been etched in atmospheric oxygen to generate randomly distributed single-layer etch pits. It was found that the ruthenium growth started from the step or pit edges, initially forming small round islands with a bimodal size distribution and at higher coverages developing into large flat layered islands with an hexagonal or truncated hexagon shape. Steps were resolved running along six directions on top of the islands, having a height consistent with the step height measured on a Ru(0001) single crystal surface. From atomically resolved images on top of the

* Corresponding author.
E-mail address: shmurphy@fysik.dtu.dk (S. Murphy).

0039-6028/$ - see front matter © 2009 Elsevier B.V. All rights reserved.
doi:10.1016/j.susc.2009.10.005

islands and on the surrounding HOPG it was determined that the ruthenium could have two possible epitaxial orientations on the surface. In both cases, the Ru(0001) plane lies parallel to the graphite (0001) surface, where one has the same orientation as the graphite hexagonal lattice and the other is rotated by 30° around the surface normal.

Here, we have used two different PVD methods to deposit Ru nanoparticles onto sputtered and unsputtered HOPG surfaces. In the first method, ruthenium nanoparticles are pre-formed in a gas-aggregation source and are mass-selected with a quadrupole mass filter before being deposited onto the HOPG surface. This offers an extremely clean method of preparing monodisperse particles on the surface. Gas-aggregation sources have been used to deposit monodisperse nanoparticles of a variety of different metals onto HOPG [12–27]. The size and shape of the nanoparticles do not depend significantly on the condition of the graphite surface, since the particles are formed before arriving at the surface. However, the kinetic energy of the particles is an important parameter that can determine whether the particles retain their shape or are completely restructured upon deposition [28,29]. In the second method, the nanoparticles are formed at the HOPG surface from a flux of ruthenium atoms generated by an electron-beam evaporation source. This method has been used in a number of studies to deposit different metals on HOPG surfaces [30–32], where it has been clearly demonstrated that surface defects play an important role in determining the size, shape and dispersion of the resulting nanoparticles. To our knowledge there has so far been only one other study where the properties of mass-selected metal particles were compared directly with those of thermally deposited particles [33]. In that case, X-ray photoelectron spectroscopy (XPS) was used to investigate the properties of mass-selected Ag clusters and similarly sized Ag islands grown by thermal evaporation. Dissimilar electronic properties were observed, which were attributed to either a difference in the particle shape or a difference in the metal-support interaction.

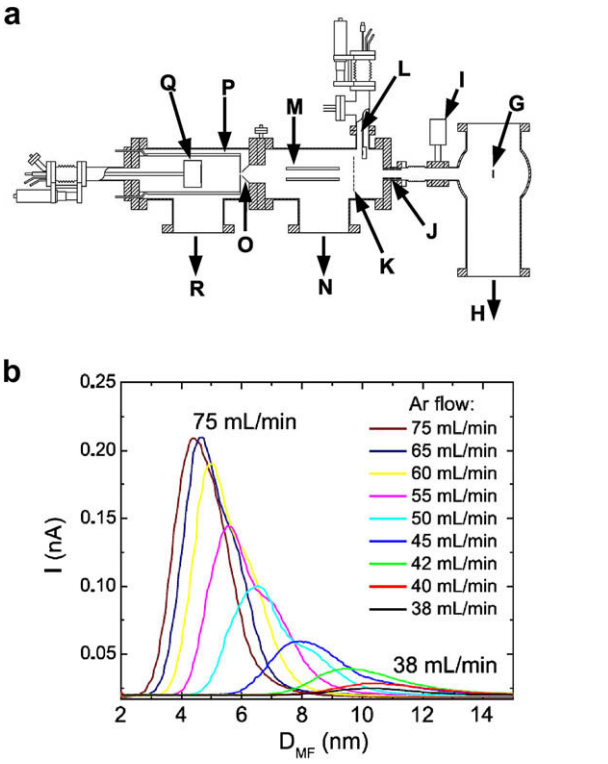

Fig. 1. (a) Schematic illustration of deposition layout using gas-aggregation source with (G) substrate located in preparation chamber, (H) pumping to preparation chamber via 260 l/s turbo pump and 400 l/s ion pump, (I) gate valve, (J) Einzel lenses, (K) grid, (L) quartz crystal balance, (M) quadrupole mass filter, (N) pumping to quadrupole chamber via 230 l/s turbo pump, (O) skimmer, (P) cooling shroud, (Q) magnetron-sputter source, (R) pumping to gas-aggregation chamber via 450 l/s turbo pump. (b) Cluster current as a function of D_{MF}, the particle size transmitted by the quadrupole mass filter, for different Ar flows into the gas-aggregation source. All other parameters such a sputter power, aggregation length, etc., have been kept constant.

2. Experimental

The experiments were performed in a multichamber ultrahigh vacuum (UHV) system (Omicron, Multiscan Lab) with a base pressure in the low 10^{-11} mbar region. The system is equipped with facilities for combined in-situ scanning tunneling microscopy (STM) and scanning electron microscopy (SEM), as well as scanning Auger microscopy (SAM), ion scattering spectroscopy (ISS), low-energy electron diffraction (LEED) and temperature programmed desorption (TPD) measurements. The HOPG substrates (SPI-1, 7 × 7 × 0.5 mm) were cleaved in air and mounted in sample holders incorporating a pyrolytic boron nitride (PBN) radiative heater, which is capable of heating the sample to temperatures in excess of 700 °C. A W – 5 at.% Re/W – 26 at.% Re thermocouple was placed in contact with the front side of each substrate in order to monitor and control the sample temperature via a PID controller (Eurotherm 2408). Upon insertion into UHV, the samples were outgassed for several hours at 660 °C to outgas adsorbed contaminants prior to use. The two different PVD methods mentioned above were then used to prepare ruthenium nanoparticles on the surface.

2.1. Gas-aggregation source

In the first method, pre-formed mass-selected Ru particles were deposited onto the substrates from a magnetron-sputter gas-aggregation source fitted with a quadrupole mass filter (Mantis Deposition Ltd., Nanogen 50). A schematic illustration of the deposition layout of the gas-aggregation source is shown in Fig. 1a. The particles are formed by gas-phase condensation from a flux of Ru atoms that are sputtered from a 99.99% pure Ru target by a direct current magnetron sputter source (Q). The magnetron is housed in a liquid nitrogen cooled enclosure (P) with a small aperture (3 mm dia.) at one end. Argon gas is flown into the volume (or gas-aggregation zone) around the magnetron at a rate of 10–120 sccm and is pumped away via the aperture so that a local pressure of 0.1–1 mbar is obtained inside the gas-aggregation zone during operation. The argon gas serves the dual purpose of providing the plasma that sputters the target, and thermalising the sputtered Ru atoms so that they condense into clusters. The size of the nanoparticles that grow from these clusters is determined by a number of factors such as sputter power (typically 20–40 W), rate of gas flow, distance between the target and the exit aperture and the diameter of the exit aperture. The latter parameters control the residence time of the clusters inside the gas-aggregation zone. This is illustrated in Fig. 1b where the mean particle size exiting the source decreases as the Ar flow into the aggregation zone is increased.[1] Nanoparticles with diameters in the approximate range of 2–15 nm are routinely produced using the source, though it is possible to produce smaller particles by introducing helium gas into the aggregation zone to improve the condensation rate. Extreme care is taken to ensure that the aggregation zone is free from impurities that might affect the particle formation. The source is baked for at least 24 h at 150 °C prior to use, which results in a base pressure

[1] The particle size D_{MF}, indicated on the x-axis of the plot corresponds to the mass transmitted by the quadrupole filter and is based on the assumption that the nanoparticles are spherical and have the density of bulk ruthenium.

in the mid 10^{-10} mbar region. Also, the Ar and He gases used are N 60 pure and are further scrubbed of trace impurities by passing them through an activated iron catalyst before entering the source. From the aggregation zone, the nanoparticles are carried by the stream of gas pumped through the exit aperture, producing a nanoparticle beam that is further refined by a skimmer (O) placed in front of the exit aperture. The nanoparticle beam is then passed through a quadrupole mass filter (M) where the particles can be filtered according to their mass-to-charge ratio. This is made possible because a significant fraction of the clusters formed by the magnetron-sputter process are ionised [34]. A mass-resolution of the order of 2% is possible with this filter. However, the throughput of nanoparticles through the filter under these conditions is very low. Consequently, a lower mass-resolution of approximately 18% (corresponding to a resolution in the particle diameter of 6%) was adopted in order to increase the throughput so that a reasonable deposition rate was obtained.[2] The beam current of ionised mass-selected particles exiting the source can be measured by a biased grid (K), which can be moved into and out of the beam path, while a quartz crystal balance (L) can be used to measure the total flux (both ionised and neutral particles). After exiting the quadrupole mass filter the nanoparticle beam passes through three Einzel lenses (J) that are used to focus the beam through the constriction between the source and the preparation chamber where the substrate (G) is located. These home-built lenses comprise three stainless steel rings, which can be separately biased with up to +500 V. The dimensions and layout of the lenses were optimised using a commercial ion optics simulation package [35]. The substrate is placed at a small positive bias ($\sim$ 36 V) so that negatively charged particles are soft-landed onto the surface with kinetic energies of $\leqslant$ 0.1 eV/atom. Moreover, the substrate can be shifted slightly off-axis of the beam in order to avoid deposition of neutral particles, though our measurements indicate that this is not necessary since the number of neutrals entering the preparation chamber is negligible. Further details on the construction and principles of operation of this type of source can be found elsewhere [34,36,37].

2.2. E-beam evaporation

Ru nanoparticles were also prepared on HOPG by electron-beam evaporation of a 99.99% purity Ru rod. In this case, a home-built evaporator was used to deposit films onto HOPG substrates both at room and at elevated temperatures. The substrates were either unsputtered or sputtered for 30 s with 500 eV Ar^+ ions at a current density of $\sim$ 0.1 μA/cm^2 and outgassed at 660 °C. The substrate was grounded while the Ru rod was held at a positive bias of 500 V. It is therefore important to note that some surface defects may have been formed on the HOPG by accelerated positive Ru ions coming from the electron-beam evaporator. A quartz crystal balance was used to monitor the deposition rate (typically 0.46–0.9 Å/min) and estimate the final film thickness.

2.3. Characterisation by STM

STM was performed at room temperature in constant current mode, using electrochemically etched (5 M NaOH, 6 V DC) W tips without any in-vacuum treatments other than applying a series of voltage pulses (typically 4–9 V for 10–100 ms) or scanning for several lines with increased bias (U $\sim$ 2 V) in order to condition the tip. The typical tunnel parameters used to image the particles in this study were U = 10—600 mV for the gap bias and I = 100—800 pA for the tunnel current. In order to minimise tip interaction with the surface through slow feedback response, slow scan speeds were adopted with a typical line scan frequency of about 0.5–1 Hz.

When imaging nanoparticles with diameters that are comparable with the radius of curvature of the STM tip, the imaged particle diameter is dilated due to tip convolution effects [38]. In the present case, the etching procedure used to produce the tips is expected to result in a tip radius on the order of $\sim$ 8 nm [39]. Consequently, we expect that for particle diameters below 8 nm the STM images of the particles will emphasise the lateral shape of the STM tip. Some considerations must also be taken into account when measuring the height of the particles. Differences in the apparent tunnel barrier height measured on the particle and on the surrounding substrate – due to differences in the local workfunction – can result in the measured particle height differing from the actual particle height [38]. Moreover, when the tip-particle separation becomes large compared to the particle diameter alternative tunnel paths to the substrate become available and the measured particle height will vary with the tunnel gap. This has been demonstrated for Au nanoparticles supported on HOPG, which decreased in height by as much as 15% when the gap bias was increased from 0.5 V to 3.5 V at a constant tunnel current [40]. To investigate the dependence of the measured particle height upon the tunnel parameters, we have measured the variation in the apparent height of a single Ru nanoparticle using the typical tunnel parameters described above. A variation of $\sim$ 0.2 nm in the height of the nanoparticle shown in Fig. 2 was found when the gap bias was increased from 10 mV to 600 mV at a tunnel current of I = 800 pA. Assuming that the actual height of the particle was close to 1.9 nm this error is comparable to the experimental error set by the scanner calibration ($\leqslant$10%).

Image analysis was performed using the scanning probe image processor, SPIP (Image Metrology Ltd.). Typically, STM images were selected that required minimal filtering other than the application of a third order polynomial plane correction, before performing a grain analysis to determine the mean particle height, diameter, standard deviation, etc. Care was taken to ensure that the selected image did not include any obvious defects such as substrate steps, which could distort the height distribution obtained from the nanoparticles. For low particle coverages the grain analysis was performed using the threshold method, while for higher coverages where particles were deposited in close proximity to one another, the watershed method was used. The particle diameter obtained from the grain analysis refers to the diameter of a circle with an area or perimeter equivalent to that of the imaged particle. As will be seen, this representation works well in the case of nanoparticles produced by the gas-aggregation source, but is more nominal in the case of the thermally evaporated nanoparticles, which do not always have a round shape. The data presented here for each particle size represent mean values and standard deviations obtained from a statistical sample taken from several STM images, each containing a large number of nanoparticles (i.e. several tens or hundreds). This averages out the influence of the STM tip, which is prone to change in shape and local electronic structure during scanning, on the particle height and diameter distributions.

3. Results

3.1. Mass-selected Ru nanoparticles

Fig. 3 shows a series of images of different sized Ru nanoparticles, which were deposited onto unsputtered HOPG, and exposed to different anneal temperatures. Depositions were carried out so that between 10% and 40% of the surface was covered by nanoparticles. When particles were deposited onto the unsputtered HOPG

[2] The diameter resolution is smaller compared to the mass-resolution since the particle mass is proportional to the cube of the particle diameter.

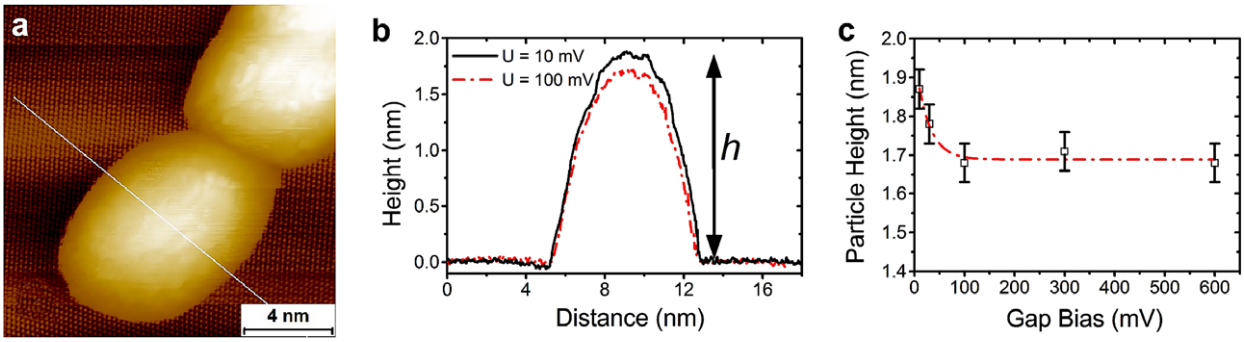

Fig. 2. (a) 15 nm × 15 nm STM image of a ruthenium nanoparticle supported on unsputtered HOPG taken with U = 100 mV and I = 800 pA. Note, the colour scale has been equalised to enhance contrast. (b) Line-profiles taken across the direction marked by the white line in (a) comparing the apparent height *h* of the particle measured when U = 10 mV and when U = 100 mV. (c) Plot of the apparent particle height measured for different gap bias values at constant I = 800 pA. The error in the measured particle height is estimated to be ±0.05 nm. The dashed line is provided as a guide to the eye.

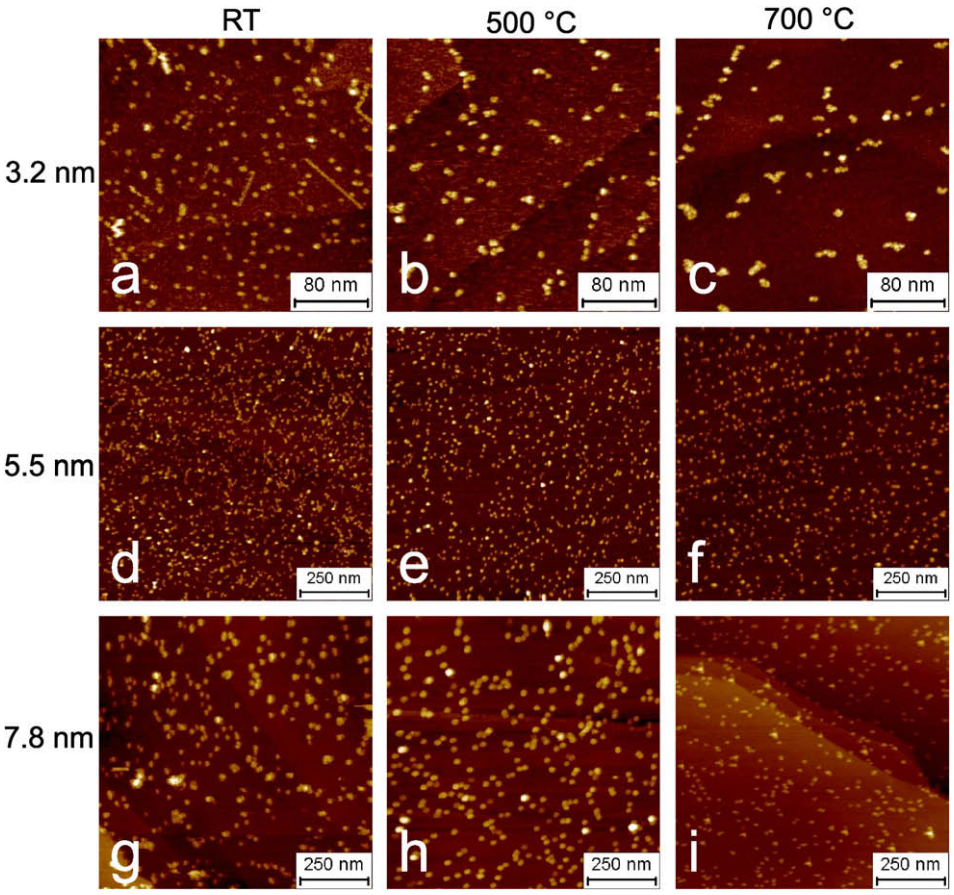

Fig. 3. STM images of three different sizes of Ru nanoparticles as-deposited at room temperature (RT) onto unsputtered HOPG and after heating to 500 °C and 700 °C. The particle diameters are (a–c) 3.2 nm, (d–f) 5.5 nm, and (g–i) 7.8 nm.

surface it was found that they were easily displaced by the STM tip during scanning. This behaviour was observed for the full range of particle sizes investigated using the gas-aggregation source. An example of this behaviour is shown in Fig. 3a, where several 3.2 nm particles have been displaced by the tip, resulting in streaks appearing at several points in the image. It is interesting to note that the particles are not simply displaced along the scan direction (*x*-axis), though short jumps along this direction were sometimes observed, but rather follow paths that suggest some influence of the underlying support. It was found that if the gap voltage was increased slightly during a scan, the particles appeared to be removed from the substrate terraces and pushed towards the substrate steps. At higher bias voltages, e.g. 2 V, only the support surface was imaged as all the particles were completely removed from the scan area. Tip-induced diffusion has been previously reported for noble metal clusters deposited onto unsputtered HOPG [13] and can be related to the weak interaction between the particles and the van der Waals surface.

In light of this weak interaction between the support and the nanoparticles, it was anticipated that nanoparticles deposited onto unsputtered HOPG would not be stable against sintering when exposed to elevated temperatures. In fact, this was found to be

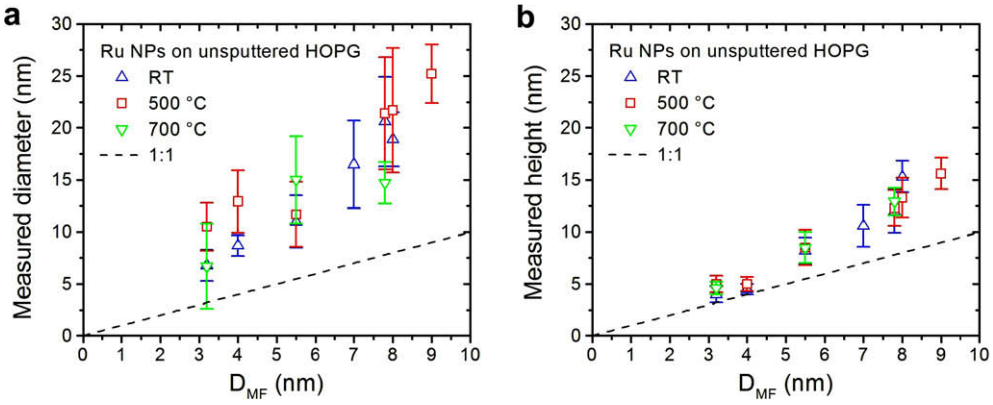

Fig. 4. Plots of (a) the measured mean particle diameter and (b) the measured mean height of Ru nanoparticles supported on unsputtered HOPG versus the particle diameter D_{MF} selected using the quadrupole mass filter for a range of sizes. The dashed line in both plots indicates where a 1:1 correspondence between the measured values and the expected diameter would lie.

the case for the 3.2 nm nanoparticles shown in Fig. 3a, which did indeed sinter when annealed for a short time at 500 °C, as shown in Fig. 3b. When first deposited, the nanoparticles are initially randomly distributed across the surface. However, upon annealing they sinter on the substrate terraces and decorate the substrate steps. As a consequence, the measured mean diameter of the particles increases from 6.8 ± 1.5 nm in Fig. 3a to 8.4 ± 2.8 nm in Fig. 3b. The mean diameter increases further still to 9.7 ± 4.4 nm when the surface is heated to 700 °C, as shown in Fig. 3c. However, even when heated to this temperature the measured mean height (4.1 ± 0.8 nm) of the particles does not change significantly, indicating that while the particles aggregate together on the terraces or at steps, they do not coalesce into larger particles.[3] The sintering effect is less pronounced or not present at all for larger particles, with the 5.5 nm nanoparticles shown in Fig. 3d–f displaying some limited mobility in the form of increased step decoration at higher temperatures, while the 7.8 nm nanoparticles shown in Fig. 3g–i did not appear to be mobile at all at these temperatures.

Fig. 4 shows plots of the measured mean diameter and height of different sized nanoparticles, which were deposited onto unsputtered HOPG. Each point in the graph represents a mean value determined from a statistical analysis of several STM images each containing a large sample of nanoparticles (several tens or hundreds). The error accompanying each value corresponds to the standard deviation derived from a Gaussian fit to the statistical sample and provides some measure of the size resolution obtained. The particle size D_{MF} indicated on the x-axis of each plot corresponds to the mass selected with the quadrupole filter and is based on the assumption that the nanoparticles are spherical and have the density of bulk ruthenium.[4] The mean values measured for the particle diameter, shown in Fig. 4a, are always larger than the values measured for the particle height, which are shown in Fig. 4b. This can be attributed to the overestimation of the lateral dimensions of the nanoparticles due to tip convolution effects. The mean height value therefore represents a more reliable measure of the actual nanoparticle size.

What is immediately apparent from Fig. 4 is that while the measured diameter and height of the particles increase as D_{MF} is increased, they do not follow a 1:1 correspondence as indicated by the dashed line in each plot. This is particularly apparent for the larger particle sizes investigated, i.e. above a D_{MF} of around 4 nm. There are several possible explanations for this; (1) the quadrupole mass filter simply does not operate as expected for these particle sizes. (2) The nanoparticles may already be sintered upon deposition at room temperature. This can probably be excluded since the same behaviour is observed when the nanoparticles are deposited onto highly sputtered HOPG surfaces. In that case the particles are immediately pinned to defects upon deposition and can not sinter at room temperature. (3) The size distributions are dominated by larger nanoparticles that were allowed through the quadrupole mass filter because they carried multiple charges. For example, in order to fit the data shown in Fig. 4b the nanoparticles would require at least two charges for $D_{MF} = 3.2$ nm and five charges for $D_{MF} = 9$ nm.[5] (4) It is possible that the nanoparticles are not completely homogeneous since they are probably formed from smaller clusters inside the aggregation source. If voids or grain boundaries are present inside the nanoparticles, this could give them a larger diameter for a selected mass. While it is as yet unclear why this deviation occurs, it is still possible to use the information in Fig. 4 to calibrate the output of the aggregation source, if we assume that the particles are approximately round and retain their shape when soft-landed onto the surface.

As mentioned earlier, the size of the errors in Fig. 4 provide a measure of the size resolution obtained after deposition. Generally, the measured heights shown in Fig. 4b display a smaller error than that obtained for the diameter measurements shown in Fig. 4a. For example, the standard deviation measured for the particle height is on average around 15%, while the standard deviation measured for the particle diameter is on average around 21%. It is clear that these errors are significantly larger than the diameter resolution of 6% determined by the quadrupole mass filter settings. However, it should be noted that the latter value applies to an idealised case where the nanoparticles are perfectly spherical and homogeneous. From the STM images it appears that the nanoparticles are round, but the true shape is not completely resolved due to tip convolution. Therefore some real spread in the size distribution of the particles can be anticipated. This could be due to either the random orientation of the particles on the surface, the deposition of different polymorphs with the same mass, or deposition of different multiply charged particles. Moreover, some additional spread in the measured size distributions can be expected due to measure-

[3] By this we mean that the nanoparticles form an aggregate where individual nanoparticles are bound together but can still be distinguished from one another by STM, and have not completely melted together, i.e. coalesced, to form a single larger particle of well-defined shape.

[4] The size of the mass-selected nanoparticles mentioned in the text refers to their D_{MF} unless stated otherwise.

[5] Since the quadrupole filters according to m/e, for a doubly charged particle to be filtered the mass of the particle must also double. The diameter of this particle is therefore $\sqrt[3]{2}$ times larger. In the case of a particle with five charges the diameter increases by a factor of $\sqrt[3]{5}$.

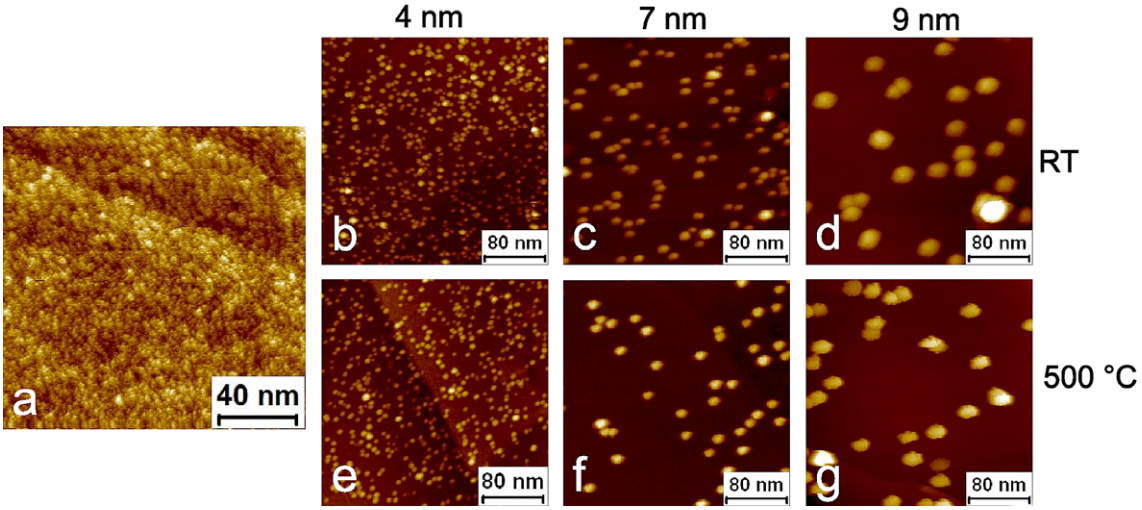

Fig. 5. (a) 156 × 156 nm STM image of the HOPG surface after sputtering with 500 eV Ar^+ ions for 15 min with a current density of ~ 0.1 μA/cm². The surface was post-annealed for 15 min at 660 °C to degas the surface of implanted argon. (b–g) STM images showing ruthenium nanoparticles of three different sizes as-deposited at room temperature (RT) on sputtered HOPG and after heating to 500 °C.

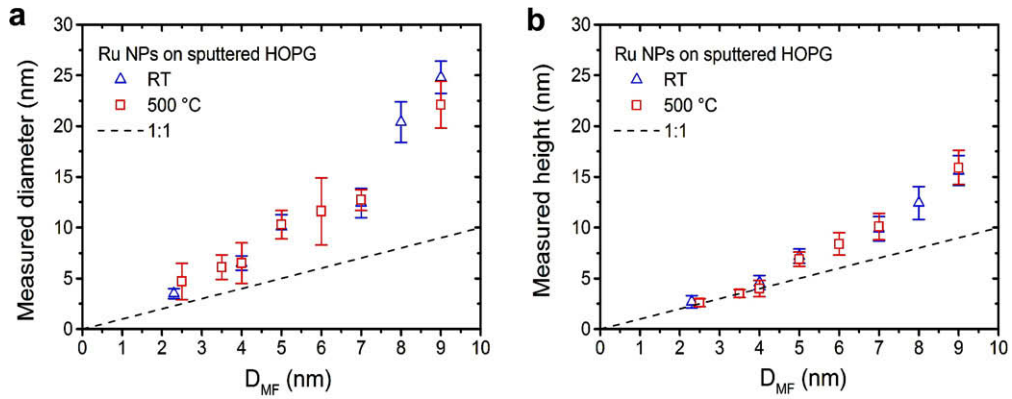

Fig. 6. Plots of (a) the measured mean particle diameter and (b) the measured mean height of Ru nanoparticles supported on sputtered HOPG versus the particle diameter D_{MF} selected by the quadrupole mass filter for a range of sizes. The HOPG surface was sputtered for 15 min with 500 eV Ar^+ ions before deposition. The dashed line in both plots indicates where a 1:1 correspondence between the measured values and D_{MF} would lie.

ment errors. For example, the height distribution is sensitive to the plane correction applied to the image before grain analysis is performed, while the diameter measurement can be influenced by smearing of the particle image due to non-ideal feedback response.

Fig. 4 also compares the effect of annealing the nanoparticles on their measured diameter and height. In some cases, the nanoparticles were exposed to temperatures of 500 °C and 700 °C after deposition. As mentioned earlier, the 3.2 nm particles were observed to sinter when annealed to these temperatures. However, while this lead to an increase in the mean diameter (not shown in Fig. 4a), the particle height did not change significantly (shown in Fig. 4b). For the remaining sizes investigated, annealing did not appear to result in a substantial change in the particle height or diameter, indicating that sintering did not occur.

In addition to investigating the morphology of mass-selected nanoparticles deposited onto unsputtered HOPG, we have also examined nanoparticles deposited onto sputtered HOPG surfaces. In order to ensure that the particles remained immobile while performing STM, the HOPG substrates were also sputtered with 500 eV Ar^+ ions for 15 min with a current density of ~ 0.1 μA/cm² to generate a high density of surface defects. This is followed by annealing for 15 min at 660 °C to degas the surface of implanted argon. This procedure produces a highly defective layer on the substrate surface, as shown in Fig. 5a. The root-mean-square roughness measured on a flat area of this surface is around 0.2 nm. The typical morphology of the mass-selected nanoparticles deposited onto the sputtered surface is displayed in Fig. 5b–g for different particle sizes both as-deposited at room temperature and after annealing to 500 °C. As with the depositions on the unsputtered surface, the depositions on the sputtered surface were carried out so that usually between 10% and 40% of the substrate surface was covered by nanoparticles. The particles are randomly distributed across the surface, with little evidence of sintering other than those instances where particles have been deposited on top of one another.

Fig. 6 shows plots of the measured mean diameter and height of different size particles deposited onto sputtered HOPG. As before, each point on the plot represents the mean value and standard deviation determined from a size distribution obtained from several STM images containing several tens or hundreds of nanoparticles. Again, the measured diameters of the particles are consistently larger than the measured heights because they are overestimated due to tip convolution effects. A good 1:1 correspondence is obtained between the measured mean height values and the diameter D_{MF} for particles with diameters up to 4 nm, suggesting that these small particles retain a very round shape when supported on the HOPG surface. For particles larger than

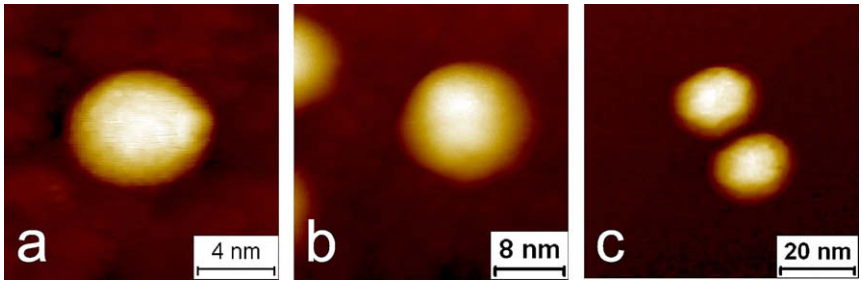

Fig. 7. STM images of individual mass-selected Ru nanoparticles. (a) $D_{MF} = 3.6$ nm, (b) $D_{MF} = 5$ nm and (c) $D_{MF} = 8$ nm.

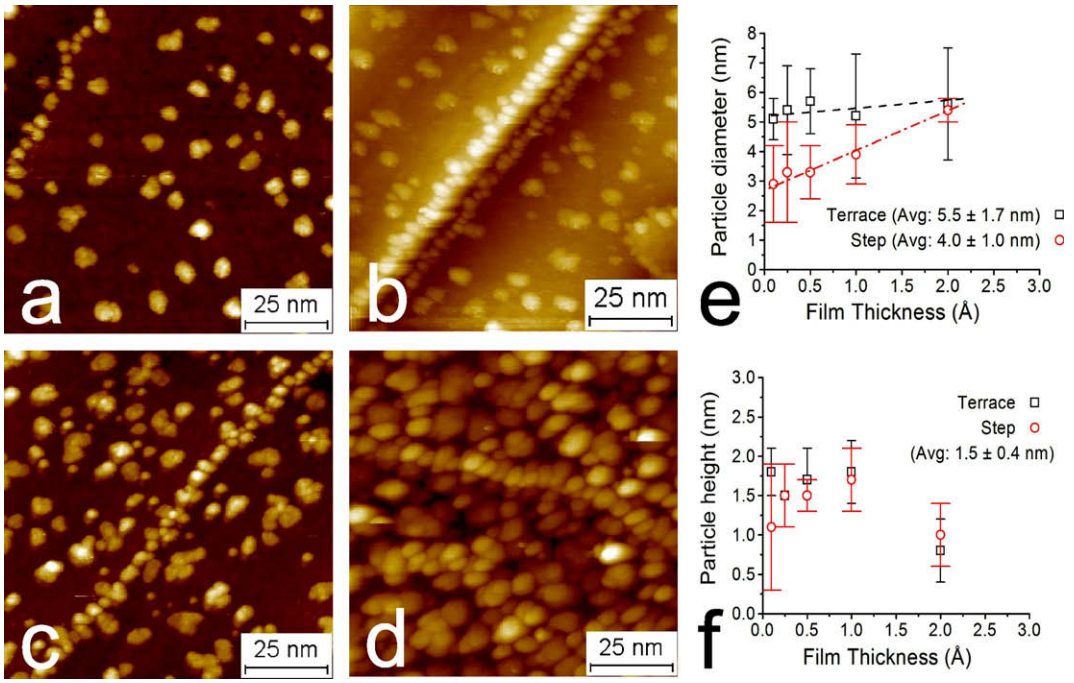

Fig. 8. 100 nm × 100 nm STM images of Ru films of (a) 0.25 Å, (b) 0.5 Å, (c) 1 Å, and (d) 2 Å nominal thickness deposited onto unsputtered HOPG at room temperature. Values for the mean diameter and mean height of particles located on terraces (squares) and at steps (circles) are plotted with their standard deviation in (e) and (f), respectively. The linear fits to the data in (e) highlight the behaviour of the particle diameter measured on the terraces and at the steps as a function of increasing film thickness. Average values for the particle diameter and height are given in brackets in both (e) and (f).

4 nm the measured height deviates from a 1:1 correspondence with D_{MF}. Annealing the nanoparticles to 500 °C did not result in any substantial change in the measured nanoparticle height or diameter, indicating that the size and shape of the particles is stable below this temperature.

The shape of individual supported particles of different sizes were resolved by STM and are shown in Fig. 7. Particles smaller than about 8 nm appear rounded in the STM images and no preferential facets are observed. Since the diameter of these particles is smaller than the radius of the STM tip, the particle image is convolved with an image of the tip and it is therefore difficult to extract information about the particle shape. However, it can at least be inferred that the particles do not possess a large and flat top facet as it would be possible to image this with STM. In contrast, it is possible to resolve facets on the larger particles, which appear hexagonal in shape and in some cases display evidence of a flat top facet, as shown in Fig. 7c.

3.2. E-beam deposited Ru nanoparticles

Fig. 8a–d shows a series of STM images of e-beam evaporated Ru films of increasing coverage, which were deposited at room temperature onto unsputtered HOPG. The films are characterised by bimodal growth with large Ru particles formed on the HOPG terraces, while smaller particles decorate the upper and lower edges of the substrate steps. Fig. 8e and f summarises the mean diameter and height measured for particles located on terraces and at substrate steps. While a large difference in diameter is observed between particles on the terrace (5.5 ± 1.7 nm) and particles at the steps (4.0 ± 1.0 nm),[6] the heights of the particles at both sites are generally the same (1.5 ± 0.4 nm). The resolution obtained in the particle diameter in this case is of the order of ±25–30%. The bimodal growth seen in Fig. 8a–d has previously been observed for a number of metals deposited onto unsputtered HOPG [30–32,41]. Metal adatoms deposited onto the HOPG surface possess a high mobility as they only weakly interact with the van der Waals surface. Surface defects like steps provide nucleation centers and limit adatom mobility, resulting in a higher density of smaller particles compared to those formed on the substrate terraces. It is interesting to note that even for the highest coverage

[6] The mean particle diameter at both sites increases continuously with increasing film thickness. However, the values given in brackets correspond to average values and errors determined from the data presented in Fig. 8e.

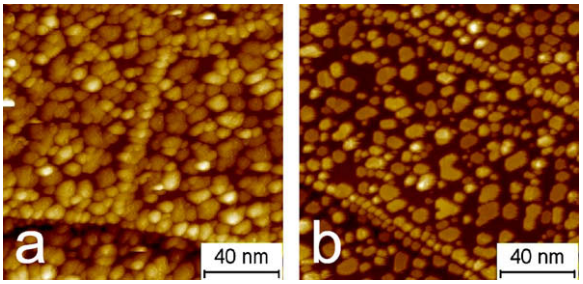

Fig. 9. 150 nm × 150 nm STM images of a 2 Å Ru film on unsputtered HOPG (a) as-deposited at room temperature, and (b) after annealing for 30 min at 400 °C in UHV.

shown in Fig. 8d the particles decorating the steps do not appear to coalesce. This suggests the presence of a barrier to coalescence, which could be due to either strain effects – as reported for Fe/W(1 1 0) submonolayer growth [42] – or antiphase boundaries between the two possible epitaxial orientations of Ru on HOPG [11]. Annealing the films to 400 °C resulted in better crystallisation of the nanoparticles, as shown in Fig. 9 for the case of a 2 Å Ru film. In this case, the percentage of the surface covered by ruthenium decreases from about 80% in Fig. 9a for the as-deposited film, to about 60% in Fig. 9b for the annealed film, while the measured mean height of the particles increases by 10–20%. The particles in Fig. 9b are flat and have in some cases an hexagonal shape, indicating that the Ru(0 0 0 1) facet is presented. Moreover, the edges of the particles appear in many cases to share a common orientation, suggesting a common epitaxial relationship with the substrate, as has previously been observed by Song et al. for CVD grown Ru films on HOPG [11].

Fig. 10a–d shows a series of STM images and their corresponding particle size distributions for Ru films evaporated onto HOPG that had been sputtered for 30 s with 500 eV Ar^+ ions. The surface defects limit the mobility of the Ru adatoms and substantially increases the number of available nucleation centres. As a result, far higher densities of smaller nanoparticles are obtained at comparable film thicknesses to those presented in Fig. 8. For example, a particle density of the order of $6.3 \times 10^3\ \mu m^{-2}$ is determined from Fig. 8a, which shows a 0.25 Å film deposited on unsputtered HOPG, while a particle density of around $7.4 \times 10^4\ \mu m^{-2}$ is obtained from Fig. 10a, which shows a comparable film thickness deposited onto a sputtered HOPG surface. There is also less evidence of preferential decoration of the substrate steps on the sputtered surface. The particles appear round in the STM and have an average diameter of 2.3 ± 0.5 nm, which is much smaller than that of the particles deposited on unsputtered HOPG, while the average height (1.3 ± 0.3 nm) is similar. The resolution in the particle diameter is of the order of ±20%, which is better than that obtained by deposition on the unsputtered surface.

Annealing the films to 430 °C results in their agglomeration into larger particles as illustrated in Fig. 11. Comparison of the mean particle diameter and height of the as-deposited and annealed films, shown in Fig. 11e and f, respectively, reveals that there is a clear increase in both the diameter and height of the particles when the films are annealed. This behaviour is different from that observed when pre-formed nanoparticles were deposited on the HOPG surface. In that case, there was some sintering for small particles deposited on unsputtered HOPG, but otherwise the particle size and shape generally appeared to be stable at temperatures up to at least 500 °C. There could be several possible reasons for this difference: (1) the pre-formed particles are closer to thermodynamic equilibrium than particles that are thermally deposited onto HOPG at room temperature. (2) The thermally deposited particles are formed at the surface, possibly in the presence of loose carbon generated by the surface sputtering pre-treatment. Should any loose carbon be incorporated into the particles during the growth phase, it might have some surfactant effect on the particles

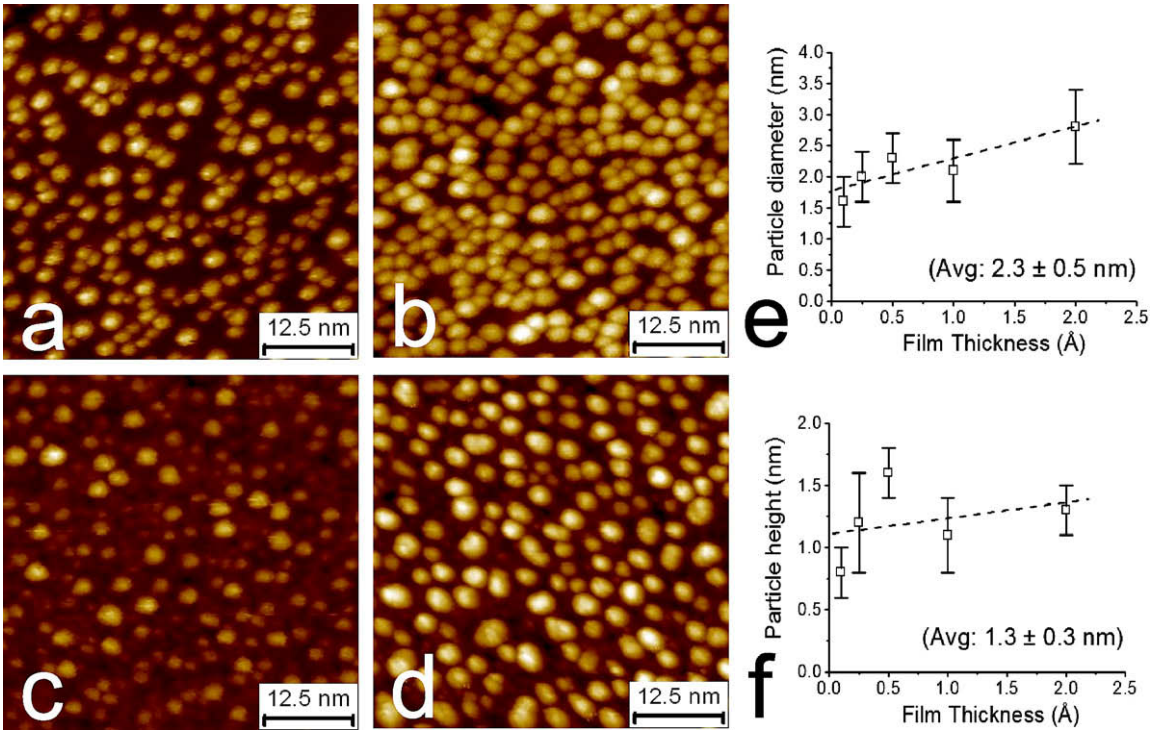

Fig. 10. 50 nm × 50 nm STM images of Ru films of (a) 0.25 Å, (b) 0.5 Å, (c) 1 Å, and (d) 2 Ånominal thickness deposited onto HOPG that has been sputtered for 30 s with 500 eV Ar^+ ions. Values for the mean diameter and mean height of the particles are plotted with their standard deviation in (e) and (f), respectively. The average values determined for the particle diameter and height are given in brackets. The dashed lines are linear fits to the data and are supplied as a guide to the eye.

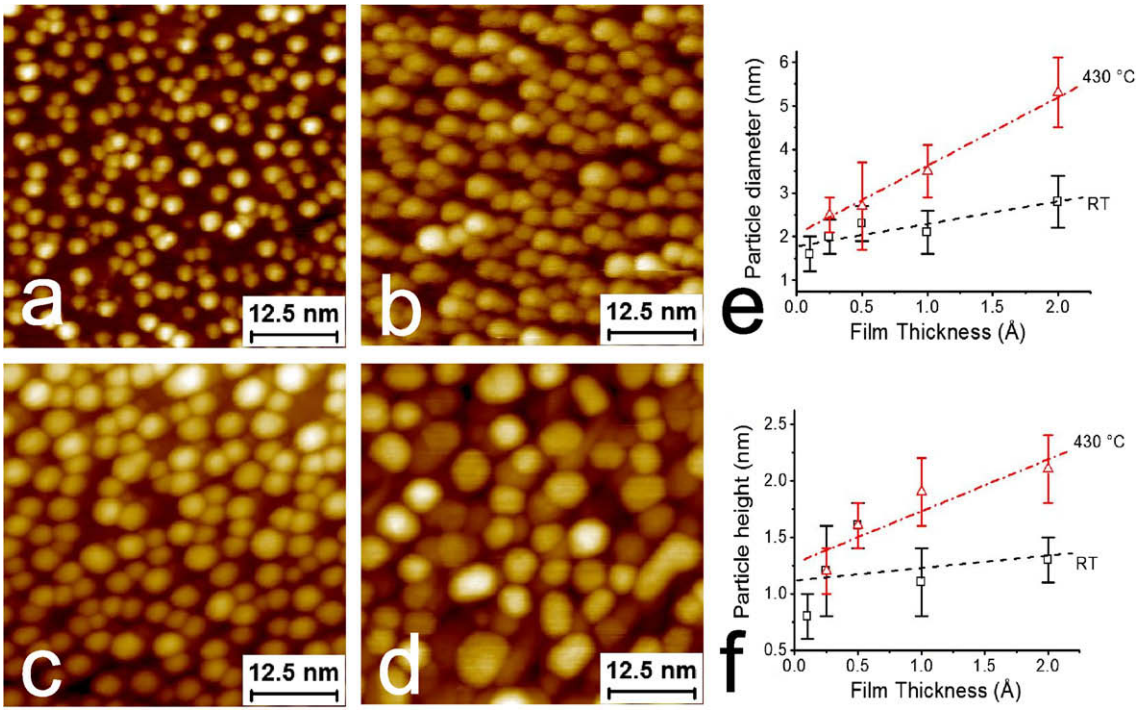

Fig. 11. 50 nm × 50 nm STM images of Ru films of (a) 0.25 Å, (b) 0.5 Å, (c) 1 Å, and (d) 2 Å nominal thickness deposited onto HOPG that has been sputtered for 30 s with 500 eV Ar^+ ions and annealed to 430 °C. Values for the mean diameter and mean height of the particles are plotted (triangles) with their standard deviation in (e) and (f), respectively, and are compared against the values plotted for the as-deposited films (squares). The dashed lines are linear fits to the data and are supplied as a guide to the eye.

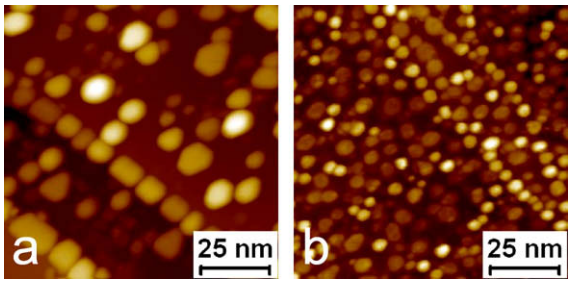

Fig. 12. 100 nm × 100 nm STM images of (a) a 2 ÅRu film deposited onto unsputtered HOPG at 660 °C and (b) a 2 ÅRu film deposited onto sputtered (30 s with 500 eV Ar^+ ions) HOPG at 660 °C.

during annealing. In the case of particles produced by the gas-aggregation source, the particles are pre-formed before landing on the surface and would be less likely to interact with any loose carbon. (3) Since the thermal deposition process sprays the surface with a flux of ruthenium atoms, this could result in a high density of very small clusters nucleating at defect sites on the exposed substrate between the larger particles. These clusters could then be consumed by the larger particles during annealing in an Ostwald ripening process. It should be noted that while these clusters were not observed in films deposited onto unsputtered HOPG, they could be present on a sputtered surface with a high density of defects. It would also not necessarily be easy to distinguish these very small clusters from the background roughness of the surface with STM.

The effects of elevated temperature deposition were also investigated. Fig. 12 compares STM images of the same nominal thickness of Ru deposited onto unsputtered and sputtered HOPG surfaces held at 660 °C. Similar to the deposition at room temperature, deposition on the unsputtered surface at elevated temperatures results in bimodal growth with randomly distributed particles on the substrate terraces and chains of particles decorating the substrate steps. The particles nucleated on the terraces have an hexagonal or truncated triangular shape and are approximately 9.4 ± 2.2 nm wide and 3.5 ± 0.9 nm high. The particles decorating the substrate steps are elongated along the step edges, but otherwise display similarly oriented edges to those of the particles on the terraces, which reflects the common epitaxial relationship of both types of Ru particles with the substrate. The lateral size of these particles is of the order of 9.6 ± 2.2 nm, while the height is around 4.5 ± 0.4 nm. The overall morphology is very similar to that obtained for CVD grown Ru nanoparticles on HOPG after oxidation and reduction treatments at high temperatures [11]. In the case of deposition onto the sputtered surface, the morphology is characterised by an almost random distribution of hexagonal particles, though some decoration of the substrate steps is observed. The diameter of these particles is of the order of 4.2 ± 1.3 nm and the average height is around 1.5 ± 0.7 nm. As was found for deposition at room temperature, a higher particle density is obtained by deposition onto sputtered HOPG compared to unsputtered surfaces at comparable film thicknesses. For example, the particle density obtained from Fig. 12a is around $6.2 \times 10^3\ \mu m^{-2}$ for a 2 Å film deposited onto unsputtered HOPG, compared with a particle density of approximately $2.1 \times 10^4\ \mu m^{-2}$ in Fig. 12b for a film of comparable thickness deposited on the sputtered surface.

4. Discussion

Our STM investigation clearly demonstrates that very different nanoparticle morphologies can be obtained depending on the preparation method used. This has important implications for structure-sensitive catalytic reactions such as methanation and ammonia synthesis [5–7]. For example, Song et al. [11] have shown

for CVD grown Ru nanoparticles on HOPG that the particle shape has a significant impact on the desorption temperature of dissociatively adsorbed nitrogen. Their results have shown that large flat particles tend to exhibit a much lower desorption temperature (~ 500 K) than small round particles in the size range of 3.5–6.5 nm (~ 650 K), consistent with the lower desorption temperature of dissociated nitrogen from close-packed Ru(0001) compared to the more open Ru$(10\bar{1}0)$ and Ru$(11\bar{2}1)$ surfaces [43–45]. On the other hand, round nanoparticles in the size range of 2–3 nm are expected to have the optimal proportion of active edge or corner sites compared to total particle surface area, implying that these will be most efficient at dissociating N_2 [8–10].

The influence of the different morphologies described above on the catalytic activity of Ru/HOPG is beyond the scope of the present study, but is currently under investigation and will be discussed in a future publication. However, it is clear that the two deposition methods described above offer the possibility to prepare both round and flat nanoparticles in the size range of interest. Of the two methods, the gas-aggregation source in particular provides a well-controlled method of obtaining round particles in the size range of 2–15 nm with a narrow size distribution. In principle, this range can be extended to smaller sizes by using helium as a cooling gas in the aggregation zone.

One issue of particular importance from a catalyst perspective is whether or not the nanoparticles can be stabilised against sintering. For example, narrow size distributions of round particles in the size range of interest can be obtained by thermal evaporation onto sputtered HOPG. However, as demonstrated in Fig. 11, these particles are not stable against sintering when heated to 430 °C. In comparison, nanoparticles deposited from the gas-aggregation source were found to be stable against sintering at temperatures up to 500 °C when deposited onto sputtered HOPG. It should be noted that sputtering the surface may not be the best route to immobilise the nanoparticles, since it is possible that loose carbon generated by the sputtering process could poison nanoparticle activity by blocking active sites. Moreover, the degree of graphitization of the support has previously been shown to be important as catalyst activity is affected over time by methanation of the support (see Ref. [46] and references therein). Alternative routes to immobilising the nanoparticles require investigation, such as oxidising the graphite surface after sputtering to remove loose carbon prior to deposition and depositing particles from the gas-aggregation source with higher kinetic energies so that they are self-pinning. The latter method in particular has been demonstrated to be a very effective method of immobilising mass-selected nanoparticles on HOPG surfaces [13,16,17,20,22].

5. Conclusions

We have used STM to compare the morphologies of ruthenium nanoparticles deposited on HOPG using a gas-aggregation source versus thermal deposition. Our findings can be summarised as follows:

- The particles generated by the gas-aggregation source appear to be round in shape over the size range investigated. Particles larger than 8 nm display evidence of well-defined facets, while it was impossible to resolve facets on smaller particles due to tip convolution effects.
- With the exception of small nanoparticles supported on unsputtered HOPG, the nanoparticles were generally found to be stable against sintering at temperatures below 500 °C.
- The size and shape of the thermally deposited nanoparticles depended to a large extent on the condition of the graphite support. Deposition on unsputtered HOPG is characterised by bimodal growth with large flat particles formed on the substrate terraces and smaller diameter particles aligned along the substrate steps.
- Deposition on sputtered HOPG results in the formation of 2 nm round particles with a narrow size distribution. However, annealing these particles to 430 °C causes them to agglomerate into larger particles.
- Deposition on both unsputtered and sputtered HOPG at 660 °C results in broader distributions of larger particles. The particles are faceted and share a common orientation with respect to the substrate, indicating that an epitaxial relationship exists between the particles and the substrate.

Acknowledgements

This work was supported by the Danish National Research Foundation and the EU FWP7 Marie Curie Intra-European Fellowship ESRCN (PIEF-GA-2008-220055).

References

[1] F. Rosowski, O. Hinrichsen, M. Muhler, G. Ertl, Catal. Lett. 36 (1996) 229.
[2] R.A. Dalla'Betta, M. Shelef, J. Catal. 48 (1977) 111.
[3] H. Abrevaya, M.J. Cohn, W.M. Targos, H.J. Robota, Catal. Lett. 7 (1990) 183.
[4] P. Waszczuk, J. Solla-Gullón, H.-S. Kim, Y.Y. Tong, V. Montiel, A. Aldez, A. Wieckowski, J. Catal. 203 (2001) 1.
[5] S. Dahl, A. Logadottir, R.C. Egeberg, J.H. Larsen, I. Chorkendorff, E. Törnqvist, J.K. Nørskov, Phys. Rev. Lett. 83 (1999) 1814.
[6] T. Zubkov, G.A. Morgan, J.T. Yates, Chem. Phys. Lett. 362 (2002) 181.
[7] T. Zubkov, G.A. Morgan, J.T. Yates, O. Kühlert, M. Lisowski, R. Schillinger, D. Fick, H.J. Jänsch, Surf. Sci. 526 (2003) 57.
[8] C.H. Jacobsen, S. Dahl, P.L. Hansen, E. Törnqvist, L. Jensen, H. Topsøe, D.V. Prip, P.B. Møenshaug, I. Chorkendorff, J. Mol. Catal. A: Chem. 163 (2000) 19.
[9] K. Honkala, A. Hellman, I.N. Remediakis, A. Logadottir, A. Carlsson, S. Dahl, C.H. Christensen, J.K. Nørskov, Science 307 (2005) 555.
[10] J. Gavnholt, J. Schiøtz, Phys. Rev. B 77 (2008) 035404.
[11] Z. Song, T. Cai, J.C. Hanson, J.A. Rodriguez, J. Hrbek, J. Am. Chem. Soc. 126 (2004) 8576.
[12] L. Bardotti, P. Jensen, A. Hoareau, M. Treilleux, B. Cabaud, Phys. Rev. Lett. 74 (1995) 4694.
[13] S.J. Carroll, P. Weibel, B. von Issendorff, L. Kuipers, R.E. Palmer, J. Phys.: Condens. Matter 8 (1996) L617.
[14] A. Bettac, L. Köller, V. Rank, K.H. Meiwes-Broer, Surf. Sci. 402–404 (1998) 475.
[15] K.W. Edmonds, C. Binns, S.H. Baker, S.C. Thornton, C. Norris, J.B. Goedkoop, M. Finazzi, N.B. Brookes, Phys. Rev. B 60 (1999) 472.
[16] R. Neuendorf, R.E. Palmer, R. Smith, Appl. Phys. Lett. 77 (2000) 3003.
[17] D.J. Kenny, S.C. Weller, M. Couillard, R.E. Palmer, C.F. Sanz-Navarro, R. Smith, Eur. Phys. J. D 16 (2001) 115.
[18] S.H. Baker, C. Binns, K.W. Edmonds, M.J. Maher, S.C. Thornton, S. Louch, S.S. Dhesi, J. Magn. Magn. Mater. 247 (2002) 19.
[19] L. Bardotti, B. Prével, P. Jensen, M. Treilleux, P. Mélinon, A. Perez, J. Gierak, G. Faini, D. Mailly, Appl. Surf. Sci. 191 (2002) 205.
[20] C. Xirouchaki, R.E. Palmer, Vacuum 66 (2002) 167.
[21] M. Couillard, S. Pratontep, R.E. Palmer, Appl. Phys. Lett. 82 (2003) 2595.
[22] S. Pratontep, P. Preece, C. Xirouchaki, R.E. Palmer, C.F. Sanz-Navarro, S.D. Kenny, R. Smith, Phys. Rev. Lett. 90 (2003) 055503.
[23] N. Vandamme, E. Janssens, F. Vanhoutte, P. Lievens, C. Van Haesendonck, J. Phys.: Condens. Matter 15 (2003) S2983.
[24] C. Xirouchaki, R.E. Palmer, Philos. Trans. R. Soc. London A 362 (2004) 117.
[25] M. Di Vece, S. Palomba, R.E. Palmer, Phys. Rev. B 72 (2005) 073407.
[26] F. Claeyssens, S. Pratontep, C. Xirouchaki, R.E. Palmer, Nanotechnology 17 (2006) 805.
[27] S. Gibilisco, M. Di Vece, S. Palomba, G. Faraci, R.E. Palmer, J. Chem. Phys. 125 (2006) 084704.
[28] H. Haberland, Z. Insepov, M. Moseler, Phys. Rev. B 51 (1995) 11061.
[29] K. Nordlund, T.T. Järvi, K. Meinander, J. Samela, Appl. Phys. A 91 (2008) 561.
[30] H. Hövel, Th. Becker, A. Bettac, B. Reihl, M. Tschudy, E.J. Williams, J. Appl. Phys. 81 (1997) 154.
[31] I. Lopez-Salido, D.C. Lim, Y.D. Kim, Surf. Sci. 588 (2005) 6.
[32] I.N. Kholmanov, L. Gavioli, M. Fanetti, M. Casella, C. Cepek, C. Mattevi, M. Sancrotti, Surf. Sci. 601 (2007) 188.
[33] R. Dietsche, D.C. Lim, M. Bubek, I. Lopez-Salido, G. Ganteför, Y.D. Kim, Appl. Phys. A 90 (2008) 395.
[34] H. Haberland, M. Karrais, M. Mall, Y. Thurner, J. Vac. Sci. Technol. A 10 (1992) 3266.
[35] <http://www.simion.com>.
[36] S.H. Baker, S.C. Thornton, A.M. Keen, T.I. Preston, C. Norris, K.W. Edmonds, C. Binns, Rev. Sci. Instrum. 68 (1997) 1853.
[37] C. Binns, Surf. Sci. Rep. 44 (2001) 1.
[38] D. Klyachko, D.M. Chen, Surf. Sci. 446 (2000) 98.

[39] Y. Nakamura, Y. Mera, K. Maeda, Rev. Sci. Instrum. 70 (1999) 3373.
[40] H. Hövel, I. Barke, Prog. Surf. Sci. 81 (2006) 53.
[41] A.R. Howells, L. Hung, G.S. Chottiner, D.A. Scherson, Solid State Ionics 150 (2002) 53.
[42] H. Bethge, D. Heuer, Ch. Jensen, K. Reshöft, U. Köhler, Surf. Sci. 331–333 (1995) 878.
[43] H. Dietrich, P. Geng, K. Jacobi, G. Ertl, J. Chem. Phys. 104 (1996) 375.
[44] H. Dietrich, K. Jacobi, G. Ertl, J. Chem. Phys. 106 (1997) 9313.
[45] L. Diekhöner, H. Mortensen, A. Baurichter, A.C. Luntz, J. Vac. Sci. Technol. A 18 (2000) 1509.
[46] Z. Li, C. Liang, Z. Feng, P. Ying, D. Wang, C. Li, J. Mol. Catal. A: Chem. 211 (2004) 103.

J Nanopart Res (2010) 12:1249–1262
DOI 10.1007/s11051-009-9830-8

RESEARCH PAPER

The morphology of mass selected ruthenium nanoparticles from a magnetron-sputter gas-aggregation source

R. M. Nielsen · S. Murphy · C. Strebel · M. Johansson · I. Chorkendorff · J. H. Nielsen

Received: 9 July 2009 / Accepted: 8 December 2009 / Published online: 27 December 2009

Abstract We have investigated the morphology of mass selected ruthenium nanoparticles produced with a magnetron-sputter gas-aggregation source. The nanoparticles are mass selected using a quadrupole mass filter, resulting in narrow size distributions and average diameters between 2 and 15 nm. The particles are imaged in situ by scanning electron microscopy and scanning tunneling microscopy (STM) as well as ex-situ using transmission electron microscopy (TEM). For each distribution of mass selected nanoparticles, the height determined by STM and the width determined by TEM are seen to be similar throughout the mass range investigated. The particles are found to have a well-defined morphology for diameters below approximately 6 nm. Larger nanoparticles are less well-defined having rough surfaces, unlike the equilibrium morphology determined from the Wulff construction. The morphology of the particles is, in general, believed to be determined by the conditions inside the gas-aggregation source and the morphology is retained as the particles are soft-landed on the substrate.

R. M. Nielsen · S. Murphy · C. Strebel · M. Johansson · I. Chorkendorff · J. H. Nielsen (✉)
Center for Individual Nanoparticle Functionality, Department of Physics, Nano-DTU, Technical University of Denmark, 2800 Kgs. Lyngby, Denmark
e-mail: jane@fysik.dtu.dk
URL: www.cinf.dtu.dk

Keywords HOPG · Magnetron-sputter gas-aggregation source · Mass selected nanoparticles · Nanoparticle morphology · Scanning tunneling microscopy · Synthesis and characterization · Transmission electron microscopy · Ruthenium

Introduction

Heterogeneous catalysts typically comprise the catalyst material distributed as nanoparticles on a high surface area support. This is a matter of twin considerations; first, the catalyst material is often costly and so the most efficient loading is sought and second, the nanosized particles often display superior catalytic behavior compared to the bulk material.

A range of intriguing examples exist where the catalytic properties depend strongly on morphological parameters such as the shape and the size of the nanoparticles. This includes, e.g., studies of gold nanoparticles for CO oxidation by O_2 (Haruta et al. 1989; Sanchez et al. 1999; Valden et al. 1998; Zanella et al. 2004; Janssens et al. 2007; Kung et al. 2007) and CO electrooxidation on gold clusters (Geng and LuG 2007) where strong size dependencies are observed. Several other transition metal nanoparticle systems have been investigated, focusing, e.g., on the size dependence of CO related surface reactivity on Rh (Frank and Bäumer 2000),

Pd (Wörz et al. 2003), Pt (Croy et al. 2007), Ni (Andersson et al. 2008), and Co nanoparticles (den Breejen et al. 2009). Also, the effect of shape of the nanoparticles has been under investigation, e.g., the methanol activity of supported Cu nanoparticles (Grunwaldt et al. 2000, Hansen et al. 2002) or the electro-oxidation activity from Pt nanocrystals (Tian et al. 2007).

In general, the catalytic activity of a surface is determined by the electronic structure of the surface atoms, and this is influenced by the local atomic structure. Changes in the number of neighbors or in the interatomic distance will, e.g., give rise to a change in the electronic structure. This is described in the d-band model (Hammer and Norskov 2000). The geometry of the surface site may also influence the catalytic activity by affecting the ability of the site to accommodate molecules or molecular fragments in an energetically favorable way (Dahl et al. 1999). As the size of a catalytic particle is changed, the availability of surface geometries changes, and the reaction rate of structure sensitive catalytic reactions can hence be strongly dependent on the size of the particles, both in the non-scalable ($<\sim 2$ nm) and scalable ($>\sim 2$ nm) regimes (Jacobsen et al. 2000; Silvestre-Albero et al. 2006; Landman et al. 2007; Andersson et al. 2008; Nørskov et al. 2008). For the purpose of studying these size effects using surface science techniques, a good representation is obtained by preparing an ensemble of monodisperse nanoparticles supported on a flat, crystallographically oriented, and well-defined substrate. Such model systems can give new insight into how the catalytic activity is influenced by the particle size and shape as well as by the support material.

Our goal is to establish a correlation between structure and activity in nanoparticulate catalysts. In this article, we study the morphology of a model catalyst comprising an ensemble of monodisperse ruthenium nanoparticles deposited onto a highly ordered pyrolytic graphite (HOPG) surface under ultrahigh vacuum (UHV) conditions. Ruthenium is a versatile catalyst with applications in the synthesis of methane through the methanation process (King 1978) as well as in the steam-reforming process (Jones et al. 2008). It has been found that the dissociation of CO, a key step in the methanation reaction, only occurs on the step sites of the ruthenium surface (Shincho et al. 1985; Zubkov et al. 2002; Zubkov et al. 2003). Ruthenium has also been put forward as an alternative to iron as a catalyst for ammonia synthesis, particularly at high ammonia concentrations (see Bielawa et al. 2001; Honkala et al. 2005 and references therein). The interaction of N_2 with ruthenium, which is believed to be the rate-limiting step in ammonia synthesis has therefore been a subject of fundamental interest. Nanoparticles of ruthenium on HOPG has, e.g., been investigated for the N_2 adsorption and desorption behavior (Song et al. 2004), and the N–N bond scission has been found to exclusively occur at step sites (the so-called B5 sites) on the Ru(001) surface (Dahl et al. 1999).

There are many relevant substrates for nanoparticle studies but in this particular study we have chosen HOPG because it is rather inert and electrically conductive. If the HOPG is freshly cleaved, it will expose large atomically flat terraces where the interaction with the nanoparticles is very weak, enabling studies of the properties of almost undisturbed nanoparticles (Yim et al. 2007; Zhang et al. 2007, 2008; Kadossov et al. 2008). It is also possible to intentionally create nucleation sites by ion bombardement of the HOPG (Kibsgaard et al. 2006; Rohmer et al. 2007; Yao et al. 2008) and a subsequent oxidation procedure can create nanopits in the surface (Song et al. 2004; Hinnemann et al. 2005) mimicking an activated carbon support in industrial catalysis (Rodriguez-reinoso 1998). In this study, we create nucleation sites on the surface by Ar^+ bombardement before nanoparticle deposition, and subsequently take advantage of the flatness of the HOPG to perform STM investigations.

The nanoparticles used in this study are produced using a magnetron-sputter gas-aggregation source. This type of source has been used for a wide range of applications (Granqvist and Buhrman 1976; Haberland et al. 1992; Binns 2001; Klipp et al. 2001; Pratontep et al. 2005), where primarily small clusters of less than a few hundred atoms have been investigated, but larger nanoparticles can also be produced with this type of source. The size range of the nanoparticles studied here is in the order of 2–15 nm, i.e., containing approximately 300–130,000 atoms, sizes well-suited for catalytic studies.

The morphology of the ruthenium nanoparticles has been investigated using a combination of scanning electron microscopy (SEM), scanning tunneling microscopy (STM), and transmission electron microscopy

(TEM). While the STM is prone to overestimating the nanoparticle diameter due to tip-convolution effects, it can provide an extremely accurate and reliable measure of the particle height (Hovel and Barke 2006). This complements data on the lateral dimensions of the particle obtained by TEM. By combining SEM, STM, and TEM data of the same samples, a detailed insight into the morphology of the nanoparticles can be obtained.

Experimental

Experiments were performed in a multichamber UHV system (Omicron Multiscan Lab) with a base pressure in the low 10^{-11} mbar region. The system consists of three separate chambers; an analysis chamber, a preparation chamber, and the nanoparticle source.

In the analysis chamber, the samples are analyzed using a combination of STM and SEM. The STM is an Omicron variable temperature microscope able to operate in a temperature interval from 70 to 650 K. The images reported here are obtained in constant current mode using a current of 100–700 pA and applying a gap voltage of 0.1–0.4 V. It was found that the measured particle height does not change substantially when changing the tunnel parameters in this range. In order to keep the noise level low and to avoid tip crashes due to slow feedback response, the scan speed was set to 0.5–1 Hz resulting in a scan time of approximately 10–20 min per image. The STM was calibrated using the well known atomic arrangement of the (7 × 7) reconstruction of Si(111) (Dujardin et al. 1996). The images were analyzed using the scanning probe image analysis software SPIP where the grain analysis tool was used to determine the mean height of the nanoparticles. The SEM is based around a Gemini column (Zeiss Supra 55VP) and operates at 1–20 kV with a working distance of 8 mm, resulting in a lateral resolution of approximately 3 nm. The SEM/STM information is supplemented with measurements using a Technai T20 200 kV TEM. The surface composition is studied with Auger electron spectroscopy (AES) using the electrons from the SEM and an Omicron NanoSAM hemispherical energy analyzer. The analyzer is also used to perform ion scattering spectroscopy (ISS) using an Omicron ISE 100 fine focus ion gun to produce He^+ ions.

The second chamber is used for sample preparation, where the sample can be Ar^+ sputtered using an Omicron ISE 10 ion gun and heated using a pyrolytic boron nitride (PBN) heater mounted on the backside of the sample. After the sample has been prepared, the nanoparticles from the gas-aggregation source can be deposited onto the sample while it remains in the preparation chamber.

The third main component of the system is the nanoparticle source from Mantis Deposition Ltd. The setup is illustrated in Fig. 1. The metal nanoparticles are formed by gas-phase condensation from a flux of ruthenium atoms, which are sputtered from a 99.99% purity ruthenium target. The flux of ruthenium atoms is provided by a magnetron sputtering head (c), located inside a liquid nitrogen cooled enclosure (d). Argon gas is used to provide the plasma at the magnetron sputtering head. It also facilitates the condensation of Ru clusters and their subsequent growth into nanoparticles. Helium gas may also be introduced into the aggregation zone to improve thermalization to obtain smaller particle sizes. The initial step in cluster formation has been suggested by Haberland et al. to involve a three body collision between two hot metal atoms and a cold argon atom (see Haberland et al. 1992 for further details). As the small clusters travel through the aggregation zone, they continue to grow by the sticking of additional Ru atoms to the cluster or by cluster–cluster collisions. By controlling key parameters, such as the sputtering power, aggregation distance, and the argon and helium flows, it is possible to control the residence time of the particles inside the aggregation zone and thereby tune the size of the nanoparticles exiting the nanoparticle source. For instance, an increased gas flow will decrease the residence time in the aggregation zone leading to smaller particles. After the particles are formed, they pass through two skimmers (e), reducing the local pressure from approximately 1–10^{-3} mbar (at an argon flow of 100 mL/min). The pressure difference gives rise to a supersonic expansion and further cooling of the nanoparticle beam. The nanoparticles enter the quadrupole mass filter (f), where the charged nanoparticles can be filtered according to their mass-to-charge ratio. According to Haberland et al. approximately 30–80% of nanoparticles exiting the aggregation zone carry a charge (Haberland et al. 1992). The mass selected particle production can be monitored by a quartz crystal

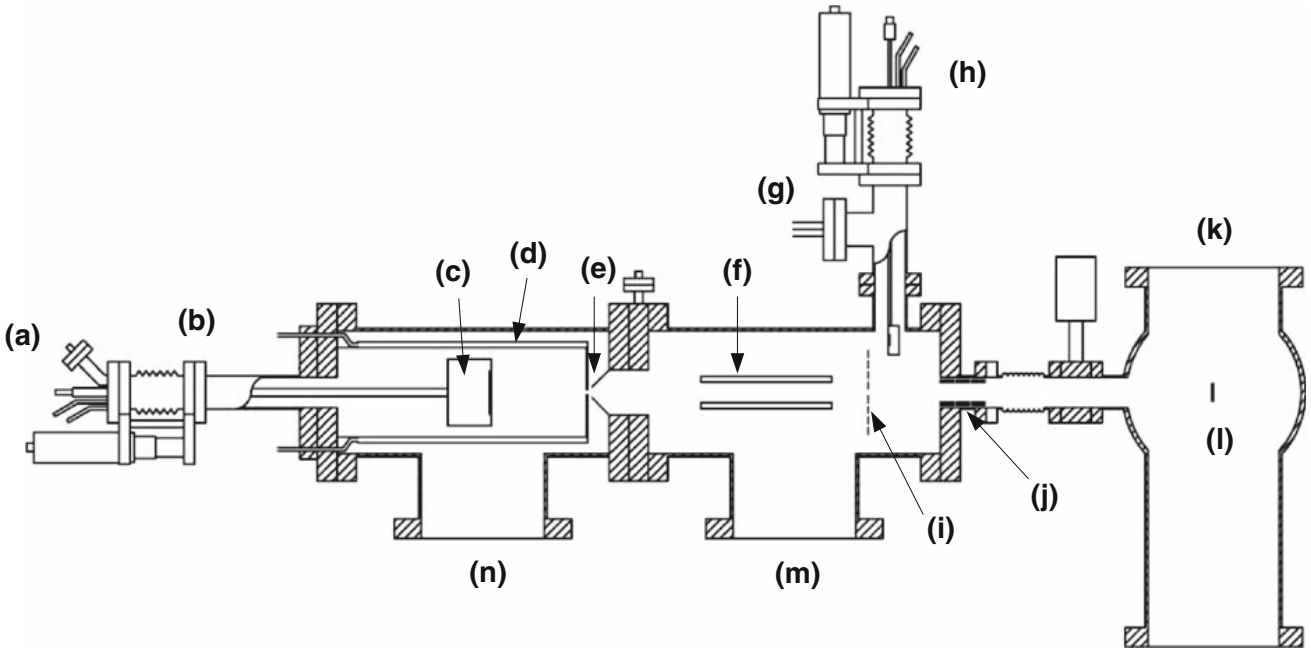

Fig. 1 Schematic of the cluster source. The gas inlet and power feedthrough to the magnetron sputtering head are seen to the left (**a**). The gas-aggregation distance can be altered using the linear translator (**b**). The magnetron sputtering head (**c**) is surrounded by a liquid nitrogen cooled enclosure (**d**). The nanoparticles pass through a 3 mm skimmer and a 6 mm conical aperture (**e**) and are then passed into the quadrupole mass filter (QMF) (**f**). The pressure is monitored using an ion-gauge (**g**). The nanoparticle production can be measured using a QCM (**h**) or a biased current plate (**i**). The nanoparticles are focused using an einzel lens (**j**) before entering the preparation chamber (**k**) and deposited onto the sample (**l**). The gas-aggregation source is pumped using 230 l/s (**m**) and 450 l/s (**n**) turbo molecular pumps

microbalance (QCM) (h) or on a biased current plate (i). A set of einzel lenses (j) are used to focus the nanoparticles onto the sample (l). The particles are soft-landed ($E_{kin} \leq 0.1$ eV/atom) onto the support surface (Moseler et al. 2002) by applying +36 V to the sample. By doing so, the nanoparticles are not deformed upon impact with the substrate which is known to occur at much larger biases (Carroll et al. 1998). A fraction of the produced nanoparticles are not charged and cannot be filtered by the quadrupole. This fraction will, however, decrease significantly going through the mass filter and the einzel lens due to focusing of the charged particles. Blind experiments show that the fraction (the relative coverage) of the neutrals when the sample is positioned in direct line-of-sight of the source is less than 1%. At times, very large particles (> 50 nm) are observed, which are believed to be neutral nanoparticles that have reached the sample.

In order to avoid contamination of the nanoparticles, the source must be baked at 150 °C under vacuum for approximately 24 h prior to use, leading to a base pressure of approximately 5×10^{-10} Torr. The helium and argon gases are of N60 purity and are further purified by passing them over an iron catalyst, which adsorbs most of the remaining contaminants, such as CO, CO_2, and H_2O. The iron catalysts are activated by baking them in a stream of hydrogen at 3 bar and 450 °C for several days.

The quadrupole rods are paired, with each pair sitting diagonally opposite from one another. In order to select masses, a DC voltage (V) and an AC voltage (U) with frequency denoted *f* are applied to the four quadrupole rods, with each pair having an opposite polarization. The mass filtered by the quadrupole is determined by *f*, *U*, and the spacing of the rods, while the resolution is determined by the ratio between U and V. The optimum resolution is achieved for a U/V ratio of approximately 0.1678 (Paul et al. 1958). However, at this high resolution only very small particle currents, less than 1 pA, are obtained at the sample. Therefore, as a compromise a theoretical resolution of approximately 6% in the particle diameter (U/V = 0.12) is chosen, where currents of 10–100 pA are achieved. The quadrupole selects a given mass according to the settings on the four rods

of the mass filter. From this mass, we calculate the corresponding diameter of a spherical nanoparticle, assuming it has the density of the bulk material. This diameter, denoted D_{MF} where MF stands for "mass filter" is defined as:

$$D_{MF} = \sqrt[3]{\frac{6 \cdot m}{\pi \cdot \rho}} \quad (1)$$

where m is the mass of the selected nanoparticle and ρ is the density of the bulk material.

The ruthenium nanoparticles were deposited onto HOPG for STM studies in UHV and onto lacey carbon grids for TEM analysis. The HOPG substrates used (SPI-1, 7 mm × 7 mm × 0.5 mm) were mounted in a sample holder incorporating a PBN heater to provide radiative heating to the back side of the substrate. A 0.25-mm W–5 at% Re/W–26 at% Re thermocouple was pressed against the front side of the HOPG substrate and the sample temperature could be regulated through a PID controller (Eurotherm 2408). The HOPG was cleaved in air before loading into the UHV system, where it was outgassed for several hours at ~650 °C. The surface was etched with 500 eV Ar^+ ions for 15 min with a current of approximately 0.1 μA/cm^2, followed by annealing at ~650 °C for 15 min to degas the surface of implanted argon. The sputtering step was performed to create a highly defected surface where the pre-formed particles could stick to prevent sintering at elevated temperatures (Claeyssens et al. 2006).

Results

Production of ruthenium nanoparticles from the magnetron aggregation source

The aggregation source was optimized to produce ruthenium particles with D_{MF} values of 2–10 nm. A principal factor in determining the particle size was found to be the flow of argon through the aggregation zone. In Fig. 2a, spectra of the particle production for different Ar flows are measured with the sputtering power held constant at 37 W. The spectra are obtained by varying the frequency of the AC voltage applied to the quadrupole rods, while keeping the amplitudes of both the AC and DC voltages constant. As shown in Fig. 2a, it is possible to create nanoparticles in the size range of 4–10 nm, solely by controlling the Ar flow through the source. As expected, the particle size increases as the flow is decreased. When very large particles are produced, the particle current is seen to drop significantly. However, if the current is integrated over the mass range, the ruthenium output is in fact almost constant.

Smaller nanoparticles can be produced by introducing helium into the aggregation zone. This is seen in Fig. 2b where the source has been optimized for small nanoparticles. Here, the aggregation distance has been decreased by 37 mm by moving the magnetron forward into the aggregation zone while keeping all other parameters unaltered. With only the Ar flow present, it is seen that almost no nanoparticles are formed under these conditions. As the helium flow is introduced, the production of nanoparticles is seen to increase, and increasing the helium flow results in a further decrease in the size of the nanoparticles. It is clearly seen in Fig. 2b that certain sizes are favored over others. Particles with D_{MF} values of 1.75, 2.5, and 3.0 nm have a higher probability of formation than other sizes. The origin of these preferred sizes is not clear at this stage.

The position and shape of the spectra seen in Fig. 2 are reproducible, even after air exposure, followed by pump down and bakeout. Without the bakeout, the nanoparticle production is unstable and changes with time. The bakeout is thus an essential part of creating ruthenium nanoparticles reproducibly from the gas-aggregation source.

Surface analysis of ruthenium nanoparticles

The purity of the nanoparticles was checked by AES. A measurement of a HOPG sample completely covered by Ru nanoparticles with a $D_{MF} = 8$ nm is shown in Fig. 3a. The characteristic ruthenium lines at 205, 235, and 277 eV, are clearly observed. The carbon line at 275 eV overlaps with ruthenium and it is thus very difficult to distinguish from ruthenium. Furthermore, it is unfortunately not possible to distinguish whether or not part of the carbon signal could originate from carbon situated on the particles or if it only originates from the substrate. No other elements could be detected by AES.

The surface cleanliness was also analyzed using ISS. An example of an ISS spectrum of particles with $D_{MF} = 7$ nm is presented in Fig. 3b. The dominant

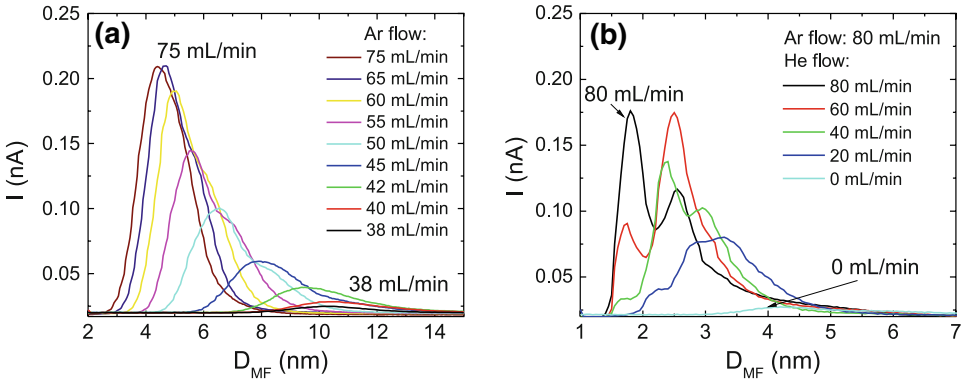

Fig. 2 Particle production (ion current) as a function of D_{MF}, derived from the mass filter settings. **a** The particle production for a range of argon flows without the presence of helium. **b** Smaller particles can be produced by introducing helium

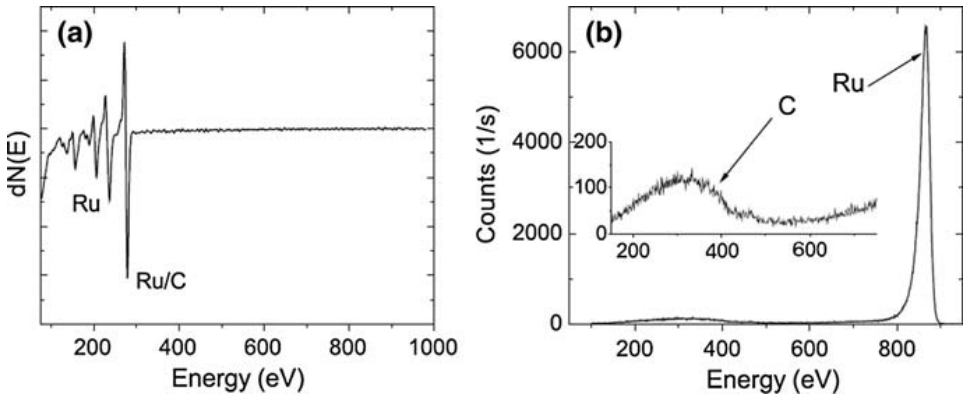

Fig. 3 Surface sensitive spectroscopy of ruthenium nanoparticles on HOPG. **a** an AES spectrum of a complete layer of ruthenium nanoparticles deposited onto HOPG is shown. **b** an ISS spectrum of ruthenium nanoparticles deposited on HOPG is shown with the Ru peak indicated. In the inset of **b**, the low energy regime is enlarged which reveals the signal from carbon. No contamination could be detected with AES or ISS

peak at 865 eV is from ruthenium. An enlargement of the low energy part of the spectra is shown in the inset, where the broad feature at 250–350 eV is believed to originate from the carbon substrate. Carbon has a very high neutralization probability, and it is very difficult to detect in ISS (Luna et al. 2008). No other elements could be detected by ISS.

Model of ruthenium nanoparticles

The expected morphology of an equilibrated hexagonal close packed ruthenium nanoparticle is the truncated hexagonal bipyramid, found for instance by Gavnholt and Schiøtz (2008). In Fig. 4, a Wulff construction of a nanoparticle consisting of 83,478 atoms is displayed. The morphology of the particle is determined from the surface energies of the various facets (Gavnholt 2009). For ruthenium, the (001), (100), and (011) facets have the lowest energies and thus dominate the surface area of the nanoparticle.

By observing the same particle from different angles, see Fig. 4, the two-dimensional projection of the particle will vary slightly. The projection of the nanoparticle in Fig. 4a is clearly hexagonal, whereas the projection appears octagonal in Fig. 4b and almost spherical in Fig. 4c. When the particles are imaged by SEM and TEM, it is the two-dimensional projection that is seen and since the particle appears slightly different depending on its orientation, two-dimensional projections of identical particles will appear differently. Consequently, the projection of the particle seen in Fig. 4 can be interpreted to have diameters in the range of 11.9–12.5 nm depending on which angle it is observed from. Furthermore, the number of atoms in the particle seen in Fig. 4 is optimized to achieve a well-terminated Wulff construction. If atoms are added to the particle or the particle has a morphology slightly different from the equilibrium state, the two-dimensional projections will become even more diverse.

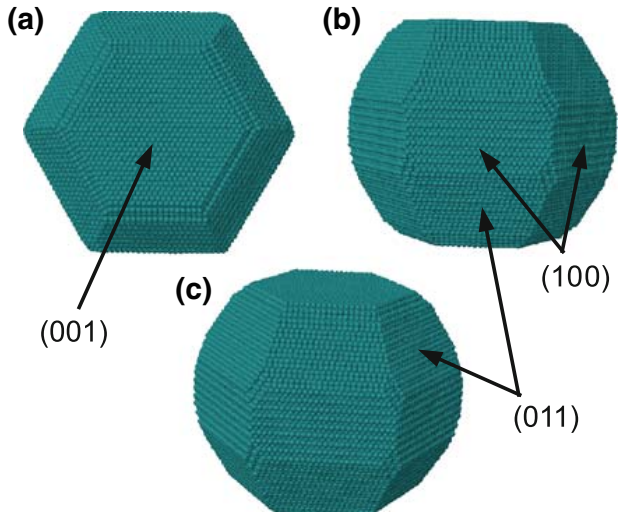

Fig. 4 Different views of a Wulff construction of a particle consisting of 83,478 atoms corresponding to $D_{MF} = 12.9$ nm according to Eq. 1. The dominating surfaces are the (001), (100), and (011) facets since these facets have the lowest surface energies. Due to the different surface energies of the facets, the observed width (the diameter) of the particle will depend on which projection the particle exhibits in the TEM

The size of ruthenium nanoparticles

SEM

The nanoparticle ensembles were first imaged with SEM under UHV to obtain a global overview of the coverage and the spatial distribution of the particles on the surface. An example is shown in Fig. 5 which shows a SEM image of particles with $D_{MF} = 9$ nm that have been soft-landed onto sputtered HOPG at room temperature. The nanoparticles are distributed across the surface and there are no signs of sintering or step decoration. It can, therefore, be concluded that when the particles arrive on the surface they are immediately pinned by defects and do not diffuse around the surface. SEM analysis was performed on different samples with different particle sizes and showed that the nanoparticles were for the most part isolated from one another on the surface, thereby minimizing any effects that may arise from particle–particle interactions. A small fraction of the particles were, however, observed in close proximity to one another, which we attribute to the random deposition process. The mean diameter of the particles as measured by SEM is 15.9 ± 0.8 nm. The particles are thus very monodisperse, but they appear to be larger than the mass from the quadrupole mass filter would suggest. The SEM resolution of 3 nm may cause smearing out of the particles, leading to a shift up in the measured particle size.

STM

Using the STM, it is possible to obtain three dimensional information of the particle morphology. Examples of nanoparticles imaged with the STM are shown in Fig. 6 along with the corresponding height distributions. Fig. 6a shows an STM image of ruthenium nanoparticles with $D_{MF} = 2.3$ nm. The image shows no sign of sintering of the nanoparticles. The height of the particles (2.4 ± 0.5 nm) extracted from the height distribution shown to the right in Fig. 6a agrees well with the size (D_{MF}) extracted from Eq. 1. In Fig. 6b, a STM image of nanoparticles with $D_{MF} = 7$ nm is presented. The particles are seen to be monodisperse, with an average height of 9.9 ± 1.2 nm, which is somewhat higher than the corresponding D_{MF} value. In Fig. 7, the height measured by STM for a range of particle sizes is presented. The spread in the measured particle height is influenced by the root-mean-square roughness of the sputtered HOPG which has been found to be approximately 1 nm. The narrow spread seen for the nanoparticle heights are thus very satisfying. The height is seen to agree well with the

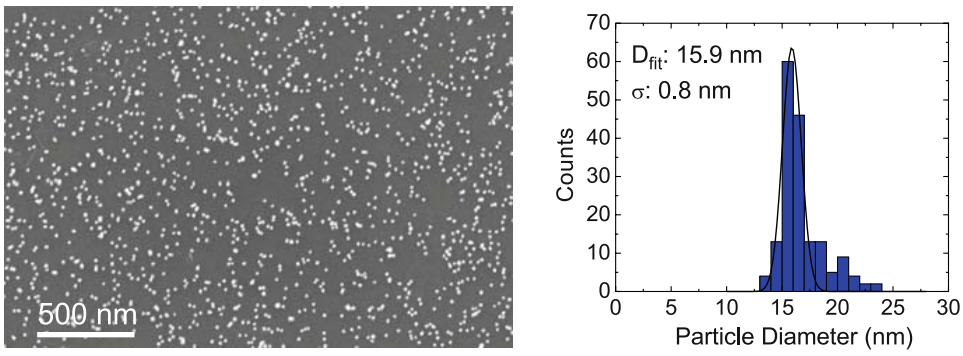

Fig. 5 SEM image (5 kV, 1 nA) of ruthenium nanoparticles with $D_{MF} = 9$ nm with the size distribution shown to the right

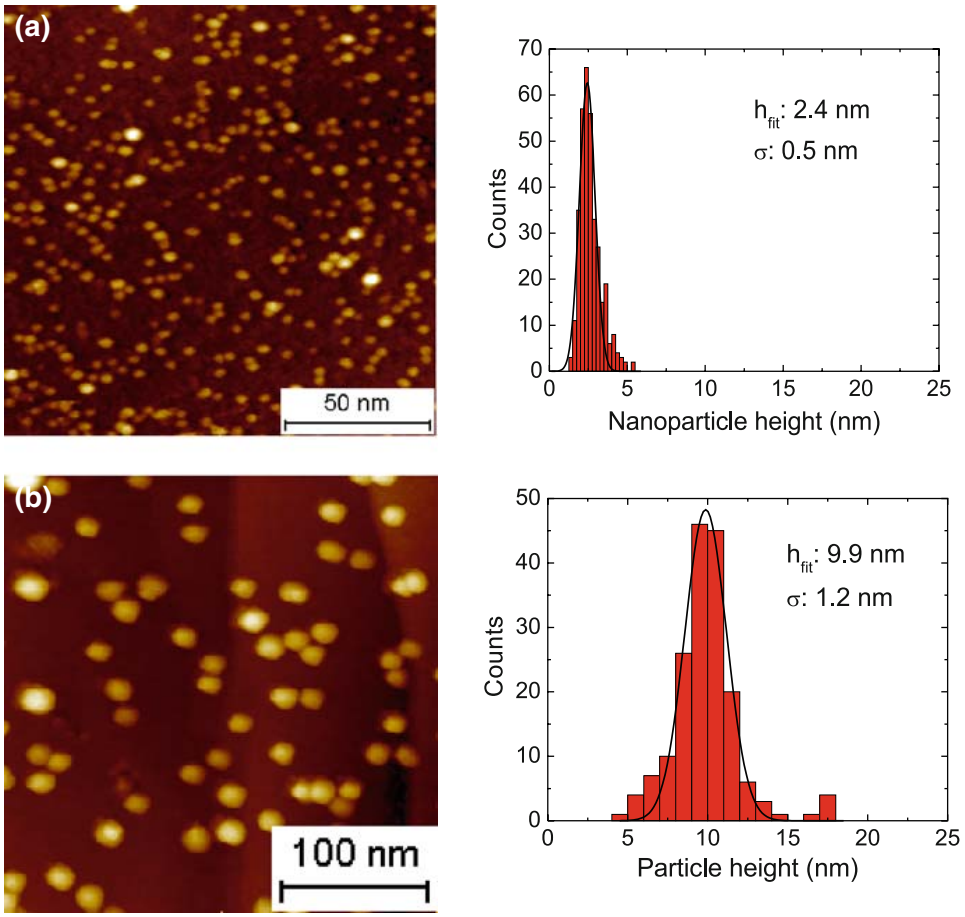

Fig. 6 STM images of ruthenium nanoparticles with $D_{MF} = 2.3$ nm (**a**) and 7 nm particles (**b**). To the right of each image, the height distribution is shown along with the average height and standard deviation

diameter of the spherical particle (D_{MF}) at the lower sizes. For sizes larger than 6 nm, however, the measured particle height is seen to deviate significantly from D_{MF}. For instance at $D_{MF} = 9$ nm, the measured particle height is 15.6 ± 1.5 nm.

As the particle is imaged with an STM tip, the final image of the particle will be a convolution of the tip and the particle and since the tip has a finite size, the nanoparticle diameter may appear larger than it actually is. This effect will be more apparent when the nanoparticle diameter becomes similar to or smaller than the radius of curvature of the STM tip which is expected to be not better than 5–10 nm (Nakamura et al. 1999; Guise et al. 2002). It is thus hard to obtain an accurate measurement of the particle diameter using STM, but very accurate measurements of the particle height can, however, be obtained with STM.

TEM

In order to investigate the diameter with a higher resolution than the in situ SEM and to avoid the tip-convolution effects in STM mentioned above, the particles are imaged with TEM. Here, the diameter of the two-dimensional projection is easily obtained, although no information about the height of the nanoparticles is provided. TEM images of two different nanoparticle sizes with $D_{MF} = 3$ and 7.5 nm are presented in Fig. 8a and b, respectively. In the size distributions in Fig. 8 (shown to the right of each image), it is seen that the nanoparticles with $D_{MF} = 3$ nm agree very well with the spherical model whereas the particles with $D_{MF} = 7.5$ nm are in fact ~10.8 nm. The spread in the diameter is 0.5 nm (± 18%) and 0.8 nm (± 7%) for the 3 and 7.5 nm particles, respectively. The expected spread in diameter is approximately 6% for the quadrupole settings used. However, as mentioned previously, the particle size distribution is expected to be slightly smeared out due to the different cross sections of the particles. The spread in particle size is thus very satisfying taking this into account.

The diameters obtained from TEM are plotted in Fig. 7 along with the STM data. It is seen, that the diameter obtained with TEM and the height measured

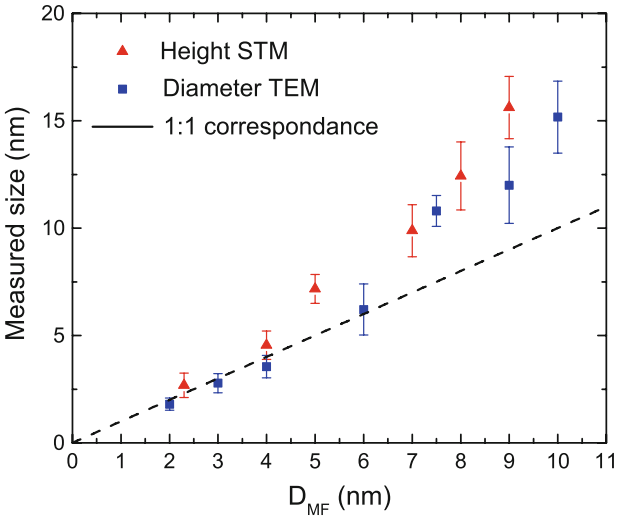

Fig. 7 The measured nanoparticle size versus D_{MF}. The *error bars* represent the standard deviation from the Gaussian fits. The *dashed line* displays the 1:1 correspondence between the measured height/diameter and D_{MF} and is shown to guide the eye. Nanoparticles are seen to have approximately the same height and diameter for all mass selections. At larger sizes, a deviation from D_{MF} is observed

by STM agree well with the size extracted from the spherical model for $D_{MF} < 6$ nm. For larger particles, the measured diameter is seen to deviate by several nanometers from the 1:1 correlation.

The height of the nanoparticles measured by STM is seen to follow the diameter obtained from TEM very well in the entire size range investigated. The particles are thus uniform in all directions with an aspect ratio of approximately one, even though the size deviates from the size extracted from the quadrupole settings. Since the deposited particles follow the same trend they are believed to retain their shape as they are deposited. This confirms that the particles are in fact soft-landed onto the surface and do not change shape significantly upon impact.

Particles with $D_{MF} = 10$ nm are seen to have an actual size of approximately 15 nm. This difference corresponds to a shift in particle mass from approximately 38,000 atoms to 130,000 atoms. The mass of the particles is, therefore, more than three times higher than expected. The size resolutions of these

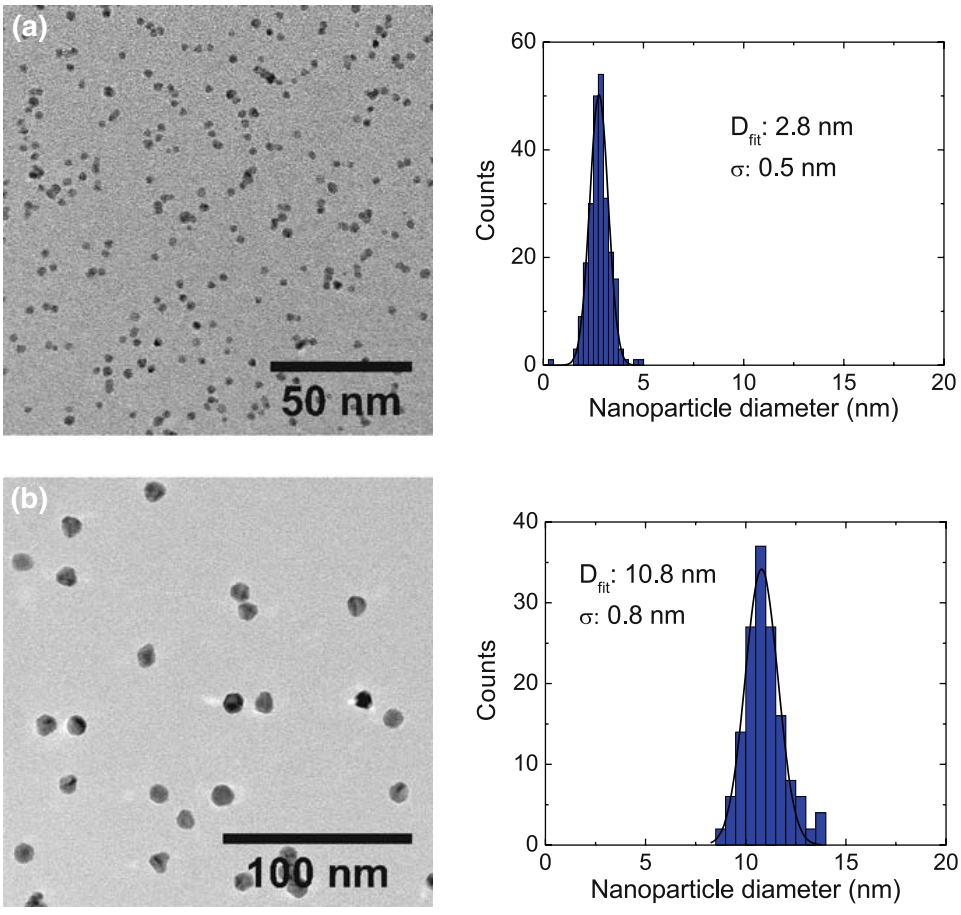

Fig. 8 TEM images of ruthenium nanoparticles with $D_{MF} = 3$ nm (**a**) and 7.5 nm (**b**). To the right of each image, the size distribution is shown along with the average diameter and the standard deviation. TEM diameters for several sizes are included in Fig. 7

particles are in all cases within the expected resolution and the actual selected masses are just shifted toward larger sizes. It is not obvious at this point why the mass filter is presumably not accurate on an absolute scale at the highest masses. However, the measurements presented in Fig. 7 can be used directly for calibration of the mass filter. Consequently, a reproducible particle production with a narrow size distribution is achievable for nanoparticles in the diameter range of 2–15 nm. This range is ideal for studies of the catalytic properties of Ru nanoparticles. For example, Gavnholt and Schiøtz have predicted an optimal Ru nanoparticle diameter of 3 nm for ammonia synthesis (Gavnholt and Schiøtz 2008).

Nanoparticle morphology

The TEM can be used to investigate the crystalline structure of the ruthenium nanoparticles as well as their morphology. Often, it is possible to detect lattice fringes from the particles deposited on the lacey carbon surface.

The particle measured by TEM shown in Fig. 9 has a diameter of approximately 15 nm and the lattice fringes are found to be approximately 0.24 nm apart. Comparing the nanoparticle to the Wulff constructed model, it is seen that the projection would agree with a nanoparticle with the (001) crystallographic plane comprising the top facet and the [100] direction pointing to the right as illustrated in Fig. 9. The (100) interplanar distance is 0.23 nm which agrees well with the lattice fringes seen in the figure.

Since ruthenium binds oxygen strongly (Madey et al. 1975) the surface of the particles may be oxidized during transfer to the TEM. The lattice fringes in Fig. 9, however, suggest that the bulk part of the particle remains metallic. This agrees well with the study by Jones et al. who found that ruthenium nanoparticles in the size range of 2–4 nm created ex-situ are not visible in the TEM due to the particles being bulk oxidized. They found that the particles had to be reduced in hydrogen to become visible in TEM (Jones et al. 2008). Consequently, our nanoparticles imaged by TEM are believed to have the same morphology and crystalline structure as the particles imaged with in situ STM.

In Fig. 10, various morphologies of 6 nm particles are shown. The particles are seen mostly to exhibit hexagonal symmetry. The specific shape is, however, not the same for all the particles. The shape varies from perfect hexagonal in Fig. 10a, through a

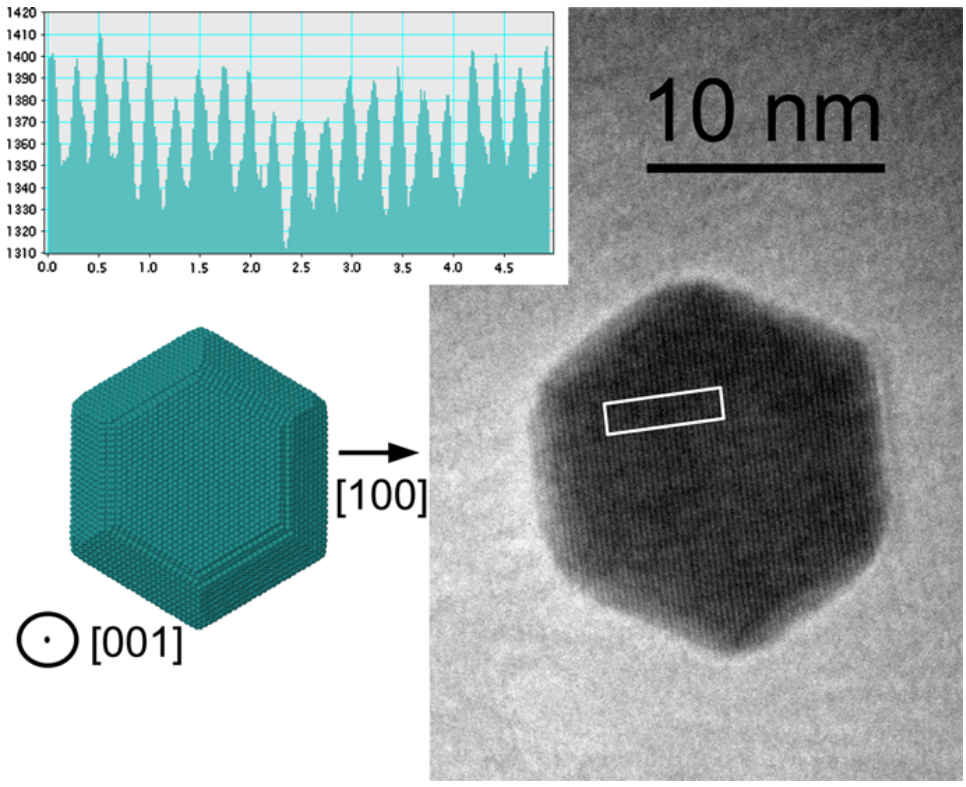

Fig. 9 TEM of a ruthenium nanoparticle with $D_{MF} = 10$ nm where lattice fringes are clearly seen. A line profile within the indicated area on the TEM image is shown in the inset, where the average periodicity is found to be 0.24 nm which fits well with the (100) interplane distance of 0.23 nm. Also shown is a possible model of a nanoparticle with the [001] direction pointing normal to the page

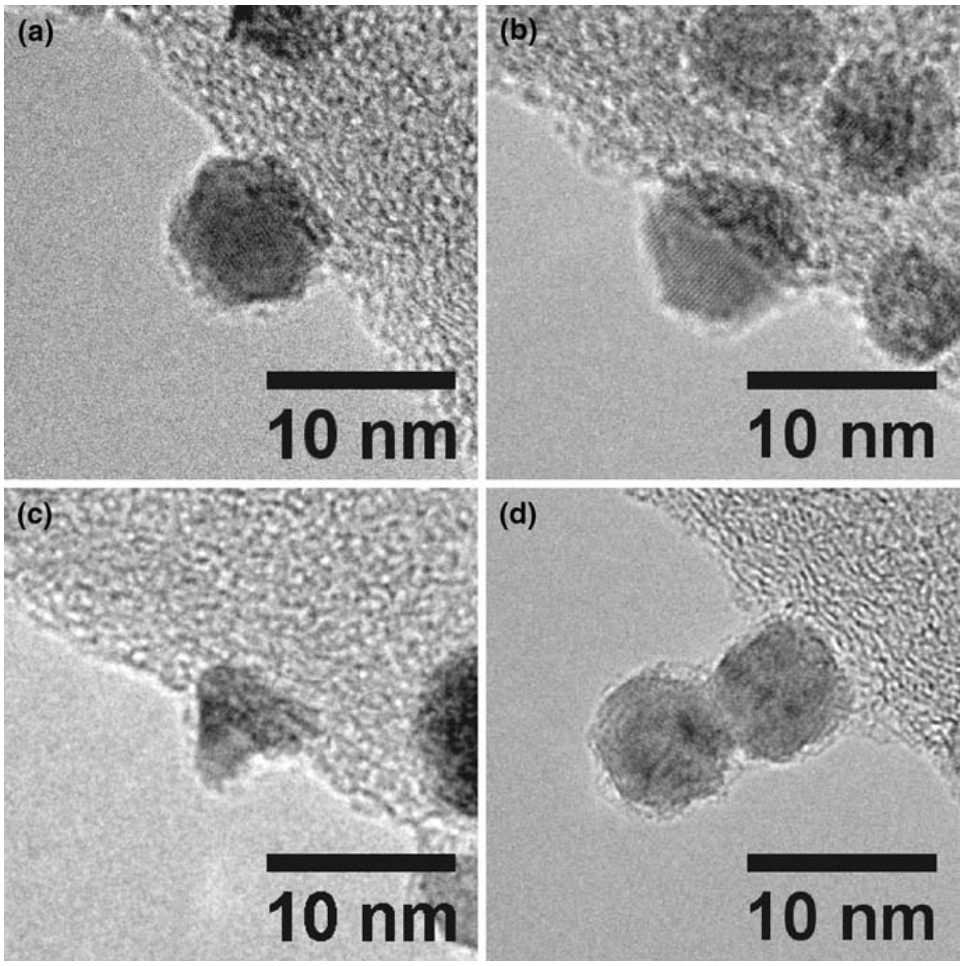

Fig. 10 Examples of high resolution TEM images of $D_{MF} = 6$ nm ruthenium nanoparticles (**a**–**d**). The morphology of the particles is mostly of hexagonal symmetry, with a range of different polymorphs

truncated hexagonal in Fig. 10b, to an almost triangular particle in Fig. 10c. The two particles on top of each other in Fig. 10d do not appear to have hexagonal symmetry. This, however, does not exclude the possibility that the particles are truncated hexagonal bipyramids. The two-dimensional projection of the particle seen in Fig. 4c is, e.g., similar to the shape seen in Fig. 10d. In general, nanoparticles smaller than approximately 6 nm appear to have well-defined surfaces. The particles are primarily found to have hexagonal symmetry with a range of different polymorphs present.

As the size is increased further to the maximum possible size of 15 nm, the diversity of morphologies becomes gradually larger. For the largest particle sizes, hexagonal particles are at times observed as observed in Fig. 9. However, the majority of the largest particles have rough surfaces (see Fig. 11a, b) and the morphology does not display the thermodynamic equilibrium shape seen in Fig. 4. Several examples of multiple particle morphologies are observed for particles above a measured diameter of approximately 10 nm. The particle displayed in Fig. 11c appears to consist of smaller particles which have agglomerated inside the nanoparticle source. The multiple particle appears to have the correct size compared to the predominant particle shape and it is thus believed that this type of particle is formed inside the cluster source rather than by sintering on the surface. These agglomerates of multiple smaller particles have been observed for all measured particle sizes above approximately 10 nm, but the fraction of these particles present on the surface is less than 1% of the total deposit and, therefore, does not contribute significantly to the size distribution.

Discussion

The height determined by STM and the diameter extracted from TEM agree well with D_{MF} up to a value of approximately 6 nm. For larger nanoparticles, the

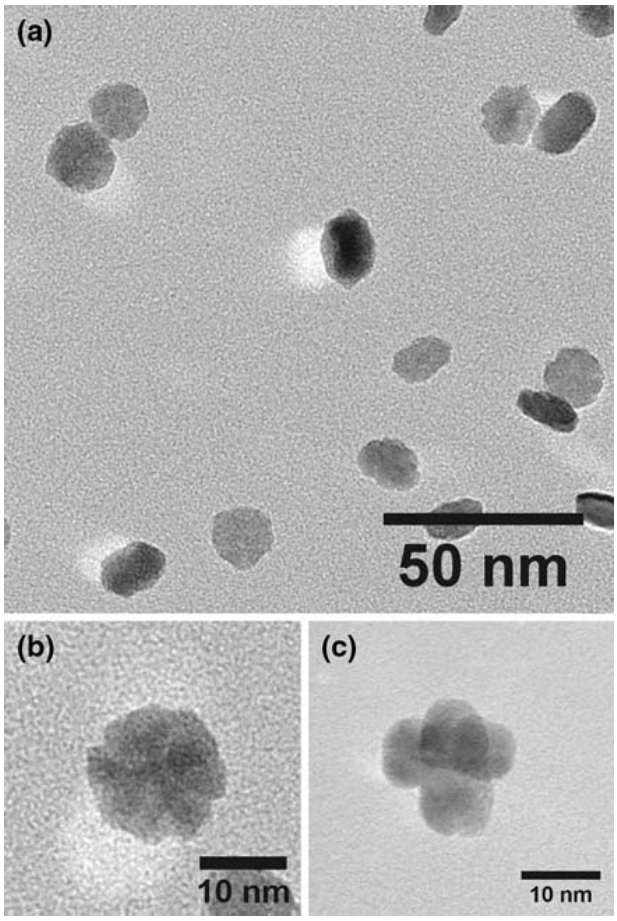

Fig. 11 Examples of different morphologies of $D_{MF} = 15$ nm ruthenium nanoparticles (**a**–**c**). The diversity of the nanoparticle morphology is obvious. Several particles are very far from equilibrium exhibiting sharp dents in the side of the particles (**b**). A particle which appears to consist of four smaller particles is also observed (**c**)

diameter and height are seen to be increasingly larger than D_{MF}. The reason for this is not clear at this stage. Small deviations could be explained by the geometry not being correctly incorporated in D_{MF}. Perhaps, these very high masses (a nanoparticle of 6–7 nm contains $\sim$10,000 atoms corresponding to roughly one million amu) may cause a non-ideal expansion from the aggregation zone into the mass filter. Additionally, there might also be a break-down of some of the basic assumptions for this type of mass filter, which is typically used for much smaller masses. Such matters are, however, beyond the scope of the present study. The larger particles might also exit the cluster source with multiple charges. If the largest particles were charged by three electrons instead of one, the size would in fact fit well. However, if multi-charged particles were present, different peaks should be visible in the particle production measurements. Since this is never seen, the number of multi-charged particles is believed to be insignificant. Despite the unexplained behavior at higher masses, our mass filter works well and can be used to produce nanoparticles with a specific diameter by calibrating according to the data presented in Fig. 7.

The high resolution TEM images of the nanoparticles in Figs. 10 and 11 showed that a number of different particle shapes are present on the surface. Particularly, the largest particles have very diverse particle morphologies. It is believed that the morphology of all these particles are determined in the gas-aggregation source. In this type of source, the particles are created by ruthenium atoms while transitioning from a hot plasma in the vicinity of the sputter target to a cold inert gas environment in the aggregation zone. This rapid quenching of the nanoparticles could of course lead to numerous non-equilibrium shapes being adopted. The smaller nanoparticles with a diameter less than 6 nm also have slightly different morphologies, but the diversity is not as evident as is observed for the larger particles. The shape of the smaller particles appears to be closer to the equilibrium shape.

The particles are intended for investigation of the structure dependency of catalytic reactions. Since the diversity of the particles become increasingly larger as the particle size is increased above 6 nm, it is difficult to correlate the catalytic properties of the large particles to the morphology. It might be possible to anneal the particles such that they reach the equilibrium shape. This annealing should ideally take place in the gas phase before deposition to prevent any sintering of the particles due to the annealing, but alternatively it could be carried out after deposition. While the larger particles are not ideal for correlation studies, they may actually be very active catalysts due to the rather rough surface and thus large quantity of low-coordinated sites. It would be very interesting to compare the catalytic activity of these non-equilibrium shaped model catalysts to commercially available Ru catalysts.

Conclusions

- By varying nanoparticle source parameters such as argon flow and aggregation distance, we are

able to produce size-selected ruthenium nanoparticles in the range from 2 to 15 nm.
- The formation of 1.75, 2.5, and 3.0 nm diameter nanoparticles is favored over other sizes at the lower end of the size range studied. For larger sizes, there is no evidence of sizes more favorable than others.
- The size distributions show a spread of approximately ±10% when deposited on either HOPG surfaces or lacey carbon films.
- Small nanoparticles are seen in the TEM to be crystalline, with various hexagonal symmetries.
- Larger nanoparticles are also crystalline as demonstrated by the fact that we observe lattice fringes consistent with metallic Ru in TEM images of these particles. However, they exhibit a large variety of shapes, including what are clearly agglomerates of smaller nanoparticles and particles with very rough surfaces. It is believed that the particle morphology is determined in the gas-aggregation source.
- The smaller particles are well-defined in shape and size and are, therefore, very suitable as model catalysts. The larger particles are on the other hand less well-defined and are thus not as ideal for correlation studies. They may, however, be quite active catalysts.

Acknowledgments This study was supported by the Danish National Research Foundation and the EU FWP7 Marie Curie Intra-European Fellowship ESRCN (PIEF-GA-2008- 220055). The use of facilities at the Center of Electron Nanoscopy (CEN) at DTU is acknowledged.

References

Andersson MP, Abild-Pedersen F, Remediakis IN, Bligaard T, Jones G, Engbæk J, Lytken O, Horch S, Nielsen JH, Sehested J, Rostrup-Nielsen JR, Nørskov JK, Chorkendorff I (2008) Structure sensitivity of the methanation reaction: H_2-induced CO dissociation on nickel surfaces. J Catal 255:6–19

Bielawa H, Hinrichsen O, Birkner A, Muhler M (2001) The ammonia-synthesis catalyst of the next generation: barium-promoted oxide-supported ruthenium. Angew Chem Int Ed 40:1061–1063

Binns C (2001) Nanoclusters deposited on surfaces. Surf Sci Rep 44:1–49

Carroll SJ, Hall SG, Palmer RE, Smith R (1998) Energetic impact of size-selected metal cluster ions on graphite. Phys Rev Lett 81:3715–3718

Claeyssens F, Pratontep S, Xirouchaki C, Palmer RE (2006) Immobilization of large size-selected silver clusters on graphite. Nanotechnology 17:805–807

Croy JR, Mostafa S, Liu J, Sohn Y-H, Cuenya BR (2007) Size dependent study of MeOH decomposition over size-selected Pt nanoparticles synthesized via micelle encapsulation. Catal Lett 118:1–7

Dahl S, Logadottir A, Egeberg RC, Larsen JH, Chorkendorff I, Törnqvist E, Nørskov JK (1999) Role of steps in N_2 activation on Ru(0001). Phys Rev Lett 83:1814–1817

den Breejen JP, Radstake PB, Bezemer GL, Bitter JH, Frøseth V, Holmen A, de Jong KP (2009) On the origin of the cobalt particle size effects in Fischer-Tropsch catalysis. J Am Chem Soc 131:7197–7203

Dujardin G, Mayne A, Comtet G, Hellner L, Jamet M, Le Goff E, Millet P (1996) New model of the initial stages of Si(111)-(7x7) oxidation. Phys Rev Lett 76:3782–3785

Frank M, Bäumer M (2000) From atoms to crystallites: adsorption on oxide-supported metal particles. Phys Chem Chem Phys 2:3723–3737

Gavnholt J (2009) The structure of individual nanoparticles and hot electron assisted chemistry at surfaces. Dissertation, Technical University of Denmark

Gavnholt J, Schiøtz J (2008) Structure and reactivity of ruthenium nanoparticles. Phys Rev B 77:035404-1-035404-10

Geng D, LuG (2007) Size effect of gold nanoparticles on the electrocatalytic oxidation of carbon monoxide in alkaline solution. J Nanopart Res 9:1145–1151

Granqvist CG, Buhrman RA (1976) Ultrafine metal particles. J Appl Phys 47:2200–2219

Grunwaldt J-D, Molenbroek AM, Topsøe N-Y, Topsøe H, Clausen BS (2000) In situ investigations of structural changes in Cu/ZnO catalysts. J Catal 194:452–460

Guise OL, Ahner JW, Jung MC, Goughnour PC, Yates JT (2002) Reproducible electrochemical etching of tungsten probe tips. Nano Lett 2:191–193

Haberland H, Karrais M, Mall M, Thurner Y (1992) Thin-films from energetic cluster impact—a feasibility study. J Vac Sci Technol A 10:3266–3271

Hammer B, Norskov JK (2000) Theoretical surface science and catalysis—Calculations and concepts. Adv Catal 45:71–129

Hansen PL, Wagner JB, Helveg S, Rostrup-Nielsen JR, Clausen BS, Topsøe H (2002) Atom-resolved imaging of dynamic shape changes in supported copper nanocrystals. Science 295:2053–2255

Haruta M, Yamada N, Kobayashi T, Iijima S (1989) Gold catalysts prepared by coprecipitation for low-temperature oxidation of hydrogen and of carbon-monoxide. J Catal 115:301–309

Hinnemann B, Moses PG, Bonde J, Jørgensen KP, Nielsen JH, Horch S, Chorkendorff I, Nørskov JK (2005) Biomimetic hydrogen evolution: MoS2 nanoparticles as catalyst for hydrogen evolution. J Am Chem Soc 127:5308–5309

Honkala K, Hellman A, Remediakis IN, Logadottir A, Carlsson A, Dahl S, Christensen CH, Nørskov JK (2005) Ammonia synthesis from first-principles calculations. Science 307:555–558

Hovel H, Barke I (2006) Morphology and electronic structure of gold clusters on graphite: Scanning-tunneling techniques and photoemission. Prog Surf Sci 81:53–111

Jacobsen CJH, Dahl S, Hansen PL, Törnqvist E, Jensen L, Topsøe H, Prip DV, Møenshaug PB, Chorkendorff I (2000) Structure sensitivity of supported ruthenium catalysts for ammonia synthesis. J Mol Catal A Chem 163:19–26

Janssens TVW, Clausen BS, Hvolbæk B, Falsig H, Christiensen CH, Bligaard T, Nørskov JK (2007) Insights into the reactivity of supported Au nanoparticles: combining theory and experiment. Top Catal 44:15–26

Jones G, Jakobsen JG, Shim SS, Kleis J, Andersson MP, Rossmeisl J, Abild-Pedersen F, Bligaard T, Helveg S, Hinnemann B, Rostrup-Nielsen JR, Chorkendorff I, Sehested J, Nørskov JK (2008) First principles calculations and experimental insight into methane steam reforming over transition metal catalysts. J Catal 259:147–160

Kadossov E, Funk S, Burghaus U (2008) CO adsorption of FeOx nanoclusters supported on HOPG—effect of oxide formation on catalytic activity. Catal Lett 120:179–183

Kibsgaard J, Lauritsen JV, Lægsgaard E, Clausen BS, Topsøe H, Besenbacher F (2006) Cluster-support interactions and morphology of MoS2 nanoclusters in a graphite-supported hydrotreating model catalyst. J Am Chem Soc 128: 13950–13958

King DL (1978) Fischer-Tropsch study of supported ruthenium catalysts. J Catal 51:386–397

Klipp B, Grass M, Müller J, Stolcic D, Lutz U, Ganteför G, Boneberg J, Leiderer P (2001) Deposition of mass-selected cluster ions using a pulsed arc cluster-ion source. Appl Phys A 73:547–554

Kung MC, Davis RJ, Kung HH (2007) Understanding Au-catalyzed low-temperature CO oxidation. J Phys Chem C 111:11767–11775

Landman U, Yoon B, Zhang C, Heiz U, Arenz M (2007) Factors in gold nanocatalysis: oxidation of CO in the non-scalable size regime. Top Catal 44:145–158

Luna NB, Bonetto FJ, Vidal RA, Goldberg EC, Ferrn J (2008) Low energy ion scattering in He/HOPG system. J Mol Catal A 281:237–240

Madey TE, Engelhardt HA, Menzel D (1975) Adsorption of oxygen and oxidation of CO on the ruthenium (001) surface. Surf Sci 48:304–328

Moseler M, Häkkinen H, Landman U (2002) Supported magnetic nanoclusters: soft landing of Pd clusters on a MgO surface. Phys Rev Lett 89:176103-1–176103-4

Nakamura Y, Mera Y, Maeda K (1999) A reproducible method to fabricate atomically sharp tips for scanning tunneling microscopy. Rev Sci Instrum 70:3373–3376

Nørskov JK, Bligaard T, Hvolbæk B, Abild-Pedersen F, Chorkendorff I, Christensen CH (2008) The nature of the active site in heterogeneous metal catalysis. Chem Soc Rev 37:2163–2171

Paul W, Reinhard HP, Vonzahn U (1958) Das elektrische massenfilter als massenspektrometer und isotopentrenner. Z für Phys 152:143–182

Pratontep S, Carroll SJ, Xirouchaki C, Streun M, Palmer RE (2005) Size-selected cluster beam source based on radio frequency magnetron plasma sputtering and gas condensation. Rev Sci Instrum 76:1–8

Rodriguez-reinoso F (1998) The role of carbon materials in heterogeneous catalysis. Carbon 36:159–175

Rohmer M, Ghaleh F, Aeschlimann M, Bauer M, Hövel H (2007) Mapping the femtosecond dynamics of supported clusters with nanometer resolution. Eur Phys J D 45:491–499

Sanchez A, Abbet S, Heiz U, Scheider WD, Häkkinen H, Barnett RN, Landman U (1999) When gold is not noble: nanoscale gold catalysts. J Phys Chem A 103:9573–9578

Shincho E, Egawa C, Naito S, Tamaru K (1985) The behavior of CO adsorbed on Ru (1, 1, 10) and Ru(001)—the dissociation of CO at the step sites of the Ru(1, 1, 10) surface. Surf Sci 149:1–16

Silvestre-Albero J, Rupprechter G, Freund H-J (2006) Atmospheric pressure studies of selective 1, 3-butadiene hydrogenation on well-defined Pd/Al2O3/NiAl(110) model catalysts: effect of Pd particle size. J Catal 240:58–65

Song Z, Cai T, Hanson JC, Rodriguez JA, Hrbek J (2004) Ru nanoclusters prepared by $Ru_3(CO)_{12}$ deposition on Au(111). J Am Chem Soc 126:8576–8584

Tian N, Zhou Z-Y, Sun S-G, Ding Y, Wang ZL (2007) Synthesis of tetrahexahedral platinum nanocrystals with high-index facets and high electro-oxidation activity. Science 316:732–735

Valden M, Lai X, Goodman DW (1998) Onset of catalytic activity of gold clusters on titania with the appearance of nonmetallic properties. Science 281:1647–1650

Wörz AS, Judai K, Abbet S, Heiz U (2003) Cluster size-dependent mechanisms of the CO + NO reaction on small Pd-n ($n \leq 30$) clusters on oxide surfaces. J Am Chem Soc 125:7964–7970

Yao Y, Fu Q, Zhang Z, Zhang H, Ma T, Tan D, Bao X (2008) Structure control of Pt–Sn bimetallic catalyst supported on highly oriented pyrolytic graphite (HOPG). Appl Surf Sci 254:3808–3812

Yim W-L, Nowitzki T, Necke M, Schnars H, Nickut P, Biener J, Biener MM, Zielasek V, Al-Shamery K, Klüver T, Bäumer M (2007) Universal phenomena of CO adsorption on gold surfaces with low-coordinated sites. J Phys Chem C 111:445–451

Zanella R, Giorgio S, Shin C-H, Henry CR, Louis C (2004) Characterization and reactivity in CO oxidation of gold nanoparticles supported in TiO_2 prepared by deposition-precipitation with NaOH and urea. J Catal 222:357–367

Zhang G, Yang D, Sacher E (2007) Structure and morphology of Co nanoparticles deposited onto highly oriented pyrolytic graphite. J Phys Chem 111:17200–17205

Zhang H, Fu Q, Yao Y, Zhang Z, Ma T, Tan D, Bao X (2008) Size-dependent surface reactions of Ag nanoparticles supported on highly oriented pyrolytic graphite. Langmuir 24:10874–10878

Zubkov T, Morgan GA, Yates JT Jr (2002) Spectroscopic detection of CO dissociation on defect sites on Ru(109): implications for Fischer-Tropsch catalytic chemistry. Chem Phys Lett 362:181–184

Zubkov T, Morgan GA, Yates JT, Kühlert O, Lisowsk M, Schillinger R, Fick D, Jänsch HJ (2003) The effect of atomic steps on adsorption and desorption of CO on Ru(109). Surf Sci 526:57–71

CARBON 49 (2011) 376–385

available at www.sciencedirect.com

ScienceDirect

journal homepage: www.elsevier.com/locate/carbon

Catalytic oxidation of graphite by mass-selected ruthenium nanoparticles

S. Murphy, R.M. Nielsen, C. Strebel, M. Johansson, J.H. Nielsen *

Center for Individual Nanoparticle Functionality (CINF), Department of Physics, Technical University of Denmark, 2800 Kongens Lyngby, Denmark

ARTICLE INFO

Article history:
Received 8 June 2010
Accepted 14 September 2010
Available online 14 October 2010

ABSTRACT

The scanning tunneling microscopy and temperature programmed oxidation methods were used to study the catalytic oxidation of graphite by mass-selected Ru nanoparticles. Channeling by the nanoparticles was observed on the unsputtered HOPG basal surface at temperatures above 750 °C in 10^{-6} mbar O_2. Ar^+ ion bombardment was used to create layers of disordered carbon of various depths on the HOPG surface. The channel propagation rate in the disordered carbon layer was found to increase for larger nanoparticles. The depth of the interface between the disordered carbon layer and the graphite determined whether the nanoparticles etched paths parallel or perpendicular to the surface. The gasification onset temperature depended on the degree of graphitisation of the surface, with more heavily sputtered surfaces undergoing gasification at much lower temperatures than the unsputtered surface.

1. Introduction

The catalytic gasification of carbon by transition metal nanoparticles plays an important role in a wide range of applications. Traditionally, it has been investigated with regard to the effect of metal catalysts on the gasification of coal [1], the removal of carbon deposits from catalysts used in processes such as Fischer–Tropsch synthesis [2], the degradation of carbon-supported catalysts through corrosion [3] and the catalytic oxidation of soot particles from diesel engine exhausts [4,5]. More recently, attention has also focussed on the degradation of electrode performance in proton-exchange membrane fuel cells [6], the corrosion stability of carbon nanotubes [7] and etching of diamond [8] and graphene [9].

Gasification of graphite has been particularly well studied, since this provides a well-defined surface that is easily accessible to various surface science and microscopy techniques. The uncatalysed gasification of graphite generally proceeds via a combination of edge recession at substrate steps and etch pit formation originating from surface vacancies and screw dislocations, followed by abstraction of carbon atoms from the basal plane at higher temperatures [10–16]. Catalysed gasification of graphite has been reported for a variety of transition metals and their compounds in various gases [17–23]. Transition metal particles deposited onto graphite either from aqueous solution or by physical vapour deposition generally form etch channels on the surface during gasification, where the channel width and length can often be related to the particle diameter. Two models have been proposed for the action of the catalyst; (1) it acts as a dissociation center for splitting the gas molecules, followed by diffusion of the atomic species to the carbon and reaction, or (2) carbon–carbon bonds are broken at the graphite-catalyst interface and carbon diffuses through or over the catalyst nanoparticle to react with gas molecules at the catalyst surface. The channeling action comes from the fact that the nanoparticles adhere to the receding step edge produced at the graphite-catalyst interface as carbon is removed.

* *Corresponding author:* Fax: +45 4593 2399.
E-mail address: jane@fysik.dtu.dk (J.H. Nielsen).
0008-6223/$ - see front matter
doi:10.1016/j.carbon.2010.09.032

In the present study, we have investigated the catalytic oxidation of highly-oriented pyrolytic graphite (HOPG) by mass-selected ruthenium nanoparticles using scanning tunneling microcopy (STM), scanning electron microscopy (SEM) and temperature programmed oxidation (TPO). We are interested in ruthenium because it is catalytically active for several processes including methanation and Fischer–Tropsch synthesis [24,25], hydrotreating of hydrocarbons [26], reduction of nitrogen oxides [27] and ammonia synthesis [28]. The elementary steps in a number of these processes may be studied using a model catalyst comprising Ru nanoparticles supported on HOPG [29]. However, it is important to identify the conditions under which the catalyst is stable against sintering and corrosion of the support. Furthermore, the catalytic process under study can lead to carbon deposition on the catalyst surface, so it is also important to establish whether accumulated carbon deposits can be removed from the surface of the catalyst nanoparticles. Previous studies of Ru-catalysed graphite gasification using transmission electron microscopy (TEM) established that the mode of attack is very dependent on both the reaction temperature and the reactant gas [30,31]. In particular, different modes of attack were observed at different temperatures under oxidising conditions, which could be attributed to the oxidation state of the catalyst and consequently its ability to wet the graphite surface [30]. These previous studies focussed on the etching of cleaved graphite surfaces containing only intrinsic defects such as steps and vacancies. In the present study, we have investigated the effect of varying the degree of graphitisation of the support, i.e. how disordered the carbon surface is, by means of Ar^+ pre-sputtering and demonstrate that it has a significant influence on the oxidation process. We have also investigated the effect of varying nanoparticle size on graphite oxidation by using mass-selected nanoparticles.

2. Experimental

The experiments were performed in a multichamber ultra-high vacuum (UHV) system (Omicron, Multiscan Lab) with a base pressure in the low 10^{-11} mbar region. HOPG substrates (SPI-1, 7 mm × 7 mm × 0.5 mm) were cleaved in air and mounted in sample holders incorporating a pyrolytic boron nitride (PBN) radiative heater, which is capable of heating the sample to temperatures in excess of 700 °C. A C-type thermocouple (W-5 at.% Re/W-26 at.% Re) was placed in contact with the substrate in order to monitor and control the sample temperature via a PID controller (Eurotherm 2408). The temperature measured using different sample holders varied somewhat as a result of small variations in how the sample, heater and thermocouple were fixed. Therefore, the accuracy of the temperature measurement was assumed to about ±50 °C. Upon insertion into UHV, the samples were outgassed for several hours at 660 °C to outgas adsorbed contaminants prior to use. The influence of the degree of graphitisation of the support on the oxidation behaviour was investigated by pre-sputtering the HOPG surfaces with 500 eV Ar^+ ions at a target current density of ~ 1 μA/cm² [1] for varying lengths of time, followed by heating to 660 °C for a further 15 min to degas the surface from implanted Ar.

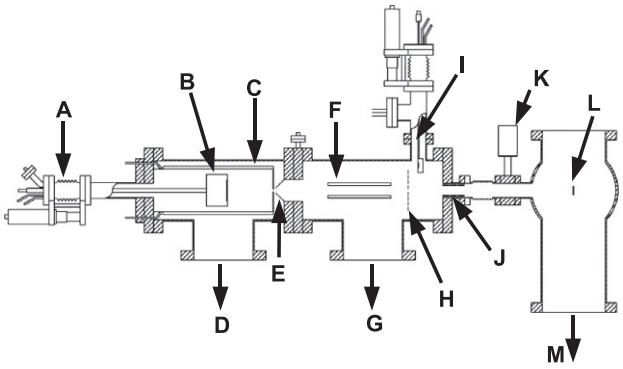

Fig. 1 – A schematic illustration of the inert gas-aggregation source used to produce the mass-selected Ru nanoparticles, with; (A) Linear translator, (B) magnetron sputter source, (C) cooling shroud, (D) pumping to gas-aggregation chamber via 450 l/s turbo pump, (E) skimmer, (F) quadrupole mass filter, (G) pumping to quadrupole chamber via 230 l/s turbo pump, (H) grid, (I) quartz crystal balance, (J) Einzel lenses, (K) gate valve, (L) substrate located in preparation chamber, (M) pumping to preparation chamber via 260 l/s turbo pump and 400 l/s ion pump.

Pre-formed mass-selected Ru particles were soft-landed onto the HOPG substrates at room temperature using an inert gas-aggregation source (Mantis Deposition Ltd., Nanogen 50). A schematic illustration of the deposition layout of the gas-aggregation source is shown in Fig. 1. The particles are formed by gas-phase condensation from a flux of Ru atoms that are sputtered from a 99.99% pure Ru target using a magnetron sputter source (B). The magnetron is housed in a liquid nitrogen cooled enclosure (C) with a 3 mm diameter aperture at one end. Argon gas is flown into the volume around the magnetron at a rate of 10–120 sccm and is pumped away via the aperture so that a local pressure of 0.1–1 mbar is obtained inside the gas-aggregation zone during operation. The cooled argon gas thermalises the sputtered Ru atoms so that they condense into clusters, which further coalesce to form nanoparticles. The size of the nanoparticles is determined by a number of factors such as magnetron sputter power (typically 20–40 W), rate of gas flow, distance between the target and the exit aperture and the diameter of the exit aperture. Ruthenium nanoparticles with diameters in the range of 2–16 nm can be produced using the source [32,33]. The nanoparticles are carried by the gas stream through the exit aperture of the aggregation zone, producing a nanoparticle beam that is further refined by a skimmer (E). The nanoparticle beam is then passed through a quadrupole mass filter (F) where the ionised fraction (60–80%) of the nanoparticles can be filtered according to their mass-to-charge ratio. The quadrupole mass filter settings were optimised to obtain a resolution of 6% in the particle diameter.[2] The ionised nanoparticle flux exiting

[1] It should be pointed out that we have mistakenly reported the sputter current density to be ~ 0.1 μA/cm² in earlier reports [32,33].
[2] A higher resolution in the particle diameter is achievable with the quadrupole, but at the expense of the deposition rate.

the source can be measured as a current on a biased grid (H), while the total flux can be measured with a quartz crystal balance (I). The nanoparticle beam is then passed through an Einzel lenses (J), which is used to focus the beam through the constriction between the source and the preparation chamber where the substrate (L) is located. The substrate is placed at a small positive bias ($\sim$36 V) so that negatively charged particles are soft-landed onto the surface with kinetic energies of $\leqslant$ 0.1 eV/atom. The substrate can be shifted slightly off-axis of the beam in order to avoid deposition of neutral particles, though our measurements indicate that the number of neutrals entering the preparation chamber is negligible. Further details on the construction and principles of operation of this type of source can be found elsewhere [34,35].

Ion scattering spectroscopy (ISS) measurements were used to confirm the surface cleanliness of the deposited particles. The measurements were performed using 1 keV He^+ ions produced by a differentially pumped electron impact ion source (ISE 100, Omicron Nanotechnology). The reflected ions were detected at a 147° scattering angle with a hemispherical energy analyser.

TPO experiments were performed by backfilling the UHV chamber with high purity O_2 via a leak valve until a partial pressure of 10^{-6} mbar was established. The sample temperature was then ramped at a rate of 1 °C/s in the oxygen atmosphere. The local gas composition evolved at the surface during the temperature ramp was monitored using a differentially pumped Balzers QMA 125 quadrupole mass spectrometer. The spectrometer was equipped with an oxygen-free high conductivity (OFHC) copper sniffer tip with a 1 mm diameter aperture, which is positioned within 0.5 mm of the sample surface. This arrangement allows the O_2, CO and CO_2 signals from the sample surface to be measured with negligible contribution from the sample holder or surroundings.

STM was performed at room temperature in constant current mode, using electrochemically etched W tips without any in-vacuum treatments other than applying a series of voltage pulses (typically 4–9 V for 10–100 ms) or scanning for several lines with increased bias ($U \sim 2$ V) in order to condition the tip. The typical tunnel parameters used to image the particles in this study were $U = 10$–600 mV for the gap bias, where the sample was biased with respect to the tip, and $I = 100$–800 pA for the tunnel current. Slow scan speeds were adopted with a typical line scan frequency of about 0.5–1 Hz. SEM images were acquired in-situ using a UHV Gemini 30 kV SEM column capable of 3 nm spatial resolution. Typically, images were obtained with a primary beam voltage of 5 kV and a probe current of 0.1–1 nA. Ex-situ TEM analysis of the nanoparticles was also performed using a Technai T20 200 kV transmission electron microscope. For these analyses, the nanoparticles were deposited onto lacey carbon films supported on 300 mesh copper TEM grids.

3. Results

3.1. *Mass-selected Ru nanoparticles*

The surface composition after deposition of 8.4 nm Ru nanoparticles onto a HOPG surface that had been sputtered for 30 s was investigated with ISS, see Fig. 2. Approximately 10% of the surface is covered by nanoparticles. The ISS shows a pronounced ruthenium peak at 865 eV, while the insert shows an enlarged view of the broad carbon peak at around 300 eV. The low signal reflected from the support can be attributed to the high neutralisation probability for He^+ ions scattering from carbon [36]. No other peaks were observed indicating a high degree of cleanliness of the as-deposited nanoparticles.

A STM image of 2.7 nm Ru nanoparticles deposited onto a HOPG surface that had been sputtered for 15 min with 500 eV Ar^+ ions is shown in Fig. 3a. Depositions were typically carried out so that 10–40% of the surface was covered by nanoparticles. The nanoparticles were found to be stable against sintering in UHV below 500 °C, with the exception of particles with diameters $\leqslant$ 3 nm supported on unsputtered HOPG [32]. The nanoparticles generally appear round in the STM with facets only evident on particles larger than around 8 nm. The mean nanoparticle diameter measured by STM is overestimated due to tip convolution effects. Therefore, the mean nanoparticle height measured by STM was used to obtain a representation of the size distribution of the supported nanoparticles. Several of these particle height distributions are shown in Fig. 3b, which were obtained using different aggregation source parameters, such as the Ar gas flow. The standard deviation measured for the nanoparticle height is on average around 20%, which is larger than the expected resolution of 6%. However, the latter value is based on an idealised assumption that the nanoparticles are spherical and homogeneous. TEM images of nanoparticles taken ex-situ, such as the examples shown in Fig. 3c–e, have shown that the nanoparticles are not homogeneous and can display a range of different polymorphs [33]. This behaviour was increasingly apparent for larger nanoparticles and is consistent with the process of formation of the nanoparticles through coalescence of smaller clusters inside the gas-aggregation source. Good agreement was obtained between the particle diameter distributions measured by TEM and the corresponding particle height distributions measured in-situ by STM [33], indicating that any oxide formed during the transfer

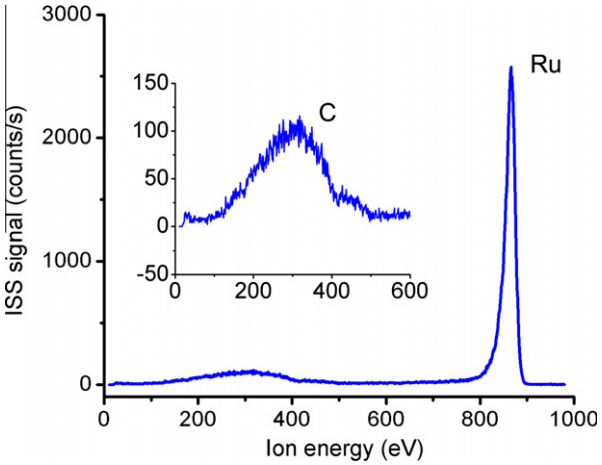

Fig. 2 – ISS spectrum of Ru nanoparticles freshly deposited onto HOPG. Approximately 10% of the surface is covered by 8.4 nm nanoparticles. The insert shows an enlarged view of the energy range around the carbon peak.

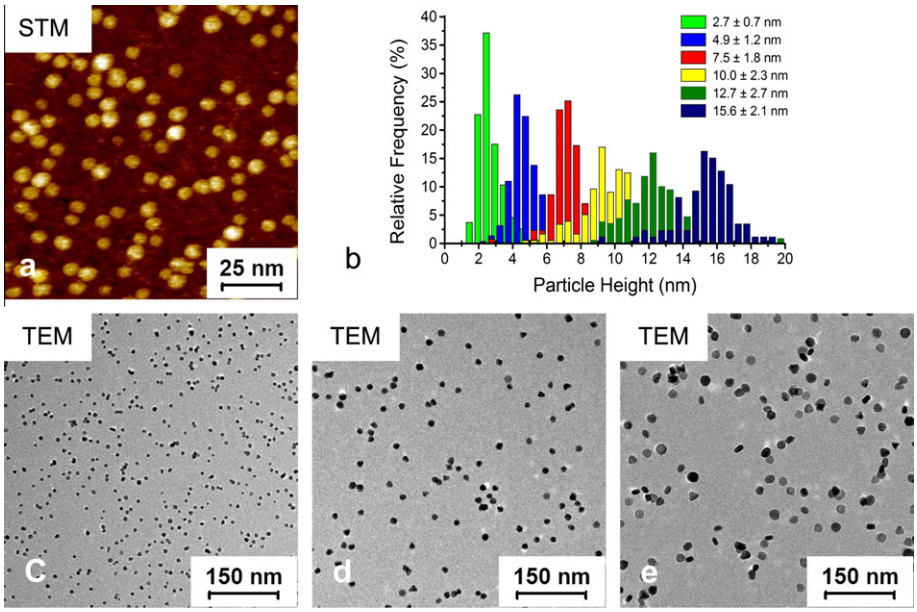

Fig. 3 – Mass selected Ru nanoparticles characterised by STM and TEM. (a) 100 nm × 100 nm STM image of 2.7 nm Ru nanoparticles deposited onto unsputtered HOPG at room temperature. (b) Height distributions obtained from STM measurements of different sized nanoparticles in the diameter range from 2 nm to 16 nm. (c–e) 512 nm × 512 nm TEM images showing (c) 6 nm, (d) 12 nm and (e) 16 nm Ru nanoparticles supported on lacey carbon films. Good agreement was obtained between the particle heights measured by STM and the particle diameters measured by TEM [33].

from the UHV system to the TEM was restricted to a thin shell around the nanoparticles. This was further supported by high-resolution TEM measurements of lattice fringes displayed by the nanoparticles, which confirmed that they comprised metallic ruthenium [33].

3.2. *Temperature programmed oxidation*

After establishing the size, shape and composition of the nanoparticles, TPO measurements were performed to investigate the support oxidation process. These were performed by heating linearly to 770 °C in 10^{-6} mbar O_2. An example of such a measurement is shown in Fig. 4, which plots the CO, CO_2 and O_2 signals measured above the sample surface during oxidation of a sputtered HOPG surface 15% covered by 2.3 nm Ru nanoparticles.[3] The oxidation of the support is initiated above an ignition temperature T_i, which we define as the temperature where the measured CO signal has risen 10% above the background level. The CO signal continues to rise for some temperature interval above T_i, before reaching a peak value at T_p. This is mirrored by a corresponding consumption in the O_2 signal at the same temperature. Above T_p the CO signal decreases again as the gasification process becomes deactivated. A negligible amount of CO_2 is also observed during the initial stage of oxidation near T_i but disappears completely before the CO signal peaks at T_p. When TPO measurements (not shown) were performed on HOPG surfaces without nanoparticles the CO background did not rise

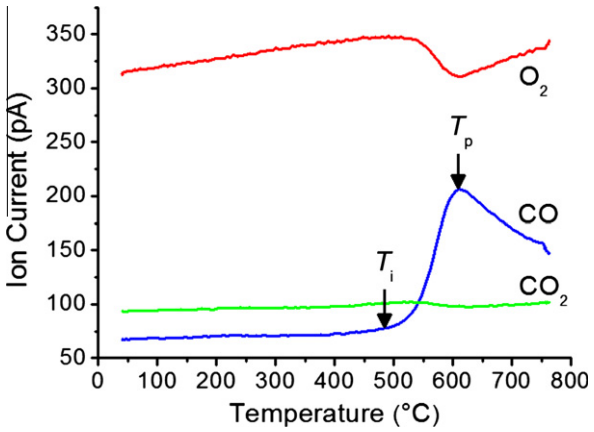

Fig. 4 – TPO spectrum obtained for 2.3 nm Ru nanoparticles supported on HOPG that was sputtered with 500 eV Ar^+ ions for 15 min. The sample temperature was increased linearly at a rate of 1 °C/s in 10^{-6} mbar O_2. The positions of the ignition temperature T_i and the CO peak temperature T_p are indicated.

in the temperature range up to 770 °C, indicating that the oxidation process is catalysed by the Ru nanoparticles.[4]

3.3. *Influence of support graphitisation*

In order to study the influence of the degree of surface graphitisation on the oxidation process, TPO measurements were

[3] It should be noted that the O_2 signal was observed to rise continuously over the course of each oxidation experiment. This was attributed to the gradual saturation of the uptake of O_2 on the walls of the UHV chamber.

[4] Both sputtered and unsputtered HOPG surfaces were tested for non-catalytic oxidation under these conditions.

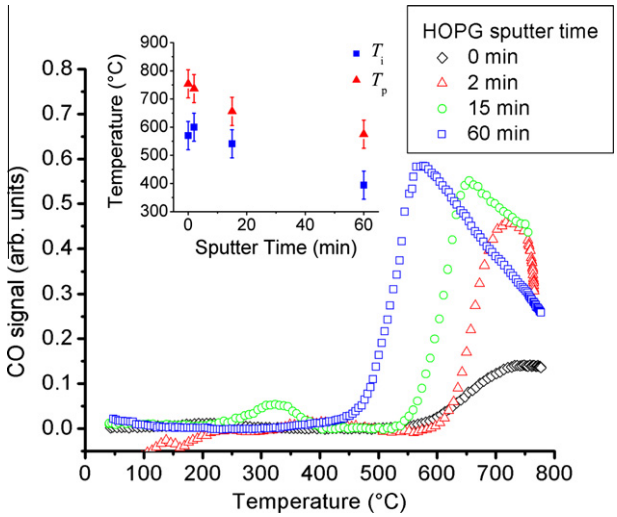

Fig. 5 – CO signal measured during TPO of 4.6 nm Ru nanoparticles supported on HOPG that was sputtered with 500 eV Ar^+ ions for 0 min, 2 min, 15 min and 60 min. The sample temperature was ramped at 1 °C/s in a background O_2 pressure of 10^{-6} mbar. The insert plots the measured ignition temperature as a function of the substrate sputter time.

performed on HOPG surfaces with different amounts of Ar^+ pre-sputtering, see Fig. 5. For these experiments, nanoparticles with a mean diameter of 4.6 nm were deposited onto HOPG surfaces that had been pre-sputtered for 0 min, 2 min, 15 min and 60 min with 500 eV Ar^+ ions.[5] In each case, the same initial nanoparticle coverage ($\sim 40\%$) was used and the oxidation was carried out by heating linearly to 770 °C in 10^{-6} mbar O_2. Each sample was held at this temperature for 10 min before removing the O_2 and cooling the sample to room temperature in UHV. The subsequent STM analysis of these surfaces will be discussed below. Fig. 5 plots the CO signal evolved from each surface versus temperature, after normalisation to the corresponding O_2 signal and background substraction.[6] The CO peaks are seen to shift to lower temperatures for the surfaces that have been more heavily sputtered, indicating that these surfaces are oxidised at lower temperatures compared to unsputtered HOPG. This is highlighted in the insert of Fig. 5, which plots T_i and T_p for each sample versus the pre-sputtering time of the support. This behaviour can be rationalised by the fact that the Ar^+ pre-sputtering produces surface defects or even a disordered carbon layer on the support surface, which can be more readily oxidised than the defect-free graphite surface. A similar behaviour has been previously observed during the non-catalytic oxidation of graphite and charcoal, where graphite oxidation was found to occur at around 100 °C higher than charcoal oxidation [37].

In order to investigate the mechanisms behind the oxidation process and its subsequent deactivation, STM measurements were performed on the same surfaces after the TPO measurements shown in Fig. 5. STM images of these surfaces are presented in Fig. 6 and show that the surfaces have undergone significant modification as a result of catalysed oxidation. Fig. 6a shows a STM image of the nanoparticles deposited on an unsputtered HOPG surface after oxidation. The nanoparticles have sintered into large hexagonal islands with a flat top facet – most likely the (0001) facet. The mean height of these nanoparticles is of the order of 8.0 ± 2.5 nm, while the lateral dimensions range from a few nm to several tens of nm. Monolayer deep etch channels are visible on the HOPG surface between the particles. These channels are generally initiated from substrate step edges. While the depth of the channels is uniformly 0.3 nm, corresponding to the interlayer spacing of HOPG [12], their lateral width depends on the lateral dimensions of the particle at which the channel terminates. Fig. 6b shows the effect of catalysed oxidation on a HOPG surface that has been sputtered for 2 min with 500 eV Ar^+ ions. The surface is decorated with well-oriented etch channels that are mostly aligned along three principal directions. This is highlighted by the corresponding polar plot shown in the insert in Fig. 6b, which shows that the etch channels are oriented by $\sim 60°$ with respect to one another.[7] The channels are 0.3–2.4 nm deep corresponding to between one and eight monolayers. The mean particle height is around 7.1 ± 3.3 nm, while the lateral size of the particles appears to be around 19.0 ± 9.7 nm. This value is an upper bound due to STM tip convolution effects. Fig. 6c shows the effect of catalytic oxidation on a HOPG surface that has been sputtered for 15 min with 500 eV Ar^+ ions. In this case, there is little evidence of preferential orientation of the etch channels; the surface is randomly etched with around ten layers of the surface exposed. Only the deepest channels, which are around 3 nm deep, display any evidence of oriented propagation. The mean height of the sintered particles is 4.5 ± 3.3 nm, while the lateral size appears to be around 16.0 ± 6.3 nm. Finally, Fig. 6d shows the effect of catalytic oxidation on a HOPG surface that has been sputtered for 60 min with 500 eV Ar^+ ions. It is difficult to discern any Ru particles on the surface. The density of etch channels is much lower than that observed in Fig. 6c – approximately 55% of the topmost surface layer remains in Fig. 6d compared to only 15–20% in Fig. 6c. Moreover, the depth of the largest channels in Fig. 6d is in the range of 4–5 nm.

[5] Assuming that every carbon atom in the HOPG surface that is hit by an Ar^+ ion is removed, then with a target current of 1 $\mu A/cm^2$ it can be shown that after 2 min of sputtering roughly 20% of the surface layer is removed. After 15 min the complete first layer and up to 50% of the next layer are removed, while after 60 min of sputtering up to six layers of the surface have been removed. It should be noted that these values are based on a simplistic model where carbon is removed from the surface in a "layer-by-layer" fashion. Our STM analysis of these sputtered surfaces reveals that they are highly disordered [32] and likely constitute a significant proportion of amorphous carbon and carbon nanoflakes.

[6] An additional CO peak is observed for the 15 min sputtered sample at around 325 °C. This is attributed to the removal of carbon deposited on top of the nanoparticles, which may have been present as a result of prolonged exposure to the residual gas in the UHV chamber prior to carrying out the oxidation experiment.

[7] It should be noted that the angles are slightly distorted due to thermal drift in the STM.

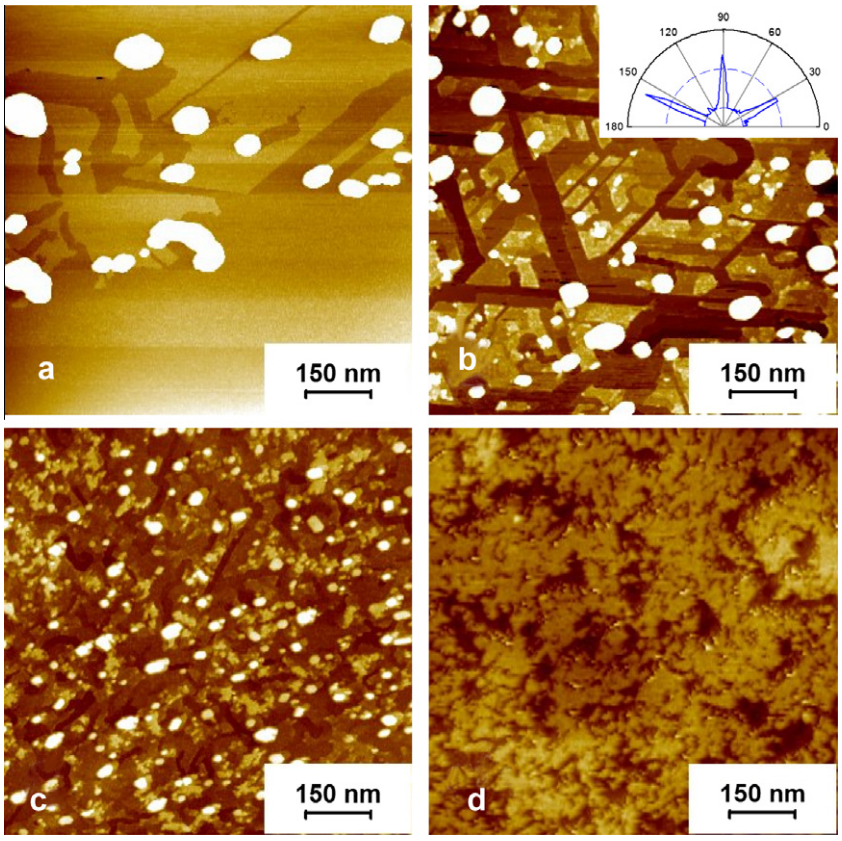

Fig. 6 – Effect of pre-sputtering on the catalysed oxidation of graphite by Ru nanoparticles. In each case, the same coverage of 4.6 nm diameter Ru nanoparticles was deposited onto the support surface, which was then oxidised in 10^{-6} mbar O_2 at 770 °C for 10 min. Each STM image is 600 nm × 600 nm and was taken after the catalysed oxidation. (a) An unsputtered HOPG support, (b) HOPG surface sputtered for 2 min with 500 eV Ar^+ ions. The insert shows a polar plot showing the orientation of the etch channels. (c) HOPG surface sputtered for 15 min with 500 eV Ar^+ ions. (d) HOPG surface sputtered for 60 min with 500 eV Ar^+ ions.

The results presented so far indicate that during catalysed oxidation the nanoparticles etch downwards through the disordered carbon layer produced by the Ar^+ pre-sputtering until the interface with the HOPG basal plane is reached, after which the etching proceeds parallel to this interface. To further elucidate the structure of the etch channels TPO was performed on a low coverage (12%) of Ru nanoparticles deposited onto a HOPG surface that was sputtered for 15 min. Fig. 7a shows a large-scale STM image of the surface after oxidation, where the randomly oriented etch channels formed by individual nanoparticles can be distinguished. From the STM image of an individual etch channel shown in Fig. 7b it can be seen that the channel width remains roughly constant. STM images (not shown) of the areas on either side of the channel reveal a surface roughness consistent with what has previously been observed after sputtering the HOPG surface for 15 min with 500 eV Ar^+ ions [32]. A line-profile taken across the etch channel, see Fig. 7c, reveals that it is about 3 nm deep, indicating the depth of the disordered carbon/graphite interface produced by the Ar^+ sputtering. The sides of the channel appear to slope inwards towards the bottom of the channel as a result of tip convolution effects, however, the bottom of the channel appears flat. High-resolution STM images taken in the area at the bottom of the etch channel, see Fig. 7d, reveal the atomic structure of the graphite basal plane.[8] Interestingly, when SEM images were obtained of this surface, see Fig. 7e, it was found that the etch channels imaged as low (dark) regions in the STM image appear brighter in the SEM image compared to the disordered carbon layer. This demonstrates that a higher secondary electron yield is obtained from ordered graphite surface at the bottom of the etch channels compared to the surrounding disordered carbon.

3.4. *Influence of nanoparticle size*

In addition to investigating the influence of surface graphitisation, the influence of nanoparticle size on the oxidation process was also investigated. In order to minimise sintering or interaction between neighbouring etch channels, these experiments were carried out by using very low coverages ($\leqslant 1\%$) of nanoparticles deposited onto HOPG surfaces that had been sputtered for 15 min. In order that a reliable comparison might be made between the ignition temperatures

[8] The atomic structure is slightly distorted by thermal drift.

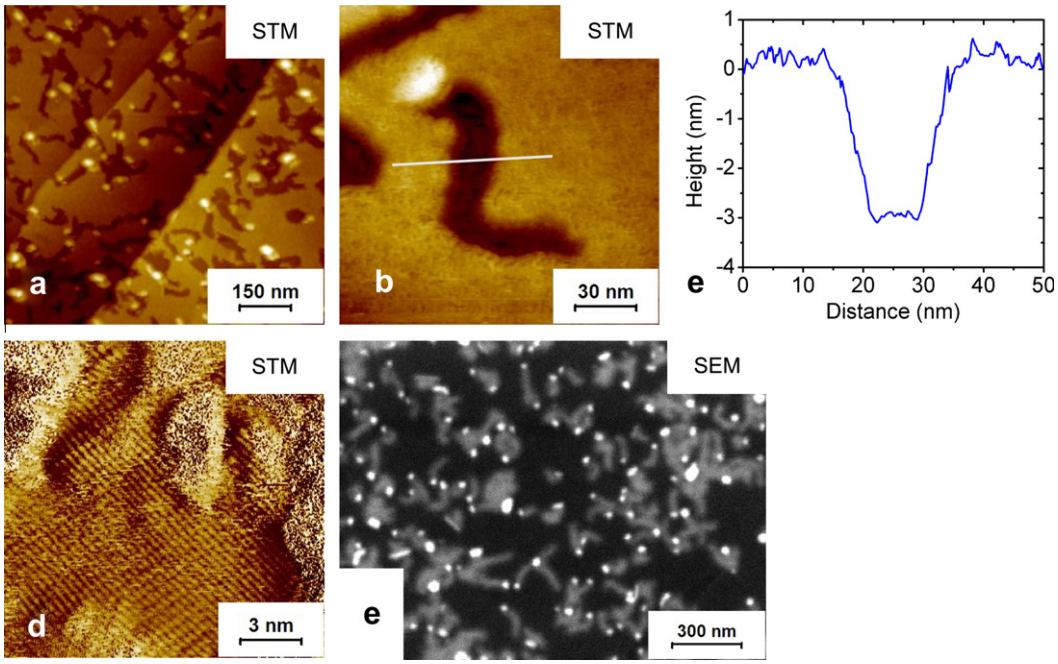

Fig. 7 – STM and SEM measurements of etch channels formed by Ru nanoparticles in a disordered carbon layer formed on HOPG by Ar^+ sputtering. (a) 600 nm × 600 nm STM image of 11 nm Ru nanoparticles deposited onto a HOPG surface that was sputtered for 15 min with 500 eV Ar^+ ions after oxidation in 10^{-6} mbar O_2 at 760 °C for 10 min. (b) 100 nm × 100 nm constant current STM image of an individual etch channel. (c) Line-profile taken across the etch channel along the direction indicated by the line in (b). (d) 10 nm × 10 nm constant current image taken at the bottom of the etch channel showing the atomic resolution of the graphite surface. (e) 1200 nm × 900 nm SEM image of the surface after catalytic oxidation, the etch channels formed by the nanoparticles appear brighter than the sputtered carbon layer.

obtained for different size nanoparticles, the experiments were performed using the same sample holder, heater and thermocouple. STM measurements were used to determine the channel length, width and depth after oxidation in 10^{-6} mbar O_2 at 760 °C for 10 min. When measuring the channel length, width and depth only individual etch channels that did not display significant branching, like the one shown in Fig. 7b, were selected. The results of these measurements are summarised in Fig. 8 for three different particle sizes; 3.2 nm, 5 nm and 7 nm. All three parameters were found to increase with particle size indicating that the particle propagation rate during catalysed oxidation is higher for larger particles. Comparing the ignition temperatures (T_i) measured for the different particle sizes, it was found that the 3.2 nm and 5 nm nanoparticles yielded similar T_i of 580 °C and 588 °C, respectively, while T_i for the 7 nm nanoparticles was much higher at 638 °C.

4. Discussion

Previous studies have shown that the oxidation state of the catalyst can significantly affect the mode of attack in an oxidising environment [2,30]. Oxidised catalyst particles were found to wet the graphite surface so that gasification proceeded largely by recession of the graphite steps edges. However, at higher temperatures the oxide wetting layer was found to decompose resulting in metallic nanoparticles, so that the dominant mode of attack switched to channeling. An intermediate mechanism was also observed where the channeling particles decreased in size over time as catalyst material was deposited on the sides of the channel. This resulted in the channel width increasing over time due to edge recession catalysed by the wetting layer, giving rise to wedge shape etch channels [38]. In the present study, the channeling action of the nanoparticles indicates that they comprise metallic ruthenium. Moreover, we observe that the width of individual etch channels remains constant as the nanoparticles propagate, implying that there is no shrinkage in size either through decomposition of ruthenium oxide or wetting of the graphite edges exposed during channeling. Thermal desorption spectra (TDS) of oxygen from RuO_2(110) epitaxial films grown on Ru(0001) indicate that the oxide decomposes in UHV between around 630 °C and 780 °C [39]. Since the oxidation process in the present study peaks at comparable temperatures, i.e. between 600 °C and 750 °C, it is probable that the nanoparticles remain largely metallic during the gasification process. The TDS measurements have also shown that oxygen chemisorbed on the Ru(0001) surface does not desorb until above 930 °C [39]. It is therefore likely that chemisorbed oxygen is present on the surface of the nanoparticles during the oxidation process in the present study.

Assuming that the nanoparticles are metallic, the question remains as to how they catalyse the oxidation of the graphite support. As mentioned earlier, two mechanisms have been suggested to explain how this might happen; (1) oxygen is dissociated on the nanoparticle surface and then diffuses to the graphite edge where it removes undercoordinated carbon

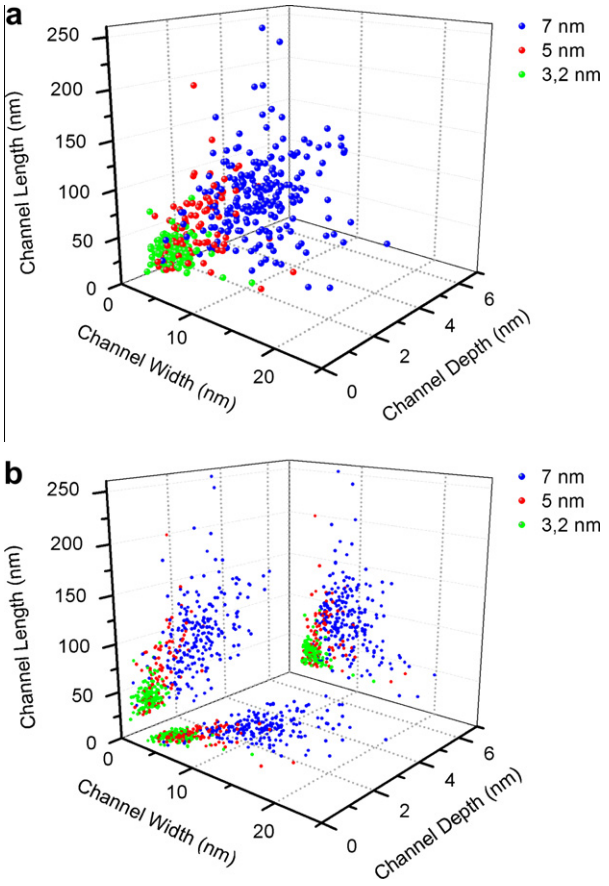

Fig. 8 – (a) 3D scatter plot of the measured channel width, depth and length after oxidation by 3.2 nm, 5 nm and 7 nm nanoparticles. (b) Projection of the same data onto the XY, XZ and YZ planes.

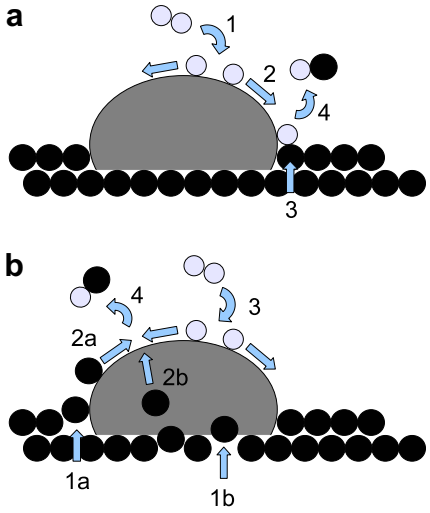

Fig. 9 – The two proposed mechanisms for the catalysed oxidation of HOPG by Ru nanoparticles. (a) Oxygen molecules adsorb dissociatively on the surface of the nanoparticles (1). The oxygen atoms diffuse to the edge of the nanoparticle (2), where they extract carbon atoms from the graphite lattice (3) and desorb as CO (4). (b) Carbon atoms leave the graphite lattice around/under the nanoparticle (1a, 1b) and diffuse over/through the Ru nanoparticle (2a, 2b). Oxygen molecules are dissociatively adsorbed on the nanoparticle surface (3). The diffusing carbon and oxygen atoms react on the surface of the nanoparticle and desorb as CO (4).

atoms, and (2) carbon diffuses through or over the nanoparticle to react with chemisorbed oxygen. Both of these mechanisms are illustrated schematically in Fig. 9. In the present study, it was found that the rate of channel propagation increased for larger nanoparticles. This behaviour indicates that the rate-limiting step is due to a reaction on the surface of the nanoparticles, rather than diffusion of carbon through the particle since the latter mechanism would imply a faster reaction rate for smaller particles. On the other hand, it is highly probable that both mechanisms participate in the oxidation process and that their relative contribution is determined by the temperature and gas pressure. For example, the carbon transport depicted in Fig. 9b should only increase with increasing temperature, and may in fact explain the eventual deactivation of the catalyst at higher temperatures, seen in Fig. 5. It should also be noted that the behaviour observed here is more analagous to the situation found for catalytic hydrogenation rather than catalytic oxidation. For example, it has been shown for hydrogenation of graphite by Pt, Ir and PtIr nanoparticles that the channel propagation rate increases with increasing particle size [40], while for oxidation of graphite using bimetallic PtIr nanoparticles the channel propagation rate decreases with increasing particle size [41]. However, those previous studies were carried out in much higher gas pressures and focussed on particle channeling on unsputtered graphite.

The data presented in Figs. 5 and 6 clearly demonstrates that the gasification process depends significantly on the degree of graphitisation of the support. Sputtered HOPG surfaces are more easily oxidised than unsputtered HOPG, as demonstrated by the shift in the gasification temperature to lower values for more heavily sputtered surfaces. This is also reflected in the etch morphology obtained on the different surfaces. Nanoparticles deposited on unsputtered HOPG form monolayer deep etch channels, which originate from surface defects such as step edges where C–C bonds can be attacked more easily than the highly-coordinated atoms of the basal plane. The orientation of these channels is influenced by the preferential breaking of certain C–C bonds at the graphite-nanoparticle interface, giving rise to channels that are typically oriented along either the $\langle 11\bar{2}0\rangle$ or $\langle 10\bar{1}0\rangle$ set of crystallographic directions [30]. On the other hand, the layer of disordered carbon formed by Ar^+ sputtering is readily attacked, allowing the nanoparticles to channel deeply into the surface in any direction. In fact, on the sputtered surfaces the nanoparticles channel through the disordered carbon layer until the interface with the intact HOPG basal plane is reached. At this point the channeling of the nanoparticles is confined to the plane parallel to the disordered carbon/graphite interface. This is illustrated schematically in Fig. 10. In the extreme case where the surface was pre-sputtered for 60 min prior, the disordered carbon layer is so thick that the nanopar-

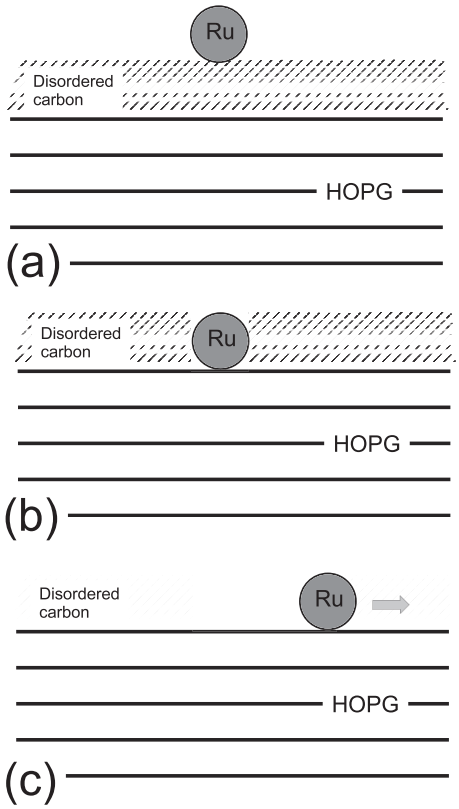

Fig. 10 – Schematic illustration showing a cross-sectional view of the interface between the disordered carbon layer formed by Ar^+ sputtering and the basal planes of the HOPG substrate. (a) The Ru nanoparticle is initially deposited on top of the disordered carbon layer. (b) During the catalysed oxidation of the surface Ru nanoparticles etch downwards through the disordered carbon layer until the interface is reached. (c) Further etching is directional and limited to the plane parallel to the interface as indicated by the arrow.

ticles can no longer be observed by STM once they have channeled into the surface.

While the unsputtered HOPG support is more stable against corrosion in an oxidising atmosphere, the sputtered surfaces are far more effective at stabilising the nanoparticles against sintering, as shown in Fig. 6. The mean size of the sintered particles decreases significantly when the nanoparticles are deposited on a pre-sputtered surface. We note that the sintering of Ru nanoparticles on unsputtered HOPG is much greater when heated in the presence of O_2 compared to heating to similar temperatures in UHV [32]. Finally, from a comparison of the data shown in Figs. 5 and 6 we can suggest four possible reasons as to why the etching process becomes deactivated at higher temperature; (1) the surface of the nanoparticles becomes poisoned by carbon from the support, (2) in the case of the disordered carbon layers the supply of loose carbon is exhausted, (3) when the nanoparticles channel into the disordered carbon layer the surface area available for O_2 adsorption is minimised and (4) the nanoparticles sinter into increasingly larger particles that may eventually become immobile due to their sheer size. We note that Baker and Chludzinski [30] demonstrated that the catalytic activity of graphite-supported Ru particles towards hydrogenation of the support is substantially reduced either by decomposing acetylene over the catalyst or heating the catalyst/support in an inert atmosphere. These experiments provide strong evidence to support the idea that carbon overlayer formation is responsible for the Ru catalyst deactivation at higher tempertaures.

5. Conclusions

The catalytic oxidation of graphite surfaces by mass-selected Ru nanoparticles was studied using STM and TPO. The main findings can be summarised as follows:

- Ar^+ ion bombardment can be used to create a layer of disordered carbon with controlled thickness on the HOPG surface. The depth of the interface between the graphite and the disordered carbon layer determines whether nanoparticles etch paths perpendicular or parallel to the surface plane.
- The etch channels are highly directional when the nanoparticles are in contact with the graphite basal plane, but follow random paths when the nanoparticles etch disordered carbon.
- The gasification temperature depends on the degree of graphitisation of the support, with more graphitic surfaces requiring higher temperatures to be catalytically etched.
- The propagation rate of the nanoparticles increases with the particle size. However, it appears that larger nanoparticles require a higher temperature to initiate gasification.

Acknowledgements

This work was supported by the Danish National Research Foundation and the EU FWP7 Marie Curie Intra-European Fellowship ESRCN (PIEF-GA-2008-220055). The use of facilities at the Center for Electron Nanoscopy (CEN) at DTU is acknowledged.

REFERENCES

[1] Moulijn JA, editor. Fundamentals of catalytic coal and carbon gasification. Fuel 1983;62(2) [Special issue].
[2] Oh SG, Baker RTK. In situ electron microscopy investigation of the behaviour of supported cobalt particles. J Catal 1991;128(1):137–47.
[3] Stegenga S, van Waveren M, Kapteijn F, Moulijn JA. Stability of carbon-supported catalysts in an oxidizing environment. Carbon 1992;30(4):577–85.
[4] Neeft JPA, Makkee M, Moulijn JA. Catalysts for the oxidation of soot from diesel exhaust gases. I. An exploratory study. Appl Catal B 1996;8(1):57–78.
[5] Neeft JPA, Makkee M, Moulijn JA. Diesel particulate emission control. Fuel Proc Technol 1996;47(1):1–69.
[6] Siroma Z, Ishii K, Yasuda K, Miyazaki Y, Inaba M, Tasaka A. Imaging of highly oriented pyrolytic graphite corrosion accelerated by Pt particles. Electrochem Commun 2005;7(11):1153–6.

[7] McKee GSB, Vecchio KS. Thermogravimetric analysis of synthesis variation effects on CVD generated multiwalled carbon nanotubes. J Phys Chem B 2006;110(3):1179–86.
[8] Chepurov AI, Sonin VM, Dereppe J-M. The channeling action of iron particles in the catalyzed hydrogenation of synthetic diamond. Diam Relat Mater 2000;9(8):1435–58.
[9] Datta SS, Strachan DR, Khamis SM, Johnson ATC. Crystallographic etching of few-layer graphene. Nano Lett 2008;8(7):1912–5.
[10] Yang RT, Wong C. Mechanism of single-layer graphite oxidation: evaluation by electron microscopy. Science 1981;214(4519):437–8.
[11] Yang RT, Wong C. Kinetics and mechanism of oxidation of basal plane on graphite. J Chem Phys 1981;75(1):4471–6.
[12] Chang H, Bard AJ. Formation of monolayer pits of controlled nanometer size on highly oriented pyrolytic graphite by gasification reactions as studied by scanning tunneling microscopy. J Am Chem Soc 1990;112(11):4598–9.
[13] Chu X, Schmidt LD. Gasification of graphite studied by scanning tunneling microscopy. Carbon 1991;29(8):1251–5.
[14] Chang H, Bard AJ. Scanning tunneling microscopy studies of carbon–oxygen reactions on highly oriented pyrolytic graphite. J Am Chem Soc 1991;113(15):5588–96.
[15] Chu X, Schmidt LD. Reactions of NO, O_2, H_2O, and CO_2 with the basal plane of graphite. Surf Sci 1992;268(1–3):325–32.
[16] Pan ZJ, Yang RT. The mechanism of methane formation from the reaction between graphite and hydrogen. J Catal 1990;123(1):206–14.
[17] McKee DW. Effect of metallic impurities on the gasification of graphite in water vapor and hydrogen. Carbon 1974;12(4):453–64.
[18] Tomita A, Tamai Y. An optical microscopic study on the catalytic hydrogenation of graphite. J Phys Chem 1974;78(22):2254–8.
[19] Keep CW, Terry S, Wells M. Studies of the nickel-catalyzed hydrogenation of graphite. J Catal 1980;66(2):451–62.
[20] Baker RTK, Sherwood RD. Catalytic gasification of graphite by nickel in various gaseous environments. J Catal 1981;70(1):198–214.
[21] Goethel PJ, Yang RT. Platinum-catalyzed hydrogenation of graphite: mechanism studied by the rates of monolayer channeling. J Catal 1986;101(2):342–51.
[22] Chu X, Schmidt LD, Chen SG, Yang RT. Catalyzed carbon gasification studied by scanning tunneling microscopy and atomic force microscopy. J Catal 1993;140(2):543–56.
[23] Konishi S, Sugimoto W, Murakami Y, Takasu Y. Catalytic creation of channels in the surface layers of highly oriented pyrolytic graphite by cobalt nanoparticles. Carbon 2006;44(11):2330–56.
[24] Dalla'Betta RA, Shelef M. Heterogeneous methanation: in situ infrared spectroscopic study of Ru/Al_2O_3 during the hydrogenation of CO. J Catal 1977;48(1–3):111–9.
[25] Madon RJ, Reyes SC, Iglesia E. Primary and secondary reaction pathways in ruthenium-catalyzed hydrocarbon synthesis. J Phys Chem 1991;95(20):7795–804.
[26] Betancourt P, Rives A, Hubaut R, Scott CE, Goldwasser J. A study of the ruthenium-alumina system. Appl Catal A: General 1998;170(2):307–14.
[27] Obuchi A, Ohi A, Nakamura M, Ogata A, Mizuno K, Ohuchi H. Performance of platinum-group metal catalysts for the selective reduction of nitrogen oxides by hydrocarbons. Appl Catal B Environ 1993;2(1):71–80.
[28] Hinrichsen O, Rosowski F, Muhler M, Ertl G. The microkinetics of ammonia synthesis catalyzed by cesium-promoted supported ruthenium. Chem Eng Sci 1996;51(10):1683–90.
[29] Song Z, Cai T, Hanson JC, Rodriguez JA, Hrbek J. Structure and reactivity of Ru nanoparticles supported on modified graphite surfaces: a study of the model catalysts for ammonia synthesis. J Am Chem Soc 2004;126(27):8576–84.
[30] Baker RTK, Chludzinski JJ. In-situ electron microscopy studies of the behaviour of supported ruthenium particles. 1. The catalytic influence on graphite gasification reactions. J Phys Chem 1986;90(20):4730–4.
[31] Goethel PJ, Yang RT. Mechanism of graphite hydrogenation catalyzed by ruthenium particles. J Catal 1988;111(1):220–6.
[32] Nielsen RM, Murphy S, Strebel C, Johansson M, Nielsen JH, Chorkendorff I. A comparative STM study of Ru nanoparticles deposited on HOPG by mass-selected gas aggregation versus thermal evaporation. Surf Sci 2009;603(24):3420–30.
[33] Nielsen RM, Murphy S, Strebel C, Johansson M, Chorkendorff I, Nielsen JH. The morphology of mass selected ruthenium nanoparticles from a magentron-sputter gas-aggregation source. J Nanopart Res 2010;12(4):1249–62.
[34] Binns C. Nanoclusters deposited on surfaces. Surf Sci Rep 2001;44(1–2):1–49.
[35] Xirouchaki C, Palmer RE. Deposition of size-selected metal clusters generated by magnetron sputtering and gas condensation: a progress review. Phil Trans R Soc Lond A 2004;362(1814):117–24.
[36] Bajales Luna N, Bonetto FJ, Vidal RA, Goldberg EC, Ferrón J. Low energy ion scattering in He/HOPG system. J Mol Catal A: Chem 2008;281(1–2):237–40.
[37] Li C, Brown TC. Carbon oxidation kinetics from evolved carbon oxide analysis during temperature-programmed oxidation. Carbon 2001;39(5):725–32.
[38] Baker RTK, Sherwood RD. Catalytic oxidation of graphite by iridium and rhodium. J Catal 1980;61(2):378–89.
[39] Kim YD, Seitsonen AP, Wendt S, Wang J, Fan C, Jacobi K, et al. Characterization of various oxygen species on an oxide surface: RuO_2(110). J Phys Chem B 2001;105(18):3752–8.
[40] Baker RTK, Sherwood RD, Dumesic JA. Catalytic hydrogenation of graphite by platinum, iridium, and platinum–iridium. J Catal 1980;66(1):56–64.
[41] Baker RTK, Sherwood RD, Dumesic JA. Catalytic gasification of graphite by bimetallic particles. J Catal 1980;62(2):221–30.

PCCP

View Online
Dynamic Article Links

Cite this: DOI: 10.1039/c1cp20371a

www.rsc.org/pccp

PAPER

Probing the crossover in CO desorption from single crystal to nanoparticulate Ru model catalysts

S. Murphy, C. Strebel, S. B. Vendelbo, C. Conradsen, Y. Tison, K. Nielsen, L. Bech, R. M. Nielsen, M. Johansson, I. Chorkendorff and J. H. Nielsen*

Received 11th February 2011, Accepted 1st April 2011
DOI: 10.1039/c1cp20371a

Using model catalysts, we demonstrate that CO desorption from Ru surfaces can be switched from that typical of single crystal surfaces to one more characteristic of supported nanoparticles. First, the CO desorption behaviour from Ru nanoparticles supported on highly oriented pyrolytic graphite was studied. Both mass-selected and thermally evaporated nanoparticles were deposited. TPD spectra from the mass-selected nanoparticles exhibit a desorption peak located around 410 K with a broad shoulder extending from around 480 K to 600 K, while spectra obtained from thermally evaporated nanoparticles exhibit a single broad feature from ~350 K to ~450 K. A room temperature deposited 50 Å thick Ru film displays a characteristic nanoparticle-like spectrum with a broad desorption feature at ~420 K and a shoulder extending from ~450 K to ~600 K. Subsequent annealing of this film at 900 K produced a polycrystalline morphology of flat Ru(001) terraces separated by monatomic steps. The CO desorption spectrum from this surface resembles that obtained on single crystal Ru(001) with two large desorption features located at 390 K and 450 K due to molecular desorption from terrace sites, and a much smaller peak at ~530 K due to desorption of dissociatively adsorbed CO at step sites. In a second experiment, ion sputtering was used to create surface defects on a Ru(0 1 54) single crystal surface. A gradual shift away from the desorption spectrum typical of a Ru(001) surface towards one resembling desorption from supported Ru nanoparticles was observed with increasing sputter time.

I. Introduction

While surface science studies of macroscopic single crystal surfaces have yielded much valuable insight into the fundamental principles of heterogeneous catalysts, the well-known materials gap between surface science and industrial catalysis exists.[1–4] Typically, industrial catalysts are much more complex in nature than the single crystal surfaces encountered in many surface science studies. A better representation of these materials can be obtained by studying an ensemble of nanoparticles supported on a well-defined planar substrate.[5–7] Such model systems can be used to investigate the effect of the particle size and the influence of the support material on reactivity. Moreover, nanoparticulate model catalysts are more suited to studying the correlation between structure and activity in structure-sensitive reactions because of the resemblance to industrial catalysts, which comprise a high density of various active sites such as edge or corner sites, as compared to single crystal surfaces where the number of equivalent step or kink sites can be outweighed by several orders of magnitude by less-active terrace sites.[8,9] As part of our efforts to understand the materials gap we have been investigating the crossover in desorption behaviour between the two model catalyst systems, *i.e.* single crystal surfaces *versus* supported nanoparticles. Here we present details of our investigation of the thermal desorption of CO from a Ru(0 1 54) single crystal surface and from Ru nanoparticles supported on highly oriented pyrolytic graphite (HOPG).

Ruthenium is a versatile catalyst, which has been particularly investigated with respect to methanation and Fischer–Tropsch synthesis.[10–12] As an elementary step in this process the adsorption of CO on single crystal Ru(001) has been studied extensively by various surface science methods.[13–22] CO adsorbs on the Ru(001) basal surface in an upright position *via* the carbon atom at all coverages up to saturation at around 2/3 of a monolayer.[23–25] The CO molecules adsorb in on-top positions up to a coverage of 1/3 of a monolayer, forming a $(\sqrt{3}\times\sqrt{3})R30^\circ$ adlayer structure.[26–28] At higher coverages, the $(\sqrt{3}\times\sqrt{3})R30^\circ$ structure is disrupted as strong repulsive interactions cause CO molecules to be displaced from on-top positions (though the exact microstructure of the higher coverage overlayers is still debated[29]).

Center for Individual Nanoparticle Functionality, Department of Physics, Technical University of Denmark, 2800 Kgs. Lyngby, Denmark. E-mail: jane@fysik.dtu.dk; Fax: +45 4593 2399

The change in adlayer structure is reflected in the CO desorption behaviour. For coverages up to 1/3 of a monolayer CO desorbs in a single peak decreasing from 480 K to 450 K with increasing coverage (α_1 peak), while for higher coverages a second peak develops around 350–400 K (α_2 peak).[18,22,30,31] In addition to these peaks, which are due to desorption of molecularly adsorbed CO, an additional much smaller peak may also be observed at around 530 K, arising from the desorption of CO that has been dissociatively adsorbed at step sites (β peak).[13,19,21,22,32] This was demonstrated by Shincho *et al.*,[13] Yamada *et al.*[19] and Zubkov *et al.*[21,22] using isotopic scrambling experiments, which rely on the recombination and desorption of atomic carbon and oxygen originating from the dissociative adsorption of CO. It was furthermore demonstrated that deposition of carbon at surface steps blocked them for dissociative adsorption of CO and resulted in the disappearance of the β peak from CO desorption spectra.[22,32]

The CO desorption from more open Ru single crystal surfaces has also been investigated and displays similarities to TPD spectra obtained from the Ru(001) plane.[33–37] For the Ru(110) plane, for example, the α_1 and α_2 peaks at similar temperatures were observed along with two β peaks attributed to dissociation of CO at different sites. The desorption of CO_2 from the Ru(110) surface at 380–450 K was furthermore observed.

If we consider the information available with regard to CO desorption from supported Ru nanoparticles, a number of studies have investigated CO desorption from Ru catalysts prepared by chemical impregnation of SiO_2 and Al_2O_3 supports.[38–42] Typically, two main features were observed in these studies, a low temperature feature located between 350 K and 475 K, and a higher temperature feature located between 600 K and 700 K.[38–42] The two features at lower temperatures agree well with the double-peak spectrum obtained from Ru(001)[18,22,30,31] and the variation in the temperatures recorded for the desorption features in the different studies could be attributed to the different heating rates used. Moreover, where desorption experiments were performed in reactors under a He carrier gas flow,[38–41] the measured desorption temperatures could also be influenced by readsorption of CO, which was found to shift desorption peaks to higher temperatures.[39] The desorption of CO_2 was also observed in some of these studies, which could be taken as evidence of CO dissociation occuring over the Ru nanoparticles.[39,40,42]

Here, we demonstrate that it is possible to link the desorption behaviour of supported nanoparticles (both mass-selected particles formed in a magnetron-sputter gas-aggregation source and vapour-deposited particles) and that of the single crystal surface using two approaches. In the first case, we demonstrate the transition from nanoparticle-like CO desorption behaviour to single-crystal surface behaviour in Ru nanoparticles supported on HOPG. In the second case, we demonstrate the reverse transition from single-crystal surface to nanoparticle-like CO desorption behaviour by means of Ar^+ ion pre-sputtering of the Ru(0 1 54) surface.

II. Experimental

The experiments were performed in three separate UHV systems. The experiments on Ru nanoparticles were performed in a multichamber ultrahigh vacuum (UHV) system (Omicron, Multiscan Lab) with a base pressure in the low 10^{-11} mbar region.[43,44] This system is equipped with facilities for combined scanning tunneling microscopy (STM) and scanning electron microscopy (SEM), as well as Auger electron spectrsocopy (AES), ion scattering spectroscopy (ISS) and temperature programmed desorption (TPD) measurements. The thermal desorption experiments on the Ru(0 1 54) surface were performed in a UHV chamber with a base pressure below 10^{-10} mbar, which is equipped with facilities for TPD and AES, as well as a high-pressure cell.[32] STM measurements on the Ru(0 1 54) surface were performed in a UHV chamber with a base pressure below 10^{-10} mbar,[45] which is equipped with X-ray photoelectron spectroscopy (XPS) and an Aarhus-type STM.[46]

A Ru nanoparticles on HOPG

The HOPG substrates (SPI-1, 7 mm × 7 mm × 0.5 mm) were cleaved in air and mounted in sample holders incorporating a pyrolytic boron nitride (PBN) radiative heater, which is capable of heating the sample to temperatures in excess of 975 K. A C-type thermocouple (W-5 at.% Re/W-26 at.% Re) was placed in contact with the substrate in order to monitor and control the sample temperature *via* a PID controller (Eurotherm 2408). Upon insertion into UHV, the samples were outgassed for several hours at 775 K to outgas adsorbed contaminants prior to use. Two different methods were used to deposit Ru nanoparticles.

In the first method, mass-selected nanoparticles were deposited from an inert-gas aggregation source (Mantis Deposition Ltd.), which is described in detail elsewhere.[43,44] Briefly, a flux of Ru atoms is produced by a magnetron sputter head, which is condensed into nanoparticles upon contact with cooled Ar gas atoms. The ionised fraction of the nanoparticle beam is filtered to select the mass of the nanoparticles to be deposited using a quadrupole mass filter, before the nanoparticles are soft-landed (*i.e.* they have a kinetic energy of $\leq$0.1 eV atom^{-1}) onto HOPG substrates. For these studies, we have investigated both as-cleaved HOPG and surfaces that have been sputtered for 15 min with 500 eV Ar^+ ions at a current density of $\sim$1 μA cm^{-2} and subsequently outgassed at 935 K. The 15 min sputtering causes defects in at least the first two layers of the surface.[47]

In the second method, Ru films were deposited on HOPG by electron-beam evaporation of a 99.99% purity Ru rod. The substrates were either as-cleaved or sputtered for 30 s with 500 eV Ar^+ ions under the same conditions as those given above. Sputtering for only 30 s produces approximately 5% of defects in the topmost surface layer. The substrate was grounded while the Ru rod was held at a positive bias of 500 V.[48] A quartz crystal balance was used to monitor the deposition rate (typically 0.46–0.9 Å min^{-1}) and estimate the final film thickness.

Ion Scattering Spectroscopy (ISS) was used to confirm the cleanliness of the HOPG substrate and the deposited Ru nanoparticles and thin films. The ISS spectra were recorded using 1 keV He^+ ions produced by a differentially pumped electron impact ion source (ISE 100, Omicron Nanotechnology). The reflected ions were detected at a 147° scattering angle with a hemispherical energy analyser.

TPD experiments were performed in the preparation chamber of the UHV system. The samples were dosed with a 1 : 1 mixture of two different isotopically labeled CO molecules, namely $^{13}C^{16}O$ (CIL, 99% ^{13}C, $<10\%$ ^{18}O)[49] and $^{12}C^{18}O$ (CIL, 2% ^{16}O). Both gases were dosed simultaneously using separate leak valves until a total chamber pressure of 2×10^{-8} mbar was attained. The ratio of the two gases was held constant by monitoring the mass spectrometer signal for each component. The samples were dosed in this manner for 10 min, corresponding to an exposure of nine Langmuir, which was sufficient to saturate the surface. It was possible to observe the saturation in the CO uptake during dosing with the mass spectrometer. The sample temperature was then ramped at a rate of 1 K s^{-1} in UHV and the CO desorption from the substrate was analysed using a differentially pumped Balzers QMA 125 quadrupole mass spectrometer. The spectrometer was equipped with an oxygen-free high conductivity (OFHC) copper sniffer tip with a 1 mm diameter aperture, which is positioned within 0.5 mm of the sample surface. This arrangement allows the local gas composition above the sample surface to be measured with negligible contribution from the sample holder or surroundings.

The isotope exchange reaction ($^{12}C^{18}O + {}^{13}C^{16}O \rightarrow {}^{12}C^{18}O + {}^{13}C^{16}O + {}^{13}C^{18}O + {}^{12}C^{16}O$) allows us to determine the relative amount of CO that has been dissociated on the surface from the TPD spectra. If the adsorbed $^{13}C^{16}O$ and $^{12}C^{18}O$ molecules dissociate on the surface, the dissociated species can scramble and recombine into the four possible CO isotopologues $^{12}C^{16}O$, $^{13}C^{16}O$, $^{12}C^{18}O$ and $^{13}C^{18}O$. The TPD mass spectrometer signals of 28 amu, 29 amu, 30 amu and 31 amu were background subtracted and integrated to find the total desorption of each isotopologue. Particular attention was paid to the $^{13}C^{18}O$ signal as this does not have a high natural background in the UHV chamber like $^{12}C^{16}O$, and does not contribute to molecular desorption like either $^{13}C^{16}O$ or $^{12}C^{18}O$. Assuming an equal probability for scrambling into each of the four products, the amount of desorbed $^{13}C^{18}O$ will account for approximately one quarter of the total amount of adsorbed CO molecules that have been dissociated.

STM was performed at room temperature in constant current mode, using electrochemically etched W tips without any in-vacuum treatments other than applying a series of voltage pulses (typically 4–9 V for 10–100 ms) or scanning for several lines with increased bias ($U \approx 2$ V) in order to condition the tip. The typical tunnel parameters used to image the particles in this study were $U = 10$–600 mV for the gap bias and $I = 0.1$–0.8 nA for the tunnel current. Slow scan speeds were adopted with a typical line scan frequency of about 0.5–1 Hz.

B Ru(0 1 54) surface

The samples used for these experiments are Ru(0 1 54) single crystals (Mateck GmbH.), which on average expose 27-atom wide (001) terraces separated by monatomic steps. Due to the hexagonal close-packed structure of Ru, the steps will be of two alternating structures, one with three-fold symmetry and the other with four-fold symmetry.[22] For the TPD experiments presented here, a Ru(0 1 54) sample was cleaned by repeated cycles of sputtering with 1 keV Ar^+ ions at 800 K for 30 min, oxidation in 10^{-7} mbar O_2 at 1100 K for 10 min, reduction in 10^{-6} mbar H_2 at 500 K for 30 min, and finally annealing to 1200 K in UHV for 1 min. The cleanliness of the sample was checked by AES and CO TPD and oxygen titration measurements (which were used to check for carbon contamination).[32] TPD measurements were performed using a (Balzers 125) quadrupole mass spectrometer fitted with a differentially pumped OFHC copper sniffer tip with a 2 mm diameter circular aperture. This orifice was positioned at a distance of 0.5 mm from the sample surface, so that only desorption from the front side of the single crystal was measured. The sample temperature was measured by means of a C-type thermocouple spot-welded to the side of the crystal. The crystal was mounted on tungsten filaments which were used to provide direct current heating. During TPD measurements the sample temperature was ramped linearly at a rate of 2 K s^{-1}. The sample was mounted in the UHV chamber out of direct line-of-sight of the ionisation gauge in order to avoid hot-filament induced chemistry.

A second Ru(0 1 54) sample was used for the STM measurements, which was cleaned using a similar procedure to that described above.[50] The sample was sputtered using 1 keV Ar^+ ions by quickly rastering a 3 mm diameter ion beam with a current density of 18 μA cm^{-2} across the sample surface. The cleanliness was checked using STM, XPS and CO TPD measurements (the TPD setup was similar to the one described above). STM measurements were performed at room temperature in constant current mode, using electrochemically etched W tips. Images were typically recorded with a gap bias of 1 V and a tunneling current of 0.4–1 nA.

III. Results

A Ru nanoparticles on HOPG

The morphology of the mass-selected nanoparticles has been described in detail elsewhere.[43,44] Depositions were carried out so that between 10% and 40% of the HOPG surface was covered by a monodisperse distribution of nanoparticles with a mean diameter in the range from 2 nm to 15 nm.[51] Transmission electron microscopy (TEM) was used to measure the particle size distributions obtained after mass filtering and it was found that the diameters of the nanoparticles were distributed within ±15% of the mean diameter. TEM measurements revealed that smaller nanoparticles displayed more well-defined facets, while larger nanoparticles were found to be irregular in shape with evidence of significant surface roughness.[44] An example of a STM image of mass-selected 9.7 nm Ru nanoparticles on HOPG is shown in Fig. 1(a). We have previously established that the morphology of nanoparticles supported on sputtered or as-cleaved HOPG is basically the same.[43] Fig. 1(b) shows the total CO desorption spectrum obtained from 9.7 nm Ru nanoparticles. The TPD spectrum is characterised by a desorption peak located around 410 K, followed by a broad shoulder extending from around 480 K to 600 K. The molecularly- and dissociatively-adsorbed components of the TPD spectrum [also shown in Fig. 1(b)] can be deconvoluted by utilising the isotope exchange reaction,

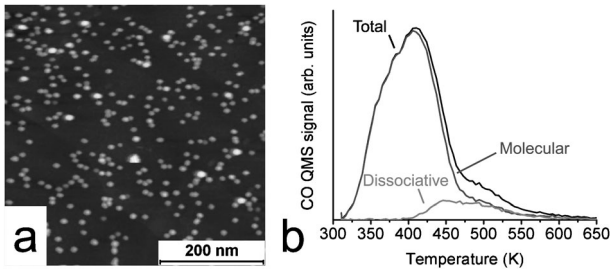

Fig. 1 STM and CO desorption from size-selected Ru nanoparticles on HOPG. (a) STM image of 9.7 nm Ru nanoparticles on sputtered HOPG. (b) CO TPD spectrum obtained from 9.7 nm Ru nanoparticles on as-cleaved HOPG, showing the total CO desorption, as well as the contributions from molecularly- and dissociatively-adsorbed CO.

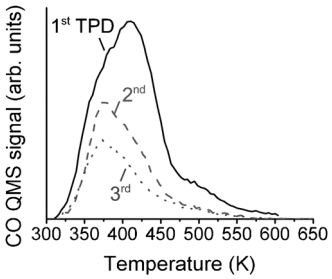

Fig. 2 Three successive CO TPD spectra obtained from 9.7 nm mass-selected Ru nanoparticles on as-cleaved HOPG, showing a drop in the desorption area.

$^{12}C^{18}O + {}^{13}C^{16}O \rightarrow {}^{12}C^{18}O + {}^{13}C^{16}O + {}^{13}C^{18}O + {}^{12}C^{16}O$, which is expected to occur after CO dissociation. It is clear that the large desorption peak located around 410 K corresponds to the molecularly desorbed component (*i.e.* mass-29 and mass-30 CO), while desorption of dissociatively adsorbed CO (here only mass-31 CO is used in the analysis), which displays peaks at 450 K and 530 K, is largely responsible for the broad shoulder up to 600 K seen in the total CO desorption spectrum.

Fig. 2 shows three successive CO TPD spectra obtained from 9.7 nm Ru nanoparticles on as-cleaved HOPG. The main desorption feature, which is located around 410 K in the first TPD, shifts to 375 K in the second and third spectra. There is also a substantial loss in the CO desorption area (63%) between the first and second TPD, and a smaller drop (30%) between the second and third TPD. This behavior was consistently observed for different nanoparticle sizes on as-cleaved and sputtered HOPG. It was usually found that the loss in desorption area became small or negligible after the second or third TPD. Three mechanisms can be identified as candidates for this deactivation: (1) sintering, (2) poisoning by loose carbon from the support, and (3) annealing-out of the initial surface roughness of the as-deposited nanoparticles. We have previously confirmed by STM that small nanoparticles (*e.g.* ~3 nm) deposited onto as-cleaved HOPG do sinter at elevated temperatures (775–975 K).[43] We have also performed oxygen titration experiments (not presented here), which indicate that carbon is present at the surface of the nanoparticles after heating to temperatures comparable to those encountered during the desorption experiments. We can therefore confirm that both of these mechanisms contribute to the deactivation of the nanoparticles, while the third proposed mechanism requires further investigation by performing annealing experiments in the TEM.

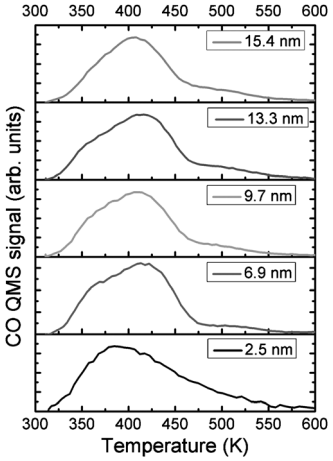

Fig. 3 CO TPD spectra obtained for different sized Ru nanoparticles supported on as-cleaved HOPG. The curves have been normalised to the same peak height.

Fig. 3 compares the total CO TPD spectra obtained from nanoparticles of different sizes supported on as-cleaved HOPG. The curves have been normalised to the same peak height in order to compare their shape. The TPD spectra are qualitatively similar being characterised by a broad desorption feature with a peak around 410–420 K and a broad shoulder extending from ~450 K to ~600 K. The low-temperature shoulder along with the high-temperature tail seems to increase as the nanoparticle size decreases, being most prominent for the 2.5 nm size. In previous studies of PVD grown Ru nanoparticles on mica, the position of the CO desorption feature was not observed to change substantially with the mean particle size.[52]

In addition to investigating the CO desorption behavior from mass-selected nanoparticles produced using the inert-gas aggregation source, we have also investigated the CO desorption behavior of PVD-grown Ru nanoparticles on HOPG. The morphology of these nanoparticles has been discussed in detail elsewhere.[43] Briefly, Ru films deposited onto as-cleaved HOPG at room temperature were found to display bimodal growth with small round nanoparticles decorating the substrate step edges and large flat nanoparticles formed on the terraces. The mean diameter of these nanoparticles was between 3 nm and 5.5 nm and their mean height was around 1.5 nm, while the spread in the measured size distributions was of the order of ±30%. On sputtered HOPG, room temperature deposition of Ru results in the formation of small round nanoparticles with a narrow size distribution. In this case, the mean particle diameter was approximately 2.3 nm and the mean height was close to 1.3 nm, while the spread in the measured particle size was ±20%. Examples of these two nanoparticle morphologies are shown in Fig. 4(a) and (c), which show STM images of 1 Å Ru films deposited on as-cleaved and sputtered HOPG, respectively. These images were obtained after CO TPD measurements were made. The average diameter of the nanoparticles from the 1 Å deposition was 5.2 ± 2.1 nm on the terraces

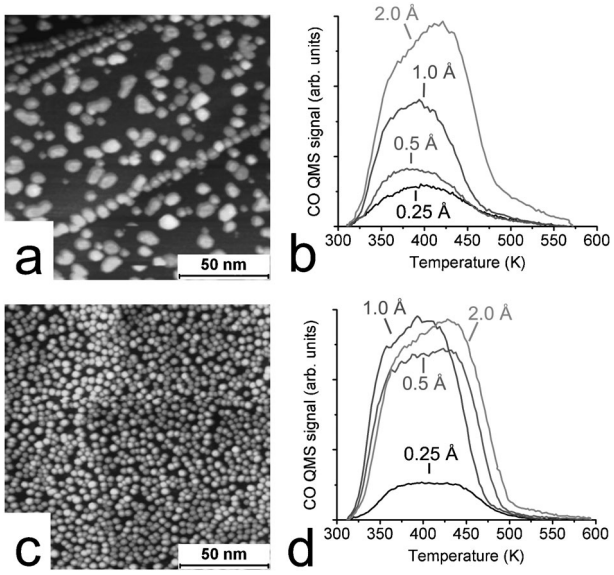

Fig. 4 STM and CO TPD measurements of Ru films deposited onto HOPG. (a) STM image of a 1 Å Ru film deposited onto as-cleaved HOPG. The average diameter of the terrace nanoparticles was 5.2 nm and their average height was 1.7 nm. (b) CO TPD spectra from 0.25–2.0 Å Ru films on as-cleaved HOPG. (c) STM image of a 1 Å Ru film deposited onto HOPG that has been pre-sputtered with 500 eV Ar^+ ions for 30 s. The average nanoparticle diameter was 2.1 nm and the average height was 1.1 nm. (d) CO TPD spectra from 0.25–2.0 Å Ru films on sputtered HOPG.

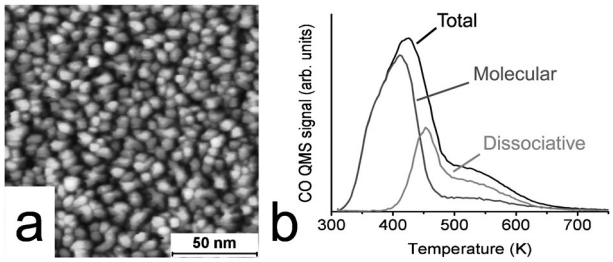

Fig. 5 (a) STM image of a 50 Å Ru film deposited on as-cleaved HOPG at room temperature. (b) The corresponding CO TPD spectrum obtained from the film, showing the total CO desorption, as well as the contributions from molecularly- and dissociatively-adsorbed CO.

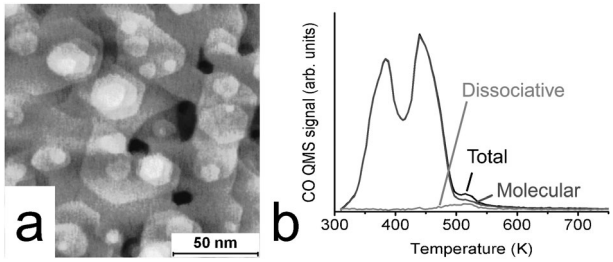

Fig. 6 (a) STM image of a 50 Å Ru film deposited on as-cleaved HOPG after annealing in UHV at 900 K for 10 min. (b) The corresponding CO TPD spectrum obtained from the film, showing the total CO desorption, as well as the contributions from molecularly- and dissociatively-adsorbed CO.

and 3.9 ± 1.0 nm along the steps, in the case of deposition on the as-cleaved HOPG surface [*cf*. Fig. 4(a)], and 2.1 ± 0.5 nm in the case of deposition on the pre-sputtered HOPG [*cf*. Fig. 4(c)]. The heights of the nanoparticles were on the order of 1–2 nm.[43] Fig. 4(b) and (d) show CO desorption spectra for different nominal film thicknesses deposited on (b) as-cleaved HOPG and (d) HOPG sputtered for 30 s with 500 eV Ar^+ ions. The desorption spectra are characterised by a single broad feature from ~350 K to ~450 K. For Ru nanoparticles deposited on as-cleaved HOPG the CO desorption area increases continuously with increasing nominal film thickness in the thickness range investigated here [see Fig. 4(b)]. This reflects the fact that the HOPG surface is gradually covered by Ru nanoparticles with increasing film thickness. By contrast, there is a substantial jump in the CO desorption area from the 0.25 Å to 0.5 Å Ru films on sputtered HOPG, after which the amount of CO desorbing from the surface remains approximately constant. In this case, the HOPG surface is partially exposed for the 0.25 Å film, but is almost completely saturated by Ru nanoparticles at a nominal film thickness of 0.5 Å [see Fig. 4(d)]. Thereafter, the total Ru surface area exposed to CO remains approximately constant for thicker films.[43] As was the case for the mass-selected nanoparticles, successive TPD spectra of the vapour-deposited nanoparticles (not shown here) also displayed deactivation of the nanoparticles between the first and second TPD measurements.

We have examined the CO desorption behaviour of these PVD-grown Ru films up to the extreme case of a 50 Å Ru thin film. Fig. 5(a) shows an image of a 50 Å Ru film deposited on as-cleaved HOPG at room temperature. The surface morphology of the film comprises nanoparticles with a mean diameter of 6 ± 2 nm. The substrate cannot be imaged by STM as the film is several layers thick. Fig. 5(b) shows the corresponding CO desorption spectrum, which shows a single broad desorption feature centered around 420 K and a broad shoulder from 500 K to 600 K. After obtaining this spectrum the film was annealed for 10 min at 900 K in UHV. The resulting film morphology, shown in Fig. 6(a), is polycrystalline with large flat terraces separated by monatomic steps. The corresponding CO desorption spectrum is shown in Fig. 6(b), and shows two desorption features at ~390 K and ~450 K. An additional, smaller peak can be seen at ~530 K. This spectrum agrees well with the typical desorption spectrum obtained from the Ru(001) facet.[18,22,30–32] The two principal peaks can be attributed to desorption of molecularly adsorbed CO from the terraces (α peaks), while the smaller peak can be attributed to desorption of dissociatively adsorbed CO from step sites (β peak).[13,22]

B Ru (0 1 54) surface

Fig. 7(a) and (b) show STM images of the non-sputtered Ru (0 1 54) surface and the same surface after sputtering for 5 min, respectively. The non-sputtered surface is characterised by terraces with a width varying between 4 nm and 10 nm, encompassing the expected average terrace width of 6.5 nm (corresponding to 27 atoms), and separated by straight monatomic steps with a measured height of 0.21 ± 0.01 nm, which is in good agreement with the distance between the (001) planes of ruthenium. In comparison, the steps on the sputtered surface display a high degree of roughness, while small islands are

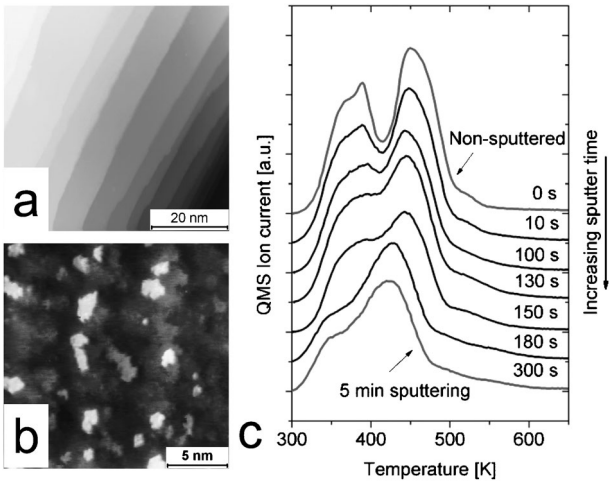

Fig. 7 STM and CO TPD measurements from a Ru(0 1 54) single crystal surface before and after Ar^+ ion sputtering. (a) STM image of the clean non-sputtered Ru(0 1 54) surface. (b) STM image of the same surface after sputtering with 1 keV Ar^+ ions for 5 min. (c) Sequence of CO TPD spectra obtained from the Ru(0 1 54) surface after sputtering with 1 keV Ar^+ ions for increasing periods of time.

evident on the terraces, which are presumably formed by surface restructuring as a result of the sputtering process.

Fig. 7(c) shows a sequence of CO desorption spectra obtained from the Ru(0 1 54) surface after different periods of sputtering with 1 keV Ar^+ ions at room temperature. The CO desorption spectrum from the non-sputtered surface shows two desorption peaks located at 390 K and 460 K that are characteristic of CO desorption from (001) terraces (α_1- and α_2-peaks) and a peak at $\sim$535 K corresponding to the dissociative adsorption at step sites (β-peak).[18,22,30–32] However, with increased surface sputtering a gradual transition is observed between the double-peak spectrum towards a single broad feature centered around 420 K. The desorption feature seen at 390 K on the non-sputtered surface gradually disappears with increased sputtering time until it is no more than a shoulder on the low-temperature side of the main desorption feature seen for the 5 min sputtered surface. In addition, the peak at 460 K on the non-sputtered surface gradually shifts down in temperature with increased sputtering time until the feature is located around 420 K.

It should be pointed out once again that the STM and TPD data of the Ru(0 1 54) surface presented here were obtained in two different UHV systems. However, in both cases the cleanliness of the surface before and after sputtering was confirmed (by XPS in the case of the STM measurements, and by AES and oxygen titration measurements in the case of the TPD experiments) to ensure that a contamination level below $\sim$1% was obtained. Moreover, CO TPD measurements were also performed in the STM system, which yielded qualitatively similar results to those presented here.

IV. Discussion

A Comparison of desorption energies

As demonstrated in Section IIIA the isotope exchange reaction unambiguously identifies molecular desorption being responsible for the main desorption feature at 410–420 K, while dissociative adsorption is responsible for smaller features at 430 K and 500 K. For comparison, Table 1 gives a summary of the CO desorption features reported from various studies (including this study) of supported Ru nanoparticles and single crystal surfaces. For the purposes of comparing our results to literature values, desorption energies based on the data presented in Table 1 are calculated and presented together in Fig. 8. The desorption features were classified into two categories corresponding to molecular (first-order) and dissociative (second-order) adsorption on the basis of the literature surveyed in Section I. The first-order desorption energies were calculated using the Redhead equation[53] and assuming a pre-exponential factor of 10^{13} s^{-1}. The second-order desorption energies were solved iteratively using the equation:[54]

$$E_{\mathrm{des}}(\theta) = RT_{\mathrm{p}} \ln\left(\frac{2\theta\nu(\theta)RT_{\mathrm{p}}^2}{E_{\mathrm{des}}(\theta)\beta}\right) \quad (1)$$

where T_{p} is the desorption peak temperature, θ is the remaining CO coverage (assumed to be half the initial coverage) and R is the gas constant. The desorption energy E_{des} and the pre-exponential factor ν are both assumed to be constant with coverage, where $\nu = 10^{13}$ s^{-1}.

From our CO TPD experiments on graphite-supported nanoparticles, we calculate desorption energies of 112–113 kJ mol^{-1}, which agree reasonably well with the values calculated from previous studies of oxide-supported nanoparticles,[38–42] particularly

Table 1 Summary of CO desorption features from saturation coverages of CO on various supported Ru nanoparticles and single crystal surfaces. The peak temperatures for the different desorption features and the heating rate are listed. Temperature intervals for some features have been indicated by hyphenated values. The desorption features have been classified into two categories; T_α representing molecular desorption and T_β representing dissociative adsorption

System	T_α/K	T_β/K	Heating rate/K s^{-1}
Ru NPs/HOPG[a]	410-420	450, 530	1
50 Å Ru/HOPG (as-deposited)[a]	420	450, 530	1
50 Å Ru/HOPG (annealed)[a]	390, 450	530	1
Ru/mica[52]	$\sim$410		1.5
Ru/Al_2O_3[38]	375	475, 600–630	1
Ru/Al_2O_3[39]	460	620	1
Ru/SiO_2[40]	450	650	1.5
Ru/SiO_2[41]	405, 473	698	0.17
(001)[18,30]	405-420, 465-480		5
(109)[22]	400, 450	535	2
(0 1 54)[32]	$\sim$390, $\sim$460	535	2
(0 1 54) non-sputtered[a]	$\sim$390, $\sim$460	535	2
(0 1 54) sputtered[a]	$\sim$420		2
Ru(S)-[15(001)×2(100)][20]	400, 470	520	9
(1 $\bar{1}$ 10)[13]	460	$\sim$580	15
(2 $\bar{1}$ 10)[19]	$\sim$460	$\sim$530	7.7
(2 $\bar{1}$ 22)[19]	$\sim$470	$\sim$530	5.2
(101)[33]	$\sim$480	$\sim$520	30
(100)[34]	$\sim$403, $\sim$495		8
(100)[35]	350, 380, 500		4
(100)[36]	375, $\sim$400, $\sim$500		8.7
(110)[37]	400, 440-460	500, 540	3

[a] This work.

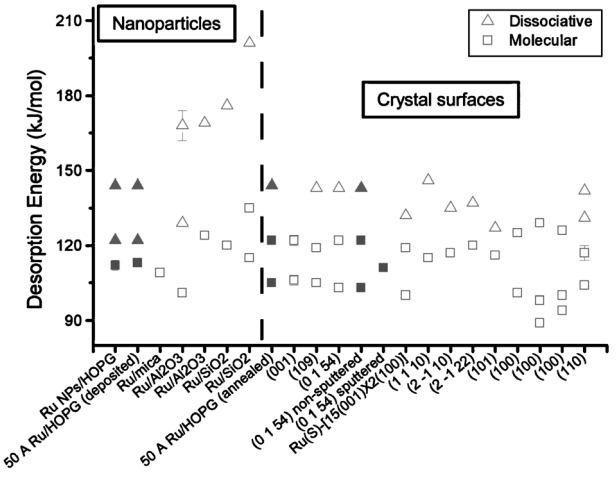

Fig. 8 Summary of the desorption energies calculated using the data presented in Table 1. Open symbols are data taken from previous studies, while filled symbols are taken from the present study. Temperature intervals for certain features are indicated by error bars.

with the case of PVD-grown nanoparticles on mica, see Fig. 8.[52] On the other hand, the desorption energies for dissociatively adsorbed CO (122 kJ mol^{-1} and 144 kJ mol^{-1}) calculated for our graphite supported nanoparticles are much lower than those estimated from the data available from these other studies, where a high temperature desorption feature was typically observed between 600 K and 700 K, corresponding to desorption energies around 164–201 kJ mol^{-1}. The origins of these high temperature peaks were investigated by McCarty and Wise[38] who used isotopic scrambling of $^{13}C^{16}O$ and $^{12}C^{18}O$ to investigate the dissociation of CO over Ru/Al_2O_3. While they observed isotope exchange at ~475 K (129 kJ mol^{-1}), which is in reasonable agreement with the results obtained in the present study, they also observed an unusual behaviour at ~600 K where the levels of ^{18}O containing isotopologues ($^{12}C^{18}O$ and $^{13}C^{18}O$) were found to decrease, while the levels of ^{16}O containing isotopologues ($^{12}C^{16}O$ and $^{13}C^{16}O$) increased. This indicated that an excess of ^{16}O was being derived from some source, though the Al_2O_3 support was ruled out as a potential source on the basis of blank TPD measurements. As a result, the nature of the higher temperature desorption feature observed between 600 K and 700 K in most of these studies has not been adequately explained and may be linked to the method of preparing the catalyst, *i.e.* wet impregnation.

B Origins of the nanoparticle desorption spectra

Compared to the single crystal surfaces, the desorption energies calculated for both molecularly- and dissociatively-adsorbed CO on the supported nanoparticles in the present study generally fall within the range of energies calculated for both the basal Ru surface and for more open surfaces. This may be attributed to the fact that the nanoparticles expose facets with different orientations. In the simplest representation of the nanoparticle shape, *i.e.* the Wulff construction, the nanoparticles will principally comprise (001), (101) and (100) facets, as these have the lowest surface free energy.[44,55] Consequently, the desorption spectra should mainly contain contributions from these facets. However, we have previously shown that the shape of the mass-selected Ru nanoparticles departs from the Wulff construction,[44] and consequently the CO desorption behaviour is expected to be more complex than one based on this simple model. In addition to the orientation of the facets exposed on the nanoparticle surface, their size may also influence the desorption spectra. For example, it has been shown that the double-peak molecular desorption feature characteristic of the Ru(001) facet appears to be inhibited on stepped Ru single crystal surfaces when the average terrace width is sufficiently narrow.[13,19] Shincho *et al.*[13] found a single desorption feature during CO desorption from a Ru(S)-[5(001)×(110)] surface comprising five-atom wide (001) terraces,[56] whereas Westre *et al.*[20] and Zubkov *et al.*[22] observed two desorption features during desorption from saturated CO coverages on Ru(S)-[15(001)×2(100)] and Ru(S)-[9(001)×2(101)] surfaces comprising fifteen- and nine-atom wide (001) terraces, respectively. There are two possible explanations for this: (1) the terraces are too small to accommodate the ordered overlayer structures found on extended (001) facets and (2) a localised lattice strain is produced in the vicinity of steps, which has been shown to influence CO adsorption.[57] In the case of nanoparticles, where facet sizes can be comparably small to the terrace widths found on highly stepped single crystal surfaces, both of these mechanisms may play a role in determining the CO desorption behaviour from the nanoparticle surface. In Fig. 4, a change in the desorption spectrum may be present for the smallest (*i.e.* 2.5 nm) of the nanoparticles with an increase in the low-temperature shoulder and in the high-temperature tail. This suggests that different sites are relatively more abundant on the very small nanoparticles. Detailed investigations of several mass-selected nanoparticle sizes in the 1–5 nm range are needed before conclusions can be made, but it is interesting to note that carbon-supported cobalt nanoparticles, which—just like ruthenium—are catalysts for the Fischer–Tropsch (FT) reaction, show an increase in FT activity for the very small sizes.[58]

It should also be pointed out that pre-adsorption of a small amount of O_2 or H_2O onto the Ru(001) surface prior to CO adsorption can substantially shift the TPD spectrum from the double-peak spectrum to a spectrum similar to that obtained from supported nanoparticles.[59,60] However, in the present study ISS measurements performed on the nanoparticles both before and after the TPD experiments showed no evidence of oxygen (*i.e.* below the detection limit of 1% of a monolayer). This indicates that the shape of the TPD spectra is related to the structure of the clean nanoparticle surface. We therefore conclude that the TPD spectrum obtained from the nanoparticles can be linked to a combination of the compact facet size on the nanoparticle surface, and the fact that more open facets may be exposed. This is particularly true when the shape of the nanoparticles departs from the equilibrium shape. Moreover, we observe two features corresponding to desorption of dissociatively adsorbed CO at 450 K and 530 K (desorption energies of 122 kJ mol^{-1} and 144 kJ mol^{-1}, respectively), which point to the presence of two main dissociation sites for CO on the nanoparticle surface.

C Crossover in desorption behaviour

A key result of the present study is that we have been able to demonstrate the crossover in CO desorption behaviour between Ru nanoparticles and the basal Ru surface simply by annealing a PVD-grown thin film to high temperature. The fact that we observe dissociative CO adsorption both before and after annealing the film proves that the surface remains free of carbon from the support, which would otherwise block the undercoordinated sites responsible for CO dissociation on the surface.[22,32] A key element in the formation of the polycrystalline film in Fig. 6 is that an epitaxial relationship exists between the vapour deposited Ru and the HOPG surface. In the case of the mass-selected nanoparticles discussed earlier, no such epitaxial relationship is obtained since the nanoparticles are formed before deposition and assume random orientations when landed on the surface. As expected, it was therefore not possible to obtain a morphology like that shown in Fig. 6(a) by annealing a thin film of mass-selected nanoparticles at 900 K. However, we believe that this should in principle be possible if higher anneal temperatures are used, which was not possible with the existing experimental set-up.

It was also possible to demonstrate the reverse transition in desorption behaviour between that of the basal Ru surface and that of Ru nanoparticles by sputtering a single crystal surface. As the amount of sputtering increases the amount and type of surface sites change as probed by the CO TPDs in Fig. 7(c). It is seen that the amount of step sites giving rise to the small shoulder at 510 K for the non-sputtered surface increases with more sputtering and changes into a broad feature ranging from below 500 K to at least 600 K for the most sputtered surface. This indicates that the sputtering introduces more undercoordinated sites, and that different kinds of sites exist giving rise to different desorption temperatures of dissociatively adsorbed C and O. More detailed STM studies of the sputtered surface would be required to identify the different site configurations.

It was found that the molecular desorption feature at 390 K gradually disappears, while the desorption feature at 460 K, corresponding to more strongly bound molecular CO, shifts downwards in temperature with increased sputtering. This can be rationalized as an effect of having smaller average terrace sizes on the sputtered surface. As mentioned earlier, the terraces may be too small to accommodate the ordered overlayer structures found on extended (001) facets. Also, it has previously been suggested by Jakob *et al.*[57] that the region 1–2 nm from the step exhibits a compressed lattice, which would result in a weaker binding of CO.[61] With a higher abundance of terrace sites in close proximity to a step, more weakly bonded CO would be expected, in excellent agreement with our CO TPDs.

It is observed that desorption of CO from the sputtered surface starts immediately upon heating from room temperature, whereas the desorption from the non-sputtered surface does not start until around $\sim$20 K above room temperature. This indicates that our CO TPD spectra from the sputtered surfaces do not probe all sites available on the surface, as the TPD spectrum from the non-sputtered surface appears to do. As such, one should not attempt to rationalise the apparent trend in Fig. 7(c) that the total CO desorption area decreases with increased sputtering time, until TPD experiments starting from below room temperature are performed.

V. Summary

We have compared the CO desorption characteristics of a stepped Ru(001) single crystal with Ru nanoparticles supported on graphite and have established the crossover in CO desorption behaviour between the two. Our main findings were:

- Mass-selected Ru nanoparticles deposited on HOPG display a single CO desorption feature around 410–420 K followed by a broad shoulder from 480 K to 600 K. Utilising the isotope exchange reaction we have established that the larger peak at 410–420 K is principally due to molecularly desorbing CO, while the shoulder is due to desorption of dissociatively adsorbed CO.
- Successive TPD measurements result in deactivation of the nanoparticles due to sintering and/or poisoning of the catalyst surface by carbon from the support. A possible third deactivation mechanism involves annealing-out the non-equilibrium surface features of the nanoparticles.
- Ru nanoparticles grown on HOPG by vapour deposition display broadly the same characteristics as the mass-selected nanoparticles. Moreover, by annealing a PVD-grown thin film we demonstrate a crossover in CO desorption spectra from that characteristic of supported nanoparticles to one characteristic of a stepped Ru(001) single crystal surface.
- Starting from a stepped Ru(001) single crystal surface we have also demonstrated the reverse transition from single crystal to nanoparticle-like CO desorption behaviour by means of Ar^+ ion sputtering.

We have shown that it is possible to vary the desorption behaviour between the two model catalyst systems by using straightforward sample preparation methods. These results demonstrate the complementary nature of both model catalyst systems and affirm the validity of studying both in order to narrow the materials gap to more complex industrial catalysts. With further work, for example using more well-defined Wulff constructed nanoparticles or mesoscale crystals,[62] even greater insight into the crossover between the desorption behavior of single crystal surfaces and supported nanoparticles can be obtained.

This work was supported by the Danish National Research Foundation and the EU FWP7 Marie Curie Intra-European Fellowship ESRCN (PIEF-GA-2008-220055).

References

1 D. W. Goodman, *Chem. Rev.*, 1995, **95**, 523.
2 G. A. Somorjai, R. L. York, D. Butcher and J. Y. Park, *Phys. Chem. Chem. Phys.*, 2007, **9**, 3500.
3 H. Oosterbeek, *Phys. Chem. Chem. Phys.*, 2007, **9**, 3570.
4 J. Assmann, V. Narkhede, N. A. Breuer, M. Muhler, A. P. Seitsonen, M. Knapp, D. Crihan, A. Farkas, G. Mellau and H. Over, *J. Phys.: Condens. Matter*, 2008, **20**, 184017.
5 C. R. Henry, *Surf. Sci. Rep.*, 1999, **31**, 231.
6 H. J. Freund, H. Kuhlenbeck, J. Libuda, G. Rupprechter, M. Bäumer and H. Hamann, *Top. Catal.*, 2001, **15**, 201.
7 S. Haq and R. Raval, *Phys. Chem. Chem. Phys.*, 2007, **9**, 3641.
8 S. Dahl, P. A. Taylor, E. Törnqvist and I. Chorkendorff, *J. Catal.*, 1998, **178**, 679.

9 S. Dahl, A. Logadottir, R. C. Egeberg, J. H. Larsen, I. Chorkendorff, E. Törnqvist and J. K. Nørskov, *Phys. Rev. Lett.*, 1999, **83**, 1814.
10 R. A. Dalla'Betta and M. Shelef, *J. Catal.*, 1977, **48**, 111.
11 H. Abrevaya, M. J. Cohn, W. M. Targos and H. J. Robota, *Catal. Lett.*, 1990, **7**, 183.
12 R. J. Madon, S. C. Reyes and E. Iglesia, *J. Phys. Chem.*, 1991, **95**, 7795.
13 E. Shincho, C. Egawa, S. Naito and K. Tamaru, *Surf. Sci.*, 1985, **149**, 1.
14 J. C. Fuggle, E. Umbach, P. Feulner and D. Menzel, *Surf. Sci.*, 1977, **64**, 69.
15 H. Pfnür, P. Feulner, H. A. Engelhardt and D. Menzel, *Chem. Phys. Lett.*, 1978, **59**, 481.
16 P. Feulner, H. A. Engelhardt and D. Menzel, *Appl. Phys.*, 1978, **15**, 355.
17 J. A. Schwarz and S. R. Kelemen, *Surf. Sci.*, 1979, **87**, 510.
18 H. Pfnür, P. Feulner and D. Menzel, *J. Chem. Phys.*, 1983, **79**, 4613.
19 T. Yamada, Y. Iwasawa and K. Tamaru, *Surf. Sci.*, 1989, **223**, 527.
20 E. D. Westre, D. E. Brown, J. Kutzner and S. M. George, *Surf. Sci.*, 1994, **302**, 280.
21 T. Zubkov, G. A. Morgan and J. T. Yates, *Chem. Phys. Lett.*, 2002, **362**, 181.
22 T. Zubkov, G. A. Morgan, J. T. Yates, O. Kühlert, M. Lisowski, R. Schillinger, D. Fick and H. J. Jänsch, *Surf. Sci.*, 2003, **526**, 57.
23 T. E. Madey, *Surf. Sci.*, 1979, **79**, 575.
24 G. E. Thomas and W. H. Weinberg, *J. Chem. Phys.*, 1979, **70**, 1437.
25 H. Pfnür, D. Menzel, F. M. Hoffmann, A. Ortega and A. M. Bradshaw, *Surf. Sci.*, 1980, **93**, 431.
26 E. D. Williams and W. H. Weinberg, *Surf. Sci.*, 1979, **82**, 93.
27 G. Michalk, W. Moritz, H. Pfnür and D. Menzel, *Surf. Sci.*, 1983, **129**, 92.
28 H. Pfnür and D. Menzel, *Surf. Sci.*, 1984, **148**, 411.
29 P. Jakob, *J. Chem. Phys.*, 2004, **120**, 9286.
30 S. Kneitz, J. Gemeinhardt and H. P. Steinrück, *Surf. Sci.*, 1999, **440**, 307.
31 S. H. Payne, J. S. McEwen, H. J. Kreuzer and D. Menzel, *Surf. Sci.*, 2005, **594**, 240.
32 S. B. Vendelbo, M. Johansson, D. J. Mowbray, M. P. Andersson, F. Abild-Pedersen, J. H. Nielsen, J. K. Nørskov and I. Chorkendorff, *Top. Catal.*, 2010, **53**, 357.
33 P. D. Reed, C. M. Comrie and R. M. Lambert, *Surf. Sci.*, 1976, **59**, 33.
34 R. Ku, N. A. Gjostein and H. P. Bonzel, *Surf. Sci.*, 1977, **64**, 465.
35 G. Lauth, T. Solomun, W. Hirschwald and K. Christmann, *Surf. Sci.*, 1989, **210**, 201.
36 G. Rotaris, A. Baraldi, G. Comelli, M. Kiskinova and R. Rosei, *Surf. Sci.*, 1996, **359**, 1.
37 J. Wang, Y. Wang and K. Jacobi, *Surf. Sci.*, 2001, **488**, 83.
38 J. G. McCarty and H. Wise, *Chem. Phys. Lett.*, 1979, **61**, 323.
39 G. G. Low and A. T. Bell, *J. Catal.*, 1979, **57**, 397.
40 E. Zağli and J. L. Falconer, *J. Catal.*, 1981, **69**, 1.
41 H. M. Miura, M. L. McLaughlin and R. D. Gonzalez, *J. Catal.*, 1983, **79**, 227.
42 N. Kakuta and J. M. White, *J. Catal.*, 1986, **97**, 150.
43 R. M. Nielsen, S. Murphy, C. Strebel, M. Johansson, J. H. Nielsen and I. Chorkendorff, *Surf. Sci.*, 2009, **603**, 3420.
44 R. M. Nielsen, S. Murphy, C. Strebel, M. Johansson, I. Chorkendorff and J. H. Nielsen, *J. Nanopart. Res.*, 2010, **12**, 1249.
45 J. H. Nielsen, L. Bech, K. Nielsen, Y. Tison, K. P. Jørgensen, J. L. Bonde, S. Horch, T. F. Jaramillo and I. Chorkendorff, *Surf. Sci.*, 2009, **603**, 1182.
46 F. Besenbacher, E. Lægsgaard, K. Mortensen, U. Nielsen and I. Stensgaard, *Rev. Sci. Instrum.*, 1988, **59**, 1035.
47 S. Murphy, R. M. Nielsen, M. Johansson and J. H. Nielsen, *Carbon*, 2011, **49**, 376.
48 Therefore, some surface defects may have been formed on the HOPG by accelerated positive Ru ions coming from the electron-beam evaporator.
49 Our measurements indicated a concentration of approximately 1% $^{13}C^{18}O$ in the $^{13}C^{16}O$ dosing gas.
50 The only differences were that the reduction step was carried out for 20 min and the final anneal step in UHV was carried out at 1400 K for 2 min.
51 The corresponding diameter of a sphere with the selected mass is used to identify the nanoparticles.
52 C. Park, W. G. Durrer, H. Poppa and J. T. Dickinson, *J. Catal.*, 1985, **95**, 361.
53 P. A. Redhead, *Vacuum*, 1962, **12**, 203.
54 I. Chorkendorff and J. W. Niemantsverdriet, *Concepts of Modern Catalysis and Kinetics*, Wiley, 2007.
55 J. Gavnholt and J. Schiøtz, *Phys. Rev. B: Condens. Matter*, 2008, **77**, 035404.
56 Here we have used the notation for stepped surfaces to describe the Ru(1 1 10) surface.
57 P. Jakob, M. Gsell and D. Menzel, *J. Chem. Phys.*, 2001, **114**, 10075.
58 G. L. Bezemer, J. H. Bitter, H. P. C. E. Kuipers, H. Oosterbeek, J. E. Holewijn, X. Xu, F. Kapteijn, A. J. van Dillen and K. P. de Jong, *J. Am. Chem. Soc.*, 2006, **128**, 3956.
59 H. I. Lee, B. E. Koel, W. M. Daniel and J. M. White, *J. Catal.*, 1982, **74**, 192.
60 K. L. Kostov, H. Rauscher and D. Menzel, *Surf. Sci.*, 1992, **278**, 62.
61 M. Mavrikakis, B. Hammer and J. K. Nørskov, *Phys. Rev. Lett.*, 1998, **81**, 2819.
62 N. Tian, Z. Y. Zhou, S. G. Sun, Y. Ding and Z. L. Wang, *Science*, 2007, **316**, 732.

PCCP

View Online / Journal Homepage / Table of Contents for this issue
Dynamic Article Links

Cite this: *Phys. Chem. Chem. Phys.*, 2012, **14**, 8005–8012

www.rsc.org/pccp

PAPER

Probing the active sites for CO dissociation on ruthenium nanoparticles

Christian Strebel, Shane Murphy, Rasmus M. Nielsen, Jane H. Nielsen and Ib Chorkendorff*

Received 7th February 2012, Accepted 29th March 2012
DOI: 10.1039/c2cp40369b

The active sites for CO dissociation were probed on mass-selected Ru nanoparticles on a HOPG support by temperature programmed desorption spectroscopy using isotopically labelled CO. Combined with transmission electron microscopy we gain insight on how the size and morphology of the nanoparticles affect the CO dissociation activity. The Ru nanoparticles were synthesized in a UHV chamber by gas-aggregation magnetron sputtering in the size range from 3 to 15 nm and the morphology was investigated *in situ* by scanning tunneling microscopy and *ex situ* by high resolution transmission electron microscopy. Surprisingly, it was found that larger particles were more active per surface area for CO dissociation. It is suggested that this is due to larger particles exposing a more rough surface than the smaller particles, giving rise to a higher relative amount of under-coordinated adsorption sites on the larger particles. The induced surface roughness is proposed to be a consequence of the growth processes in the gas-aggregation chamber.

1 Introduction

Heterogeneous catalysis is a surface phenomenon, so accordingly the surface-to-volume ratio must be maximized to utilize the active material most efficiently, and the active material is thus typically highly dispersed into nanoparticles on a high surface area support. Apart from gaining surface area, decreasing the particle size below ~10 nm significantly changes the structure as well as the catalytic properties of metal nanoparticles, and in this size range the catalytic properties have in many cases been reported to be strongly dependent on the particle size.[1–6] A clear example is the size dependence of low temperature CO oxidation over supported Au nanoparticles, which shows a remarkable increase in turnover frequency when the particle diameter is reduced below ~5 nm,[7,8] reaching a maximum at ~2–3 nm.[9] CO oxidation over supported Ru nanoparticles in the range of 2–6 nm has on the other hand been shown to increase with increasing particle size.[10] It has also been shown that the Fischer–Tropsch reaction over supported Co nanoparticles is strongly size dependent and it was demonstrated that the activity drops when the particle diameter is reduced below 6–8 nm.[11] The origin of the size dependence observed in the aforementioned examples as well as the nature of the active sites are still under debate in the literature and are currently being studied intensively.

For decades, the origin of the structure dependence of different chemical reactions over various metal surfaces has been investigated in detail by reducing complexity to a minimum, studying well-defined single crystals as model catalysts under ultra-high vacuum (UHV) conditions by surface science techniques.[12–15] N_2 dissociation on Ru, the rate-limiting step in ammonia synthesis, was found to be extremely structure sensitive with nine orders of magnitude higher adsorption rate at step sites (so-called B_5 sites) relative to the facets on the Ru(001) surface.[16,17] Recently, these B_5 sites were also shown to be active for N_2 dissociation on Ru nanoparticles.[18] Additionally, a recent computational study on the structure and reactivity of Ru nanoparticles for ammonia synthesis by Gavnholt and Schiøtz combined detailed structural calculations with calculated single site activities and found the optimal particle diameter to be approximately 3 nm.[19] In the case of CO dissociation, which is believed to be the rate-limiting step in both methanation and Fischer–Tropsch synthesis, it has been found by thermal desorption studies and density functional theory (DFT) calculations to occur predominantly at step sites on close packed Ru single crystal surfaces,[20–25] but more open surfaces have also been reported to be active.[26–28] The influence of monoatomic steps and defect sites for the methanation reaction was investigated by Vendelbo *et al.* on the Ru(0 1 54) (Ru(001) with 4% steps) surface, and it was shown that under-coordinated sites such as steps and kinks were the active sites, thus concluding that the methanation reaction over Ru is structure sensitive.[29] These studies demonstrate the sensitivity of the catalytic behaviour to the atomic structure and the important role of under-coordinated surface sites. Detailed insight on structure sensitivity is thus highly relevant for understanding the reactivity of nanoparticles as the structure of nanoparticles is more composite. Equilibrium shaped crystalline nanoparticles predominantly expose the low index facets along with under-coordinated sites which may also be

Center for Individual Nanoparticle Functionality, Technical University of Denmark, 2800 Kgs. Lyngby, Denmark. E-mail: ibchork@fysik.dtu.dk

found on their single crystal counterpart, whereas highly under-coordinated surface atoms like edges and corners cannot directly be described by a single crystal model system, as is the case with any support effects. For equilibrium shaped particles the size and crystal structure will dictate the morphology and decreasing the particle size will inherently increase the concentration of corner and edge atoms and other under-coordinated atoms due to edge reconstructions and the existence of partially filled facets or ad-atoms. However, the results presented in this paper show that the particles have rough surfaces and non-equilibrium shapes. The concentration of active sites is therefore governed by the degree of surface roughness and not by particle size.

Model catalyst systems consisting of mass selected nanoparticles deposited on well-defined planar supports can act as a link between reactivity studies on single crystals and high surface area support catalysts. The model system can simulate the complexities of reactions on supported catalysts, and has the advantage that this approach facilitates greater control over particle size distribution and support structure and enables a detailed structural and compositional analysis through already known surface science techniques. Such detailed control and analysis can be challenging on high surface area catalysts. Such model systems are therefore well suited to investigate the effect of particle size and support material on the reactivity.[30–35]

Recently, we have investigated the morphology of mass selected Ru nanoparticles by scanning tunnelling microscopy (STM) and transmission electron microscopy (TEM)[36] and compared the CO desorption behaviour of Highly Ordered Pyrolytic Graphite (HOPG) supported Ru nanoparticles to that of a Ru single crystal by a method that allowed us to follow the gradual change from single crystal like behaviour to nanoparticle like behaviour and *vice versa*.[37]

In this paper, we probe the active sites for CO dissociation on mass-selected Ru nanoparticles on a HOPG support. The sample preparation as well as sample characterisation, CO dosing and desorption measurements were performed under UHV conditions, which allow excellent control over particle size, composition and cleanliness without the need for removing surfactants or other contaminants. In the following we will show that the activity per surface area for CO dissociation on Ru particles with diameters of 3–15 nm increases with increasing particle size. These findings are based on thermal desorption experiments while monitoring the isotopic exchange reaction using isotopically labeled CO, combined with structural characterization by *in situ* STM and by *ex situ* TEM. The increase in activity is correlated to the surface roughness since the shape of larger nanoparticles is more non-equilibrated, thereby exposing a higher proportion of under-coordinated active sites for CO dissociation. It is proposed that the non-equilibrium shape is due to the particle formation process.

2 Experimental

The experiments were performed in a multichamber ultrahigh vacuum (UHV) system (Omicron, Multiscan Lab) with a base pressure in the 10^{-11} mbar region. The system is equipped with facilities for STM, scanning electron microscopy (SEM), Auger electron spectroscopy (AES), ion scattering spectroscopy (ISS) and temperature programmed desorption (TPD) measurements. The HOPG substrates (SPI-1, 7 mm × 7 mm × 0.5 mm) were cleaved in air and mounted on sample holders incorporating a pyrolytic boron nitride (PBN) radiative heater, which is capable of heating the sample to temperatures in excess of 700 °C. A W–5 at% Re/W–26 at% Re thermocouple was placed in contact with the substrate in order to monitor and control the sample temperature *via* a PID controller (Eurotherm 2408). Upon insertion into UHV, the samples were outgassed for >5 hours at 500 °C to outgas adsorbed contaminants prior to use. The influence of the degree of graphitisation of the support on the catalyst behaviour was investigated by comparing non-sputtered HOPG surfaces with those that had been sputtered with 500 eV Ar^+ ions at a target current density of ~1 μA cm^{-2} for 15 min. The sputtered surfaces were heated to 527 °C for a further 15 min to de-gas the surface from implanted Ar prior to nanoparticle deposition.

Gas aggregated mass-selected Ru particles were deposited onto the HOPG substrates at room temperature using an inert gas-aggregation source (Mantis Deposition Ltd., Nanogen 50). A full description of the source and the deposition layout is given elsewhere.[36,38] In brief, nanoparticles are formed by gas-phase condensation of a flux of Ru atoms that are sputtered from a 99.99% pure Ru target using a magnetron sputter source. The magnetron is housed in a liquid nitrogen cooled enclosure with a small aperture at one end. Argon gas is introduced locally around the magnetron and is pumped away *via* the aperture. The relatively cold argon gas thermalises the sputtered Ru atoms so that they condense into clusters and afterwards grow into nanoparticles. The size of the nanoparticles is determined by a number of factors such as sputter power, Ar pressure controlled by the flow rate, distance between the target and the exit aperture and the diameter of the exit aperture (held fixed in this study). The source parameters were optimized for each deposition to produce ruthenium nanoparticles with diameters in the range of 3–15 nm. The nanoparticles exiting the aggregation zone are passed through a quadrupole mass filter (QMF) where the negatively ionized fraction of the particles is filtered according to their mass-to-charge ratio.† The quadrupole mass filter settings were optimized to obtain a particle diameter resolution of $(\Delta d/d) \pm 6\%$. A higher resolution in the particle diameter is achievable with the quadrupole, but at the expense of the deposition rate. The beam of negatively ionized mass-filtered nanoparticles is condensed and focused by a series of electrostatic lenses onto the sample, which is located in a separate chamber connected to the aggregation source. The substrate is placed at a small positive bias (~36 V) so that the nanoparticles are attracted to and yet soft-landed onto the surface with kinetic energies of ≤0.1 eV per atom, avoiding impact effects on the nanoparticle morphology.

† The positively charged portion of the produced nanoparticles is repelled by the positively biased lens system, thus preventing them from being deposited onto the sample. The aggregation chamber exit aperture is in line of sight with the sample, but it has been verified by TPD experiments and SEM that the non-ionized, and therefore unfiltered, fraction of the nanoparticle beam is lost in the constriction between the two chambers, and the deposition of neutral particles can be neglected at particle deposition time-scales.

Ion Scattering Spectroscopy (ISS) and Auger Electron Spectroscopy (AES) were performed to confirm the cleanliness of the HOPG substrate and the deposited particles, and the results are shown elsewhere.[38,39]

TPD experiments were performed in the preparation chamber of the UHV system. The samples were dosed with a 1 : 1 mixture of two different isotopically labelled CO molecules, namely $^{13}C^{16}O$ (CIL, 99% ^{13}C, $<10\%$ ^{18}O) and $^{12}C^{18}O$ (CIL, 2% ^{16}O). Both gases were dosed simultaneously using separate leak valves until a total chamber pressure of 2×10^{-8} mbar was attained. The ratio of the two gases was held constant by monitoring the mass spectrometer signal for each component. The samples were dosed in this manner for 10 min, corresponding to an exposure of 9 Langmuir, which was sufficient to saturate the surface. The sample temperature was then ramped at a rate of 1 °C s^{-1} in UHV and the CO desorption from the substrate was analysed using a differentially pumped Balzers QMA 125 quadrupole mass spectrometer (QMS). The spectrometer was equipped with an oxygen-free high conductivity (OFHC) copper sniffer tip with a 1 mm diameter aperture, which is positioned within 0.5 mm of the sample surface. This arrangement allows the local gas composition above the sample surface to be measured with negligible contribution from the sample holder or surroundings.

For TEM analyses, the nanoparticles were deposited directly onto standard lacey or holey carbon films supported on 300 mesh copper TEM grids. High resolution TEM of various size nanoparticles was performed using a Technai T20 microscope operated at 200 keV in bright field mode, to measure size distributions for each sample of mass selected nanoparticles and to image the morphology of the nanoparticles.

3 Results

3.1 Particle shape and size distribution

Depositions were typically carried out so that 10–40% of the substrate surface was covered by nanoparticles. A TEM image of a sample with a typical coverage is shown in Fig. 1a. We have previously investigated the size-distribution of the Ru nanoparticles produced by the magnetron sputter source using *in situ* STM and *ex situ* TEM.[38] It was shown that the height measured by STM was in very good agreement with the diameter measured by TEM.‡ Size-distributions from samples with selected sizes of Ru nanoparticles are presented in Fig. 1b, which show that the diameter resolution ($\Delta d/d$) lies between $\pm 10\%$ and $\pm 20\%$. The particle diameter was derived from image analysis of TEM images, by measuring the projected area of each particle and, by using the spherical approximation, calculating an effective diameter d given by projected area $= \pi(d/2)^2$. The measured diameter resolution is larger than that theoretically predicted, which is suggested to be due to imperfection in the mass filter apparatus and/or due to the image analysis of particles that deviate from a sphere.

To obtain detailed information on the nanoparticle shape and structure, high-resolution TEM measurements were performed on Ru nanoparticles deposited directly onto TEM grids. The TEM micrographs shown in Fig. 2 reveal that the nanoparticles do not all adopt the expected truncated hexagonal bipyramidal equilibrium shape.[19] The particles have most likely hcp crystal structure as the particles primarily exhibit hexagonal symmetry and lattice fringes periodicity was found to match the (100) interplanar distance, see ref. 38 for further details. A variety of polymorphs are observed for larger particles, including particles that seem to be composed of smaller nanoparticles or clusters as opposed to single crystal nanoparticles. The formation of the structural composite nanoparticles is speculated to be consistent with the formation process that is mediated by aggregation of smaller nanoparticles and clusters. None of the observed Ru particles were observed to be flat, neither by STM nor by TEM, as has been reported when growing Ru nanoparticles by chemical vapour deposition.[40] From the TEM investigations it is evident that the particles larger than ~ 6 nm exhibit a high degree of surface roughness. It was, however, not possible to resolve the atomic structure of the small particles to a degree where the surface roughness could be quantified. Accurate determination of the surface atomic structure by any form of microscopy is extremely challenging and will thus require a comprehensive study.[41] The general trend is that smaller particles exhibit more well-defined facets and are closer to the equilibrium shape, while larger particles have rougher surfaces and thereby expose a surface with a relatively larger fraction of under-coordinated sites.

The possible sintering of Ru nanoparticles on HOPG was also studied by Nielsen *et al.*[36] It was found that sintering was not observed at room temperature for the ~ 3–15 nm size range on either sputtered or unsputtered HOPG, but it was found that 3.2 nm particles on unsputtered HOPG sintered into aggregates after heating to 500 °C. Additionally it was found that 4 nm Ru particles deposited onto sputtered HOPG were stable against sintering, even when heated to 500 °C. In this study, we did not observe a significant difference between the TPD spectra from 2.8 nm Ru supported on sputtered HOPG compared to un-sputtered HOPG. The activity for scrambling of isotopic labelled CO was also not influenced by the amount of defects in the support (see later), suggesting that the particles have not undergone substantial sintering during the TPD experiment. It was, however, observed that annealing the sample to ~ 700 °C leads to a decrease in the total CO desorption signal as well as reduction in desorption of scrambling products. The origin of this loss of Ru surface area and active sites is not yet understood, but it could be due to particle annealing or contamination from mobile carbon on the substrate.

3.2 Isotopic CO scrambling experiments

Simultaneous dosing with two of different isotopically labelled CO molecules makes it possible to determine the relative amount of CO that is dissociated on the surface from the TPD spectra. If randomly adsorbed $^{13}C^{16}O$ and $^{12}C^{18}O$ molecules dissociate on the surface, the dissociated species may scramble and recombine into the four possible CO isotopologues $^{12}C^{16}O$, $^{13}C^{16}O$, $^{12}C^{18}O$ and $^{13}C^{18}O$. From the CO

‡ Due to STM tip convolution effects, limited information could be obtained by STM about the width of nanoparticles smaller than about 8 nm.

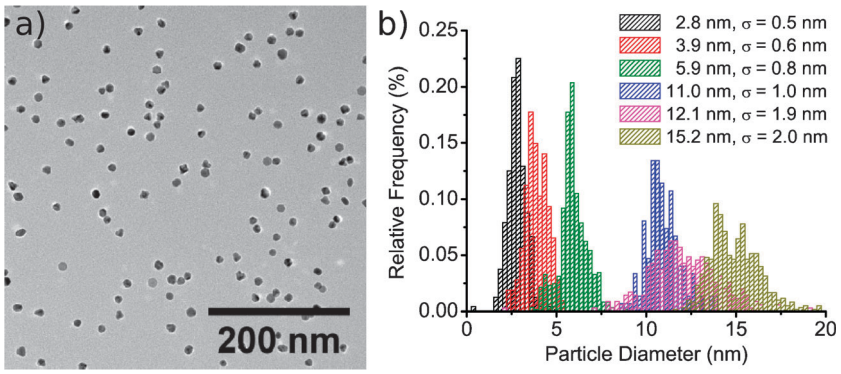

Fig. 1 (a) Low magnification TEM image from 11.0 nm Ru particles deposited onto a holey carbon coated copper TEM grid, recorded on a Tecnai T20 microscope. This is a typical TEM image used for size distribution image analysis. (b) Nanoparticle size distributions measured from TEM images of samples with nanoparticles of different sizes. The imaged TEM samples that were used to produce the size distributions were prepared similar to the samples for the TPD measurements.

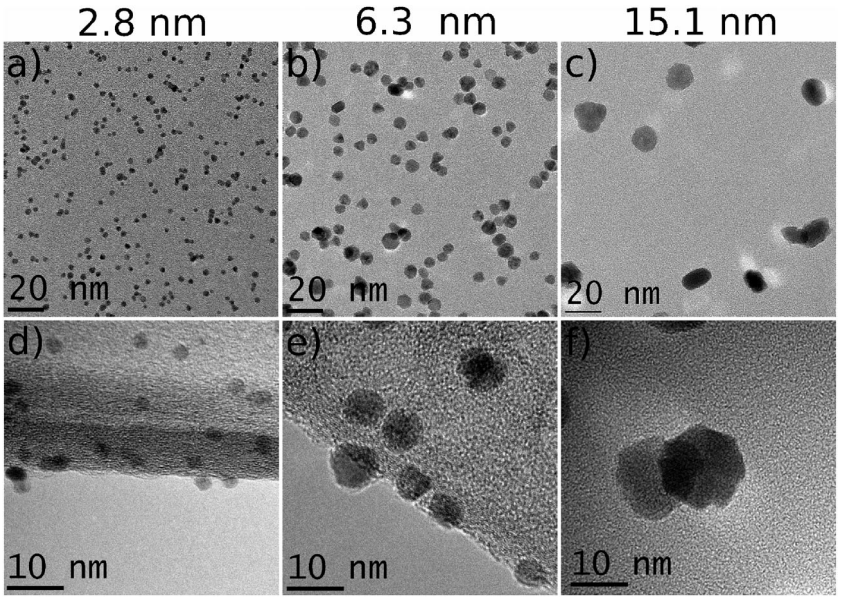

Fig. 2 TEM and high-resolution TEM micrographs showing Ru nanoparticles of various sizes and shapes. The given nanoparticle diameters are mean values obtained from Gaussian fits to experimentally measured distributions.

desorption we would like to distinguish between CO that has been dissociated and molecular adsorbed CO. The procedure for this is illustrated in Fig. 3a where the raw mass spectrometer data recorded at 28 amu, 29 amu, 30 amu and 31 amu from a sample with 11.0 nm Ru particles on unsputtered HOPG are shown. The two high intensity signals are 29 amu (red) and 30 amu (green), which correspond to the dosed CO isotopologues. The 28 amu (black) and 31 amu (blue) signals can ideally only originate from scrambling events of dissociated $^{13}C^{16}O$ and $^{12}C^{18}O$, but a relatively high background of $^{12}C^{16}O$ is unavoidable in UHV chambers in general and locally in the QMS in particular even under UHV conditions, due to hot filaments.

To achieve TPD spectra that quantitatively represent the desorption products, a background subtraction has been performed for each of the recorded TPD spectra, followed by a subtraction for $^{12}C^{16}O$ and $^{13}C^{18}O$ trace impurities contained in the dosed CO isotopologues. The corrected spectrum is shown in Fig. 3b.

The background UHV pressure of CO gives rise to a minor undesirable adsorption of $^{12}C^{16}O$ onto the Ru surface in the time period from nanoparticle deposition to CO dosing. The enlarged 28 amu signal is most pronounced at high desorption temperatures around 500 K, which shows that CO initially will decorate the surface sites that bind CO strongly. These surface sites are also the active sites for CO dissociation, so the unwanted dosing of $^{12}C^{16}O$ from the background will block a fraction of the active sites from the subsequent adsorption and scrambling of $^{13}C^{16}O$ and $^{12}C^{18}O$. Thus, it is crucial to minimize the background dose by reducing the amount of hot filaments in the chamber and the time from nanoparticle deposition to the $^{13}C^{16}O$ and $^{12}C^{18}O$ dosing.

We used the 31 amu signal, as the background pressure of $^{13}C^{18}O$ is negligible and thus, the 31 amu signal originates solely from scrambling events of adsorbed CO that has been dissociated and is assumed to represent 1/4 of the total amount of scrambling products. This is a conservative estimate since

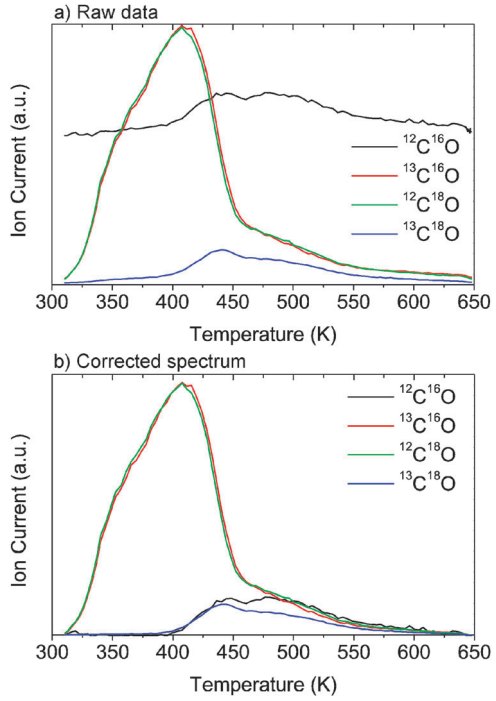

Fig. 3 TPD spectra obtained at a heating rate of 1 °C s^{-1} from 11.0 nm Ru nanoparticles supported on un-sputtered HOPG. (a) Raw mass spectrometer data from the 28 amu (black), 29 amu (red), 30 amu (green) and 31 amu (blue) signals. (b) Corrected spectrum obtained from the raw data in (a) as described in the text.

small amounts of CO coming from the background may dilute this.

The amount of active sites for CO dissociation on the nanoparticles is measured by probing the fraction of adsorbed CO that undergoes dissociation and subsequent association and desorption. CO desorption spectra were obtained from saturation coverages of equal amounts of $^{13}C^{16}O$ and $^{12}C^{18}O$ adsorbed on 3–15 nm Ru nanoparticles supported on both non-sputtered and Ar^+ ion sputtered HOPG.

In order to measure the amount of dissociated CO, we separate the desorption spectra into a contribution from molecular adsorbed CO (*i.e.* non-dissociated CO) and from CO that has been dissociated, recombined and then desorbed. When a fraction of the dosed $^{13}C^{16}O$ and $^{12}C^{18}O$ molecules has been dissociated we assume equal probability for scrambling into each of the four possible isotopologues $^{12}C^{16}O$, $^{13}C^{16}O$, $^{12}C^{18}O$ and $^{13}C^{18}O$. Due to the assumption of equal scrambling probability the $^{13}C^{18}O$ signal can be used to represent the scrambling into each of the four possible isotopologues. The total amount of scrambling is therefore represented as four times the 31 amu signal. The desorption spectrum originating purely from molecular CO is represented by subtracting the contribution from self-scrambling (*i.e.* $^{13}C^{16}O$ and $^{12}C^{18}O$ into $^{13}C^{16}O$ and $^{12}C^{18}O$), which is represented as two times the 31 amu signal, from the sum of the desorption signal from the dosed $^{13}C^{16}O$ and $^{12}C^{18}O$ molecules. Fig. 4 shows the resulting molecular and dissociative desorption components from samples with (a) 2.8 nm, (b) 5.9 nm, (c) 11.0 nm and (d) 15.2 nm particles. It is seen that the molecular adsorbed CO has a desorption peak at ~410 K and the associative desorption from dissociated CO results in a broad feature at 400–600 K with two main features at ~440 K and ~475 K. Furthermore, the spectra show that CO molecules that have been dissociated desorb from sites that bind CO stronger than CO adsorbed onto sites that do not dissociate CO. The obtained TPD spectra do not vary substantially with particle size, as the shape and position of the desorption peaks

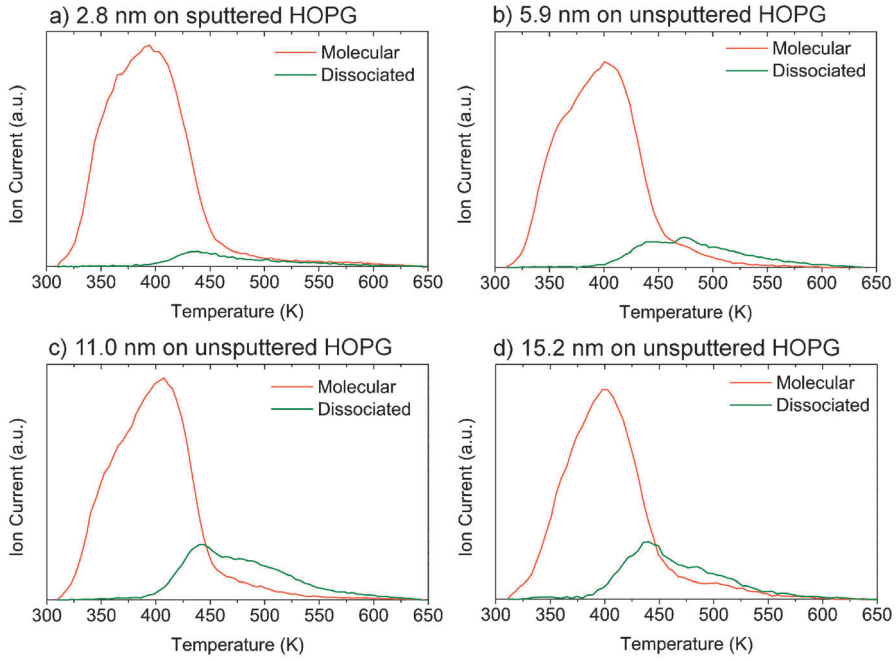

Fig. 4 TPD spectra are separated into contributions from the desorption of dissociated CO (green) and molecular adsorbed CO (orange) (see text). The TPD spectra are shown for samples with (a) 2.8 nm Ru particles supported on sputtered HOPG, (b) 5.9 nm Ru particles supported on unsputtered HOPG, (c) 11.0 nm Ru particles supported on unsputtered HOPG and (d) 15.2 nm Ru particles supported on unsputtered HOPG.

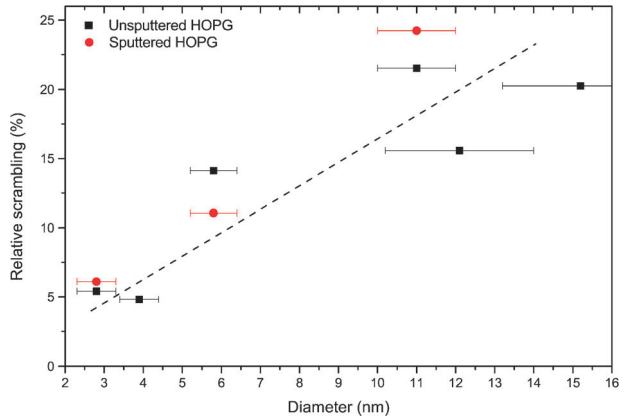

Fig. 5 Relative amount of dissociated CO (*i.e.* dissociated CO divided by molecular CO for each experiment) as a function of nanoparticle size. The dashed line is drawn to guide the eye.

remain approximately the same. The most significant particle size effect is the variation in activity for CO dissociation, which is expressed as the integrated amount of dissociated CO normalised to the total CO desorption signal, presented in Fig. 5. By this normalisation the CO dissociation activity is relative to the total Ru surface area accessible for CO adsorption and can hence be compared directly across particle sizes. The results show that the relative amount of CO dissociation was found to increase with increasing particle size. The maximum amount of CO scrambling was measured from a sample with 11 nm particles where ~25% of the adsorbed CO was dissociated.

4 Discussion

CO desorption has previously been studied from a variety of Ru single crystal surfaces, *e.g.* Ru(001),[42] Ru(109),[24] Ru(1 0 54),[25] Ru(11$\bar{2}$0)[26] and Ru(11$\bar{2}$1),[27] and each surface results in different desorption spectra. Supported nanoparticles will expose a combination of various crystal facets (close packed and more open surfaces) along with a number of under-coordinated sites like steps, kinks and atoms located at the edges and corners. For larger nanoparticles and neglecting support interactions, the particle surface may be assumed to be an unknown superposition of the various single crystal surfaces. For smaller particles or for the highly irregular and rough particles found in this study, under-coordinated sites become dominant. The transition from a well-defined Ru(0 1 54) single crystal surface to a highly defective surface induced by Ar-ion sputtering was previously studied by Murphy *et al.*[37] With increasing sputtering the morphology changed from that of a stepped Ru(001) single crystal surface to a highly defective surface with flat 2–5 nm diameter patches (imaged by STM), and the CO desorption behaviour evolved from that of a stepped Ru(001) to a CO desorption behaviour with similar desorption features and peak positions as the investigated nanoparticulate system. Similar CO desorption spectra were found from the corrugated Ru(11$\bar{2}$0)[26] and Ru(11$\bar{2}$1).[27] These findings suggest that the CO adsorption behaviour of the nanoparticles is related to a high density of under-coordinated sites possibly in combination with corrugated facets. The good resemblance to the previously reported desorption spectra also gives strong confidence that the TPD experiments were not influenced by contaminants such as oxygen present on the surface of the particles.

The dissociation of CO has also been studied on various Ru single crystal surfaces. The work by Zubkov *et al.*[24] showed that CO only dissociates on step sites on Ru(109) and not on the (001)-terraces, as the dissociation was completely suppressed when the steps were blocked by carbon atoms. Combined infrared spectroscopy and TPD experiments indicated that CO dissociates at 450–500 K to recombine and desorb at 500–550 K. Wang *et al.* showed by TPD and high resolution electron energy loss spectroscopy (HREELS) experiments that the more open Ru(11$\bar{2}$0) surface dissociates CO already from 300 K and that 20% of the adsorbed CO monolayer was dissociated until associative desorption with maxima at 500 K and 540 K.[26] It was also concluded that both defect sites and the (11$\bar{2}$0)-terrace sites are active for CO dissociation, leaving the explanation for dissociation to be limited to 20% unknown. A similar study on Ru(11$\bar{2}$1) by Fan *et al.* showed that the onset temperature for CO dissociation at high initial coverage is ~380 K[27] followed by association and desorption maxima at around 540 K. Additionally, a DFT study of the same surface determined the 4F hollow site to be the active site.[28] From these previous studies it is evident that the activation barrier for CO dissociation is highly dependent on the geometry of the adsorption sites. The TPD spectra from dissociated CO presented in this paper show a broad desorption feature (400–600 K) and the presence of two main peaks at ~440 K and ~475 K, which suggest that there exist several types of active sites for CO dissociation on the nanoparticles. This suggests that the particles expose a large variety of active sites, in good agreement with the structural information from the TEM images showing non-equilibrium shaped nanoparticles.

The relative scrambling for particles of various sizes presented in Fig. 5 shows that the larger particles expose a higher proportion of active sites for CO dissociation. The increasing activity is most likely correlated to a higher tendency for non-equilibrium shapes of the larger nanoparticles, which thereby expose an increasing relative amount of under-coordinated surface sites. The tendency of larger particles to adopt highly non-equilibrium shapes compared to smaller particles can be attributed to the particle formation process in the aggregation source, where the large particles grow through coagulation of small primary particles of various sizes, whereas the small particles are built by addition of single atoms, and thereby adopt a more compact morphology closer to the equilibrium shape. Ruthenium is a high melting point material and the rapid cooling during the aggregation process quenches the particles into non-equilibrium shapes.[43] The TEM data presented earlier show that the nanoparticles are not equilibrium shaped and that different morphologies are present. Hence, it is, however, not possible to unambiguously identify and quantify the active sites. To identify the active sites an ensemble of mono-morphic nanoparticles must be produced, making it possible to identify a more rigorous correlation between nanoparticle structure and activity.

In the case of equilibrium shaped Ru nanoparticles, the activity of N_2 dissociation was studied in the size range of 1.5–5 nm by computational methods, and it was shown that the optimal particle size is ~3 nm, as the particles of this size have the optimal number of active step sites.[19] A combination of experiments and DFT calculations has shown that CO and N_2 dissociate at the same step site (the B_5-site) on Ru single crystals.[16,25] On the corrugated Ru(11$\bar{2}$1) surface, CO and N_2 prefer a six-fold and five-fold active site, respectively, but both CO and N_2 involve six Ru atoms in the complete dissociated state.[28,44] Regardless of the differences in the reaction path, the geometries of the sites active for CO and N_2 are very similar, so it is expected that the optimal particle size for dissociation of CO and N_2 is comparable for particles with the equilibrium structure.

The assumption that the adsorbed C and O isotopes produced by dissociation will have equal probability to recombine into the four possible combinations of CO isotopologues is based on high mobility of the dissociated species. Oxygen atoms are able to diffuse away from the step and onto the terrace after dissociation whereas the carbon atom is tightly bound to the bottom of the step with a high diffusion barrier.[15,25,45] Having a high defect density and consequently very small facets could suppress the mobility and thereby hinder the isotopic exchange reaction, which would increase the probability of the dissociated CO molecule to recombine with itself. It is difficult to estimate how pronounced this phenomenon is, but in any case, the calculated relative amount of scrambling would be a lower estimate, if "self-scrambling" is pronounced.

5 Conclusions

TPD measurements with isotopically labelled CO were performed to probe the active sites for CO dissociation from mass-selected Ru nanoparticles in the size range of 3–15 nm supported on HOPG. The CO scrambling experiments demonstrate that molecular adsorbed CO desorb showing a broad peak from 300 to 450 K and CO may dissociate at numerous types of under-coordinated surface sites followed by recombination and desorption at temperatures between 400 K and 600 K. The relative amount of active sites was found to increase with increasing particle size, which is attributed to the increasing surface roughness for larger particles. A maximum of ~25% isotopic scrambling was measured from a sample with 11 nm particles. This is not what is expected from equilibrium conditions where the optimum size is expected to be ~3 nm. This suggests that if such under-coordinated sites can be made stable or annealing can be avoided, highly active catalysts can be made where highly under-coordinated sites are called for, such as CO and N_2 dissociation.

Acknowledgements

This work was supported by the Danish National Research Foundation and the EU FWP7 Marie Curie Intra-European Fellowship ESRCN (PIEF-GA-2008-220055). The use of facilities at the Center of Electron Nanoscopy (CEN) at DTU is acknowledged.

References

1 R. van Hardeveld and A. van Montfoort, *Surf. Sci.*, 1966, **4**, 396–430.
2 G. C. Bond, *Surf. Sci.*, 1985, **156**, 966–981, part 2.
3 M. Che and C. O. Bennett, *Adv. Catal.*, 1989, **36**, 55–172.
4 G. C. Bond, *Chem. Soc. Rev.*, 1991, **20**, 441–475.
5 M. Frank and M. Baumer, *Phys. Chem. Chem. Phys.*, 2000, **2**, 3723–3737.
6 D. Ligthart, R. van Santen and E. Hensen, *J. Catal.*, 2011, **280**, 206–220.
7 M. Haruta, N. Yamada, T. Kobayashi and S. Iijima, *J. Catal.*, 1989, **115**, 301–309.
8 M. Haruta, *Catal. Today*, 1997, **36**, 153–166.
9 M. Valden, X. Lai and D. W. Goodman, *Science*, 1998, **281**, 1647–1650.
10 S. H. Joo, J. Y. Park, J. R. Renzas, D. R. Butcher, W. Huang and G. A. Somorjai, *Nano Lett.*, 2010, **10**, 2709–2713.
11 G. Bezemer, J. Bitter, H. Kuipers, H. Oosterbeek, J. Holewijn, X. Xu, F. Kapteijn, A. van Dillen and K. de Jong, *J. Am. Chem. Soc.*, 2006, **128**, 3956–3964.
12 G. A. Somorjai, R. W. Joyner and B. Lang, *Proc. R. Soc. London, Ser. A*, 1972, **331**, 335–346.
13 D. Blakely and G. Somorjai, *J. Catal.*, 1976, **42**, 181–196.
14 J. John and T. Yates, *J. Vac. Sci. Technol., A*, 1995, **13**, 1359–1367.
15 T. Zambelli, J. Wintterlin, J. Trost and G. Ertl, *Science*, 1996, **273**, 1688–1690.
16 S. Dahl, A. Logadottir, R. C. Egeberg, J. H. Larsen, I. Chorkendorff, E. Törnqvist and J. K. Nørskov, *Phys. Rev. Lett.*, 1999, **83**, 1814–1817.
17 S. Dahl, E. Törnqvist and I. Chorkendorff, *J. Catal.*, 2000, **192**, 381–390.
18 K. Honkala, A. Hellman, I. N. Remediakis, A. Logadottir, A. Carlsson, S. Dahl, C. H. Christensen and J. K. Nørskov, *Science*, 2005, **307**, 555–558.
19 J. Gavnholt and J. Schiøtz, *Phys. Rev. B: Condens. Matter Mater. Phys.*, 2008, **77**, 035404.
20 E. Shincho, C. Egawa, S. Naito and K. Tamaru, *Surf. Sci.*, 1985, **149**, 1–16.
21 T. Yamada, Y. Iwasawa and K. Tamaru, *Surf. Sci.*, 1989, **223**, 527–550.
22 T. Zubkov, G. A. Morgan and J. T. Yates, *Chem. Phys. Lett.*, 2002, **362**, 181–184.
23 I. M. Ciobica and R. A. van Santen, *J. Phys. Chem. B*, 2003, **107**, 3808–3812.
24 T. Zubkov, G. A. Morgan, J. T. Yates, O. Kühlert, M. Lisowski, R. Schillinger, D. Fick and H. J. Jänsch, *Surf. Sci.*, 2003, **526**, 57–71.
25 S. B. Vendelbo, M. Johansson, D. J. Mowbray, M. P. Andersson, F. Abild-Pedersen, J. H. Nielsen, J. K. Nørskov and I. Chorkendorff, *Top. Catal.*, 2010, **53**, 357–634.
26 J. Wang, Y. Wang and K. Jacobi, *Surf. Sci.*, 2001, **488**, 83–89.
27 C. Y. Fan, H. P. Bonzel and K. Jacobi, *J. Chem. Phys.*, 2003, **118**, 9773–9782.
28 S. Shetty, A. P. J. Jansen and R. A. van Santen, *J. Phys. Chem. C*, 2008, **112**, 14027–14033.
29 S. B. Vendelbo, M. Johansson, J. H. Nielsen and I. Chorkendorff, *Phys. Chem. Chem. Phys.*, 2011, **13**, 4486–4493.
30 C. R. Henry, *Surf. Sci. Rep.*, 1998, **31**, 231–325.
31 D. Rainer and D. Goodman, *J. Mol. Catal. A: Chem.*, 1998, **131**, 259–283.
32 R. A. Bennett, P. Stone and M. Bowker, *Catal. Lett.*, 1999, **59**, 99–105.
33 M. Bäumer and H.-J. Freund, *Prog. Surf. Sci.*, 1999, **61**, 127–198.
34 U. Heiz and W.-D. Schneider, *Crit. Rev. Solid State Mater. Sci.*, 2001, **26**, 251–290.
35 S. McClure, M. Lundwall, F. Yang, Z. Zhou and D. W. Goodman, *J. Phys.: Condens. Matter*, 2009, **21**, 474223.
36 R. M. Nielsen, S. Murphy, C. Strebel, M. Johansson, J. H. Nielsen and I. Chorkendorff, *Surf. Sci.*, 2009, **603**, 3420–3430.
37 S. Murphy, C. Strebel, S. B. Vendelbo, C. Conradsen, Y. Tison, K. Nielsen, L. Bech, R. M. Nielsen, M. Johansson, I. Chorkendorff and J. H. Nielsen, *Phys. Chem. Chem. Phys.*, 2011, **13**, 10333–10341.

38 R. M. Nielsen, S. Murphy, C. Strebel, M. Johansson, I. Chorkendorff and J. H. Nielsen, *J. Nanopart. Res.*, 2010, **12**, 1249–1262.
39 S. Murphy, R. M. Nielsen, C. Strebel, M. Johansson and J. H. Nielsen, *Carbon*, 2011, **49**, 376.
40 Z. Song, T. Cai, J. C. Hanson, J. A. Rodriguez and J. Hrbek, *J. Am. Chem. Soc.*, 2004, **126**, 8576–8584.
41 L. C. Gontard, L.-Y. Chang, C. J. D. Hetherington, A. I. Kirkland, D. Ozkaya and R. E. Dunin-Borkowski, *Angew. Chem., Int. Ed.*, 2007, **46**, 3683–3685.
42 H. Pfnür, P. Feulner, H. A. Engelhardt and D. Menzel, *J. Phys. Chem. Lett.*, 1978, **59**, 481–486.
43 R. Alayan, L. Arnaud, M. Broyer, E. Cottancin, J. Lermé, J. L. Vialle and M. Pellarin, *Phys. Rev. B: Condens. Matter Mater. Phys.*, 2006, **73**, 125444.
44 S. Shetty, A. P. J. Jansen and R. A. van Santen, *J. Phys. Chem. C*, 2008, **112**, 17768–17771.
45 J. Wintterlin, J. Trost, S. Renisch, R. Schuster, T. Zambelli and G. Ertl, *Surf. Sci.*, 1997, **394**, 159–169.

Oxygen Reduction Reaction

DOI: 10.1002/anie.201200586

The Effect of Size on the Oxygen Electroreduction Activity of Mass-Selected Platinum Nanoparticles**

*Francisco J. Perez-Alonso, David N. McCarthy, Anders Nierhoff, Patricia Hernandez-Fernandez, Christian Strebel, Ifan E. L. Stephens, Jane H. Nielsen, and Ib Chorkendorff**

The use of proton exchange membrane fuel cells (PEMFCs) could become widespread by improving the kinetics of the oxygen reduction reaction (ORR), where Pt is the typical electrocatalyst. Improvements to the reaction kinetics, however, require understanding of the fundamental factors that control the ORR activity of Pt, in particular the dependence of the ORR rate as a function of the particle size. This has been the topic of numerous studies in the last few decades.[1] Most articles report an increase in the specific activity with increasing particle size. Nørskov, Rossmeisl, and co-workers rationalized this phenomenon using density functional calculations.[2] They proposed that the active sites for the ORR are located on the terrace sites of Pt. Undercoordinated sites at terrace edges or steps should provide a negligible contribution to the activity, because they bind strongly to the O-containing intermediates of the ORR.[2b,d] The increased population of undercoordinated sites on small nanoparticles (especially below 5 nm) explains their lower activity. Moreover, they predicted that the activity of nanoparticles with diameters greater than around 10 nm should be equal to that of extended surfaces.[2d]

Recently, Arenz and co-workers raised doubts regarding the reliability of earlier measurements of the ORR activity on Pt nanoparticles on high surface area supports because of the influence of uncompensated resistance and support capacitance.[1e] By correcting for these effects, they observed results that could not be explained by the theoretical model described above, namely that 1) there was no size effect on the ORR activity for Pt nanoparticles with a diameter below 5 nm, 2) Pt-black particles with a diameter of around 30 nm exhibited a two-fold improved ORR activity relative to particles with a diameter of 5 nm, and 3) the extended Pt surfaces showed a two-fold improved ORR activity relative to Pt-black particles. Also, some stepped Pt single-crystal surfaces, for example, Pt(331), actually exhibit an improved oxygen reduction activity relative to Pt(111),[3] even though the stepped crystals have a high density of undercoordinated sites. The higher activity of the stepped single crystals, could, at first glance, seem to be in contradiction with the theoretical models described above.[2b,d] However, it turns out there are sites on these single crystals, presumably on the terrace sites, that bind more weakly to O-containing species than Pt(111), which explains their higher activity[4] as discussed in greater detail elsewhere.[4b] Nonetheless, it is unknown whether this phenomenon, observed upon extended surfaces of Pt, should occur on nanoparticulate catalysts. In summary, the controversies regarding the ORR activity of Pt nanoparticles strongly motivate the use of model systems, with control over variables such as the particle size, dispersion, and the influence of the support material.

Herein, we investigate the effect of size upon the ORR activity of Pt particles with diameters ranging from 2 to around 11 nm. The particles prepared through the gas aggregation technique, mass-selected, and deposited directly onto planar glassy carbon supports under ultrahigh vacuum (see details in the Supporting Information). By supporting the catalysts on planar surfaces, we avoid the need to correct for capacitive currents. By using mass-selected particles, we avoid effects from surfactant molecules that would be present on particles produced by chemical synthesis methods. Earlier studies taking similar approaches to ours have restricted the nanoparticle size to below 3.5 nm, albeit without mass selection.[1i] By encompassing a larger size range in the current study, we make a link between extended surfaces and nanoparticulate catalysts.

To determine whether the active sites for the ORR are located on terrace sites, as predicted by theory, we have quantified the proportion of the terraced surface area of the Pt nanoparticles by performing in vacuum CO temperature programmed desorption (TPD) experiments. Figure 1 shows the CO desorption spectra obtained from four different samples, in comparison to the particle size histograms and representative transmission electron microscopy (TEM) micrographs.

The features of the CO TPD spectra on Figure 1 are redolent of those obtained on Pt single crystals,[5] despite variations in the nanoparticle morphologies and their unknown facet terminations. On the basis of the single-crystal studies, we have fitted the TPD spectra to three Gaussian

[*] Dr. F. J. Perez-Alonso, Dr. D. N. McCarthy, A. Nierhoff, Dr. P. Hernandez-Fernandez, C. Strebel, Dr. I. E. L. Stephens, Prof. J. H. Nielsen, Prof. I. Chorkendorff
Center for Individual Nanoparticle Functionality
Department of Physics, Technical University of Denmark
Building 312, 2800 Lyngby (Denmark)
E-mail: ibchork@fysik.dtu.dk
Homepage: http://www.cinf.dtu.dk

[**] F.J.P.A. acknowledges funding from the Spanish Government Ministry of Education's, "Programa Nacional de Movilidad de Recursos Humanos del Plan Nacional de I-D+I 2008–2011". I.E.L.S. acknowledges funding by a PSO-financed ForskEL/EL grant (High Performance MEA's, project number 010076) from energinet.dk. P.H.F. acknowledges funding from the Danish Council for Strategic Research in Sustainable Energy and Environment—project "MEDLYS". D.N.M.C. is the recipient of a H.C. Ørsted fellowship. The Center for Individual Nanoparticle Functionality is supported by the Danish National Research Foundation.

Supporting information for this article is available on the WWW under http://dx.doi.org/10.1002/anie.201200586.

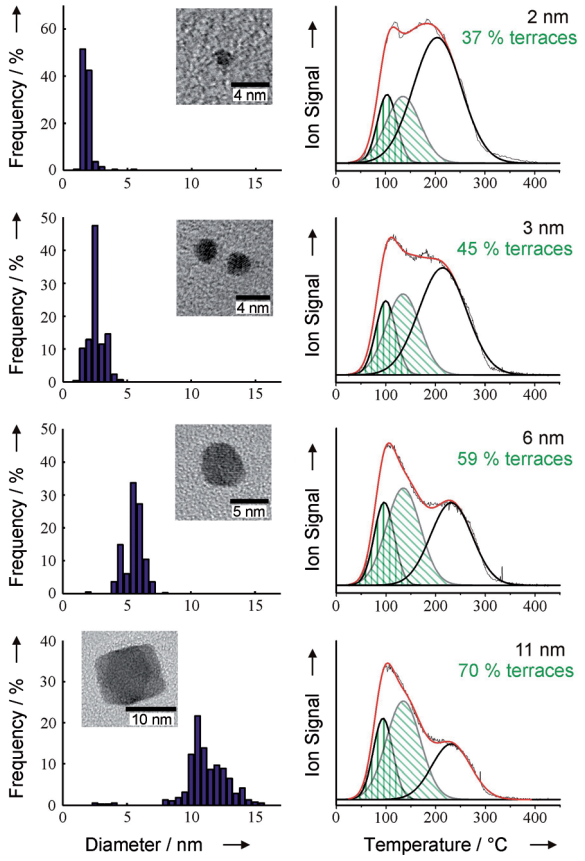

Figure 1. Nanoparticle size distributions and the associated CO desorption profiles of Pt/SiO_2 samples for particle sizes of 2, 3, 6, and 11 nm. Included with each TPD profile are the integrated proportions of the terraced particle surface area.

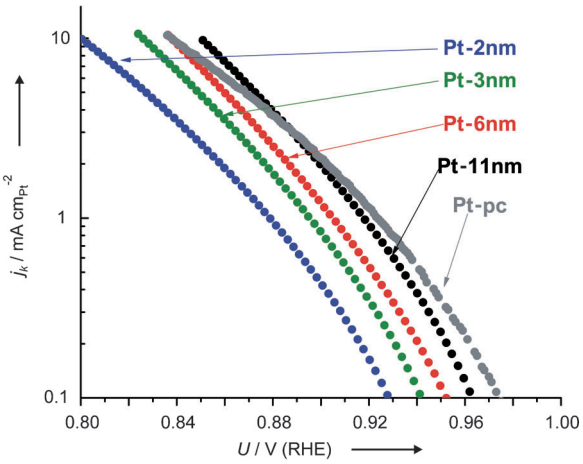

Figure 2. ORR Tafel plots of Pt-pc (grey), Pt-2 nm (blue), Pt-3 nm (green), Pt-6 nm (red) and Pt-11 nm (black) extracted from polarization curves recorded in oxygen-saturated electrolyte solutions (0.1 M $HClO_4$) at 50 mVs^{-1} and 1600 rpm.

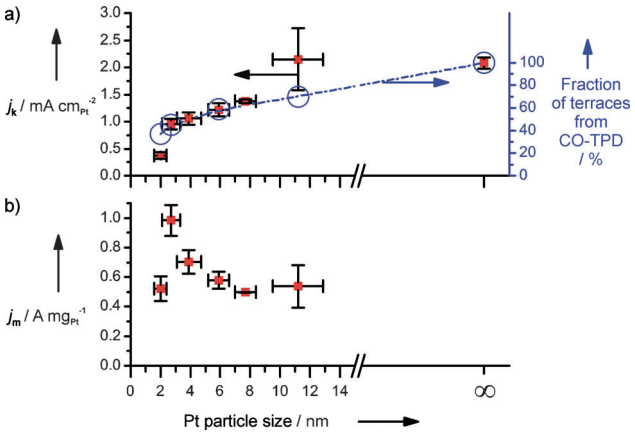

Figure 3. a) ORR kinetic current densities and b) mass activities at 0.9 V (reversible hydrogen electrode, RHE) of different particle sizes, from cyclic voltammograms in a O_2-saturated 0.1 M $HClO_4$ solution at a sweep rate of 50 mVs^{-1} and 1600 rpm at 23 °C. The blue circles in plot (a) represent proportions of the terraced particle surface area calculated from CO TPD profiles.

functions: a low-temperature peak, corresponding to CO bound weakly at high coverages on the terrace sites, an intermediate-temperature peak at around 400 K corresponding to more strongly bound CO at low coverages on the terrace sites, and a high-temperature peak extending to 600 K, corresponding to CO bound strongly to undercoordinated sites. A similar deconvolution of oxygen TPD curves into Gaussian functions has been used to interpret the coordination-dependent binding interactions of oxygen on stepped Pt surfaces.[6] We used the fit functions to determine the proportions of the terraced surface area (see the Supporting Information). Evidently, the fraction of terrace sites increases with increasing particle size, which is in line with our expectations.

The ORR activity of the glassy carbon-supported Pt nanoparticles and a polycrystalline Pt sample (Pt-pc), have all been measured by voltammetry in a 0.1 M $HClO_4$ electrolyte solution using a rotating ring disc electrode (RRDE) assembly (see the Supporting Information). Tafel plots of ORR specific activity are shown in Figure 2. Clearly the ORR specific activity increases with the particle size. The ORR specific activity and mass activity for the different catalysts studied is plotted in Figure 3. Our results agree well with earlier theoretical predictions (see the Supporting Information). In particular 1) extended Pt surfaces exhibit the same activity as nanoparticles with a diameter of 11 nm, and 2) there is a four-fold increase in the ORR activity going from 2 nm Pt particles to extended surfaces.[2b,d] Moreover, we confirm that the Pt mass activity for the ORR shows a maximum for a particle size of 3 nm.[1a,2d]

The electrochemical experiments are also supported by the CO-TPD results: the ORR activity approximately scales with the proportion of terraces, as shown in Figure 3. The main outlier to this trend, given the experimental error, is the smallest nanoparticle with a diameter of 2 nm. This modest discrepancy could be explained by the differences in the surface structure induced by the electrochemical environment.[2d] Small particles are more susceptible to corrosion than the larger nanoparticles.[7] Corrosion would reduce the lateral size of each exposed facet and increase the number of undercoordinated sites.[2d]

Our study complements earlier investigations of industrial catalysts, which generally reported lower ORR activities[1a,d,e] than those reported here. We consider that our experimental conditions provide a more accurate measure of the intrinsic activity of Pt nanoparticles. We hypothesize that the high activity of our samples compared with commercial catalysts is due to the more idealized environment: high diffusion of oxygen and the absence of surfactant molecules.

In summary, we have shown that the specific activity of the oxygen reduction reaction on Pt nanoparticles decreases with decreasing particle size, with a maximum in mass activity for particles with a diameter of 3 nm. The ORR activity roughly correlates with the proportion of the terrace sites. We conclude that the active sites for the ORR are only located on the terrace sites of the nanoparticles, in agreement with earlier theoretical predictions.[2b,d] The close agreement between experiment and theory confirms that we are starting to build a more coherent picture of the factors that control the activity of nanoparticles for the ORR and other (electro)-catalytic reactions.

Received: January 20, 2012
Published online: March 29, 2012

Keywords: electrochemistry · fuel cells · heterogeneous catalysis · nanoparticles · platinum

[1] a) H. A. Gasteiger, S. S. Kocha, B. Sompalli, F. T. Wagner, *Appl. Catal. B* **2005**, *56*, 9–35; b) K. Kinoshita, *J. Electrochem. Soc.* **1990**, *137*, 845–848; c) K. Kinoshita, *Electrochemical Oxygen Technology*, Wiley, New York, **1990**; d) K. J. J. Mayrhofer, B. B. Blizanac, M. Arenz, V. R. Stamenkovic, P. N. Ross, N. M. Markovic, *J. Phys. Chem. B* **2005**, *109*, 14433–14440; e) M. Nesselberger, S. Ashton, J. C. Meier, I. Katsounaros, K. J. J. Mayrhofer, M. Arenz, *J. Am. Chem. Soc.* **2011**, *133*, 17428; f) M. Shao, A. Peles, K. Shoemaker, *Nano Lett.* **2011**, *11*, 3714–3719; g) Y. Takasu, N. Ohashi, X. G. Zhang, Y. Murakami, H. Minagawa, S. Sato, K. Yahikozawa, *Electrochim. Acta* **1996**, *41*, 2595–2600; h) M. Watanabe, H. Sei, P. Stonehart, *J. Electroanal. Chem.* **1989**, *261*, 375–387; i) E. Toyoda, R. Jinnouchi, T. Hatanaka, Y. Morimoto, K. Mitsuhara, A. Visikovskiy, Y. Kido, *J. Phys. Chem. C* **2011**, *115*, 21236–21240; j) S. P. F. Maillard, E. R. Savinova in *Handbook of Fuel Cells: Advances in Electrocatalysis, Materials, Diagnostics, and Durability*, *Vol. 5* (Ed.: H. A. G. Wolf Vielstich, H. Yokokawa), Wiley, New York, **2009**, pp. 91–11; k) M. T. M. Koper, *Nanoscale* **2011**, *3*, 2054.

[2] a) J. K. Nørskov, J. Rossmeisl, A. Logadottir, L. Lindqvist, J. R. Kitchin, T. Bligaard, H. Jonsson, *J. Phys. Chem. B* **2004**, *108*, 17886–17892; b) J. Greeley, J. Rossmeisl, A. Hellman, J. K. Norskov, *Z. Phys. Chem. Int. J. Res. Phys. Chem. Chem. Phys.* **2007**, *221*, 1209–1220; c) J. Rossmeisl, G. S. Karlberg, T. Jaramillo, J. K. Nørskov, *Faraday Discuss.* **2009**, *140*, 337–346; d) G. A. Tritsaris, J. Greeley, J. Rossmeisl, J. K. Nørskov, *Catal. Lett.* **2011**, *141*, 909–913.

[3] A. Kuzume, E. Herrero, J. M. Feliu, *J. Electroanal. Chem.* **2007**, *599*, 333–343.

[4] a) J. Clavilier, A. Rodes, K. Elachi, M. A. Zamakhchari, *J. Chim. Phys. Phys.-Chim. Biol.* **1991**, *88*, 1291–1337; b) I. E. L. Stephens, A. S. Bondarenko, U. Grønbjerg, J. Rossmeisl, I. Chorkendorff, *Energy Environ. Sci.* **2012**, DOI: 10.1039/C1032EE03590A.

[5] a) G. Ertl, M. Neumann, K. M. Streit, *Surf. Sci.* **1977**, *64*, 393–410; b) M. R. McClellan, J. L. Gland, F. R. McFeeley, *Surf. Sci.* **1981**, *112*, 63–77; c) H. Steininger, S. Lehwald, H. Ibach, *Surf. Sci.* **1982**, *123*, 264–282; d) H. R. Siddiqui, X. Guo, I. Chorkendorff, J. T. Yates, Jr., *Surf. Sci. Lett.* **1987**, *191*, L813–L818.

[6] a) M. J. T. C. Van Der Niet, A. Den Dunnen, L. B. F. Juurlink, M. T. M. Koper, *Angew. Chem.* **2010**, *122*, 6722–6725; *Angew. Chem. Int. Ed.* **2010**, *49*, 6572–6575; b) M. J. T. C. Van Der Niet, A. Den Dunnen, L. B. F. Juurlink, M. T. M. Koper, *J. Chem. Phys.* **2010**, *132*, 174705.

[7] a) E. F. Holby, W. C. Sheng, Y. Shao-Horn, D. Morgan, *Energy Environ. Sci.* **2009**, *2*, 865–871; b) F. J. Perez-Alonso, C. F. Elkjaer, S. S. Shim, B. L. Abrams, I. E. L. Stephens, I. Chorkendorff, *J. Power Sources* **2011**, *196*, 6085–6091; c) L. Tang, B. Han, K. Persson, C. Friesen, T. He, K. Sieradzki, G. Ceder, *J. Am. Chem. Soc.* **2010**, *132*, 596–600.

Angewandte Chemie
Eine Zeitschrift der Gesellschaft Deutscher Chemiker

Supporting Information

69451 Weinheim, Germany

The Effect of Size on the Oxygen Electroreduction Activity of Mass-Selected Platinum Nanoparticles**

*Francisco J. Perez-Alonso, David N. McCarthy, Anders Nierhoff, Patricia Hernandez-Fernandez, Christian Strebel, Ifan E. L. Stephens, Jane H. Nielsen, and Ib Chorkendorff**

anie_201200586_sm_miscellaneous_information.pdf

Supporting information

Preparation of mass-selected Pt nanoparticles and UHV CO desorption experiments

The preparation of platinum nanoparticles was performed in a multichamber ultrahigh vacuum (UHV) system (Omicron, Multiscan Lab) with a base pressure in the low 10^{-10} mbar region. The system is equipped with facilities for combined in-situ scanning tunneling microscopy (STM) and scanning electron microscopy (SEM), ion scattering spectroscopy (ISS), and temperature programmed desorption (TPD) measurements. Pre-formed mass-selected Pt particles were deposited onto the glassy carbon electrode from a magnetron-sputter gas-aggregation source fitted with a quadrupole mass filter (Mantis Deposition Ltd., Nanogen 50). The particles are formed by the gas-phase condensation of Pt atoms sputtered from a 99.99% pure Pt target via direct current magnetron sputter source. The magnetron is housed in a liquid nitrogen cooled enclosure with a small aperture (4 mm diameter) at one end. Argon gas is flown into the volume (or gas-aggregation zone) around the magnetron at a rate of 20–100 sccm and is pumped away via the aperture so that a local pressure of 0.1–1 mbar is obtained inside the gas-aggregation zone during operation. The argon gas serves the dual purpose of providing the plasma that sputters the target, and thermalizes the sputtered Pt atoms so that they condense into particles. The size of the nanoparticles that grow is determined by a range of factors: sputter power (typically 5–20 W), rate of gas flow, distance between the target and the exit aperture. Further details on the construction and principles of operation of this type of source can be found elsewhere [1].

TPD experiments were performed in the preparation chamber of the UHV system. For these TPD experiments, mass-selected Pt nanoparticles of the same sizes as those studied in the electrochemical experiments were deposited onto SiO_2/Si(111) supports As Pt particles do not diffuse and sinter on SiO_2 until ~800K [2], a temperature higher than that used in our TPD study, we expect that the TPD spectra of the particles supported on SiO_2 are directly related to the structure of the as-deposited particles. Unpublished TPD experiments from Ruthenium nanoparticles on both SiO_2 and Highly Oriented Pyrolitic Graphite show no significant differences in the shape of the TPD spectra, however due to difficulties with measuring temperature reliably on HOPG, SiO_2 was chosen as the support material. The samples were dosed with isotopically labeled CO molecules, namely 12C18O (CIL, 2% 16O). Isotopically labeled gas was used to distinguish from background CO (mass 28), which proved to be negligible in any case. The gas was dosed into the vacuum chamber via a leak valve until a total chamber pressure of 10^{-7} mbar was attained, for 10 min, corresponding to an exposure of 50 Langmuir, sufficient to saturate the surface. The sample temperature was then ramped at a rate of 1 K s^{-1} in UHV, and the CO desorption from the substrate was analysed using a differentially pumped Balzers QMA 125 quadrupole mass spectrometer. The spectrometer was equipped with an oxygen-free high conductivity (OFHC) copper sniffer tip with a 1 mm diameter aperture, which is positioned within 0.5 mm of the sample surface. This arrangement allows the local gas composition above the sample surface to be measured with negligible contribution from the sample holder or surroundings.

Quantitative interpretation of the CO desorption from nanoparticulate samples is challenging, due to the varied particle shapes, and their unknown facet terminations. However, from single crystal studies we may consider three different CO adsorption states: CO that is bound weakly

due to strong CO-CO repulsion effects, lower coverage CO bound at intermediate temperatures centered near 400K, and CO bound strongly to undercoordinated surface atoms. Thus for our system, we have chosen to decompose all fitted curves into three Gaussians, where we have chosen to fix the centre of the 2nd Gaussian in temperature, T_{cent}=410K, and range T_{range}=69K, but with the fitted area free. The fits of the low and high temperature Gaussians were completely free. It was chosen to fix the 2nd Gaussian, as both the repulsion effects seen at low temperature, and the under coordinated atoms represented at high temperature, are strongly dependent on the nanoparticle size. We expect the 2nd Gaussian, representative of low coverage CO bound on (111) facets, to have a weak dependence on particle size. The centre and width of the 2nd Gaussian were chosen to match the centre of CO desorption spectra from the Pt(111) surface, so that the Gaussian decay is complete near 500K, as expected for the clean Pt(111). The values of terraced area presented in the text were determined by comparing the summed areas of the first and second Gaussians (representing CO bound on terraces), as a proportion of the area of all three Gaussians.

TEM and SEM characterization

Nanoparticle size distributions were obtained using Transmission Electron Microscopy (TEM) images performed using a TECNAI T20 electron microscope with primary electron energy of 200 keV. SEM images were obtained using a Helios EBS3, with accelerating voltages of 5kV.

Electrochemical experiments

The electrochemical experiments were performed with Bio-Logic Instruments' VMP2 potentiostat, controlled by a computer. The rotating ring disk electrode (RRDE) assemblies were provided by Pine Instruments Corporation. All glassware was cleaned in 96% H_2SO_4 and 30% H_2O_2 (3:1 v/v). This was subsequently sonicated and rinsed several times in milipore water (>18.2 MΩ cm-1, TOC<5 ppb). A standard three-compartment glass cell was used for all electrochemical experiments. The electrolyte, 0.1 M $HClO_4$ (Merck, Suprapur) was prepared using Millipore water (>18.2 MΩ cm-1, TOC<5 ppb). The counter electrode was a platinum wire and the reference was Hg/Hg_2SO_4 electrode. However, all potentials are quoted with respect to the RHE and corrected for Ohmic loses[3] . The reference electrode and the counter electrode were separated from the working electrode compartment using ceramic frits. A RRDE assembly was used in lieu of a rotating disk electrode (RDE) assembly. When an RDE assembly was used, there was a significant electrochemical response from the walls of the glassy electrode, due to the relatively loose fit between the electrode and the PTFE arbour. On the other hand, the arbour of the RRDE provided a tighter fit, eliminating the contribution from the electrode walls. The ring electrode was not specifically used, for instance to determine the % H_2O_2 yield; within the potential range of interest is above the thermodynamic potential for H_2O_2 production from O_2.

The electrode prepared under UHV conditions was transferred to the electrochemical cell and was immersed under potential control at 0.05 V in N_2 saturated 0.1 M $HClO_4$ electrolyte. The potential was then constantly cycled between 0.5 V and 1.15 V till stable cyclic voltagramm was recorded. The ORR activity was carried out by cycling the potential between 0 V and 1 V, at 50 mVs^{-1}, 1600 RPM and 23± 1 C, after saturating the solution in O_2.

The kinetic current density for the oxygen reduction, jk, was calculated using the following equation[4]:

$1/j_{meas} = 1/j_k + 1/j_d$,

where j_{meas} is the measured current density, and j_d is the diffusion limited current density.

To establish the influence of different capacitive current contributions toward the overall current we have used analog compensation of the electrolyte resistance and a background subtraction that eliminates such capacitive current contributions. Figure S1 shows ORR Tafel plots of the different samples with and without capacitance correction. No important differences can be observed confirming that under our measuring conditions, e.g. without a high surface area support, we can neglect the effect of capacitance.

Additionally, the CO-stripping analysis were carried out in CO-free Ar purged solution, after adsorbing CO at a constant potential of 0.05 V for 20 minutes to establish the electrochemical surface area of the Pt samples. CO stripping polarization curves were then recorded by scanning the potential until 1.0 V at 50 mVs^{-1} The active surface area was estimated using the area under the CO-stripping peak assuming a CO linearly binding on Pt that provides a charge equivalence of 420μC/cm^2Pt[4].

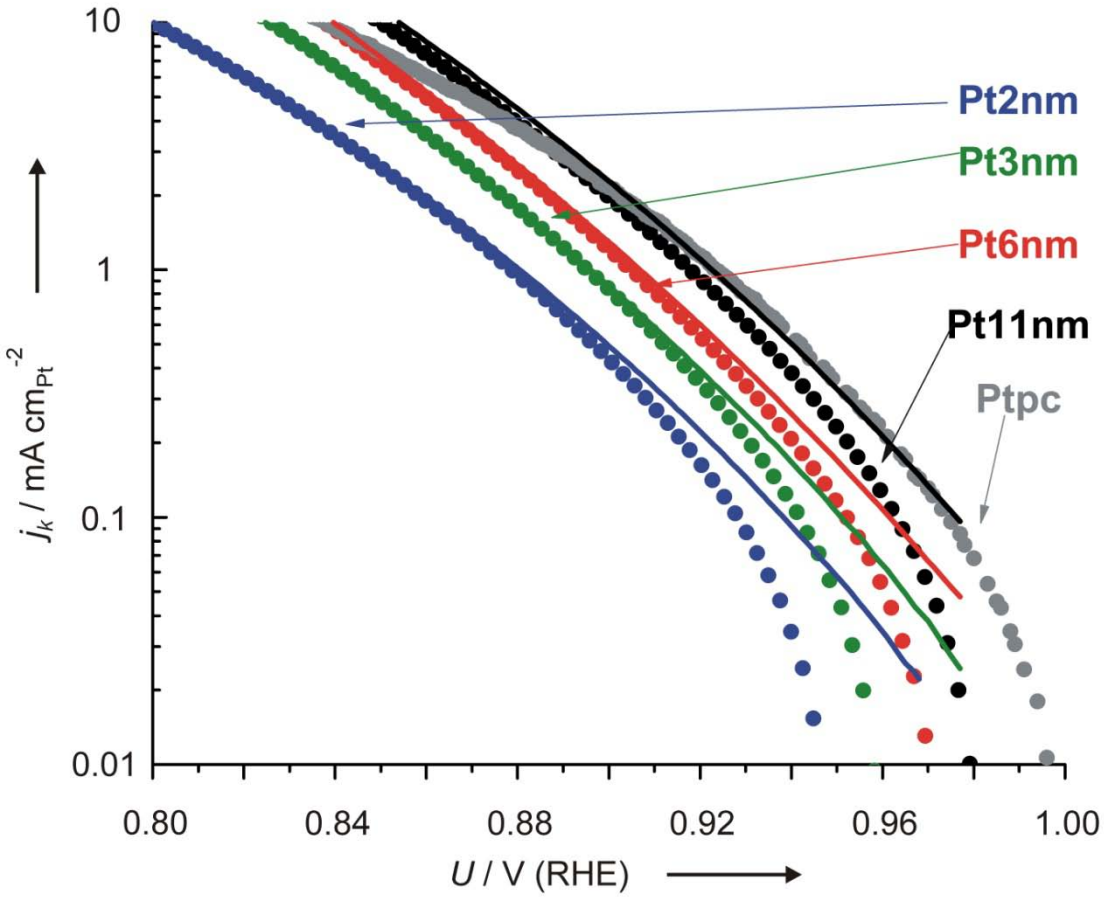

Figure S1. ORR Tafel plots of samples Ptpc (grey), Pt-2 nm (blue), Pt-3nm (green), Pt-6 nm (red) and Pt-11 nm (black) extracted from polarization curves recorded in oxygen saturated electrolyte (0.1 M $HClO_4$) at 50 mVs^{-1} and 1600 rpm . Lines correspond to Tafel plots after eliminating such capacitive current contributions.

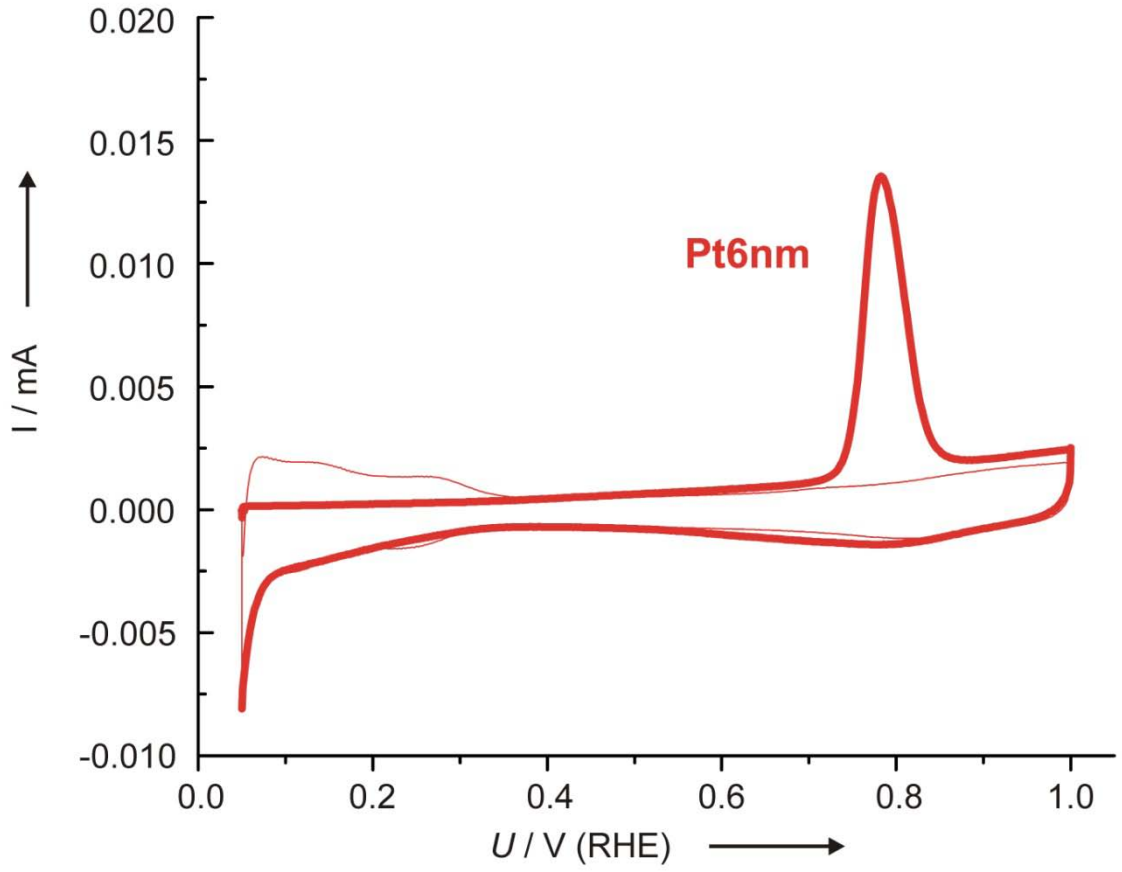

Figure S2. Example of CO stripping curve (thicker line) and CV (after oxidation of CO preadsorbed monolayer) recorded at 50 mVs-1 in 0.1 M $HClO_4$ solution for sample Pt6 nm.

Calculation Pt surface areas and coverage on the glassy carbon electrode

One key parameter to establish the ORR electrocatalytic properties of Pt clusters with size is their coverage on the glassy carbon electrode. There are two complementary methods via which we can estimate the coverage of Pt nanoparticles on the glassy carbon electrode. The first is to measure and integrating the neutralization current during the cluster deposition, which takes advantage of the fact that the particles are singly charged. In addition, the coverage can be calculated using the electrochemically active surface area determined from the oxidation of a pre-adsorbed CO adlayer (CO stripping), and considering the geometric surface area of the

electrode. Figure S3 shows and compares the coverage results obtained with CO stripping and current integration methods. Both methodologies allow the calculation of the surface area of the Pt nanoparticles, and consequently the electrode coverage for different nanoparticle sizes, assuming spherical geometry for the clusters.

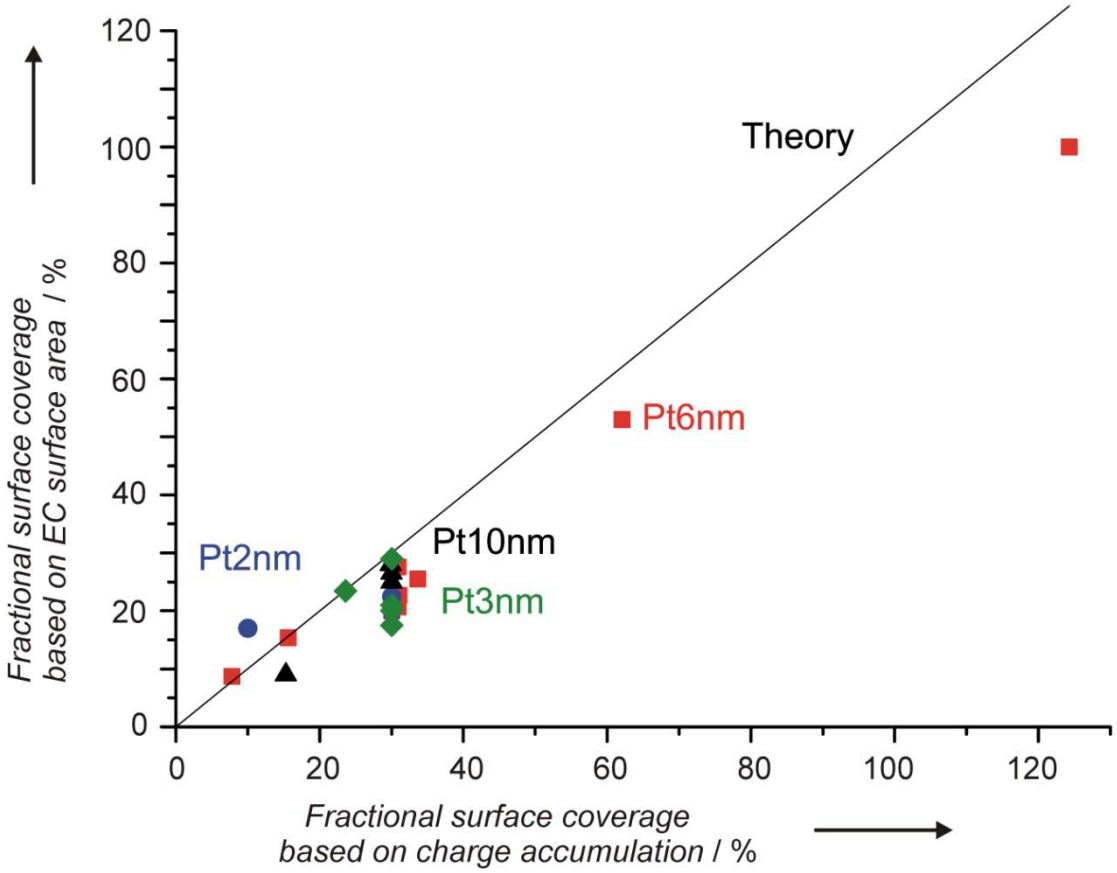

Figure S3. Comparison of Pt surface coverage on GC calculated by means of current integration and CO stripping curves for samples Pt2nm (blue), Pt3nm (green), Pt6nm (purple) and Pt10nm (black). Black line depicts the theoretical relationship between both approaches if the calculation of surface area would be similar with both methods.

The results show good agreement for the two different methods, although the CO stripping method typically shows less surface area than that predicted by the current integration method, especially for higher deposition coverages. These differences can be understood on the basis that the current integration provides a measure of the total surface area of the nanoparticles, whilst CO stripping supplies a measure of the electrochemically accessible surface area of the catalysts. Experimentally, the surface area available for catalysis should be reduced from the current integration method, due to effects such as particle-support contact area, and particle agglomeration. A small amount of particle agglomeration due to electrochemical experiments has been observed, via comparison of high resolution SEM images of a sample surface before and after electrochemical measurements (see Figure S4 example for the 2 nm sample). Agglomeration acts to reduce the surface area, and would certainly be more noticeable at high

coverage. The observation that the surface area of the Pt nanoparticles supported on glassy carbon decreases below expectations as the coverage is consistent with the work of Arenz and co-workers[5] . Consequently, the ORR activity results which we report are based on the Pt coverage calculated from CO stripping experiments.

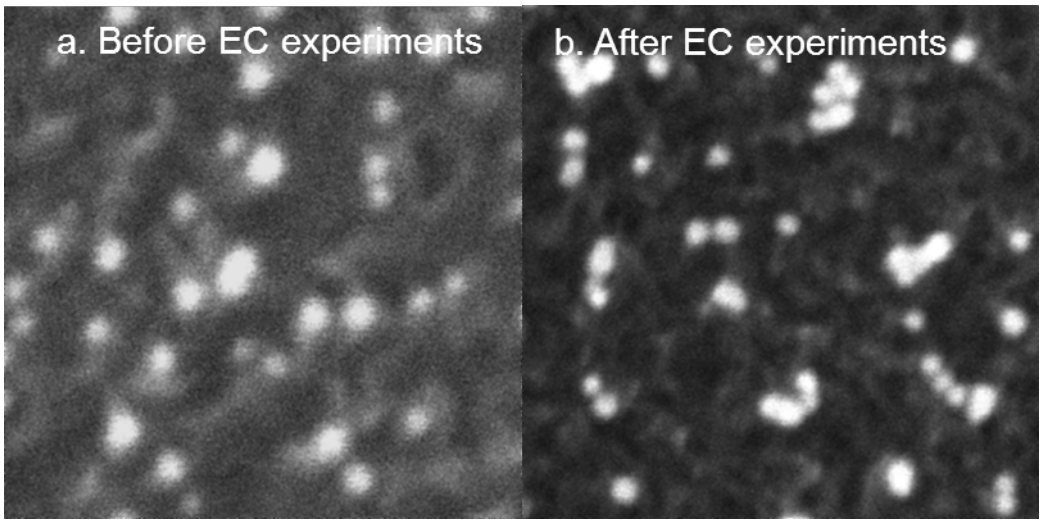

Figure S4. SEM micrographs of Pt 2 nm sample before and after electrochemical experiments (ORR and CO stripping)

The mass activity was established using the mass of Pt calculated from _____,
where *APt* is the surface area calculated from CO stripping experiments, ρPt is the density of Pt and *dPt* is the diameter of Pt particle. As such, the resulting mass activity is a measure of the hypothetical activity if the particles were spherical, like conventional Pt nanoparticles, rather than hemispherical.

Comparison between ORR specific and mass activity and earlier theoretical predictions

Figure S5 compares the ORR specific activity and mass activity at 0.9 V (RHE) obtained for the different catalysts studied with theoretical predictions by Tritsaris et. Al [6]. ORR specific activities presented here are in good agreement with those predictions, i.e. extended Pt surfaces exhibit the same activity as 11 nm nanoparticles, and there is a four-fold increase in ORR activity going from 2 nm Pt particles to extended surfaces[6-7].

The Pt mass activity for the ORR shows a maximum for a particle size of 3nm, consistent with the maxima observed experimentally and theoretically by Gasteiger et al. and Tritsaris et al., respectively[6, 8].

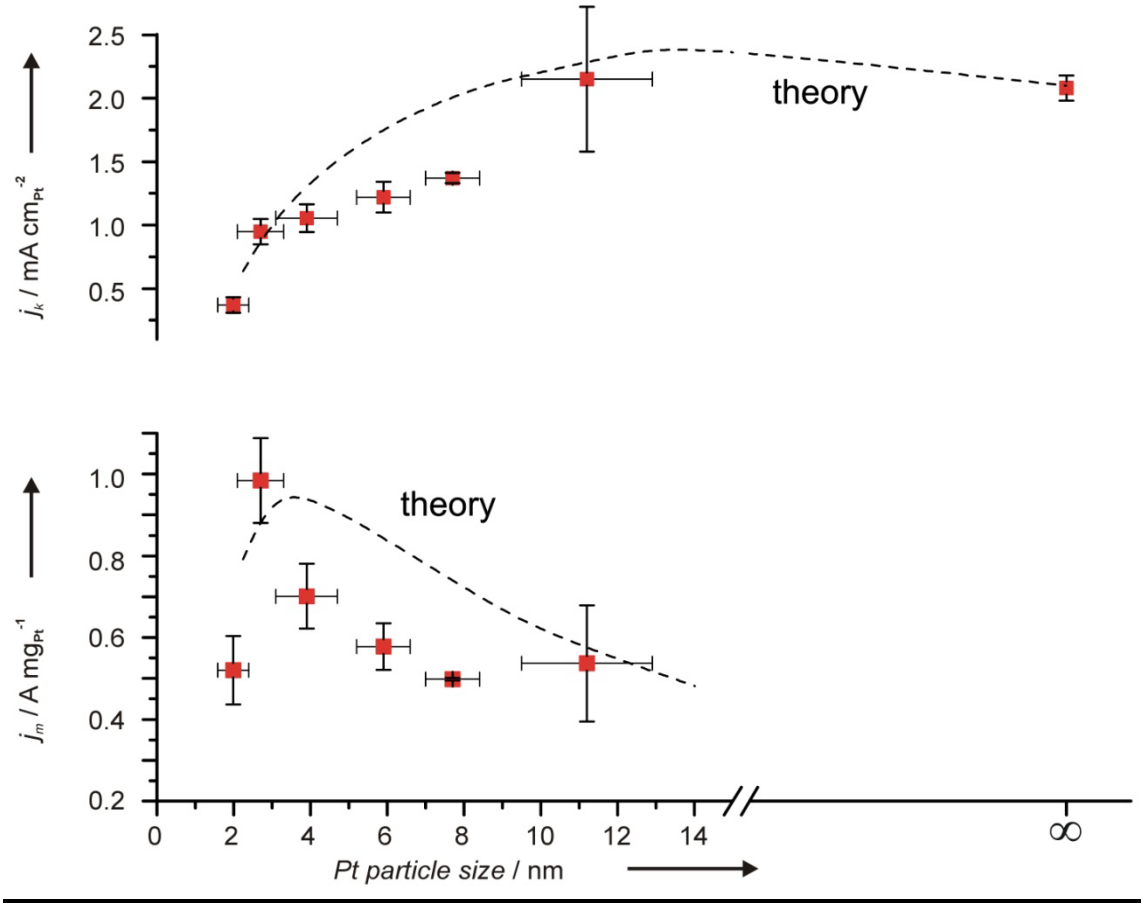

Figure S5. ORR kinetc current densities (above) and mass activities (below) at 0.9 V (RHE) of different samples studied, from CV's in O_2-saturated 0.1 M $HClO_4$, sweep rate= 50 mVs-1, 1600 rpm at 23 ºC. The dashed lines represent recent theoretical predictions[6]

References

[1] R. M. Nielsen, S. Murphy, C. Strebel, M. Johansson, J. H. Nielsen, I. Chorkendorff, *Surf. Sci.* **2009**, *603*, 3420-3430.

[2] S. B. Simonsen, I. Chorkendorff, S. Dahl, M. Skoglundh, J. Sehested, S. Helveg, *Journal of the American Chemical Society* **2010**, *132*, 7968-7975.

[3] J. Greeley, I. E. L. Stephens, A. S. Bondarenko, T. P. Johansson, H. A. Hansen, T. F. Jaramillo, J. Rossmeisl, I. Chorkendorff, J. K. Norskov, *Nature Chemistry* **2009**, *1*, 552-556.

[4] K. J. J. Mayrhofer, D. Strmcnik, B. B. Blizanac, V. Stamenkovic, M. Arenz, N. M. Markovic, *Electrochimica Acta* **2008**, *53*, 3181-3188.

[5] S. Kunz, K. Hartl, M. Nesselberger, F. F. Schweinberger, G. Kwon, M. Hanzlik, K. J. J. Mayrhofer, U. Heiz, M. Arenz, *Phys. Chem. Chem. Phys.* **2010**, *12*, 10288-10291.

[6] G. A. Tritsaris, J. Greeley, J. Rossmeisl, J. K. Norskov, *Catalysis Letters* **2011**, *141*, 909-913.

[7] J. Greeley, J. Rossmeisl, A. Hellman, J. K. Norskov, *Zeitschrift Fur Physikalische Chemie-International Journal of Research in Physical Chemistry & Chemical Physics* **2007**, *221*, 1209-1220.

[8] H. A. Gasteiger, S. S. Kocha, B. Sompalli, F. T. Wagner, *Applied Catalysis B-Environmental* **2005**, *56*, 9-35.

THE JOURNAL OF PHYSICAL CHEMISTRY C

Article

pubs.acs.org/JPCC

Structural Modification of Platinum Model Systems under High Pressure CO Annealing

D. N. McCarthy,[†] C. E. Strebel,[†] T. P. Johansson,[†] A. den Dunnen,[†,‡] A. Nierhoff,[†] J. H. Nielsen,[†] and Ib Chorkendorff*,[†]

[†]Center for Individual Nanoparticle Functionality, Department of Physics, Technical University of Denmark, 2800 Kgs. Lyngby, Denmark

[‡]Leiden Institute of Chemistry, Leiden University, Einsteinweg 55, P.O. Box 9502, 2300 RA Leiden, The Netherlands

ABSTRACT: Using temperature-programmed desorption experiments, we have studied the coordination dependent adsorption of CO on a platinum (Pt) single crystal, and mass-selected Pt nanoparticles in the size range of 3 to 11 nm, for CO dosing pressures in 10^{-7} mbar and mbar ranges. From low pressure CO adsorption experiments on the Pt(111) crystal, we establish a clear link between the degree of presputtering of the surface prior to CO adsorption, and the amount of CO bound at high temperature. It was found that for rougher surfaces, i.e., with more undercoordinated surface atoms, a feature appears in the CO desorption spectra at high temperature. The result is consistent with literature results from stepped single crystals that have found high temperature CO desorption features due to the presence of undercoordinated step and kink sites on the crystal facets. For the nanoparticles, a study of the dependence of the CO desorption profile with particle size found more prominent high temperature CO desorption features as the nanoparticle size was decreased, consistent with the expectation for a higher proportion of undercoordinated sites at smaller particle sizes. Thus, for both systems there is a clear relation between surface atom coordination, and the desorption temperature of CO. Investigation of these structural features was then made for CO dosing pressures in the mbar range. Intriguingly, from the mbar pressure experiments it was observed that elevated CO pressures enhanced the annealing of the Pt(111) surface, but on the otherhand, caused an apparent roughening of the nanoparticles.

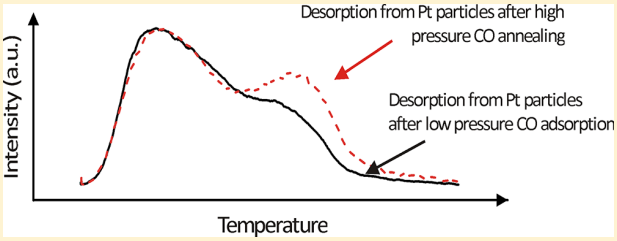

INTRODUCTION

Currently, there is significant interest in Pt and Pt alloys in electrochemical environments, due to their high activity for reactions such as oxygen reduction and methanol oxidation, where the noble properties of Pt are especially important for its high activity and long-term stability in typically acidic environments. Pt catalysts are also important in heterogeneous reactions such as in the oxidation of soot and hydrocarbons in exhaust systems. Knowledge of the modifications that Pt surfaces undergo due to gas composition and temperature is clearly important for understanding the performance of Pt as a catalyst, both in terms of its activity, but also with regards to its long-term stability against processes such as sintering, or dissolution. Advances to our understanding of environmentally induced changes to a catalyst could help lead to fundamental advances in catalyst design, leading to their implementation in environmentally friendly fuel cell technologies. In this report, we present investigations into a Pt(111) crystal and Pt nanoparticles.

The structural modification of nanoscale systems due to adsorbate−surface interactions can be observed via a number of spectroscopic techniques: transmission electron microscopy (TEM),[1,2] scanning tunneling microscopy (STM) in both gaseous and liquid environments,[3−5] and also through techniques such as X-ray diffraction (XRD).[6] The modification of surfaces due to environmental conditions is important for applications such as catalysis, where reaction rates can be strongly influenced by surface structure,[7,8] for instance in the formation of steps that could aid bond dissociation. With the advent of atom-sensitive techniques that operate nearer to reaction conditions (e.g., high pressure X-ray photoelectron spectroscopy (XPS), Environmental-TEM), the richness of the surface dynamics during reactions can be observed. Surface dynamics are interesting in many respects, but in particular to heterogeneous catalysis, where nanoparticulate catalysts have traditionally been considered to play a static role in reactions. Modern studies now reveal the dynamics of particle surfaces; changes to oxidation state, surface roughness, and surface elemental composition of alloy materials, have all been observed. These types of changes are all relevant to catalytic activity—a recent example reported by Hendriksen and co-workers[6] (for an earlier review, see ref 9) where spontaneous oscillations in CO oxidation rates over a Pd crystal were related to rapid oscillatory changes of the oxidation state and surface

Received: March 12, 2012
Revised: June 13, 2012
Published: June 18, 2012

roughness of the crystal surface. Further investigations into different material systems are then warranted.

In contrast to the expensive spectroscopic techniques such as E-TEM, HP-XPS (which typically requires synchrotron facilities), a comparatively simple way to probe surface structure is to use gas adsorption, combined with temperature-programmed desorption. Changes to surface structure, in particular changes to the coordination of the surface atoms, should be apparent in the desorption profile due to the coordination dependent binding energies of gas molecules.[10] The adsorption of CO on Pt has been studied thoroughly in recent decades, for various surface terminations of the Pt single crystal. For low index surface orientations, adsorbate structures of CO have been studied with high precision using techniques such as STM, low energy electron diffraction (LEED), temperature-programmed desorption (TPD), and electron energy loss spectroscopy (EELS). From the annealed Pt(111) crystal surface, Steininger et al.[11] observed the desorption of CO over a broad temperature range, from 300 to 500 K. From LEED experiments, a variety of different CO adsorbate structures were observed, depending on the CO coverage. In order to investigate the CO desorption temperatures of less coordinated atoms, McClellan et al.[12] performed similar CO desorption experiments on the Pt(321) surface (essentially a (111) surface with monatomic steps every three atoms). From these experiments the desorption of CO was observed in two distinct temperature ranges: from 300 to 500 K, and from 500 to 600 K. The two desorption features were respectively attributed to CO bound on fullly coordinated Pt terrace atoms, and to under-coordinated Pt atoms at steps and kinks. Thus, it is possible to distinguish desorption sites using TPD.

The main objective of the present work is to investigate the structural changes induced by CO adsorption on both a roughened Pt(111) single crystal and nanoparticulate samples. Our work is motivated by STM experiments which have shown reconstructions of Pt surfaces in CO atmospheres,[3,4,10,13] for CO pressures ranging from high vacuum to near atmospheric pressure. In those experiments, the reconstruction of the Pt surface due to CO coverages has been variously argued to result from entropic considerations for Pt(110) surfaces, or elastic strain and or electronic effects for the vicinal Pt(557) and Pt(332) surfaces. Vicinal surfaces are interesting as they have small terraces and a large density of undercoordinated Pt atoms, similar to the case of nanoparticles, though without the associated characterization difficulties. Strain is certainly an important consideration for nanoparticles, and it is therefore interesting to investigate the effect of CO on nanoparticles of different sizes, and at different pressures/temperatures. Using TPD experiments, we demonstrate the similarity between the desorption features of CO from roughened single crystals and nanoparticles, linking the undercoordinated sites of the two systems. We then perform comparative experiments at ∼10 mbar, and different temperatures, and discover modifications to the desorption spectra for the two systems, which are interpreted as an annealing out of the single crystal, versus a roughening of the nanoparticles. An apparent size dependence to the roughening of the nanoparticles suggests some strain dependence.

EXPERIMENT

The experimental results described in this report were performed in two separate ultra high vacuum (UHV) systems. Experiments on Pt nanoparticles were performed in a multichamber UHV system (Omicron, Multiscan Lab) with a base pressure in the low 10^{-11} mbar region. This system is equipped with facilities for combined STM, and scanning electron microscopy (SEM), Ion scattering spectroscopy (ISS), and TPD measurements. A second UHV system with a base pressure below 10^{-10} mbar was used for the Pt(111) experiments. This chamber is equipped with facilities for TPD, ISS, and XPS. Both vacuum systems are equipped with high pressure cells into which samples can be transferred and dosed at pressures up to 1 bar. The high pressure cells are attached directly to the main vacuum chambers, and have dedicated pumping and gas dosing lines, which allows for sample transfer and dosing without exposure of the samples to outside contamination.

Nanoparticle Production and Analysis Setup. Mass-selected nanoparticles were deposited from an inert-gas aggregation source (Mantis Deposition Ltd.), which is described in detail elsewhere.[14−16] Briefly, a flux of Pt atoms is produced in a source chamber by magnetron sputtering of a 99.9% purity Pt target (Williams Advanced Materials Inc.). Sputtered atoms are then condensed into nanoparticles using cooled Ar or He atoms, and emitted from the source chamber through an exit nozzle into a second vacuum chamber. As 30 to 80% of the nanoparticles produced using this method are ionized[15,17] a quadrupole mass filter mounted in the second vacuum chamber filters the nanoparticles according to their mass-to-charge ratio. The nanoparticles exiting the quadrupole are then focused via electrostatic lenses onto SiO_2/Si wafers mounted in Omicron VT sample holders in the main vacuum chamber. For these experiments the nanoparticles are deposited in a soft-landing regime (i.e., ∼they have a kinetic energy of ≤0.1 eV/atom).

An interesting aspect of this work is the choice of substrate, which in this case is a 100 nm thick SiO_2 layer grown via wet chemistry on 300 μm thick Si(111) wafers. The wafer design will be described more fully in a future publication, but certain important details should be mentioned. First, the wafer has a sandwich type structure, with a 100 nm thick SiO_2 on the topside, the middle section is Si(111), and on the wafer backside is a platinum resistance-temperature device (RTD) lithographically integrated to allow for accurate temperature measurements. During the temperature-programmed desorption experiments, the wafers were heated resistively by passing direct current through the Si wafer, with the wafer temperature monitored by measurement of the resistance of the RTD and comparison of the resistance to externally calibrated temperature/resistance curves. The RTD was electrically isolated from the Silicon wafer via a 100 nm thick silicon nitride layer. The wafers were designed and produced at DTU-Nanotech.

To ensure the cleanliness of the samples prior to the CO adsorption experiments, after insertion into UHV the entire manipulator head (including sample holder and sample) was degassed at 600 °C for 12 h. The SiO_2/Si wafers were then annealed to 500 °C based on the RTD calibration, and then exposed to 10^{-6} mbar O_2 for 30 min, to oxidize any hydrocarbons that might be present on the SiO_2 surface. After the oxidation, the samples were cooled to room temperature (typically 45 min) before the nanoparticles were deposited onto the surface. Ion scattering spectroscopy (ISS) was used to confirm the cleanliness of the as cleaned SiO_2 surface, and of the surface directly after the deposition of Pt nanoparticles. The ISS spectra were recorded using 980 eV He^+ ions produced by a differentially pumped electron impact ion

dx.doi.org/10.1021/jp302379x | J. Phys. Chem. C 2012, 116, 15353−15360

source (ISE 100, Omicron Nanotechnology). The reflected ions were detected at a 147° scattering angle with a hemispherical energy analyzer.

TPD experiments were performed in the preparation chamber of the UHV system. The samples were dosed with isotopically labeled 30 amu $^{12}C^{18}O$ molecules (CIL, two percent 16O), to distinguish from the background $^{12}C^{16}O$. The $^{12}C^{18}O$ was dosed through a leak valve until a chamber pressure of 10^{-7} mbar was attained, for a dosing time of 10 min, corresponding to an exposure of 60 langmuir, sufficient to saturate the surface. After dosing was completed, the chamber was evacuated, then the sample temperature was ramped at a rate of 1 K/s in UHV and the $^{12}C^{18}O$ desorption from the substrate was analyzed using a differentially pumped Balzers QMA 125 quadrupole mass spectrometer (QMS). The spectrometer was equipped with an oxygen-free high conductivity copper sniffer tip with a 1 mm diameter aperture, positioned within 0.5 mm of the sample surface. This arrangement allows the local gas composition above the sample surface to be measured with negligible contribution from the sample holder or surroundings. The temperature ramp of the TPD was controlled via a Labview script that regulated the power supply heating the SiO_2/Si-wafer based on the resistance measured across the RTD. The maximum temperature during the ramps was 700 K, which is below the onset temperature of ~770 K and 2 mbar of O_2 for Ostwald ripening of Pt nanoparticles supported on SiO_2.[18,19] Thus, we do not expect the nanoparticles to coarsen during the TPD experiments.

Single Crystal. For the single crystal experiments, performed in the second vacuum system, we used a 5 mm diameter Pt(111) single crystal supplied by MaTecK. The crystal has three holes drilled parallel to the surface (111) plane. A 0.38 mm tungsten wire used for heating is looped through two of these holes, while a K-type thermocouple is secured into the third hole to allow for measurement of the crystal temperature. The back ends of the tungsten loop are screwed onto a cryostat, which could be air cooled to 300 K, or to 80 K using liquid nitrogen. A PID algorithm is used to regulate the power supplied to the tungsten wire based on the temperature read from the thermocouple, allowing for stable temperature control.

The Pt(111) single crystal was cleaned by sputtering with 1.2 keV Ar ions, with the crystal temperature maintained at 1273 K. After sputtering, the crystal was further annealed for 1 min at 1273 K. The cleanliness of the crystal was verified by LEED, ISS, and XPS. In order to roughen the Pt crystal surface, the crystal was sputtered with Ar ions at various temperatures between 88 and 673 K. In these experiments, the crystal was sputtered under the same conditions as for the cleaning procedure, however with the crystal temperature kept constant, and with no post sputter annealing treatment. It was observed that annealing of the sputtered crystal at 1273 K for 1 min could restore the crystal surface to the state of the purely annealed crystal, as determined by XPS, and CO desorption experiments, in agreement with ref 20. We therefore conclude that the sputtering process does not contaminate the surface.

In the TPD experiments, $^{12}C^{16}O$ was dosed at 2×10^{-7} mbar in the main vacuum chamber for 500 s while cooling the crystal down from the temperature at which it was sputtered. When air cooling was used, the crystal did not cool down sufficiently fast and dosing CO for an extra 500 s was needed until the sample reached a temperature of 313 K. The total CO dose was on the order of 100 L, more than sufficient to saturate the surface with CO.

Mbar Range CO Experiments. For CO dosing pressures in the mbar range, an important consideration is the potential for traces of Ni−carbonyl contamination in the gas to react on the Pt surface, and deposit Ni. In order to minimize the potential for Ni contamination, the $^{12}C^{16}O$ gas was passed through an active carbon filter, and second through a liquid nitrogen cold trap. In addition to the gas cleaning procedures, the gas lines leading from the filters to the high pressure cell are made from copper, rather than stainless steel, and the high pressure cells are constructed from Ni free steel. After the high pressure experiments, the lack of any Ni contamination in both the nanoparticle and single crystal systems was verified by ISS, and/or XPS.

RESULTS

Structural Features for Low Pressure CO Dosing. In Figure 1, we show the CO TPD spectra from the Pt(111) single crystal, prepared with different degrees of sputtering: annealed at 1273 K, sputtered at 373 K, sputtered at 573 K, and sputtered at 673 K. In the figure, the QMS-signals from the desorbing CO have been normalized to their maximum signal height to enhance the sputter dependent desorption features of each spectra. From the purely annealed crystal, the CO desorption spectra is a single broad feature spanning from 300 to 500 K, consistent with results by Steininger.[11] In comparison, for sputtered crystal surfaces a second desorption feature appears in the spectra between 500 and 550 K. It is clear from the figure that the lower the sputtering temperature, and therefore the rougher the surface,[20] the more significant the shoulder at high temperature. This trend is consistent with the expectation for undercoordinated Pt atoms present on the rougher/sputtered surface to provide stronger adsorption sites for CO molecules,[10] which should be apparent as a shift in CO desorption to higher temperatures. To summarize, the rougher the surface, the higher the proportion of strongly bound CO.

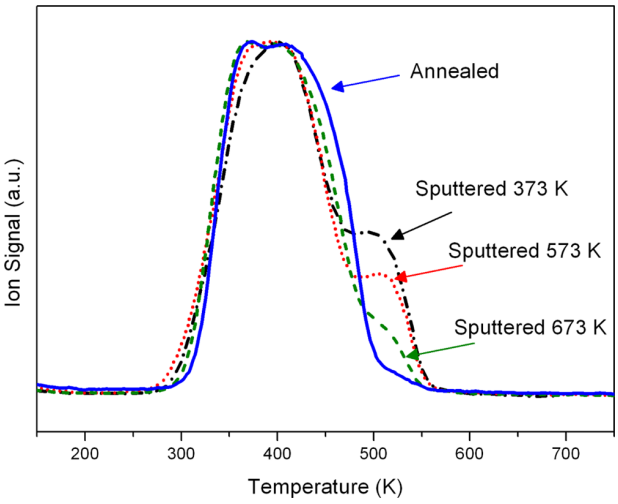

Figure 1. CO TPD spectra from the Pt(111) crystal after different preparations. The crystal was cooled to RT from the indicated sputter temperature in a background CO pressure of 10^{-7} mbar for 10 min. The TPD ramp rates were 2 K/s.

dx.doi.org/10.1021/jp302379x | J. Phys. Chem. C 2012, 116, 15353−15360

A second, less obvious feature of the CO desorption spectra from the single crystal is the narrowing of the low temperature desorption feature for increased surface roughness. The narrowing of the main desorption peak due to lower sputter temperatures, and therefore rougher surface topography, suggests a disruption of the ordering of CO on the terraced surface regions. The narrowing of the peak is reminiscent of the narrow desorption feature observed by Steininger for low coverage CO doses on a clean Pt(111) crystal e.g. 30% coverage of the CO monolayer, as well as the comparatively narrow low temperature desorption features observed on the stepped Pt(321)[12] and Pt(112)[21] surfaces.

In Figure 2, we present TPD spectra taken from the single crystal, both after annealing and after room temperature

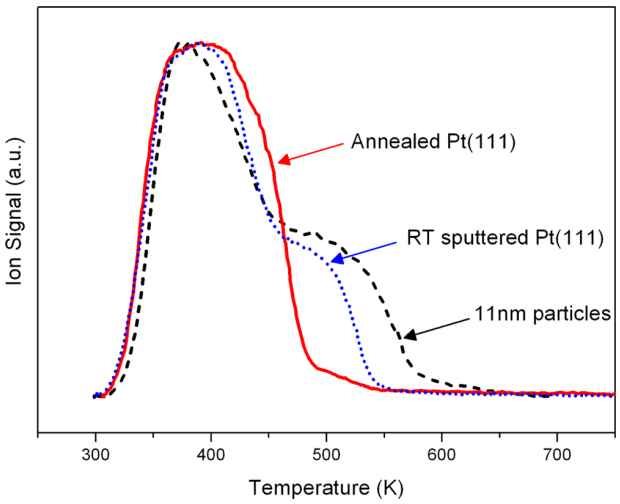

Figure 2. Comparison of CO TPD spectra from the annealed Pt(111) crystal, a sputtered Pt(111) surface, and from 11 nm particles supported on SiO_2/Si. Each of the samples was dosed at room temperature, in a background CO pressure of 10^{-7} mbar for 10 min, and the ramp rate of each TPD was 1 K/s.

sputtering, and compare these with the TPD spectra of ~11 nm Pt nanoparticles supported on SiO_2. As the samples were prepared in different vacuum systems, the CO dosing and TPD procedures were made as similar as possible. In the case of the single crystal, CO was dosed at 10^{-7} mbar for 10 min, directly after annealing or sputtering of the crystal. The CO TPD's were then performed at a heating rate of 1 K/s. For the nanoparticle sample, $^{12}C^{18}O$ was dosed immediately after the particle deposition was completed (depositions typically take 10 min from start to finish), at 10^{-7} mbar for 10 min, before performing the temperature ramp at 1 K/s. Again the spectra have been normalized to their respective maxima to better compare the shapes of the desorption spectra. The desorption spectra taken from the single crystal are similar to those shown in Figure 1, consistent with the minor change in ramp rate. More noteworthy is the desorption profile from the 11 nm particles. Here the $^{12}C^{18}O$ desorption kicks off at essentially the same temperature as the single crystal (SC), then forms a comparatively narrow main feature centered at 390 K, followed by a shoulder at high temperature that extends to 575 K. For comparison, in the TPD spectra of the sputtered SC the CO is fully desorbed by 540−550 K.

In parts a−f in Figure 3, we show size distributions of the three nanoparticle sizes investigated in this manuscript, along

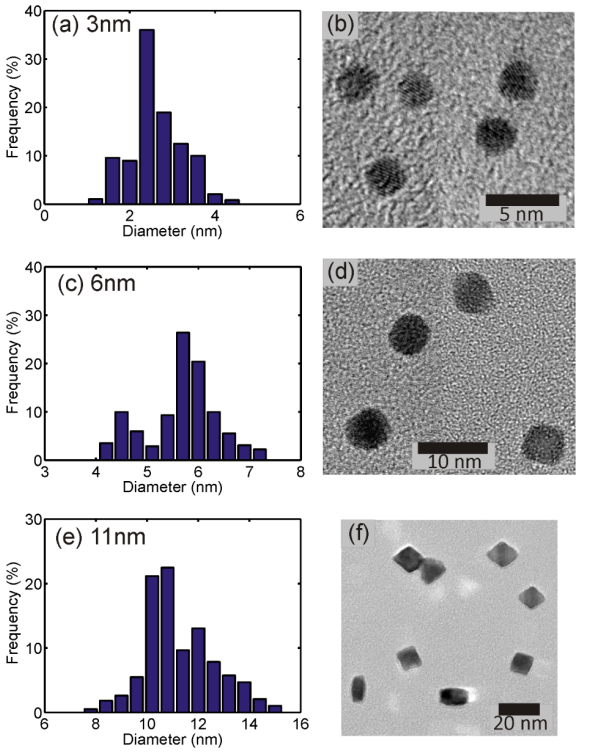

Figure 3. Pt particle size distributions and TEM micrographs of particles prepared under different source conditions. (a and b) 3 nm, (c and d) 6 nm, (e and f) 11 nm.

with some representative TEM micrographs. The size distributions were determined by measuring the particle cross sections from TEM images, and then assuming a spherical morphology in order to determine a diameter. The images are of the as-deposited nanoparticles, supported on either amorphous carbon or SiO_2 grids. The (b) 3 nm and (d) 6 nm particles have very circular cross sections, suggestive of near-spherical geometries, whereas the majority of (f) 11 nm particles have well-defined facet edges, and morphologies consistent with octahedra or cuboctahedra. When lattice fringes were observed under high resolution imaging, the fringe separations were always consistent with separations expected for the bulk Pt fcc structure. In general, the particle shapes are not perfect Wulff constructions, i.e., not in the lowest energy configuration. This is not surprising, as the gas aggregation growth method is a far from equilibrium process, and consequently the particles should not be expected to have uniform shapes.

Part a and b of Figure 4 show TPD spectra from SiO_2 supported samples of the 3, 6, and 11 nm particles shown in Figure 3. In Figure 4a, we show the first TPDs after the depositions, while in Figure 4b the second TPD is shown. The QMS-signals have been normalized to the maximum signal height to make apparent the different desorption profiles for the different particle sizes. From Figure 4a, we can see that as the mean nanoparticle size is reduced from 11 to 3 nm, the high temperature feature in the CO desorption spectra becomes more prominent. The trend is consistent with smaller nanoparticles having a higher proportion of undercoordinated sites. In Figure 4b, which shows the second TPD of each sample, there are only minor differences from the spectra shown in Figure 4a. The reduction in the shoulder in Figure 4b

dx.doi.org/10.1021/jp302379x | J. Phys. Chem. C 2012, 116, 15353−15360

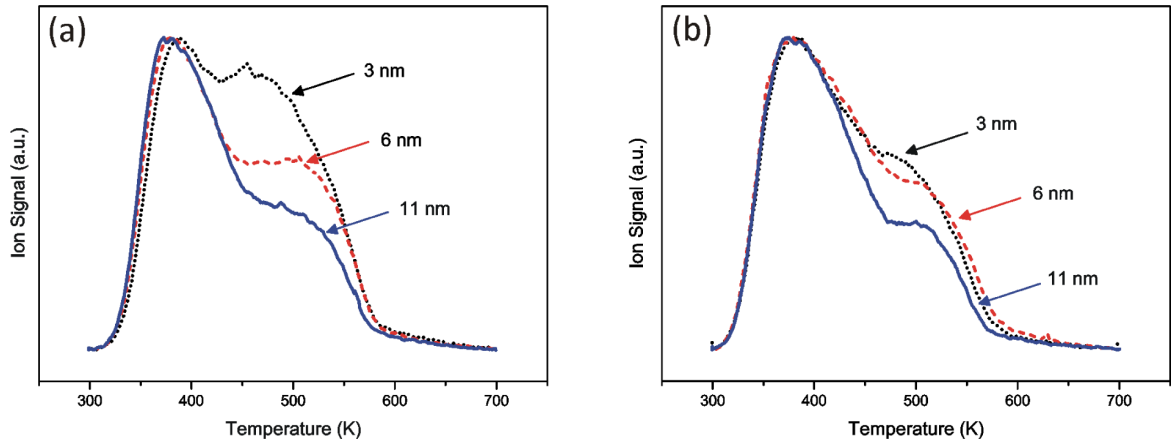

Figure 4. $^{12}C^{18}O$ TPD spectra from Pt nanoparticles produced using source conditions and filtering for 3, 6, and 11 nm particles, deposited onto SiO_2/Si supports: (a) first TPD; (b) second TPD. The ramp rate was 1 K/s.

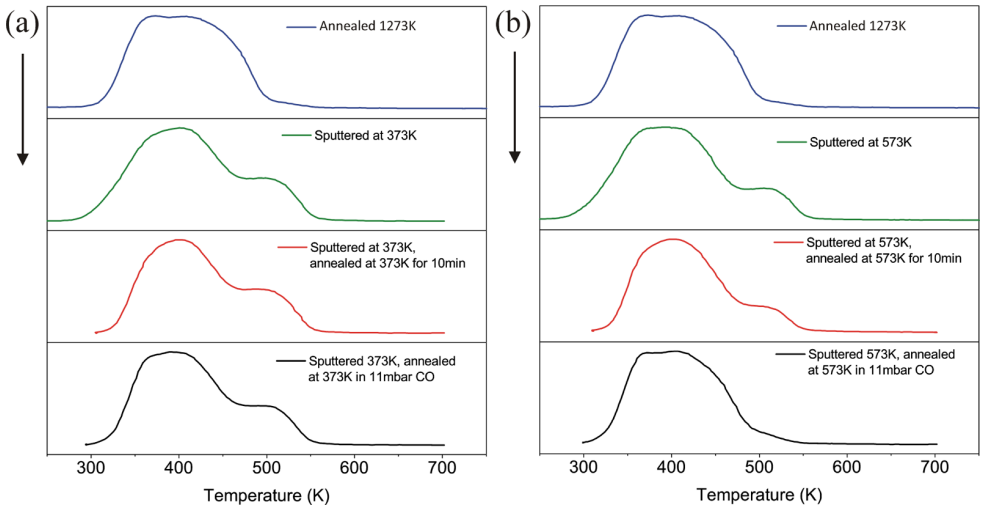

Figure 5. CO TPD spectra from (a) the annealed Pt(111) crystal, sputtered at 373 K, sputtered then annealed for 10 min at 373 K, and sputtered at 373 K with a 10 min anneal in 10 mbar CO and (b) the annealed Pt(111) crystal, sputtered at 573 K, sputtered then annealed for 10 min at 573 K, and sputtered at 573 K with a 10 min anneal in 10 mbar CO. The ramp rate of each TPD was 2 K/s.

is consistent with our expectation that the first TPD will reduce some of the initial roughness of the particles inherent to the aggregation process, due to a brief annealing during the temperature ramp. On selected samples, we performed three successive TPD's, and confirmed that the second and third TPDs have exactly the same shape (not shown), supportive of the idea of some minor rearrangement of the particle morphology with annealing.

To summarize the results presented in this section, Figures 1, 2, and 4 demonstrate that the temperature dependence of the CO desorption is closely linked to the coordination of the exposed Pt atoms, and that CO TPDs are a useful probe of surface structure.

Structural Features for High Pressure CO Dosing and Annealing. Having established the use of CO TPDs as a way to probe the surface structure of Pt, in the next set of experiments, we investigate the effects of higher CO pressures on the surface structure of the different Pt systems. In Figure 5, we show CO desorption spectra from a crystal sputtered at 373 K, then transferred to the high pressure cell, and maintained at this temperature in 10 mbar CO for 10 min. The sample was allowed to cool in the CO until a temperature of 300 K was reached, at which point the CO was evacuated, and the TPD performed. We also show the corresponding experiment from a sample sputtered and annealed at 573 K. Each high pressure spectra is compared against spectra from the purely annealed crystal, the freshly sputtered crystal, and the sputtered crystal after vacuum annealing for 10 min at the relevant temperature. It can be seen from Figure 5a that at 373 K the presence of 10 mbar CO has virtually no effect on the desorption spectra, while from Figure 5b for the crystal at 573 K the presence of 10 mbar CO produces a large annealing effect. Note that the same annealing effect on the crystal maintained at 573 K was observed for a 2 mbar CO pressure. It is apparent from the results that CO has the effect of aiding the diffusion of underlying Pt atoms, beyond the effect of the temperature alone.

To extend the high pressure experiments to the nanoparticle system, a similar procedure was followed for the Pt/SiO_2 samples with 3, 6, and 11 nm particles. In each case, the samples had first been treated to two prior $^{12}C^{18}O$ dosing/TPD cycles, so that the particles had already been through two

dx.doi.org/10.1021/jp302379x | J. Phys. Chem. C 2012, 116, 15353−15360

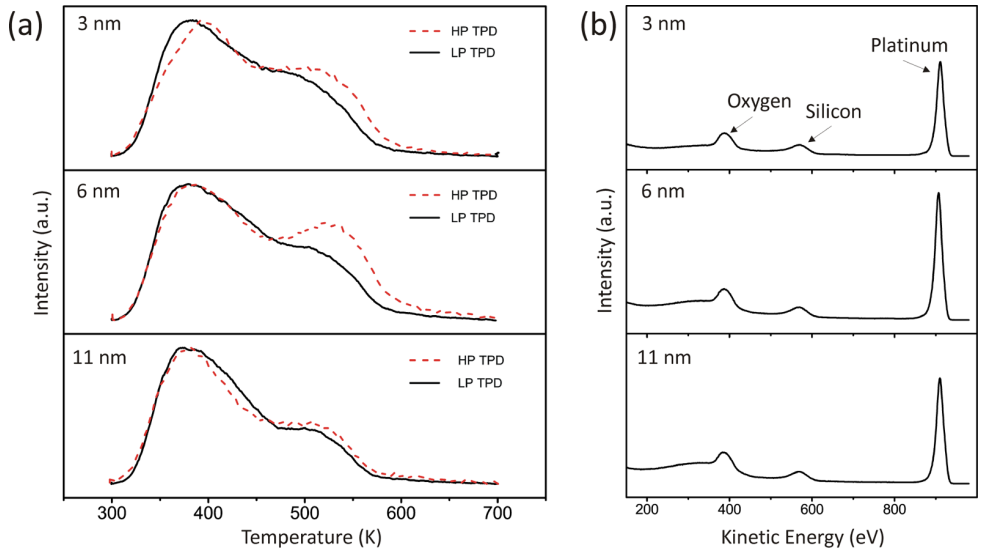

Figure 6. (a) CO TPDs from nanoparticle samples for particles of 3, 6, and 11 nm. The full lines are the spectra measured for the second $^{12}C^{18}O$ TPD of each sample, as shown in Figure 4 . The dashed lines are the $^{12}C^{16}O$ signals measured after the subsequent annealing of the samples at 573 K in 5 mbar $^{12}C^{16}O$. (b) ISS spectra from the corresponding samples taken after the high pressure TPD was completed.

temperature ramps, and thus should have attained a stable structure. After the second low pressure TPD, the samples were inserted into the high pressure cell, where they were annealed at 573 K in ~5 mbar of $^{12}C^{16}O$. After annealing at 573 K for 10 min, the samples were cooled in the CO atmosphere until a temperature of 300 K was reached, at which point the CO in the cell was evacuated, the samples transferred to the main vacuum chamber, and the TPD performed. The TPDs from each sample are shown in Figure 6, where the full line is from the second $^{12}C^{18}O$ TPD, and the dashed line is from the subsequent HP TPD.

Beginning with the TPDs of the 3 nm particles, after annealing in CO there is a slight shift of the low temperature desorption feature, but the main difference is the more prominent high temperature shoulder, which does not decay fully until well past 550 K. For the 6 nm particle sample, the low temperature desorption feature is very similar for the low and high pressure dosings, however the high temperature feature of the high pressure sample is much more prominent, forming a separate peak. The increased prominence of the high temperature feature was observed for three different 6 nm samples, prepared under similar conditions. For the 11 nm particles, there are no significant differences in the desorption spectra for low or high pressure dosings.

Along with the TPD spectra, we also include ISS spectra taken from the samples after the HP experiments. From the ISS spectra of these three samples, we observe only the expected oxygen, silicon, and platinum peaks. We show the ISS spectra because of the possibility of Ni−carbonyls being deposited on the particle surface during the high temperature dosing, unless the appropriate cleaning procedures are followed. We should stress that when the correct gas cleaning procedure was not followed, a clear feature in the ISS spectra was observed at 770 eV, which we assigned to Ni. Hence, we are confident that the features seen in the TPD spectra of Figure 6 are related to structural changes of the Pt particles and are not a consequence of sample contamination.

DISCUSSION

Low Pressure Dosing Experiments. From the roughened single crystal, the additional desorption feature between 500 and 550 K is consistent with results from stepped single Pt crystals, such as the Pt(112) surface, where a desorption feature is observed between 500 and 550 K,[21] assigned to CO bound solely at Pt(100) step-edges. Thus, we expect the roughened single crystal to consist of close packed step edges, as in the Pt(112) crystal, and unlike the Pt(321) crystal,[12] which has severely undercoordinated step atoms, where the steps consist of a kink site for every step site. This seems likely as, unlike on the Pt(321) surface, there should be no long-range elastic strain on a roughened single crystal driving the surface to form such energetically unfavorable kink sites. On the otherhand, for the nanoparticle samples where the desorption does not fully decay until ~575 K, the desorption temperature is consistent with CO desorption from the kinked Pt(321) surface.[12] Per unit surface area, nanoparticles have a large number of highly undercoordinated atoms at facet edges and vertices, similar to the coordination of atoms on the Pt(321) surface. Of course, the smaller the nanoparticle, the higher the surface area fraction of these undercoordinated sites. This is seen in the TPD spectra shown in Figure 4, where the smaller particles have a higher shoulder feature, and also more CO desorption above 550 K than the 11 nm particles.

Aside from our observation of changes to the coordination dependent binding of CO to the nanoparticles and single crystal, an interesting topic is the particle size dependence of the binding energy itself—the phenomena where for instance CO molecules bind more (or less) strongly to fully coordinated facet sites of 2 nm particles, than to the equivalent sites of 11 nm particles, possibly due to strain effects. For example, it has been reported that oxygen atoms bind more strongly to small Pt particles than to larger Pt particles.[22] On the contrary, however, from a recent CO adsorption study of Pt particles grown on HOPG, lower CO desorption temperatures were observed for smaller particle sizes, suggesting a decreasing CO binding energy for decreasing particle size.[23] This latter result is

dx.doi.org/10.1021/jp302379x | J. Phys. Chem. C 2012, 116, 15353−15360

comparable to the decrease in binding energy of CO with decreasing nanoparticle size for Pd nanoparticles supported on Fe3O4, observed by microcalorimetry.[24] From the TPD spectra of our nanoparticles in Figure 4, there is no clear indication of a size dependence to the binding energy. If anything, from Figure 4b, where the CO TPD's of each of the nanoparticle ensembles desorbs at exactly the same temperature, there is evidence against a particle size dependence for the sizes investigated in this study.

Mbar Pressure Annealing Experiments. The annealing out of the single crystal under high CO pressures is a likely consequence of the greater binding energies of CO molecules to undercoordinated Pt atoms at the sputter induced defects. Studies have shown that CO can cause a breaking of Pt−Pt bonds on the surface of Pt crystals,[10,13] as the increased binding energy of CO to undercoordinated Pt atoms is on the order of the strength of the intermetallic bonds, i.e., the difference in intermetallic bonds of a 5-fold coordinated Pt atom compared with 6-fold coordinated atom is similar to the additional bond energy of CO to a 5-fold coordinated rather than to a 6-fold coordinated atoms. The fact that CO can actively increase the number of undercoordinated Pt atoms with only minor enthalpy changes is considered to be driven by the higher entropy of the roughened surface. Our observations illustrate that an additional consequence of the CO−Pt binding is a reduced diffusion barrier for the Pt atoms, as signaled by Figure 5, where the presence of CO hastens the reorganization of the crystal into a state of low surface roughness. This reduction in adatom diffusion barrier due to gas adsorption has been observed for the hydrogen/Pt(110) system, where the binding of atomic hydrogen to Pt adatoms was visible by STM.[25]

The benefits of annealing in CO has been observed before in other systems, for instance Kibler et al.[26] have studied the effects of cooling flame annealed Pt single crystals in gases such as hydrogen, carbon monoxide, and air, and demonstrated the different surface morphologies that can result under the different gas conditions. In these experiments, there was a noticeable reduction in the surface roughness, and a higher degree of surface ordering, when the crystals were cooled in reducing environments. In electrochemical environments, the sweeping of the cell potential in a CO saturated electrolyte has been shown to induce surface structure changes on Pt electrodes,[5] suggesting enhanced mobility of Pt atoms when bonded to CO. It has also been observed for nanoparticulate samples supported on high surface area carbon supports, where electrochemical annealing in CO is found to aid the formation of defect free CO adlayer structures.[27] As far as we are aware, our experiments are the first to evidence the annealing effect of CO in vacuum environments.

Reversible roughening of the vicinal Pt(557) and Pt(332) crystals due to ∼mbar CO pressures has been reported in the literature[4] (reversible in the sense that after evacuation of the CO, the crystal surface restructured back to its original configuration), but without an in situ probe it is difficult from our experiments to conclude whether the mbar CO pressures induced a roughening of the crystal. Certainly from the TPD of the samples heated at 373 and 573 K in 11 mbar CO, there is no increase in the amount of CO adsorbed on the crystal surface at high temperature (i.e., the shoulder feature is not more prominent); however, we cannot exclude the possibility that a pressure dependent reconstruction took place when evacuating the cell and transferring the sample to high vacuum, as has been suggested previously by experiments involving the IR sum generation technique.[28] However, the lack of evidence for CO induced roughening from our experiments is consistent with a pressure dependent study of Besenbacher et al.,[29] which did not observe any structural changes to the Pt(111) surface for CO pressures up to 1 bar.

It is interesting to note that the nanoparticles exhibit the opposite effect to the Pt single crystal when annealed in mbar CO pressures. For the nanoparticles, mbar CO pressures and elevated temperatures leads to an increase in the amount of CO bound at high temperature, at least for the 3 and 6 nm particles, which we interpret as a consequence of a CO induced restructuring to the facets, to accommodate more CO. A recent work by Yoshida et al.[30] observed via E-TEM that 3 nm Pt particles become more rounded in 1 mbar of CO, consistent with our interpretation of the TPD results. The particle roughening is similar to the breakup of stepped Pt surfaces.[4] Interestingly, the observed roughening of the particles was most noticeable for the 3 nm and especially 6 nm particles, while it was virtually un-noticed for the 11 nm particles. From the stepped Pt(557) and Pt(332) crystals,[4] which respectively have terrace widths of 12 or 6 atoms after CO adsorption, the terrace widths are similar in magnitude to the diameters of the smaller nanoparticles of this study. From the experimental evidence of both systems, we therefore speculate that the CO induced restructuring of the nanoparticles could be a consequence of surface strain, though further insight requires detailed calculations (e.g., density functional theory), or more sophisticated experiments. We expect however that the roughening phenomenon we have observed could have implications in a number of areas of catalysis, e.g., for dissociation reactions that occur on sites with differing nearest neighbor geometries, e.g., steps, or for fuel cell applications where the Pt particle size with the highest mass activity is 3 to 4 nm.

■ CONCLUSIONS

We have demonstrated the use of temperature-programmed desorption as a structure sensitive probe, that can establish the presence of undercoordinated Pt atoms on single crystals and nanoparticles. By applying this technique to two model systems, the Pt(111) crystal and mass-selected nanoparticles, we have found good agreement between the desorption characteristics of the roughened single crystal, and the undercoordinated sites that predominate on nanoparticles. The high temperature desorption features of the nanoparticles were consistent with both the roughened single crystal, and literature results from vicinal Pt crystal surfaces.

In our high pressure CO experiments on the single crystal, the presence of CO was found to be beneficial for annealing a rough crystal surface. This phenomenon is considered to be due to CO induced weakening of the intermetallic bonds of undercoordinated surface Pt atoms, allowing more mobillity of these atoms, which leads to a faster relaxation of the surface to a thermodynamically favorable configuration. From the nanoparticles of 3 and 6 nm diameters, there was a clear increase in the proportion of CO bound at high temperature when annealed at 5 mbar, which we interpret as an increase in the density of undercoordinated Pt atoms on the particle surface. The increased CO adsorption was not so apparent for the 11 nm particles, which we speculate is due to a size dependent strain effect.

In future, high resolution environmental TEM experiments would also shed light on any morphological changes that the

3−6 nm Pt nanoparticles undergo in reaction conditions. We also consider it worthwhile to examine whether the CO induced roughening of the particles has any bearing on the reactivity of the nanoparticles, e.g., for methanation or CO oxidation.

AUTHOR INFORMATION

Corresponding Author

*E-mail: ibchork@fysik.dtu.dk.

Notes

The authors declare no competing financial interest.

ACKNOWLEDGMENTS

The Center for Individual Nanoparticle Functionality is supported by the Danish National Research Foundation. We acknowledge Thomas Pedersen and Prof. Ole Hansen of DTU Nanotech for helpful discussions and supply of the integrated resistance temperature devices.

REFERENCES

(1) Hansen, P.; Wagner, J.; Helveg, S.; Rostrup-Nielsen, J.; Clausen, B.; Topsoe, H. *Science* **2002**, *295*, 2053−2055.
(2) Vesborg, P. C. K.; Chorkendorff, I.; Knudsen, I.; Balmes, O.; Nerlov, J.; Molenbroek, A. M.; Clausen, B. S.; Helveg, S. *J. Catal.* **2009**, *262*, 65−72.
(3) Tao, F.; Dag, S.; Wang, L.-W.; Liu, Z.; Butcher, D. R.; Salmeron, M.; Somorjai, G. A. *Nano Lett.* **2009**, *9*, 2167−2171.
(4) Tao, F.; Dag, S.; Wang, L.-W.; Liu, Z.; Butcher, D. R.; Bluhm, H.; Salmeron, M.; Somorjai, G. A. *Science* **2010**, *327*, 850−853.
(5) Strmcnik, D. S.; Tripkovic, D. V.; van der Vliet, D.; Chang, K.-C.; Komanicky, V.; You, H.; Karapetrov, G.; Greeley, J.; Stamenkovic, V. R.; Markovic, N. M. *J. Am. Chem. Soc.* **2008**, *130*, 15332−15339.
(6) Hendriksen, B. L. M.; Ackermann, M. D.; van Rijn, R.; Stoltz, D.; Popa, I.; Balmes, O.; Resta, A.; Wermeille, D.; Felici, R.; Ferrer, S.; Frenken, J. W. M. *Nature Chem.* **2010**, *2*, 730−734.
(7) Dahl, S.; Logadottir, A.; Egeberg, R.; Larsen, J.; Chorkendorff, I.; Tornqvist, E.; Norskov, J. *Phys. Rev. Lett.* **1999**, *83*, 1814−1817.
(8) Andersson, M. P.; Abild-Pedersen, E.; Remediakis, I. N.; Bligaard, T.; Jones, G.; Engbwk, J.; Lytken, O.; Horch, S.; Nielsen, J. H.; Sehested, J.; Rostrup-Nielsen, J. R.; Norskov, J. K.; Chorkendorff, I. *J. Catal.* **2008**, *255*, 6−19.
(9) Imbihl, R.; Ertl, G. *Chem. Rev.* **1995**, *95*, 697−733.
(10) Thostrup, P.; Christoffersen, E.; Lorensen, H.; Jacobsen, K.; Besenbacher, F.; Norskov, J. *Phys. Rev. Lett.* **2001**, *87*, 126102.
(11) Steininger, H.; Lehwald, S.; Ibach, H. *Surf. Sci.* **1982**, *123*, 264−282.
(12) McClellan, M.; Gland, J.; McFeeley, F. *Surf. Sci.* **1981**, *112*, 63−77.
(13) Thostrup, P.; Vestergaard, E.; An, T.; Laegsgaard, E.; Besenbacher, F. *J. Chem. Phys.* **2003**, *118*, 3724−3730.
(14) Nielsen, R. M.; Murphy, S.; Strebel, C.; Johansson, M.; Nielsen, J. H.; Chorkendorff, I. *Surf. Sci.* **2009**, *603*, 3420−3430.
(15) Nielsen, R. M.; Murphy, S.; Strebel, C.; Johansson, M.; Chorkendorff, I.; Nielsen, J. H. *J. Nanoparticle Res.* **2010**, *12*, 1249−1262.
(16) Murphy, S.; Strebel, C.; Vendelbo, S. B.; Conradsen, C.; Tison, Y.; Nielsen, K.; Bech, L.; Nielsen, R. M.; Johansson, M.; Chorkendorff, I.; Nielsen, J. H. *Phys. Chem. Chem. Phys.* **2011**, *13*, 10333−10341.
(17) Haberland, H.; Karrais, M.; Mall, M.; Thurner, Y. *J. Vacuum Sci. Technol. A: Vacuum Surf. Films* **1992**, *10*, 3266−3271 Topical Conference on Surface Science at the Solid-Liquid Interface, Seattle, WA, Nov 11−15, 1991..
(18) Simonsen, S. B.; Chorkendorff, I.; Dahl, S.; Skoglundh, M.; Sehested, J.; Helveg, S. *J. Am. Chem. Soc.* **2010**, *132*, 7968−7975.
(19) Simonsen, S. B.; Chorkendorff, I.; Dahl, S.; Skoglundh, M.; Sehested, J.; Helveg, S. *J. Catal.* **2011**, *281*, 147−155.
(20) Michely, T.; Comsa, G. *Surf. Sci.* **1991**, *256*, 217−226.
(21) Siddiqui, H. R.; Guo, X.; Chorkendorff, I.; Yates, J. *Surf. Sci.* **1987**, *191*, L813−L818.
(22) Ono, L. K.; Yuan, B.; Heinrich, H.; Cuenya, B. R. *J. Phys. Chem. C* **2010**, *114*, 22119−22133.
(23) Julukian, A.; Fadnes, T.; Raaen, S.; Balci, M. *J. Appl. Phys.* **2011**, *109*, 123502.
(24) Flores-Camacho, J. M.; Fischer-Wolfarth, J. H.; Peter, M.; Campbell, C. T.; Schauermann, S.; Freund, H. J. *Phys. Chem. Chem. Phys.* **2011**, *13*, 16800−16810.
(25) Horch, S.; Lorensen, H.; Helveg, S.; Laegsgaard, E.; Stensgaard, I.; Jacobsen, K.; Norskov, J.; Besenbacher, F. *Nature* **1999**, *398*, 134−136.
(26) Kibler, L.; Cuesta, A.; Kleinert, M.; Kolb, D. *J. Electroanal. Chem.* **2000**, *484*, 73−82.
(27) Mayrhofer, K. J. J.; Hanzlik, M.; Arenz, M. *Electrochim. Acta* **2009**, *54*, 5018−5022.
(28) Su, X.; Cremer, P.; Shen, Y.; Somorjai, G. *Phys. Rev. Lett.* **1996**, *77*, 3858−3860.
(29) Longwitz, S.; Schnadt, J.; Vestergaard, E.; Vang, R.; Laegsgaard, E.; Stensgaard, I.; Brune, H.; Besenbacher, F. *J. Phys. Chem. B* **2004**, *108*, 14497−14502.
(30) Yoshida, H.; Matsuura, K.; Kuwauchi, Y.; Kohno, H.; Shimada, S.; Haruta, M.; Takeda, S. *Appl. Phys. Express* **2011**, *4*, 065001.